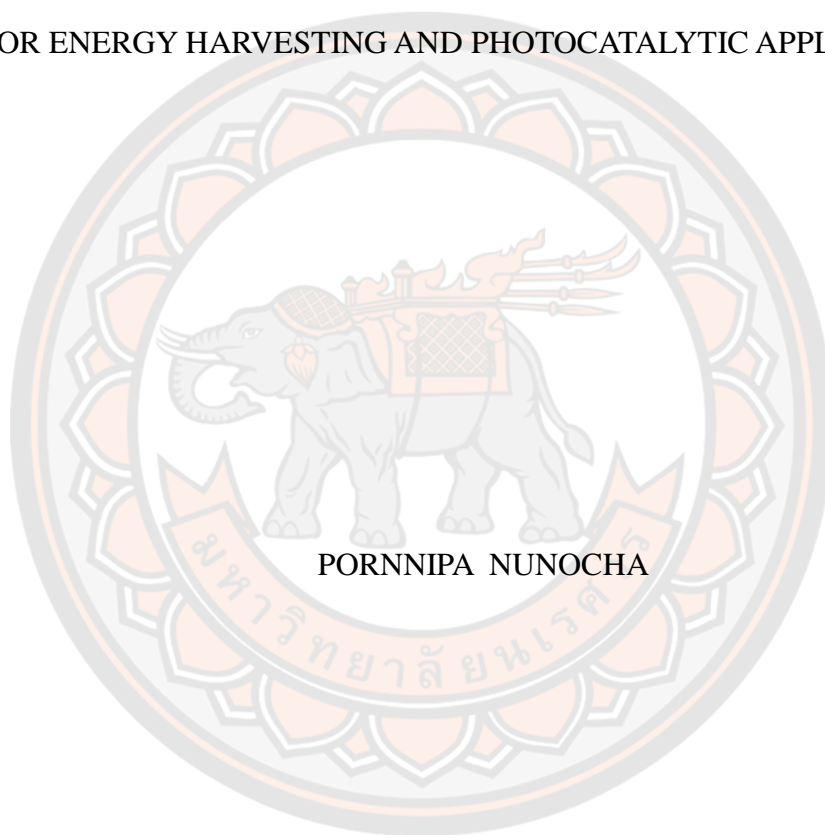




SOL-GEL AUTO COMBUSTION SYNTHESIS OF METAL OXIDE MATERIALS
FOR ENERGY HARVESTING AND PHOTOCATALYTIC APPLICATIONS.



PORNNIPA NUNOCHA

A Thesis Submitted to the Graduate School of Naresuan University
in Partial Fulfillment of the Requirements
for the Doctor of Philosophy in Renewable Energy

2023

Copyright by Naresuan University

SOL-GEL AUTO COMBUSTION SYNTHESIS OF METAL OXIDE MATERIALS
FOR ENERGY HARVESTING AND PHOTOCATALYTIC APPLICATIONS.



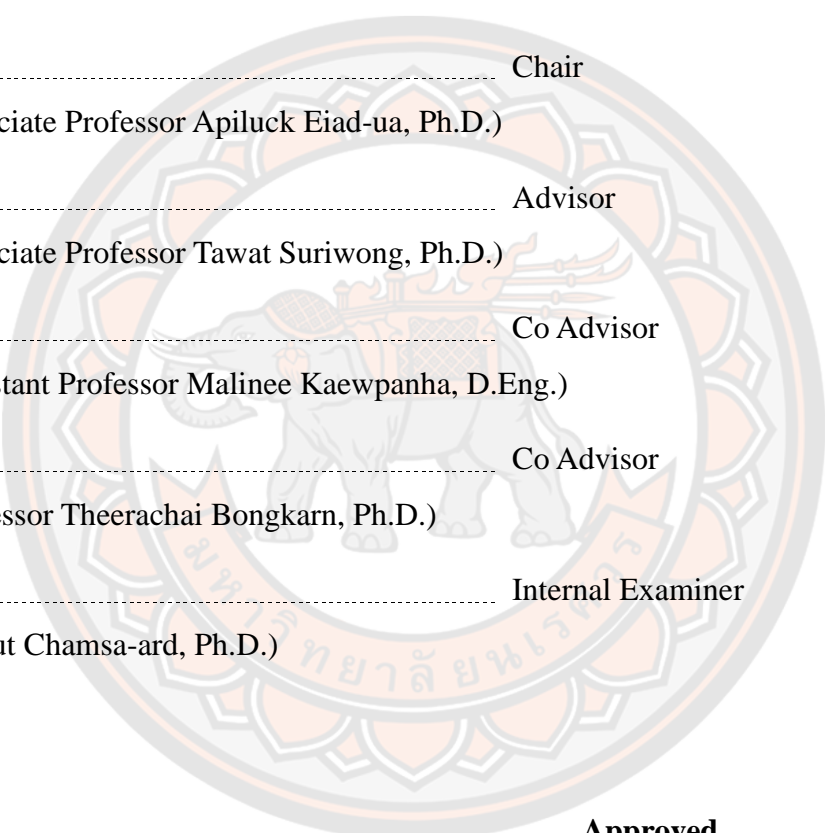
A Thesis Submitted to the Graduate School of Naresuan University
in Partial Fulfillment of the Requirements
for the Doctor of Philosophy in Renewable Energy
2023
Copyright by Naresuan University

Thesis entitled "Sol-gel auto combustion synthesis of metal oxide materials for energy harvesting and photocatalytic applications."

By Pornnipa Nunocha

has been approved by the Graduate School as partial fulfillment of the requirements for the Doctor of Philosophy in Renewable Energy of Naresuan University

Oral Defense Committee



..... Chair
(Associate Professor Apiluck Eiad-ua, Ph.D.)

..... Advisor
(Associate Professor Tawat Suriwong, Ph.D.)

..... Co Advisor
(Assistant Professor Malinee Kaewpanha, D.Eng.)

..... Co Advisor
(Professor Theerachai Bongkarn, Ph.D.)

..... Internal Examiner
(Wisut Chamsa-ard, Ph.D.)

Approved

.....
(Associate Professor Krongkarn Chootip, Ph.D.)
Dean of the Graduate School

Title	SOL-GEL AUTO COMBUSTION SYNTHESIS OF METAL OXIDE MATERIALS FOR ENERGY HARVESTING AND PHOTOCATALYTIC APPLICATIONS.
Author	Pornnipa Nunocha
Advisor	Associate Professor Tawat Suriwong, Ph.D.
Co-Advisor	Assistant Professor Malinee Kaewpanha, D.Eng. Professor Theerachai Bongkarn, Ph.D.
Academic Paper	Ph.D. Dissertation in Renewable Energy, Naresuan University, 2023
Keywords	Thermoelectric oxide, Thermoelectric properties, a Sol-gel combustion method, Nb-doped, La-doped, Ag-addition, photocatalytic activity, $\text{Ca}_3\text{Co}_4\text{O}_9$, SrTiO_3

ABSTRACT

This study explored the properties of different types of oxide materials synthesized using a sol-gel auto-combustion technique. The study investigated n-type materials such as $\text{Sr}_{1-x}\text{La}_x\text{TiO}_3$ (SLTO) and $\text{SrTi}_{1-x}\text{Nb}_x\text{O}_3$ (STNO), and p-type materials such as $\text{Ca}_{3-x}\text{Ag}_x\text{Co}_4\text{O}_9$ (CACO). The materials were characterized for their structural, optical, photocatalytic, and thermoelectric properties using various techniques such as XRD, SEM, SEM-EDS, UV-Vis, etc.

First, the study investigated the effect of La^{3+} substitution in Sr^{2+} on the structural and photocatalytic properties of SLTO powder. The results showed an increase in lattice parameters, unit cell density, and specific surface area with higher La doping content, while the crystallite and particle size decreased. The photocatalytic activity of SLTO increased with increasing La content and reached a maximum at $x = 0.07$, with the proposed mechanism highlighting the role of oxygen vacancies in the structure. The study also found that SLTO bulk ceramics produced using spark plasma sintering (SPS), exhibited promising thermoelectric properties, with the highest values of electrical conductivity, negative Seebeck coefficient, and dimensionless figure of

merit (ZT) at $x = 0.01$ at 800 K.

Second, the study investigated the effect of Nb doping on STNO powder properties. The results showed that Nb doping increased the number of lattice parameters and unit cell density, and decreased the particle size. The photocatalytic activity of STNO increased with increasing Nb content, peaking at $x = 0.05$. The study suggests that Nb doping can enhance the photocatalytic performance of STNO.

Lastly, the study successfully synthesized the high-density CACO bulk by using sol-gel auto combustion, followed by SPS technique. The thermoelectric properties of CACO bulk samples were investigated. The addition of Ag resulted in porosity and non-uniform chemical distributions. All samples exhibited a positive Seebeck coefficient and decreasing thermal conductivity with increasing temperature. The maximum ZT value of 0.18 at 950 K for $x = 0$ suggests the potential of CACO-based materials as thermoelectric materials.

Overall, the study findings suggest that the synthesized oxide materials by sol-gel auto combustion technique, have promising potential for use in energy harvesting and conversion and could be useful in various photocatalytic applications.

ACKNOWLEDGEMENTS

I am grateful for the support of the Thailand Science Research and Innovation (TSRI) and the National Research Council of Thailand (NRCT) through the Royal Golden Jubilee Ph.D. Program (PHD/0049/2560). Their generous funding allowed me to carry out this thesis, and their continuous support throughout the thesis has been invaluable.

I would like to express my deepest gratitude to my supervisor, Assoc. Prof. Dr. Tawat Suriwong, for his guidance, patience, and invaluable advice throughout my thesis research. His insightful comments and suggestions were instrumental in shaping the direction of my research. I would also like to thank my co-advisor, Asst. Prof. Dr. Malinee Kaewpanha, and Prof. Dr. Theerachai Bongkarn for their comments, suggestions, and support. I am truly grateful for their assistance.

I would also like to thank the members of my thesis committee, Assoc. Prof. Dr. Apiluck Eiad-Ua and Dr. Wisut Chamsa-ard, for their constructive feedback and valuable input. Their expertise and guidance have been crucial in helping me refine my research and make it a more comprehensive study.

I am deeply indebted to my family for their unwavering support and encouragement throughout my academic journey. Their love and encouragement have been my constant source of strength and motivation.

I would like to extend my appreciation to my colleagues and friends, for their support, encouragement, and friendship. Their moral support, invaluable advice, and stimulating discussions have been instrumental in shaping my research and making it a more rewarding experience.

Lastly, I am grateful to the staff and School of Renewable Energy and Smart Grid Technology, Naresuan University, for their unwavering support and for providing me with a stimulating academic environment that has enriched my intellectual growth.

Thank you all for your support and encouragement.

Pornnipa Nunocha

TABLE OF CONTENTS

	Page
ABSTRACT.....	C
ACKNOWLEDGEMENTS.....	E
TABLE OF CONTENTS.....	F
TABLE OF CONTENT.....	H
FIGURE OF CONTENT.....	I
CHAPTER I INTRODUCTION.....	1
1.1 Purposes of the Study	4
1.2 Scope of the Study	4
CHAPTER II THEORIES AND RELATED LITERATURE.....	6
2.1 Thermoelectric.....	6
2.1.1 The Seebeck effect	6
2.1.2 The Peltier effect	7
2.1.3 Dimensionless figure of merit	9
2.1.4 The development of thermoelectric materials	10
2.2 Related Works.....	12
2.2.1 Thermoelectric oxide.....	12
2.2.2 SrTiO ₃ - based TE materials	21
2.2.3 Ca ₃ Co ₄ O ₉ - based TE materials	38
2.2.4 Sol-Gel auto-combustion method.....	47
CHAPTER III RESEARCH METHODOLOGY	56
3.1 Chemical reagents and equipment	56
3.2 Methodology.....	57
3.2.1 Synthesis and Characterize of La-doped SrTiO ₃ for photocatalytic applications.....	57
3.2.2 Synthesis and Characterize of La-doped SrTiO ₃ for thermoelectric applications.....	60

3.2.3 Synthesis and Characterize of Nb-doped SrTiO_3 for photocatalytic applications.....	62
3.2.4 Synthesis and Characterize of Ag dope $\text{Ca}_3\text{Co}_4\text{O}_9$ for thermoelectric applications.....	65
CHAPTER IV RESULT AND DISCUSSION	67
4.1 La dope SrTiO_3	67
4.1.1 Characterization of phase, morphology, and optical properties	67
4.1.2 Characterization of thermoelectric properties	85
4.2 Nb dope SrTiO_3	98
4.2.1 Characterization of phase, morphology, and optical properties	98
4.3 Ag dope $\text{Ca}_3\text{Co}_4\text{O}_9$	115
4.3.1 Characterization of thermoelectric properties	115
CHAPTER V CONCLUSION AND RECOMMENDATION	135
5.1 Conclusion.....	135
REFERENCES	137
APPENDIX.....	150
BIOGRAPHY	186

TABLE OF CONTENT

	Page
Table 1 Room-temperature thermoelectric responses of La-doped and Nb-doped single crystal SrTiO_3	32
Table 2 Lattice parameter, Chi squared (χ^2), Rietveld discrepancy factors (R_p , R_{wp} , R_{exp}) and Calculated cell density (d_{cal}) and crystallite size of SLTO ($x = 0, 0.03, 0.05, 0.07$ and 0.1)	70
Table 3 The pore distribution of the SLTO sample	75
Table 4 Chi-square (χ^2), R-factors (R_p , R_{wp} , R_{exp}), lattice parameter, cell volume, and calculated cell density (d_{cal}) of SLTO ($x = 0, 0.01, 0.05, 0.07$, and 0.10) powder and bulk.	87
Table 5 Lattice parameter, Chi-squared (χ^2), Rietveld discrepancy factors (R_p , R_{wp} , R_{exp}) and Calculated cell density (d_{cal}) and crystallite size of STNO ($x = 0, 0.01, 0.03$ and 0.05)	102
Table 6 The summary of the photodecolorization efficiency (%DE) of several dyes using undoped-STO and metal-doped STO photocatalysts with different preparation methods, light sources, and photocatalytic conditions.	114
Table 7 Chi-square (χ^2), R-factors (R_p , R_{wp} , R_{exp}), lattice parameter, occupancy, and percentage of phase refinement for the CACO bulk sample.	119
Table 8 The summary of the thermoelectric properties of dope/addition $\text{Ca}_3\text{Co}_4\text{O}_9$ with different preparation methods.	134

FIGURE OF CONTENT

	Page
Figure 1 Illustration of how a thermoelectric material can convert heat directly to electricity (Seebeck effect) and also how the material can heat up or cool down at an electrified junction (Peltier effect)	2
Figure 2 Thermoelectric diagrams for power generation modules.	7
Figure 3 Diagram of a thermoelectric module used for cooling or heat pump.....	9
Figure 4 Maximizing the efficiency (ZT) of a thermoelectric involves a compromise of thermal conductivity and Seebeck coefficient with electrical conductivity	10
Figure 5 The timeline for the highest ZT of oxide thermoelectric materials	12
Figure 6 (a) Thermoelectric module (b) a measurement system for generated power and (c) Thermoelectric power generation properties	13
Figure 7 Summary of thermoelectric material structure from the macro- to nanoscale	14
Figure 8 Maximum theoretical efficiencies for thermoelectric oxides using $T_{\text{cold}} = 300\text{K}$ and maximum ZT values	15
Figure 9 Comparison of various nanostructures between random nanocomposites (a–e) and ordered nanocomposite (f–j)	15
Figure 10 The ZT as a function of temperature and year revealing the important development of thermoelectric materials.....	16
Figure 11 History of Efforts in increasing ZT	17
Figure 12 Maximizing the efficiency (ZT) of a thermoelectric involves a compromise of thermal conductivity with electrical conductivity.....	18
Figure 13 Figure of Merit, ZT of Thermoelectric, as a function of temperature and year illustrating important milestones.....	19
Figure 14 Schematic illustration of the ZT optimization strategies based on defect engineering from the perspective of multiple degrees of freedom synergistic modulation	20
Figure 15 Thermoelectric materials research is an application-driven multidisciplinary topic of fundamental research	20
Figure 16 SEM micrograph of $\text{Sr}_{0.94}\text{Ti}_{0.9}\text{Nb}_{0.1}\text{O}_{3-\delta}$ powder.....	21

Figure 17 TEM image of the synthesized SrTiO_3 powders calcined at 673 K for 2h .	22
Figure 18 Temperature dependence of dimensionless figures of merit for various holding times during sintering	22
Figure 19 Temperature dependence of ZT for $\text{La}_{0.08}\text{Sr}_{0.92}\text{TiO}_3$ bulks SPSed at 1203 K, 1373 K and 1473 K	23
Figure 20 Temperature dependence of the ZT of $\text{La}_{0.1}\text{Sr}_{0.9-x}\text{Dy}_x\text{TiO}_3$	24
Figure 21 Temperature dependence of the ZT of $\text{Sr}_{0.9}\text{La}_{0.1}\text{Ti}_{1-x}\text{Ta}_x\text{O}_3$ ceramics	25
Figure 22 Temperature dependence of the ZT of $\text{La}_{0.1}\text{Sr}_{0.9-x}\text{Yb}_x\text{TiO}_3$ ceramics.....	25
Figure 23 Comparison of the PF between 5LaSTO and Nb-5LaSTO, showing an effective PF increase in the case of Nb-5LaSTO	26
Figure 24 Temperature dependence of the ZT for the compound $\text{Sr}_{0.9}\text{La}_{0.1}\text{TiO}_{3/x}\text{Ag}$ (a) and $\text{Sr}_{2.7}\text{La}_{0.3}\text{Ti}_2\text{O}_{7/x}\text{Ag}$ (b) ($x = 0$ and 15%)	27
Figure 25 Temperature dependence of thermal conductivity of (a) undoped SrTiO_3 single crystal and (b) La-doped (10 mol.%) ceramics with different grain size in linear	28
Figure 26 Temperature dependence of the figure of merit for $(\text{Sr}_{1-x}\text{Gd}_x)\text{TiO}_{3-\delta}$ ceramics. Data for $(\text{Sr}_{0.9}\text{Gd}_{0.1})\text{TiO}_3$, $(\text{Sr}_{0.9}\text{Pr}_{0.1})\text{TiO}_3$, $(\text{Sr}_{0.92}\text{La}_{0.08})\text{TiO}_3$, and $\text{Sr}(\text{Ti}_{0.8}\text{Nb}_{0.2})\text{O}_3$ are taken for comparison	28
Figure 27 (a) XRD patterns and (b) Thermoelectric figure of merit ZT versus temperature for $\text{Sr}_{1-1.5x}\text{Y}_x\text{TiO}_{3-\delta}$	29
Figure 28 SEM images of samples after SCS prepared, calcined and washed.....	30
Figure 29 Temperature dependence of (a) The PF and (b) The ZT value for the $\text{Sr}_{0.9}\text{La}_{0.1}\text{TiO}_{3/x}\text{Ti}$ compounds ($x = 5, 10, 15$ and 20 wt%, numbered as SLT1#, SLT2#, SLT3#, SLT4#, respectively)	31
Figure 30 Temperature dependence of ZT for $\text{Sr}_{1-x}\text{La}_{x/2}\text{Sm}_{x/2}\text{TiO}_{3-\delta}$ ($0.05 \leq x \leq 0.30$) ceramics sintered in 5% H_2/N_2 at 1773 K for 6 hours	33
Figure 31 Temperature dependence of ZT for the $\text{La}_{0.1}\text{Dy}_x\text{Sr}_{1-1.25(0.1+x)}\text{TiO}_3$ ceramics	34
Figure 32 (a) Schematic diagram of the scattering mechanism for the non-stoichiometric samples with step-like microstructure and (b) Temperature dependence of the ZT for the $\text{La}_{0.1}\text{Dy}_{0.1}\text{Sr}_x\text{TiO}_3$ ceramics	34
Figure 33 Temperature dependence of (a) electrical conductivity (σ), (b) Seebeck coefficient (S), (c) thermal conductivity (κ) and (d) dimensionless figure-of-merit (ZT) of the bulk SrTiO_3 samples with different La contents.....	35

Figure 34 Micrographs and maps for samples containing Fe: (a) Backscattered electron (SE) image; (b-f) Elemental maps:(b) Sr, (c) Ti, (d) Nb, (e) Fe, (f) O; (g-i) EBSD maps:(g) Band contrast map with grain boundaries showing sharp contrast, (h) Phase distribution map of Fe particles (red) and rutile based phase (yellow) in the $\text{Sr}_{0.8}\text{La}_{0.06}\text{Ti}_{0.8}\text{Nb}_{0.2}\text{O}_3$ primary phase, (i) Euler false color maps indicating random orientation of primary phase grains	37
Figure 35 Dimensionless figure of merit ZT of the $\text{Ca}_{2.9}\text{M}_{0.1}\text{Co}_4\text{O}_9$ ($\text{M} = \text{Ca}, \text{Ba}, \text{La}, \text{Ag}$) bulk samples	38
Figure 36 Temperature dependence of the power factor as a function of Cr content in $\text{Ca}_3\text{Co}_{4-x}\text{Cr}_x\text{O}_9$ samples, for $x = 0.00$ (●); 0.01 (◆); 0.03 (■); 0.05 (▲); and 0.10 (▼)...	39
Figure 37 The temperature dependence of the ZT measured along the \perp and \parallel directions	40
Figure 38 Temperature dependence of Seebeck coefficient (S) of $\text{Ca}_{3-x}\text{B}_x\text{Co}_4\text{O}_9$ ($x = 0, 0.5, 0.75$, and 1)	41
Figure 39 SEM images of $\text{Ca}_3\text{Co}_4\text{O}_9$	42
Figure 40 Temperature variation of (a) thermopower and (b) ZT for $\text{Ca}_{3-x}\text{Pb}_x\text{Co}_4\text{O}_9$ ($x = 0 - 0.5$) samples	43
Figure 41 Temperature dependence of the thermal diffusivity as a function of the Co_3O_4 content	44
Figure 42 The ZT of the Ba and Pr dual doped $\text{Ca}_3\text{Co}_4\text{O}_{9+\delta}$ bulk specimens	45
Figure 43 Temperature dependencies of ZT in the $\text{Ca}_{3-x}\text{Na}_x\text{Co}_4\text{O}_{9-x}\text{F}_x$ samples	45
Figure 44 Thermoelectric parameters of a $\text{Ca}_3\text{Co}_4\text{O}_9$ ceramic	46
Figure 45 (a-d) SEM micrographs of SrTiO_3 at calcination temperature (a) 773 K, (b) 873 K, (c) 973 K and (d) 1073 K and (e-f) TEM micrographs of SrTiO_3 (e) before and (f) after coupled with an acid treatment process calcined at temperature of 873 K	48
Figure 46 SEM images of the powders calcined at different temperatures for 2 h: (a) 1173 K and (b) 1273 K	49
Figure 47 SEM micrographs of the $\text{Ba}_{0.7}\text{Sr}_{0.3}\text{TiO}_3$ ceramics with urea as fuel sintered at different temperatures : (a) 1223 K, (b) 1323 K, (c) 1423 K, (d) 1523 K, (e) 1623 K	50
Figure 48 Thermoelectric properties of the synthesized Cu_2SnSe_3 samples	51
Figure 49 (a) Various stages involved in the synthesis of $\text{Zn}_{1-x}\text{Co}_x\text{O}$ ($x = 0.00, 0.06, 0.12$ mol) nanoparticles. (b) Scheme of sol-gel auto combustion synthesis method of $\text{Zn}_{1-x}\text{Co}_x\text{O}$ ($x = 0.00, 0.06$ and 0.12 mol) nanoparticles	52

Figure 50 (a) Seebeck coefficient and (b) power factor of STNO synthesized using various surfactant concentrations.....	53
Figure 51 Scheme of synthesized La-doped SrTiO_3 by sol-gel auto combustion.	58
Figure 52 Scheme of synthesized La-doped SrTiO_3 by sol-gel auto combustion followed by SPS.....	61
Figure 53 Scheme of synthesized Nb-doped SrTiO_3 by sol-gel auto combustion.....	63
Figure 54 Scheme of synthesized Ag-doped $\text{Ca}_3\text{Co}_4\text{O}_9$ by sol-gel auto combustion followed by SPS.....	65
Figure 55 Weight loss (TG) and DTG curves of as-prepared SLTO ($x = 0$) precursor.	67
Figure 56 (a) XRD patterns of the SLTO ($x = 0, 0.03, 0.05, 0.07$ and 0.1) nanopowder (b) magnified view of the main XRD peak.....	68
Figure 57 Typical Rietveld refinement analysis of SLTO, (a) $x = 0$ and (b) $x = 0.1$	70
Figure 58 (a) Variation of the lattice parameter and calculated cell density (d_{cal}) of SrTiO_3 JCPDS no 00-035-0734 and SLTO ($x = 0, 0.03, 0.05, 0.07$ and 0.1) (b) The simulate structure of SLTO with $x = 0.1$	71
Figure 59 (a-e) SEM image and (f) the average particle size of SLTO nanopowder...	73
Figure 60 SEM-EDS images of the $\text{Sr}_{0.9}\text{La}_{0.1}\text{TiO}_3$ nanopowder.....	74
Figure 61 The specific surface area and total pore volume of the SLTO samples, (inset) the Nitrogen adsorption-desorption isotherms of typical SLTO ($x = 0.07$) sample.	74
Figure 62 UV-vis spectra of the SLTO ($x = 0, 0.03, 0.05, 0.07$ and 0.1) nanopowder, together with an inset plots of $(\alpha h\nu)^2$ as a function of phonon energy ($h\nu$).....	79
Figure 63 (a) Photocatalytic decolorization efficiency (%DE) of MB irradiated under the UV lamps (b) Pseudo-first order kinetics of the photocatalytic decolorization of MB (c) Time dependent UV-Vis spectra of MB solution for SLTO nanopowder for $x = 0.07$ and (d) Photoluminescence (PL) spectra of the SLTO nanopowders for $x = 0$ and 0.07	80
Figure 64 A schematic of the PL emissions of SLTO due to the recombination of conduction electron-valence holes.	82
Figure 65 A schematic diagram for photocatalysis of SLTO nanopowder.....	84
Figure 66 XRD pattern of SLTO sample with different La content ($x = 0, 0.01, 0.05, 0.07$, and 0.10): a) after calcination, and b) after SPS process	85

Figure 67 Typical Rietveld refinement analysis of SLTO sample for $x=0.10$: (a) powder and (b) bulk samples	86
Figure 68 Variation of the measured densities (d) and relative density of SLTO bulk samples as a function of La content (x)	89
Figure 69 SEM of the SLTO powder sample with different La content ($x = 0, 0.01, 0.05, 0.07, \text{ and } 0.10$)	89
Figure 70 SEM and EDS mapping analysis of the SLTO bulk samples.....	91
Figure 71 Temperature dependence of the electrical properties of SLTO bulk samples: (a) electrical conductivity (σ), (b) Seebeck coefficient (S), and (c) power factor (PF, $S^2\sigma$).	92
Figure 72 Temperature dependence of (a) thermal conductivity (κ) and (b) lattice thermal conductivity (κ_{lat}) of the SLTO bulk samples.....	95
Figure 73 Temperature dependence of dimensionless figure-of-merit ZT of the bulk SLTO sample with different La concentrations.	97
Figure 74 (a) XRD patterns of STNO powder with $x = 0, 0.01, 0.03 \text{ and } 0.05$ and JCPDS of STO (b) magnified view of the main XRD peak.	99
Figure 75 Rietveld refinement analysis of STNO samples: (a) $x = 0$, (b) $x = 0.01$, (c) $x = 0.03$ and (d) $x = 0.05$	100
Figure 76 (a) The lattice parameter and calculated cell density (d_{cal}) of STNO nanopowder and (b) the crystal structure of STNO with $x = 0.05$ from Rietveld refinement analysis compared with SrTiO_3 database.	101
Figure 77 SEM image of STNO nanopowder: (a) $x = 0$, (b) $x = 0.01$, (c) $x = 0.03$, and (d) $x = 0.05$	103
Figure 78 SEM-EDS images and spectrum of the STNO nanopowder with $x = 0.05$	103
Figure 79 UV-vis spectra of the STNO samples ($x = 0, 0.01, 0.03 \text{ and } 0.05$) and inset plots of $(\alpha h\nu)^2$ as a function of photon energy ($h\nu$).....	105
Figure 80 (a) The photocatalytic decolorization efficiency (%DE) of MB irradiated beneath the UV lamp (b) The Pseudo-first order kinetics of photocatalytic decolorization of MB (c) Time-dependent absorption spectra of MB solution using STNO photocatalyst with $x = 0.05$ (d) photoluminescence spectra of the STNO sample with $x = 0$ and 0.05	108
Figure 81 Experimental data and simulation of EIS Nyquist plot of STNO photocatalyst sample.....	109

Figure 82 A Mott-Schottky plot of STNO nanopowder.	111
Figure 83 The charge transfer and photocatalytic mechanism of STNO nanopowder.	112
Figure 84 (a) The XRD pattern of the Ag addition $\text{Ca}_3\text{Co}_4\text{O}_9$ ($x = 0, 0.1, 0.2, 0.3, 0.4$, and 0.5) powder sample (b) magnified view of the main XRD peak	115
Figure 85 (a) The XRD pattern of the Ag addition $\text{Ca}_3\text{Co}_4\text{O}_9$ ($x = 0, 0.1, 0.2, 0.3, 0.4$, and 0.5) bulk sample, and (b) magnified view of the main XRD peak.	116
Figure 86 Rietveld refinement analysis of CACO bulk sample.	120
Figure 87 The measured densities (d) and relative density of CACO bulk sample...	121
Figure 88 Fractured cross-section SEM images of the CACO bulk sample with different Ag content.	122
Figure 89 The surface SEM images of the CACO bulk sample with different Ag content.....	122
Figure 90 (a-b) Fractured cross-section and (c) surface SEM and EDS mapping analysis of the CACO bulk samples	124
Figure 91 The Vickers hardness result of the CACO sample	125
Figure 92 Temperature dependence of the electrical properties of CACO bulk samples: (a) electrical conductivity (σ), (b) Seebeck coefficient (S), and (c) power factor ($PF, S^2\sigma$).....	126
Figure 93 Temperature dependence of (a) thermal conductivity (κ) and (b) lattice thermal conductivity (κ_{lat}) of the CACO bulk samples.	130
Figure 94 Temperature dependence of dimensionless figure-of-merit ZT of the bulk CACO sample with different La concentrations.....	132

CHAPTER I

INTRODUCTION

The data indicates that a significant portion, specifically 65%, of the energy generated from burning fossil fuels or fission nuclear power plants is lost, primarily in the form of waste heat [1, 2]. This waste heat can be recycled as a heat source, also known as Heat Recovery. Thermoelectric (TE) technology is a kind of renewable energy approach, that can be directly converted between heat and electricity as shown in Figure 1 [3]. This technology is environmentally friendly and offers several benefits such as small size, high reliability, no pollution, and the ability to operate within a wide range of temperatures. Thermoelectric efficiency depends on the difference between the source and sinks temperatures. Physical properties of the thermoelectric material affect the figure of merit, ZT which is $ZT = S^2 \sigma T / \kappa$ where, S is the Seebeck coefficient, σ is the electrical conductivity, κ is the thermal conductivity and T is the mean operating temperature [4]. For a good thermoelectric, the properties are high electrical conductivity, high Seebeck coefficient, and low thermal conductivity [3, 5]. That is a type of “phonon glass - electron crystal” (PGEC). For applications in waste heat recovery and refrigeration, there exists a range of TE materials that differ in terms of their operating temperature range, an abundance of constituent elements, and environmental friendliness [6].

The ZT values of several materials, including Bi_2Te_3 and PbTe , are above 1. Their unattractiveness, especially for high-temperature ($T \sim 1000$ K) operations, stems from the fact that their components can readily decay, evaporate, or melt. In addition, the utilization of these heavy metals must be confined to particular settings, such as space, due to their usual toxicity, limited abundance, and environmental unsoundness [7]. On the basis of this background, metal oxides have attracted a great deal of interest because they are basically stable and environmentally friendly at high temperatures [8]. Thermoelectric oxides made up of inexpensive, naturally abundant, non-toxic, and lightweight elements are anticipated to have a significant impact on various waste heat recovery applications in an air atmosphere [9]. The oxides have

advantages over traditional heavy-element based compounds because they have upper thermal stability and ability to resist oxidation reactions, that may release toxic substances [10].

In the last ten years, the most studied thermoelectric materials are the p-type ($\text{Ca}_3\text{Co}_4\text{O}_9$) and n-type (ZnO , SrTiO_3 , and CaMnO_3) [11]. Although Na_xCoO_2 based materials have better thermoelectric performance, $\text{Co}_3\text{Co}_4\text{O}_9$ based materials possess better stability and are more widely used. Out of the three commonly researched n-type oxides, CaMnO_3 doped with impurities exhibits lower thermal conductivity, whereas doped SrTiO_3 and ZnO exhibit higher electrical conductivity [12].

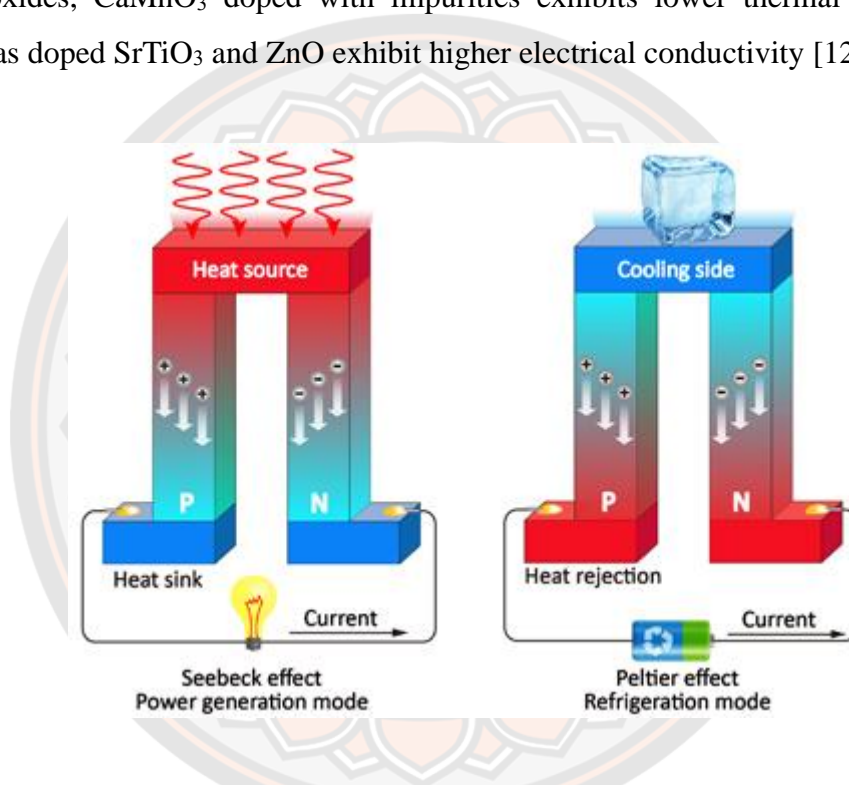


Figure 1 Illustration of how a thermoelectric material can convert heat directly to electricity (Seebeck effect) and also how the material can heat up or cool down at an electrified junction (Peltier effect) [3].

Nowadays, high-performance n-type oxide thermoelectric materials are rare with ZT value barely exceeding 0.5 [13]. Perovskite oxide SrTiO_3 , one of the best n-type thermoelectric oxides known to date, with a high-power factor at room temperature which is comparable to commercial thermoelectric materials such as Bi_2Te_3 [14, 15]. The SrTiO_3 (STO) perovskite shows potential as a suitable contender for n-type thermoelectric materials designed to function at high temperatures [12, 16,

17], and for the next generation thermoelectric devices; because there are several advantages including good environmental compatibility, and high thermal and chemical stability [7, 14]. The $\text{Ca}_3\text{Co}_4\text{O}_9$ (CCO) has been reported as one of the promising p-type thermoelectric oxide materials for high-performance applications [5, 18-20]. The best thermoelectric properties of p-type oxides are layered cobaltite compounds [12]. Whereas the ZT value of undoped $\text{Ca}_3\text{Co}_4\text{O}_9$ at 1000 K has been specified as 0.3 by Walia et al. [21].

Advancements in thermoelectric performance have been made in various types of materials, including low-dimensional materials, bulk nanostructured materials, and conventional bulk materials. These developments particularly highlight the role of nanostructure in nanostructured composites, confinement effects in one-dimensional nanowires, and doping effects in conventional bulk composites, which are crucial for enhancing ZT [22]. The metal doping with elements such as Ba, Nb, Bi can improve thermoelectric properties. As reported, Ba is an effective dopant in enhancing electrical transport properties for lowering valance electron and decreasing thermal conductivity for large atomic mass [23, 24]. The Nb-doped SrTiO_3 was fabricated as epitaxial films, poly, and single crystals. Recent attempts have been made to lower the thermal conductivity of Nb-doped STO, including the combination of bulk materials with low-thermal-conductivity constituents such as mesoporous silica with ZT values reaching 0.37 at 1000 K, 0.35 at 1000 K, and 0.17 at 1073 K, respectively [16, 25-28].

Current methods of producing thermoelectric materials typically involve multi-step processes that consume significant time and energy, including solid-state reactions, hydrothermal synthesis, combustion synthesis, sol-gel methods, ultrasonic spray pyrolysis, co-precipitation, peroxide-based synthesis, polymeric precursor methods, solvothermal synthesis, molten salt synthesis, and sol-gel combustion synthesis [29]. However, some of these methods are time-consuming (ranging from hours to days), require high input energy, characterized with difficult process temperature control, and their operating temperatures are usually above 1973 K; except the sol-gel combustion method. The latter process has the advantages such as completing the synthesis in a very short period of time (minutes), utilizing simple equipment and technology, being feasible at very high processing temperatures (up to

4273 K), achieving precise stoichiometric control, producing high-purity materials, and ensuring homogeneity [29-35].

This research focuses on the phase, morphological, optical properties, and thermoelectric properties of oxides materials; p-type $\text{Ca}_3\text{Co}_4\text{O}_9$ and n-type SrTiO_3 , with doped oxide metal (Nb-doped SrTiO_3 , La-doped SrTiO_3 , and Ag-doped $\text{Ca}_3\text{Co}_4\text{O}_9$), which are promising materials with improved ZT values. The thermoelectric material synthesis will encompass an amalgamation of the sol-gel method and the combustion technique.

1.1 Purposes of the Study

1. To prepare thermoelectric oxide materials by sol-gel auto combustion and characterize phase, morphology, and optical properties of Nb-doped SrTiO_3 , La-doped SrTiO_3 , and Ag-doped $\text{Ca}_3\text{Co}_4\text{O}_9$ samples.
2. To determine thermoelectric properties (Seebeck coefficient, electrical resistivity, and thermal conductivity) of Nb-doped SrTiO_3 , La-doped SrTiO_3 , and Ag-doped $\text{Ca}_3\text{Co}_4\text{O}_9$ bulk samples.
3. To determine photocatalytic properties of Nb-doped SrTiO_3 and La-doped SrTiO_3 .

1.2 Scope of the Study

1. Synthesis of the thermoelectric oxide materials by sol-gel auto combustion: n-type (Nb-doped SrTiO_3 and La-doped SrTiO_3) and p-type (Ag-doped $\text{Ca}_3\text{Co}_4\text{O}_9$).
2. Characterization of phase, morphology, and optical properties of Nb-doped SrTiO_3 , La-doped SrTiO_3 , and Ag-doped $\text{Ca}_3\text{Co}_4\text{O}_9$ samples using XRD, Raman, SEM, SEM/EDX, Luminescent and UV-vis Near IR
3. Determination of thermoelectric properties of Nb-doped SrTiO_3 , La-doped SrTiO_3 , and Ag-doped $\text{Ca}_3\text{Co}_4\text{O}_9$ bulk samples using TEP (ULVAC ZAM-1) and Thermal-constant (ULVAC, TC 700), including the feasibility study for TE applications based on simulation.

4. Determination of photocatalytic properties of Nb-doped SrTiO_3 and La-doped SrTiO_3 by considering the decolorization of methylene blue (MB) in an aqueous solution under UV irradiation.



CHAPTER II

THEORIES AND RELATED LITERATURE

2.1 Thermoelectric

Thermoelectric is the direct conversion between heat (temperature differences) and electricity (voltage). This phenomenon was discovered in 1821 and is called the “Seebeck effect,” while the reverse process of this phenomenon, called Peltier effect, was discovered by Peltier in 1834. Thermoelectric applications can be classified based on the direction of energy conversion. The Peltier effect is typically employed in thermoelectric cooling systems, whereas the Seebeck effect facilitates the conversion of temperature differences into an electric voltage. The advantages of the thermoelectrics are that: it is environmentally friendly; recycle wasted heat energy; scalable (i.e. the TE can be applied to any size heat source); dependable energy source, and lower production cost. However, thermoelectrics has certain limitations, including low energy conversion efficiency rates, slow technological advancement, and dependence on a relatively consistent heat source.

2.1.1 The Seebeck effect

The Seebeck effect is the direct conversion of heat into electricity that occurs at the junction of two dissimilar wires. It was first observed by Thomas Johann Seebeck, who noticed that a compass needle would deviate from its usual orientation when placed near a junction of two dissimilar metals with a temperature difference. At first, Seebeck believed this to be a magnetic effect, but he later realized that it was an electromotive force that could result in a measurable voltage or current in a closed loop between two ends of a material due to a temperature gradient across that material. This effect is a classic example of an electromotive force and produces measurable currents or voltages in the same way as any other emf in thermoelectric materials. Seebeck phenomenon can be written in terms of potential difference and temperature difference, as in Equation 1.

$$S = \frac{\Delta V}{\Delta T} \quad (1)$$

Where:

S = Seebeck coefficient, V/K

ΔV = Potential difference, V

ΔT = Temperature difference between hot and cold side, K

Since the voltages generated by the Seebeck effect are generally low, the Seebeck coefficient, which measures the magnitude of the effect, is typically expressed in microvolts per kelvin of temperature difference (μ V/K). The Seebeck effect is utilized in thermocouples for measuring temperature or converting waste heat into electrical power in power plants, provided there is a significant temperature difference across the material. Typically, n-type materials (with negative values) exhibit larger Seebeck coefficients compared to p-type materials (with positive values) at a given carrier concentration due to the higher effective mass of electrons compared to holes. Figure 2 show the utilization of the Seebeck phenomenon through thermoelectric material for thermoelectric power generation.

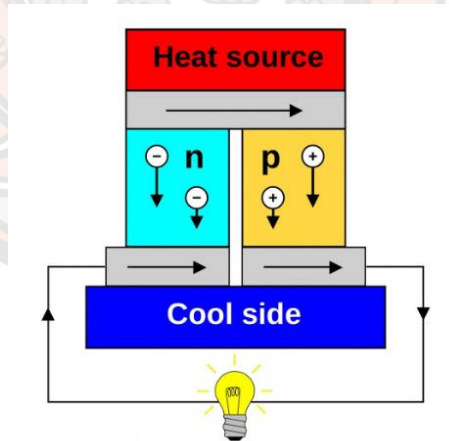


Figure 2 Thermoelectric diagrams for power generation modules.

2.1.2 The Peltier effect

In 1834, Jean Charles Athanase Peltier discovered that the flow of current through a circuit composed of two different conductors would cause a heating or cooling effect at the junctions between the two materials, which is now known as the

Peltier effect. This phenomenon is characterized by a change in temperature at the electrified junction between two dissimilar conductors, where the temperature can either increase or decrease, leading to heat generation or removal at the junction. The Peltier effect is essentially the reverse process of the Seebeck effect. In a simple thermoelectric circuit, the Seebeck effect drives a current, which in turn, through the Peltier effect, transfers heat from the hot junction to the cold junction. The Peltier effect can be utilized in cooling devices like refrigerators or heat pump devices that involve multiple current-carrying junctions in series. The Peltier coefficient is related to the Seebeck coefficient, as in Equation 2.

$$\Pi = ST \quad (2)$$

Where:

$$\begin{aligned} \Pi &= \text{Peltier coefficient, V/K} \\ S &= \text{Seebeck coefficient, V/K} \\ T &= \text{Temperature, K} \end{aligned}$$

The Peltier heat (Q) generated per unit time at the junction of two dissimilar metals A and B, is equal to:

$$Q = \Pi_{AB} I \quad (3)$$

When representing equation 2 in equation 3

$$Q = SIT \quad (4)$$

Where:

$$\begin{aligned} Q &= \text{Peltier heat, W} \\ \Pi_{AB} &= \text{Peltier coefficient, V/K} \\ S &= \text{Seebeck coefficient, V/K} \\ I &= \text{Electric current across this junction, A} \\ T &= \text{Temperature, K} \end{aligned}$$

Peltier effect devices produce a temperature difference where one junction becomes cooler, and the other junction becomes hotter. Although they may not be as efficient as some other cooling devices, Peltier coolers are precise, easy to regulate,

and simple to adjust. Figure 3 depicts a thermoelectric module used in cooling or heat pump application.

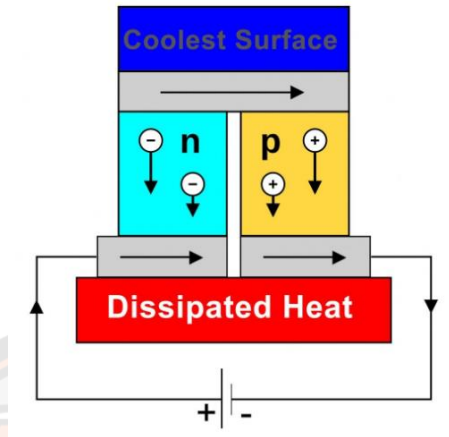


Figure 3 Diagram of a thermoelectric module used for cooling or heat pump

2.1.3 Dimensionless figure of merit

Thermoelectric materials utilize the Seebeck and Peltier effects to convert heat energy into electrical energy, allowing for the efficient utilization of thermal energy that would otherwise be unusable or lost in various applications. The efficiency of heat conversion is characterized by the figure of merit (ZT) as given in the relation:

$$ZT = \frac{S^2 \sigma T}{\kappa} = \frac{S^2 T}{\rho \kappa} \quad (5)$$

Where:

ZT	=	Figure of merit
S	=	Seebeck coefficient, V/K
σ	=	Electrical conductivity, $1/\Omega \cdot m$, S/m
ρ	=	Electrical resistivity, $\Omega \cdot m$
T	=	Absolute temperature, K
κ	=	Total thermal conductivity, W/m·K

To assess the suitability of a material for use in a thermoelectric generator or cooler, the power factor is computed using the Seebeck coefficient and electrical conductivity of the material under a specific temperature difference:

$$PF = S^2 \sigma = \frac{S^2}{\rho} \quad (6)$$

Where:

PF	=	Power factor
S	=	Seebeck coefficient, V/K
σ	=	Electrical conductivity, $1/\Omega\text{m}$, S/m
ρ	=	Electrical resistivity, Ωm

Materials with low thermal conductivity and high electrical conductivity are required to get high ZT or higher efficiency. To make the thermoelectric efficiency dimensionless, it is multiplied by the absolute temperature T , which results in the commonly used form of thermoelectric efficiency known as the dimensionless figure of merit, ZT . This value is as given in Figure 4.

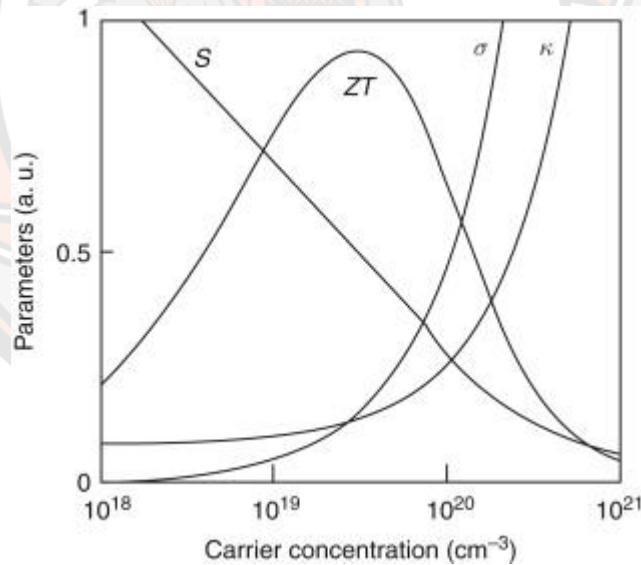


Figure 4 Maximizing the efficiency (ZT) of a thermoelectric involves a compromise of thermal conductivity and Seebeck coefficient with electrical conductivity [36]. 2.1.4 The development of thermoelectric materials

Nanostructured thermoelectric materials show significant potential for enhancing the performance of cooling devices and power generation through thermoelectric conversion. However, there is still ample improvement since neither

the materials nor the devices have been optimized. So far, a ZT value exceeding 3 has not been achieved in low-dimensional systems. However, rapid advancements in nanotechnologies, including the synthesis of materials and the discovery of novel physical and/or chemical properties, hold significant promise for achieving a remarkable improvement in thermoelectricity.

Achieving high ZT values in thermoelectric materials depends on attaining a combination of a high Seebeck coefficient (S), high electrical conductivity (σ) and low thermal conductivity (κ); all in the same material. A high Seebeck coefficient is related to a high open circuit voltage ($V = S\Delta T$) of a thermoelectric material subjected to a temperature gradient, thereby determining the power output. A high electrical conductivity can reduce ohmic losses when current flows through the device. On the other hand, heat transfer occurs at a quicker rate in materials with a high thermal conductivity than in those with low thermal conductivity. Consequently, low thermal conductivity creates a large thermal gradient.

Unluckily, it is impossible to optimize all these properties in a single material. Metals have high electrical conductivity but also high thermal conductivity and low Seebeck coefficient. Glasses and polymers, on the other hand, exhibit low thermal conductivity and generally low electrical conductivity. This has led to the development of "phonon-glass, electron-crystal" (PGEC) materials. The most effective thermoelectric materials are crystalline materials that can scatter phonons without considerably disrupting electrical conductivity while still maintaining charge carriers with high mobility. This approach involves striking a balance between the required compromises to achieve optimal ZT .

2.2 Related Works

2.2.1 Thermoelectric oxide

Ohtaki, M (2010) conducted research on thermoelectric materials, where oxide materials were identified as a promising candidate. Among the promising oxide thermoelectric materials discovered were CaMnO_3 -based perovskites, Al-doped ZnO , layered cobalt oxides like NaCo_2O_4 and $\text{Ca}_3\text{Co}_4\text{O}_9$, and SrTiO_3 -related phases. As discussed earlier, while some p-type oxides have achieved $ZT = 1$ in single crystal form, the performance of practical polycrystalline bulk oxide materials is still not adequate. Figure 5 provides a timeline of the development of oxide thermoelectric materials [37].

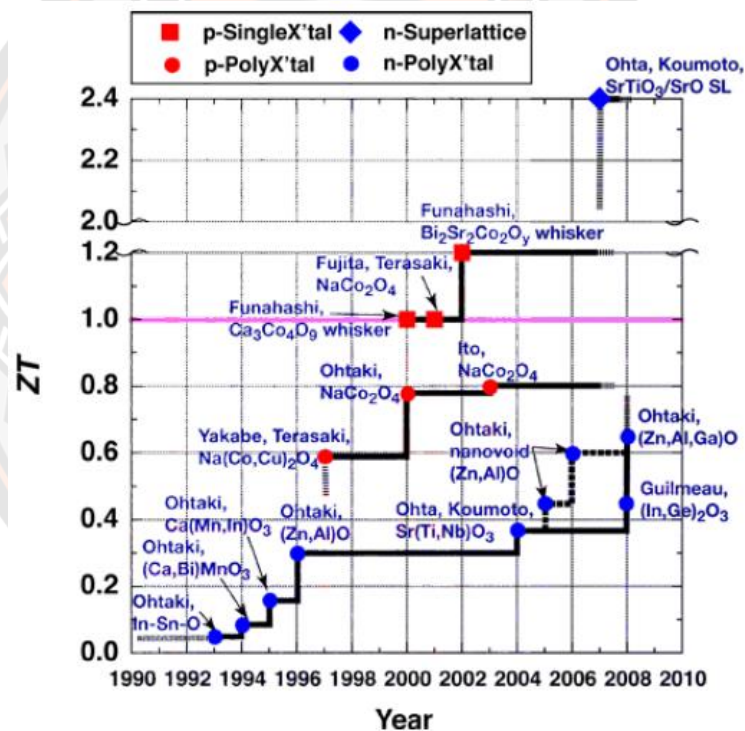


Figure 5 The timeline for the highest ZT of oxide thermoelectric materials [37].

Koumoto, K., et al. (2010) demonstrated the potential of thermoelectric oxides composed of non-toxic, naturally abundant, lightweight, and inexpensive elements. These materials were expected to have a crucial role in various applications for waste heat recovery in an air atmosphere. Therefore, the development of thermoelectric oxide materials and their application in thermoelectric modules is necessary, as shown in Figure 6 [9].

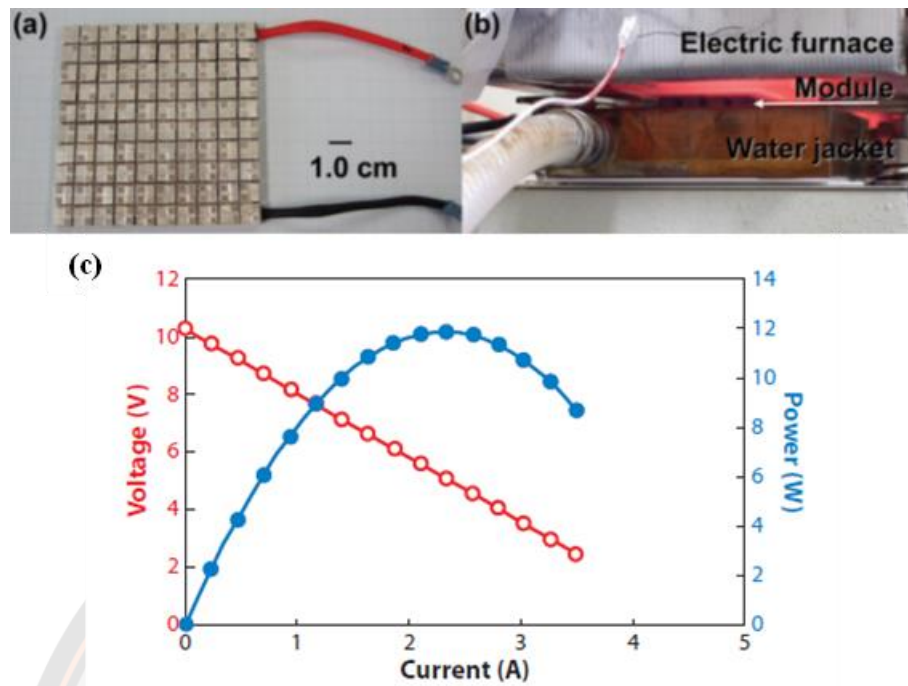


Figure 6 (a) Thermoelectric module (b) a measurement system for generated power and (c) Thermoelectric power generation properties [9].

Li, J.-F., et al. (2010) provided a summary of recent progress in developing materials with high thermoelectric performance and the related fabrication processes for producing nanostructured materials. Several types of materials were highlighted, including Bi-Te alloys, skutterudite compounds, Ag-Pb-Sb-Te quaternary systems, half-Heusler compounds, and high- ZT oxides. Also noted were that enhancing thermoelectric properties can be achieved through band structure engineering, such as doping and exploring new materials with a complex crystalline structure. This study presented Figure 7 to illustrate the different dimensionality and grain mixtures of thermoelectric materials from the macro- to nanoscale, as well as the size evolution of isolated distinct phases or atoms in the composite. Figure 7(a–d) shows the change in dimensionality with (a) representing bulk, (b) thin film, (c) nanowire, (d) atomic cluster. (e–h) grain mixtures from micro- to nanoscale, (e) normal micro-grained bulk, (f) mixture of coarse and fine grains, (g) nano-grained bulk, (h) amorphous. (i–l) size evolution of isolated distinct phases or atoms in the composite: (i) normal composite, (j) nano-dispersions located inside grains or at grain boundaries, (k) nano-inclusions or nanodots, boundary modification, (l) atomic doping or alloying, and vacancies. The

figure highlights how the properties of materials can be improved by adjusting their structure and composition at various scales [38].

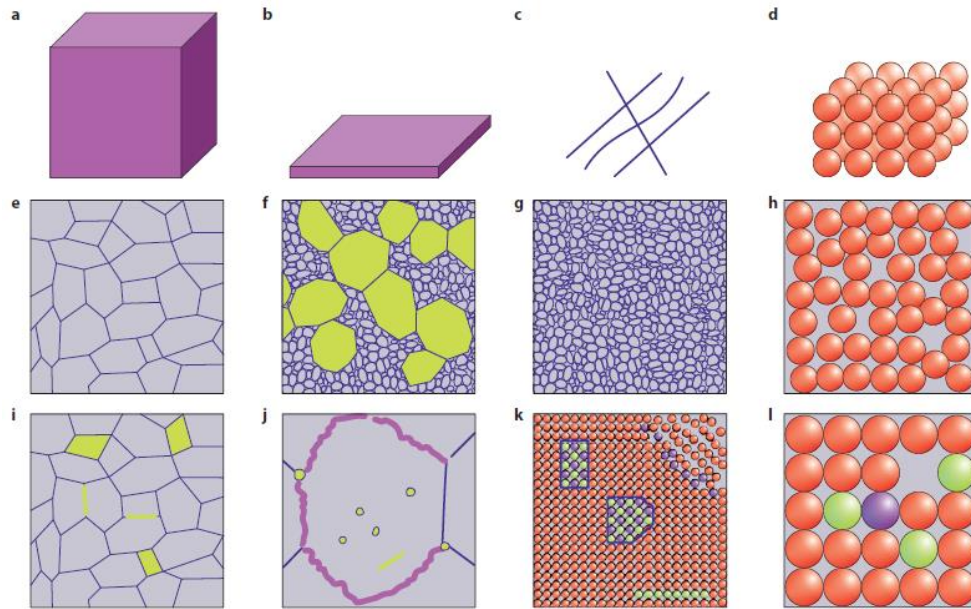


Figure 7 Summary of thermoelectric material structure from the macro- to nanoscale [38].

Fergus, J.W. (2012) discussed the availability of p-type and n-type oxides for use in thermoelectric energy conversion devices. Figure 8 shows some of the oxides that are commonly used. The best p-type oxides with thermoelectric properties are layered cobaltite compounds, although Na_xCoO_2 and $\text{Co}_3\text{Co}_4\text{O}_9$ based materials have better thermoelectric performance, better stability and are more widely used. For n-type oxides, doped CoMnO_3 has a lower thermal conductivity, while doped SrTiO_3 and doped ZnO have higher electrical conductivity. Although the thermoelectric properties of these oxides are not as good as those of some non-oxide compounds. For instance, tellurides and antimonides have better stability and thus may be suitable for high-temperature applications. Additional improvements in materials properties and the associated fabrication processes are needed for the development of economically feasible devices [12].

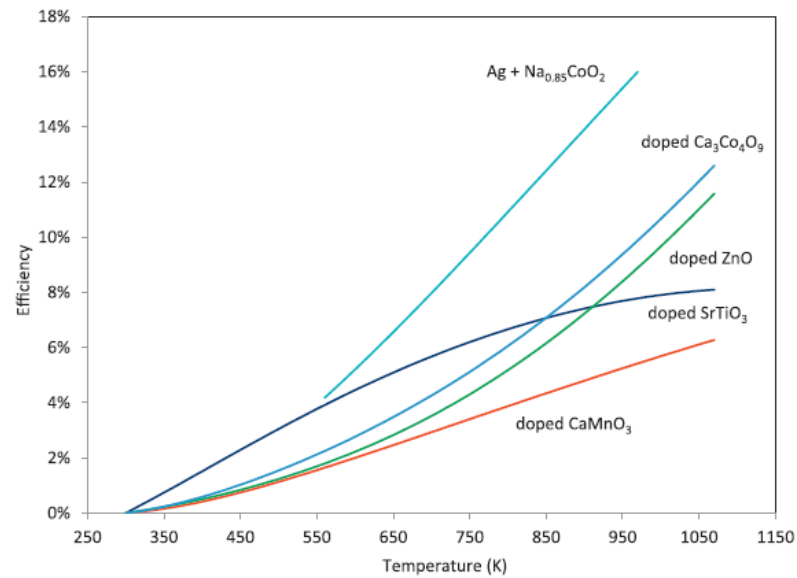


Figure 8 Maximum theoretical efficiencies for thermoelectric oxides using $T_{\text{cold}} = 300\text{K}$ and maximum ZT values [12].

Liu, W., et al. (2012) proposed some key characteristics for the new generation nanocomposites called *ordered nanocomposite*. This is in contrast with those of the current disordered nanocomposites, called *random nanocomposite*. These characters along size scale from doping atom, nano-inclusions, grain boundaries, grain shape, to void morphology as shown juxtaposed in Figure 9 [39].

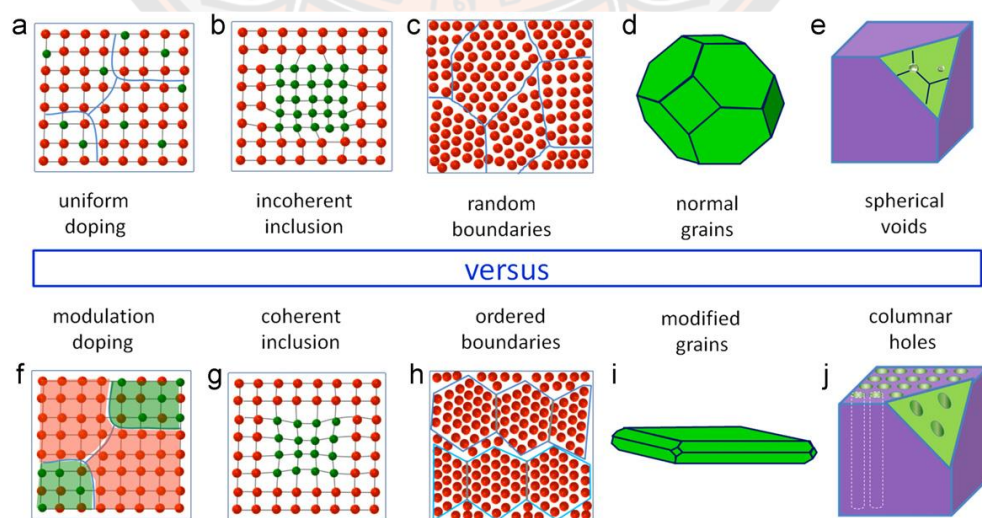


Figure 9 Comparison of various nanostructures between random nanocomposites (a–e) and ordered nanocomposite (f–j) [39].

Chen, Z.-G., et al. (2012) summarized the progress of the nanostructures thermoplastic to understand and explain the history and innovation of the past two decades. Two main methods are used to search for thermoelectric materials with high ZT . One of these is known as the "phonon glass electron crystal" (PGEC) approach, which proposes that the optimal thermoelectric material should have glass-like thermal conductivity and crystal-like electronic properties. The other method for seeking thermoelectric materials with high ZT involves nano-structuring the materials. This approach suggests that enhancing ZT can be achieved by using nanoscale or nanostructured morphologies. Figure 10 shows the ZT plotted as a function of temperature and year, there have been significant advancements in the development of thermoelectric materials over time. However, no material has been able to achieve the target $ZT \geq 3$ goal. In addition, thermoelectric material synthesized by various synthetic methods consists of PGEC, low-dimensional, and nanostructured [40].

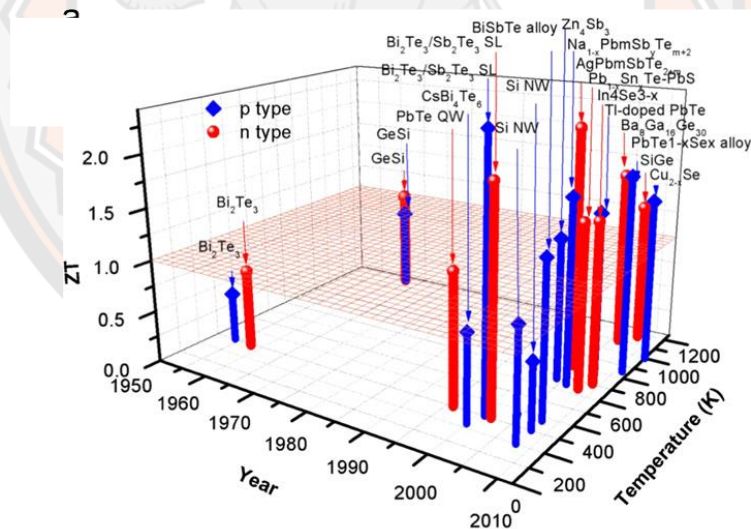


Figure 10 The ZT as a function of temperature and year revealing the important development of thermoelectric materials [40].

Alam, H. and S. Ramakrishna (2013) reported the thermoelectric concept and explain briefly the challenge in enhancing the figure of merits. The best thermoelectric materials were succinctly defined as PGEC, which stands for "phonon glass electron crystal." This term indicates that the materials should exhibit low lattice

thermal conductivity similar to glass, along with high electrical conductivity similar to crystal. Favorably, the laws of thermodynamics do not set an upper limit on ZT . Figure 11 shows the direction of the development of thermoelectric materials since the 1950s [41].

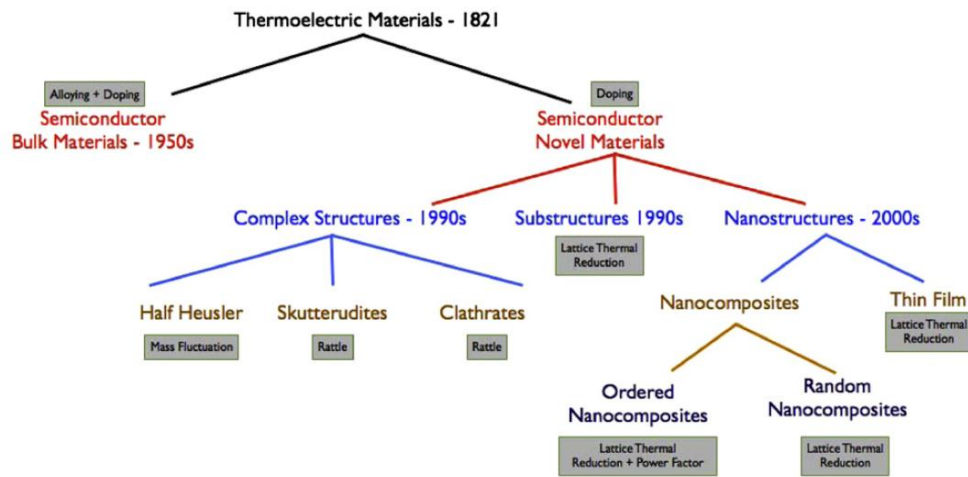


Figure 11 History of Efforts in increasing ZT [41].

Ohta, H., et al. (2013) review focuses on the thermoelectric properties of two representative oxide epitaxial films, p-type $\text{Ca}_3\text{Co}_4\text{O}_9$, and n-type SrTiO_3 which exhibit the best thermoelectric ZT . Both materials presented ZT value of 0.05 at 300 K and 0.3 at 1000 K respectively. The authors suggested that the approach used in the 2DEG of SrTiO_3 may offer a promising pathway for creating practical thermoelectric materials that don't rely on toxic heavy elements [7].

Hamid Elsheikh, M., et al. (2014) reviewed principal parameters of thermoelectric material that were essential to improving thermoelectric properties. Thermoelectric materials have high electrical conductivity, low thermal conductivity, and a high Seebeck coefficient. Figure 12 shows Maximized efficiency (ZT). Recent research has primarily focused on developing highly efficient thermoelectric structures and materials. They reviewed the principal parameters that have driven improvements in the efficiency of TE materials in the past and provided an overview of parameters that affected the figure of merit ZT , as well as the optimization of thermoelectric materials and their applications [36].

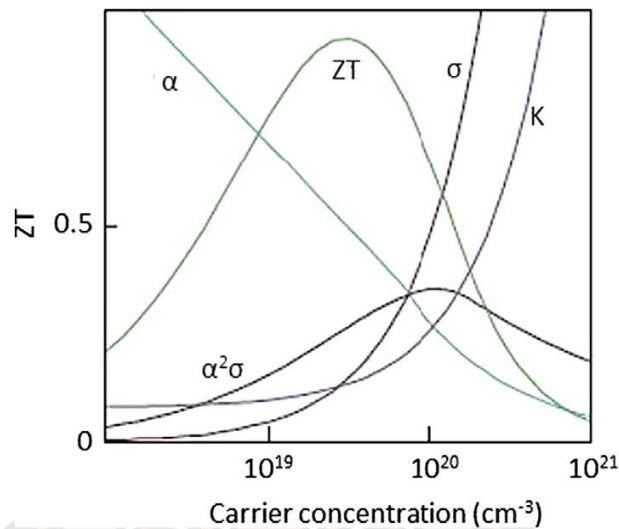


Figure 12 Maximizing the efficiency (ZT) of a thermoelectric involves a compromise of thermal conductivity with electrical conductivity [36].

Fitriani, et al. (2016) conducted a review of high-temperature thermoelectric materials for waste heat recovery. They noted that so far, no material has been able to achieve the $ZT \geq 3$, to compete with conventional mechanical systems for energy conversion, as shown in Figure 13. Two main approaches have been proposed to improve the ZT of TE materials. The first is the “phonon glass electron crystal” (PGEC) concept, which suggested that an ideal TE material should have glass like thermal conductivity and crystal-like electronic properties. The second approach involves nano-structuring, which enhances the density of states (DOS) near the Fermi level energy and thus increases the Seebeck coefficient. This method provides a way to decouple the Seebeck coefficient and electrical conductivity, based on the idea that the mean-free path (mfp) of the electron is much shorter than that of photons in heavily doped semiconductors [42].

13 Figure of Merit, ZT of Thermoelectric, as a function of temperature and year illustrating important milestones [42].

Wang, H., et al. (2016) focused on the potential high-performance thermoelectric materials. They identified SrTiO_3 and CaMnO_3 as two promising perovskite oxides and found that traditional doping modifications could not significantly improve the properties of these oxides. The authors suggested that future research should focus on the nano-structuring oxides to optimize their alloys. They also noted that the effects of nano-structuring, nanocomposite fabrication, and chemistry engineering on the thermoelectric performance of SrTiO_3 materials have already been demonstrated. Therefore, further research should include the combination of nano-structuring and nanocomposite fabrication, as well as the combination of nano-structuring and defect chemistry engineering, to enhance the thermoelectric performance of these oxides. By utilizing these methods, the development of enhanced thermoelectric materials is expected in future [43].

Li, Z., et al. (2016) focused on the underexploited aspects of defects for thermoelectric materials. These aspects include defect-mediated atom or charge migration effects, and defect-re-

When combined with the existing strategies for optimizing crystal structure, these new enhancements can result in the high efficiency of defect engineering, as shown in (Figure 14). Ultimately, the optimization of thermoelectric materials [44].

When combined with the existing strategies for optimizing electronic and phonon structure, these new enhancements can result in the highest possible efficiency of defect engineering, as shown in (Figure 14). Ultimately, this could lead to the optimization of thermoelectric materials [44].

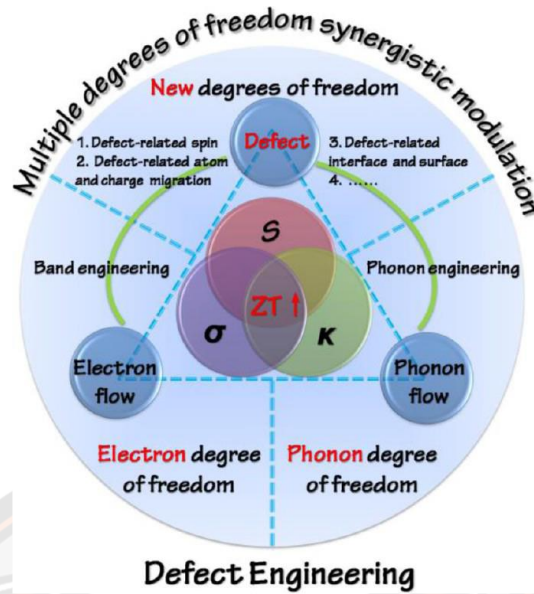


Figure 14 Schematic illustration of the ZT optimization strategies based on defect engineering from the perspective of multiple degrees of freedom synergistic modulation [44].

He, J. and T.M. Tritt (2017) reviewed several potentially paradigm-changing mechanisms enabled by various factors such as defects, size effects, critical phenomena, anharmonicity, and the spin degree of freedom. (Figure 15) depicts these mechanisms, which decouple physical quantities that would otherwise be adversely interdependent and enable higher material performance [45].

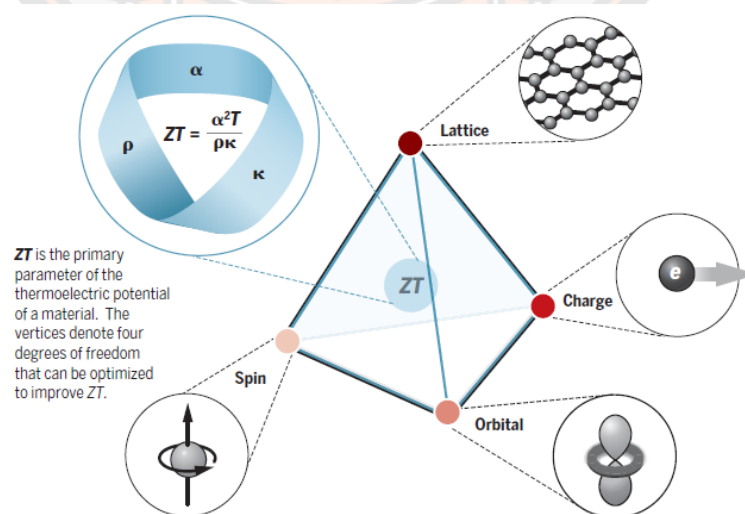


Figure 15 Thermoelectric materials research is an application-driven multidisciplinary topic of fundamental research [45].

2.2.2 SrTiO₃ - based TE materials

Blennow, P., et al. (2007) presented the Nb-doped SrTiO₃ by glycine nitrate combustion process (GNP). After the synthesis of Sr_{0.94}Ti_{0.9}Nb_{0.1}O₃. Impurities were clearly present in the as-synthesized and calcined powders when precipitates formed during the thermal evaporation and/or no auto-ignited combustion reaction occurred. The SEM showed the grain sizes on average about 100 nm, as shown in Figure 16. The structural characterization and microstructure analysis of powder showed a single phase after calcination and consisted of submicronic grains [46].

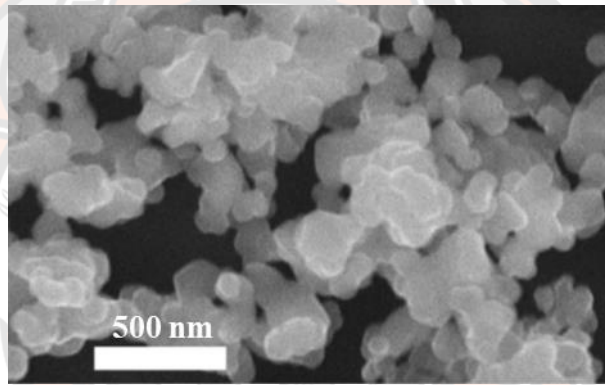


Figure 16 SEM micrograph of Sr_{0.94}Ti_{0.9}Nb_{0.1}O_{3-δ} powder. [46].

Liu, S., et al. (2008) presented the characterization of perovskite SrTiO₃, that synthesized by sol-gel combustion method using citric acid (CA) as a reductant/fuel and nitrate as an oxidant at a low temperature of 673 K for 2 hours. The XRD pattern of the SrTiO₃ was a cubic perovskite structure. The TEM images showed the most particles, that was fine and nearly spherical with some agglomeration and their sizes are in the range of 20–30 nm as shown in Figure 17 [47].

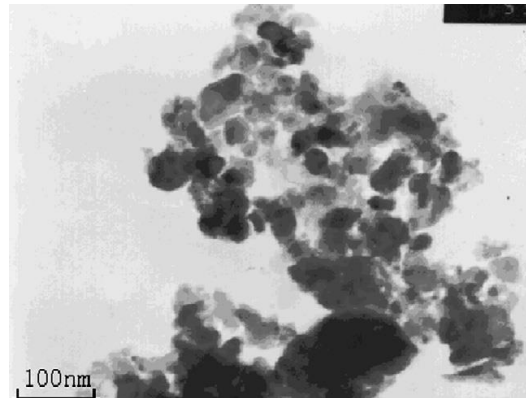


Figure 17 TEM image of the synthesized SrTiO_3 powders calcined at 673 K for 2h [47].

Kikuchi, A., N. Okinaka, and T. Akiyama (2010) investigated the figures of merit of La-doped SrTiO_3 that were prepared through combustion synthesis (CS) with post-spark plasma sintering (SPS), with focus on the effect of sintering time. Thermoelectric properties were measured from room temperature to 1173 K, and the sample sintered for 5 minutes recorded the highest figure of merit of 0.37 at 1045 K. Figure 18 shows the temperature dependence of dimensionless figures of merit for various holding times during sintering, compared to ZT data for heavily Nb-doped SrTiO_3 and La-doped SrTiO_3 previously reported by Ohta et al. and Zhang et al. respectively [48].

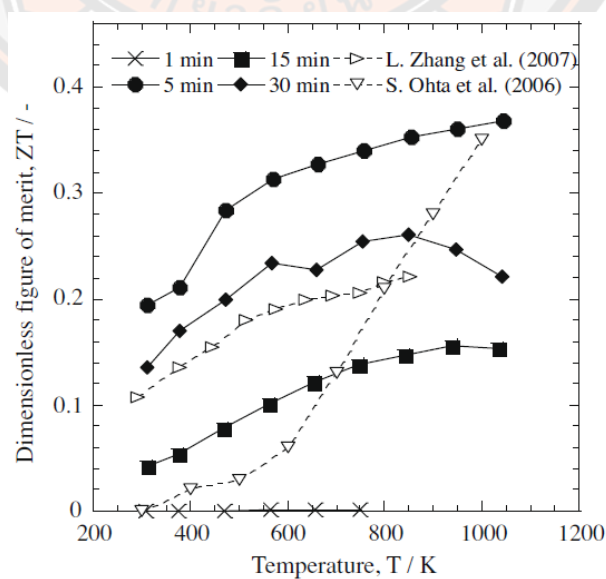


Figure 18 Temperature dependence of dimensionless figures of merit for various holding times during sintering [48].

Shang, P.-P., et al. (2010) demonstrated the preparation of $\text{La}_{0.08}\text{Sr}_{0.92}\text{TiO}_3$ through the sol-gel process and spark plasma sintering (SPS). The samples were calcined at 803 K for 1 hour in the air and sintered from 1203 to 1473 K. The authors found that the electrical conductivity increased with SPS-processing temperature due to the increase in relative density, grain size, and oxygen vacancies resulting from the reducing atmosphere of SPS. The absolute value of the Seebeck coefficient increased as the SPS temperature increased from 1203 to 1373 K, and then decreased when further increasing the SPS temperature to 1473 K. The sample SPSed at 1373 K showed the largest absolute value of Seebeck coefficient of $196 \mu\text{V/K}$ at 679 K. Furthermore, the sol-gel process and SPS can significantly reduce the thermal conductivity of SrTiO_3 based ceramics, with the lowest value of 1.19 W/mK at 773 K achieved in the sample SPSed at 1203 K. The maximum ZT value of 0.08 was obtained at 679 K for the sample SPSed at 1473 K, as shown in Figure 19, and this value increased with temperature [49].

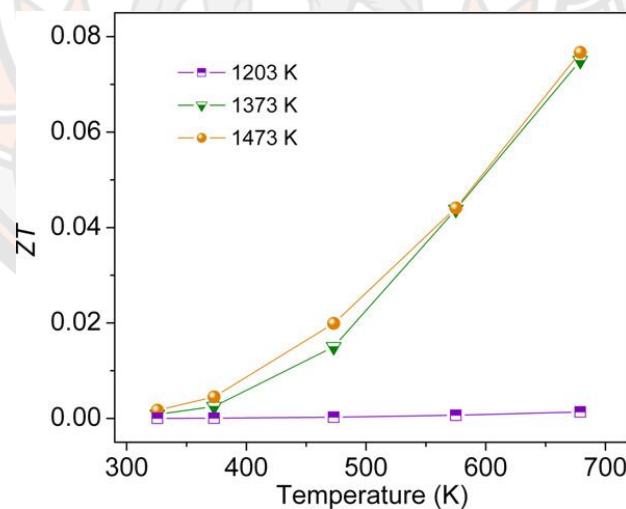


Figure 19 Temperature dependence of ZT for $\text{La}_{0.08}\text{Sr}_{0.92}\text{TiO}_3$ bulks SPSed at 1203 K, 1373 K and 1473 K [49].

Wang, H.C., et al. (2010) showed thermoelectric properties of $\text{La}_{0.1}\text{Sr}_{0.9-x}\text{Dy}_x\text{TiO}_3$ ($x = 0.01, 0.03, 0.07, 0.10$), which were prepared through the solid-state reaction method. The X-ray diffraction revealed a change in the crystal structure from

cubic to tetragonal phase. The electrical and thermal transport properties were measured in the temperature range of 300-1100 K, and n-Type thermoelectric behavior with a large Seebeck coefficient was observed. The researchers found that the figure of merit was markedly improved due to the Dy doping effect, which resulted in a relatively lower electrical resistivity and thermal conductivity. Specifically, $\text{La}_{0.1}\text{Sr}_{0.8}\text{Dy}_{0.1}\text{TiO}_3$ showed a much lower electrical resistivity of 0.8 mV cm at room temperature and a relatively lower thermal conductivity of 2.5 W/mK at 1075 K. The maximum figure of merit of ~ 0.36 at 1045 K was achieved for $\text{La}_{0.1}\text{Sr}_{0.83}\text{Dy}_{0.07}\text{TiO}_3$, which is the highest value among n-type oxide thermoelectric as shown in Figure 20 [50].

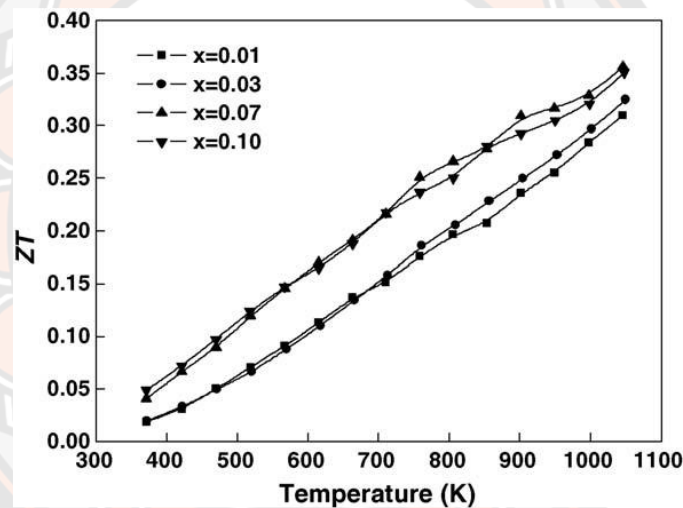


Figure 20 Temperature dependence of the ZT of $\text{La}_{0.1}\text{Sr}_{0.9-x}\text{Dy}_x\text{TiO}_3$ [50].

Wang, H.C., et al. (2011) reported the highest thermoelectric figure of $\text{Sr}_{0.9}\text{La}_{0.1}\text{Ti}_{1-x}\text{Ta}_x\text{O}_3$, that were synthesized by conventional solid-state reaction method. X-ray powder diffraction analysis revealed that all samples were single-phase with cubic symmetry. The high-temperature electrical resistivity decreased with increasing Ta content, except for the $x = 0.05$ sample. All samples exhibited negative Seebeck coefficients, indicating n-type conduction mechanism. The absolute Seebeck coefficient decreased with increasing tantalum concentration, while the PF decreased with increasing Ta substitution. A small amount of Ta doping was found to reduce thermal conductivity, with the lowest value of 2.9 W/mK obtained for $x = 0.03$ at

1074 K. Despite the decrease in PF , the highest ZT was still observed in $Sr_{0.9}La_{0.1}TiO_3$, reaching 0.29 at 1046 K, as shown in Figure 21. This value is relatively high compared to other n-type oxide thermoelectric materials [51].

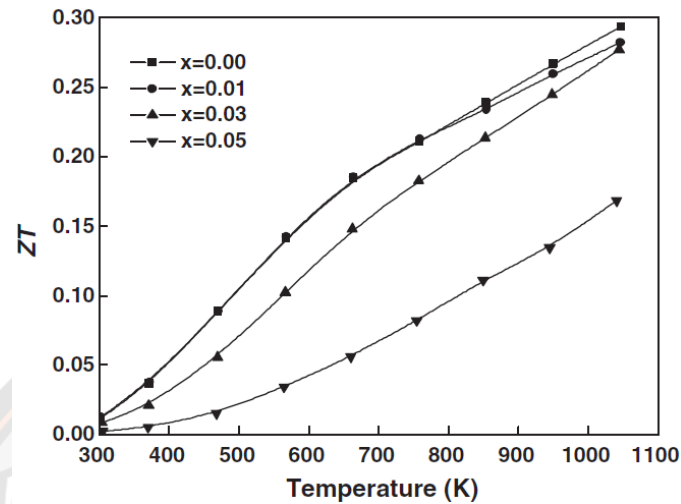


Figure 21 Temperature dependence of the ZT of $Sr_{0.9}La_{0.1}Ti_{1-x}Ta_xO_3$ ceramics [51].

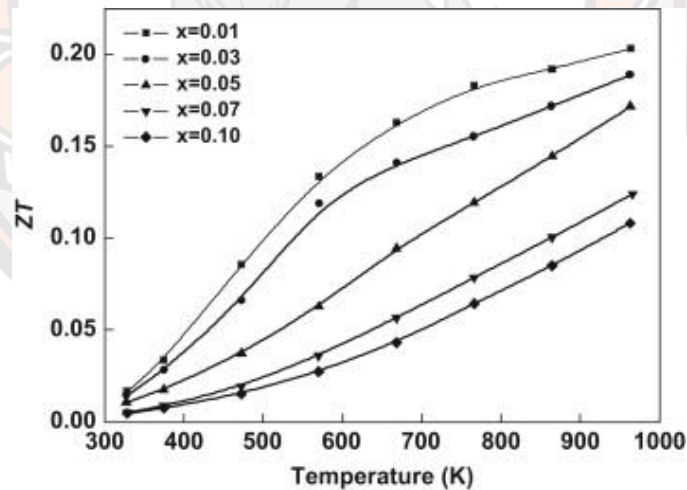


Figure 22 Temperature dependence of the ZT of $La_{0.1}Sr_{0.9-x}Yb_xTiO_3$ ceramics [52].

Wang, H. and C. Wang (2013) investigated the effect of Yb doping on the thermoelectric properties of $La_{0.1}Sr_{0.9}TiO_3$ ceramics synthesized through a conventional solid-state reaction method. The study was carried out in the temperature range of 300 K to 1000 K. The minimum values of electrical resistivity were observed

for the sample with $x = 0.01$ Yb doping at $1.5 \text{ m}\Omega \text{ cm}$. The doping of Yb led to a significant increase in electrical resistivity, a minor increase in Seebeck coefficients, and a moderate reduction in thermal conductivities. The sample with $x = 0.01$ Yb doping recorded the lowest thermal conductivity of 3.9 W/mK , and exhibited the highest figure of merit of 0.20 at 963 K (Figure 22) compared to other samples with higher Yb concentrations [52].

Wang, Y., et al. (2013) reported effective increase in the Seebeck coefficient for 5% La-doped SrTiO_3 nano-ceramics at temperatures of 300 - 800 K through grain boundary doping with Nb. The Seebeck coefficient was increased effectively relative to normal La-doped SrTiO_3 . The power factor was increased by 35% as compared with normal La-doped SrTiO_3 ceramics (Figure 23). The observed improvement in thermoelectric properties may be attributed to the energy filtering effect occurring at the Nb-doped grain boundaries, where an increased potential barrier arises from the band offset between the boundaries and the interior of the grains. The strategy is particularly applicable in thermoelectric polycrystalline ceramics [53].

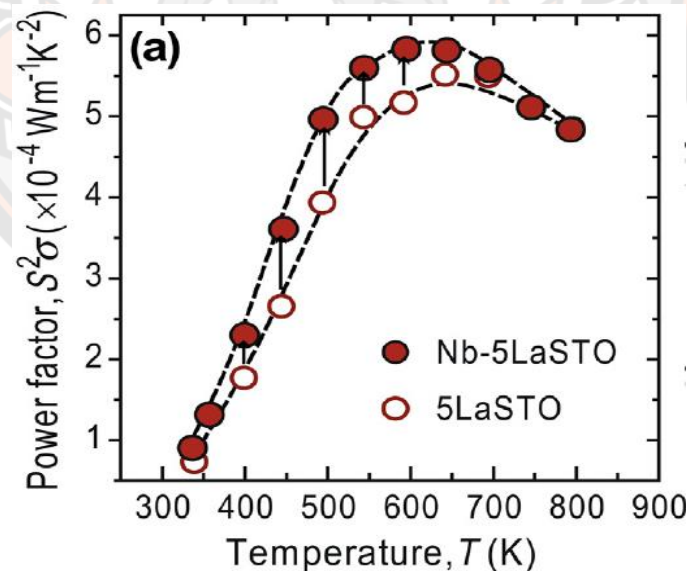


Figure 23 Comparison of the PF between 5LaSTO and Nb-5LaSTO, showing an effective PF increase in the case of Nb-5LaSTO [53].

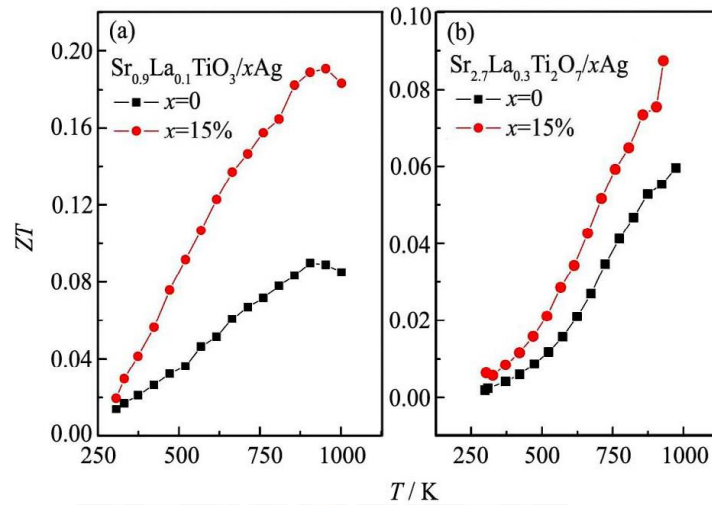


Figure 24 Temperature dependence of the ZT for the compound

$\text{Sr}_{0.9}\text{La}_{0.1}\text{TiO}_3/x\text{Ag}$ (a) and $\text{Sr}_{2.7}\text{La}_{0.3}\text{Ti}_2\text{O}_7/x\text{Ag}$ (b) ($x = 0$ and 15%) [54].

Hanbo, L.I., et al. (2014) showed the thermoelectric properties of $\text{Sr}_{0.9}\text{La}_{0.1}\text{TiO}_3$ and $\text{Sr}_{2.7}\text{La}_{0.3}\text{Ti}_2\text{O}_7$ with 15% Ag addition, fabricated through hydrothermal synthesis, cold pressing, and high-temperature sintering. Ag was found to precipitate as a second phase and its addition enhanced the electrical conductivity and absolute Seebeck coefficient, leading to improved ZT values for both series. The highest ZT values of approximately 0.08 and 0.18 for $\text{Sr}_{0.9}\text{La}_{0.1}\text{TiO}_3$ without and with 15% Ag addition, respectively, and 0.06 and 0.08 for $\text{Sr}_{2.7}\text{La}_{0.3}\text{Ti}_2\text{O}_7$ without and with 15% Ag addition were obtained. The temperature dependence of ZT for both cases with and without 15% Ag addition is illustrated in Figure 24 [54].

Buscaglia, M.T. (2014) studied the effect of La doping on SrTiO_3 using high-pressure field assisted sintering (HP-FAST) to prepare La-doped (10 at %) SrTiO_3 from nano-crystalline powders. The resulting ceramics show a glass-like behavior and a suppression of the thermal conductivity peak observed in undoped single crystals. A progressive reduction of thermal conductivity is observed with decreasing grain size, becoming more pronounced at grain sizes below 35 nm. Scattering from dopant ions and lattice defects related to charge compensation have a significant impact on thermal conductivity and can lead to a reduction at room temperature down to 4 - 5 W/mK. The ceramic with the finest grains (24 nm) exhibits a thermal conductivity at

room temperature of 1.2 W/mK, one order of magnitude lower than that of the undoped single crystal (11 W/mK), as shown in Figure 25 [55].

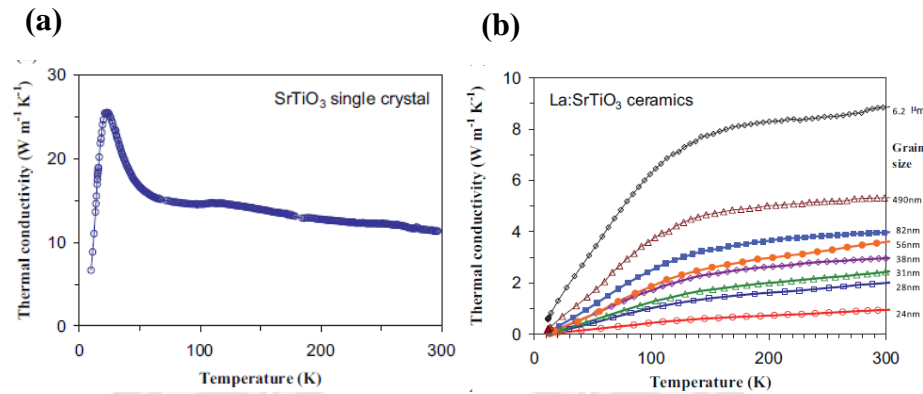


Figure 25 Temperature dependence of thermal conductivity of (a) undoped SrTiO₃ single crystal and (b) La-doped (10 mol.%) ceramics with different grain size in linear [55].

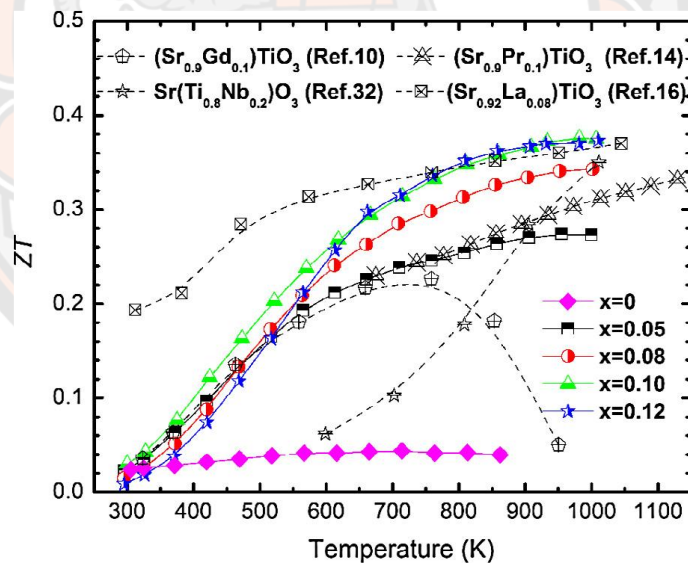


Figure 26 Temperature dependence of the figure of merit for (Sr_{1-x}Gd_x)TiO_{3-δ} ceramics. Data for (Sr_{0.9}Gd_{0.1})TiO₃, (Sr_{0.9}Pr_{0.1})TiO₃, (Sr_{0.92}La_{0.08})TiO₃, and Sr(Ti_{0.8}Nb_{0.2})O₃ are taken for comparison [56].

Li, L., et al. (2014) investigated thermoelectric properties of (Sr_{1-x}Gd_x)TiO_{3-δ} ceramics ($x = 0.05 - 0.12$), that were fabricated using a sol-gel process and spark plasma sintering. The results showed that the $|S|$ increased with temperature, while

ρ and $|S|$ decreased with an increase in Gd content for temperatures above 450 K for ρ . At high temperatures ranging from 400 - 1000 K, the PF for $(\text{Sr}_{0.9}\text{Gd}_{0.1})\text{TiO}_{3-\delta}$ was higher than $10 \mu\text{W/cm K}^2$, and the maximum value of $16 \mu\text{W/cm K}^2$ was obtained at 570 K. The highest ZT value of 0.37 was obtained at 1006 K (Figure 26). These results suggest that achieving an effective enhancement of the thermoelectric performance of STO-based systems requires a combination of high densities with fine-grained microstructures, proper doping such as rare earth Gd doping with $x = 0.1$, and oxygen deficiency.[56].

Wang, J., et al. (2015) utilized a molten salt synthesis (MSS) method to synthesize Nb-doped SrTiO_3 and investigated the impact of all-scale grain boundaries and inclusions on the thermoelectric performance of the material. Their results indicated that the reduction of thermal conductivity by 30% due to nano- to microscale grain boundaries and inclusions led to a 2.6 times enhancement in the ZT value. This was attributed to a combination of all-sized crystals, energy filtering effect, and multilevel scattering behaviors of nano/microscale grain boundaries and inclusions [57].

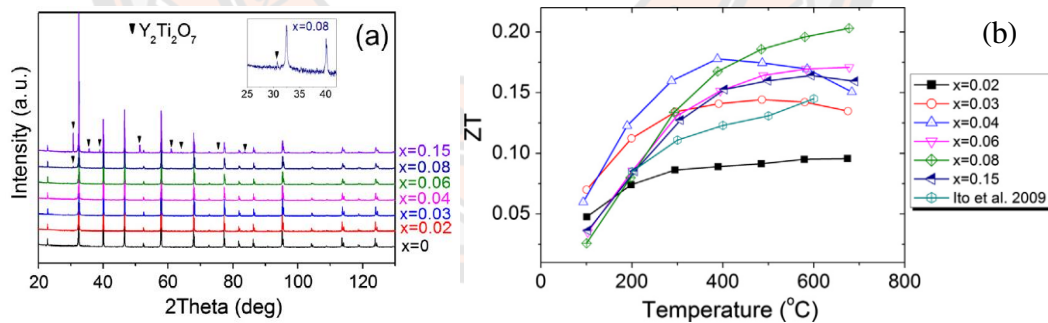


Figure 27 (a) XRD patterns and (b) Thermoelectric figure of merit ZT versus temperature for $\text{Sr}_{1-1.5x}\text{Y}_x\text{TiO}_{3-\delta}$ [58].

Chen, C., et al. (2015) studied the phase composition, microstructural and thermoelectric properties of n-type $\text{Sr}_{1-1.5x}\text{Y}_x\text{TiO}_{3-\delta}$ ($0 \leq x \leq 0.15$) that were synthesized by a solid-state reaction method. The electrical conductivity was found to increase with x , while the absolute values of the Seebeck coefficient decreased with x in the range of $0.02 \leq x \leq 0.08$. A further increase in x ($x \geq 0.08$) resulted in the

formation of $\text{Y}_2\text{Ti}_2\text{O}_7$, which had no effect on the Seebeck coefficient however caused a larger decrease in electrical conductivity than thermal conductivity. As a result, the thermoelectric performance of $\text{Sr}_{1-1.5x}\text{Y}_x\text{TiO}_{3-\delta}$ decreased with increasing $\text{Y}_2\text{Ti}_2\text{O}_7$ content, and the highest ZT value of ~ 0.20 at 953 K was observed in $\text{Sr}_{0.88}\text{Y}_{0.08}\text{TiO}_{3-\delta}$, as shown in Figure 27 [58].

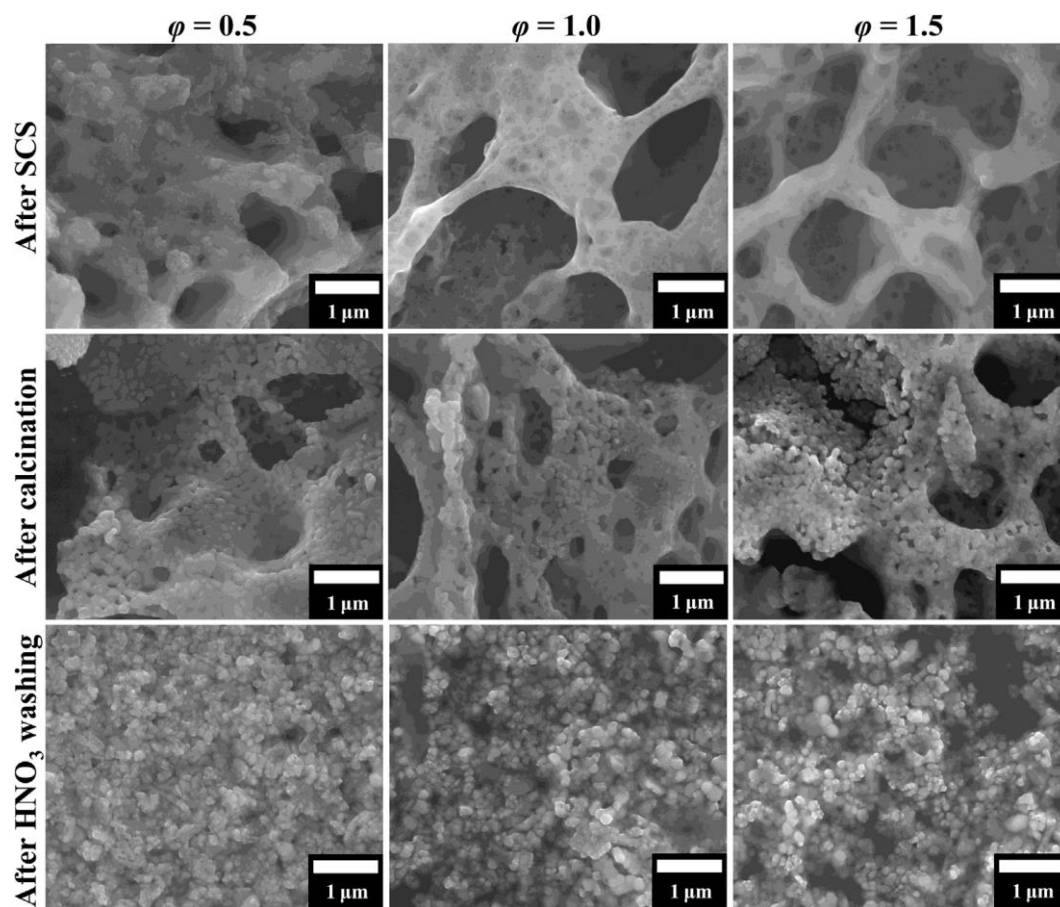


Figure 28 SEM images of samples after SCS prepared, calcined and washed [59].

Saito, G., et al. (2015) investigated the synthesis of SrTiO_3 using glycine-nitrate-based solution combustion synthesis with different fuel ratios (ϕ) and washing treatment by HNO_3 . X-ray diffraction analysis indicated that the samples were mainly SrTiO_3 , and samples with a porous structure were formed with an increase in ϕ , likely due to the ejection of more gases during SCS. The particle size decreased with increasing ϕ , as glycine acted as both a fuel and a dispersant and stabilizer. After been washed in HNO_3 solution, the porous structure decomposed into

particles with a high crystalline structure. As shown in Figure 28, the porous material was synthesized first with an increasing φ , followed by the synthesis of nanoparticles less than 100 nm in diameter through calcination. After washing, the particles reverted their initial by breaking down the porous structure. The photocatalytic activity of SrTiO_3 was significantly improved by HNO_3 -washing, likely due to the elimination of impurities, the increase in surface area, and the uncovering of the surface that consisted of (100) planes [59].

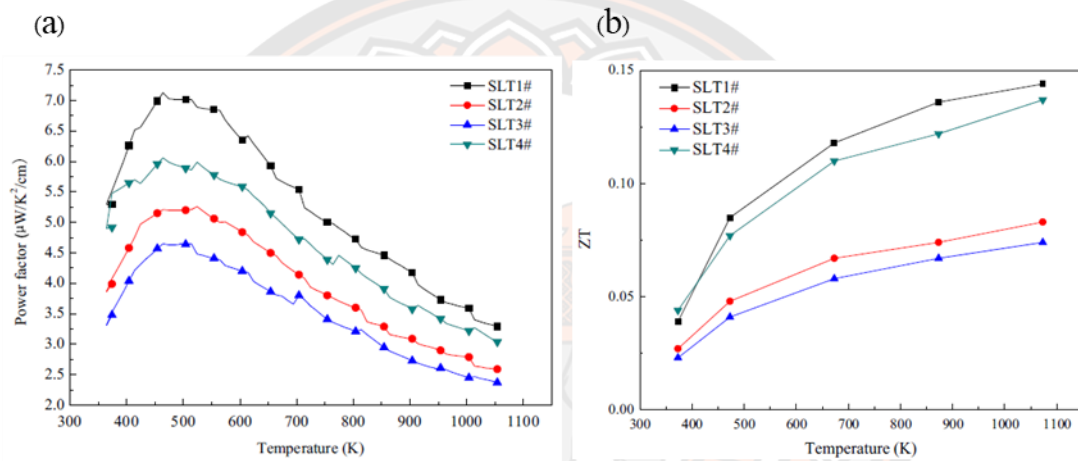


Figure 29 Temperature dependence of (a) The PF and (b) The ZT value for the $\text{Sr}_{0.9}\text{La}_{0.1}\text{TiO}_{3-x}\text{Ti}$ compounds ($x = 5, 10, 15$ and 20 wt%, numbered as SLT1#, SLT2#, SLT3#, SLT4#, respectively) [60].

Qin, M., et al. (2016) reported the successful preparation of Ti-doped $\text{Sr}_{0.9}\text{La}_{0.1}\text{TiO}_3$ ceramics with high density through conventional solid-state reaction in an Ar atmosphere. The study revealed that titanium was oxidation during the calcination process, resulting in the coexistence of TiO_2 phase with $\text{Sr}_{0.9}\text{La}_{0.1}\text{TiO}_3$ phase in the sintered ceramics. The S showed an increase from -163 to $-259 \mu\text{V/K}$ as the temperature increased from 350 K to 1073 K, while the thermal conductivity was significantly reduced by Ti doping. The ZT first decreased and then increased with increasing Ti doping content. The ceramics showed the best thermoelectric properties at 5 wt% Ti doping, with the maximum PF of $7.13 \mu\text{W/K}^2/\text{cm}$, and a ZT value of 0.144 at 1073 K, as illustrated in Figure 29 [60].

Yin, Y., B. Tudu, and A. Tiwari (2017) reported the study to improve the electrical conductivity of La, Nb, and SrTiO₃. The authors found that oxygen vacancy had a more significant effect on the electronic structure at and near the Fermi energy compared to La-substitution in SrTiO₃. They observed that when the distance between adjacent vacancies reduced to a critical value, a small mid-gap was formed in the bottom region of the conduction band, resulting in a decrease in the total number of delocalized electrons. The authors found that substitutions of La and Nb were more effective in improving electrical conductivity. The study found that substitutions of La and Nb were more effective in improving electrical conductivity. They showed that electrical conductivity and ZT could be increased by increasing the carrier concentration in both La and Nb-doped SrTiO₃. The heavily La-doped SrTiO₃ single crystal ($n = 8.4 \times 10^{20} \text{ cm}^{-3}$) showed a maximum ZT of 0.27 at 1073 K, as shown in Table 1 [11].

Table 1 Room-temperature thermoelectric responses of La-doped and Nb-doped single crystal SrTiO₃ [11].

STO	σ (S cm ⁻¹)	n (10 ²⁰ cm ⁻³)	μ (cm ² V ⁻¹ s ⁻¹)	S (mV K ⁻¹)	$S\sigma^2$ (10 ⁻⁴ W m ⁻¹ K ⁻²)	κ (W m ⁻¹ K ⁻²)	Z (10 ⁻⁵ K ⁻¹)	ZT (-)
(a) La-doped ($8.4 \times 10^{19} \text{ cm}^{-3}$)	54	0.5	7.0	-0.42	9.5	12	7.9	0.02
(b) La-doped ($8.4 \times 10^{20} \text{ cm}^{-3}$)	1000	6.8	9.2	-0.15	23	9.1	25	0.08
(c) Nb-doped ($1.6 \times 10^{20} \text{ cm}^{-3}$)	95	1.5	6.2	-0.33	10	11	9.3	0.03
(d) Nb-doped ($3.3 \times 10^{20} \text{ cm}^{-3}$)	353	3.7	6.0	-0.24	20	9.6	21	0.06

Iyasara, A.C., et al. (2017) reported thermoelectric properties of Sr_{1-x}La_{x/2}Sm_{x/2}TiO_{3-δ} ($0.05 \leq x \leq 0.30$) that was synthesized by solid-state reaction and sintered in 5% H₂/N₂ at 1773 K 6 hours. The XRD patterns showed a cubic perovskite phase and SEM confirmed homogeneous grain structure with a relative density ≥ 89 %. The σ of $x = 0.15$ exhibited metallic behavior with $\sigma < 1000$ S/cm, while for $x = 0.20$, it was semiconducting with $\sigma < 250$ S/cm. The negative Seebeck coefficient indicated n-type behavior. Among the samples, $x = 0.20$ displayed the lowest thermal conductivity of ~ 3 W/m·K (at 973 K), $x = 0.10$ showed the highest PF of $1400 \mu \text{ W/K}^2 \cdot \text{m}$ (at 573 K) and $x = 0.15$ exhibited the highest ZT of 0.24 (at 875 K), as shown in Figure 30 [61].

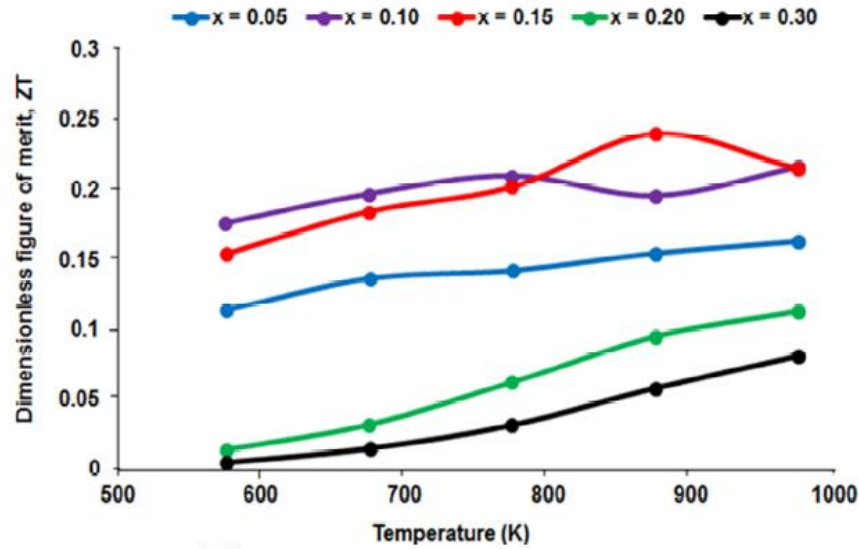


Figure 30 Temperature dependence of ZT for $\text{Sr}_{1-x}\text{La}_{x/2}\text{Sm}_{x/2}\text{TiO}_{3-\delta}$ ($0.05 \leq x \leq 0.30$) ceramics sintered in 5% H_2/N_2 at 1773 K for 6 hours [61].

Han, J., Q. Sun, and Y. Song (2017) showed the thermoelectric properties of La and Dy co-doped, Sr-deficient SrTiO_3 ceramics. The researchers synthesized $\text{La}_{0.1}\text{Dy}_x\text{Sr}_{1-1.25(0.1+x)}\text{TiO}_3$ ($x = 0, 0.05, 0.075, 0.1$) powders using the sol-gel method and sintered them at 1823K under a reducing atmosphere of 5 vol% H_2/N_2 . It was found that excess Dy doping could effectively inhibit the growth of grains, and Sr vacancies and La-Dy co-doping had the remarkable effect of enhancing the electrical properties and decreasing thermal conductivity. The $\text{La}_{0.1}\text{Dy}_x\text{Sr}_{1-1.25(0.1+x)}\text{TiO}_3$ ceramic with $x = 0.1$; achieved a large power factor of $1216 \mu\text{W/mK}^2$ at 373 K. The appropriate amount of defects in the $\text{Dy}_2\text{Ti}_2\text{O}_7$ phase and the smallest grain size in the sample with $x = 0.1$ provided the lowest thermal conductivity of 1.92 W/mK at 773 K. Therefore, a remarkable $ZT = 0.29$ at 773K was obtained for the sample with $x = 0.1$, suggesting that the synergistic effect of Sr vacancies and co-doping represents a promising strategy for improving the thermoelectric performance of SrTiO_3 , as shown in Figure 31 [62].

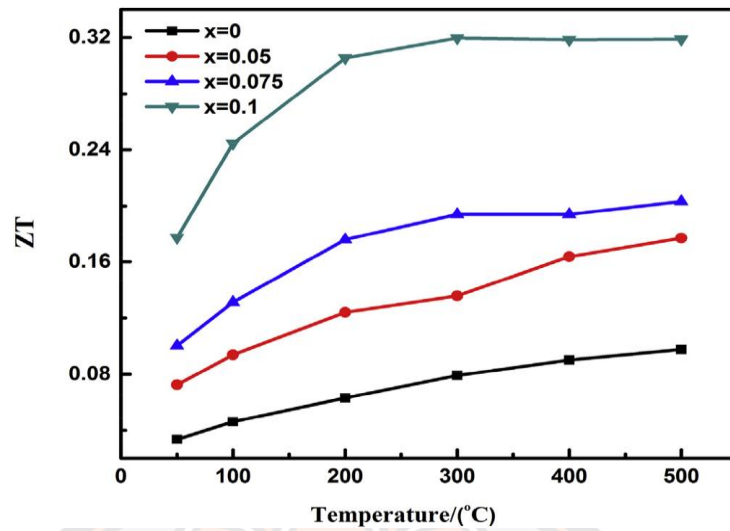


Figure 31 Temperature dependence of ZT for the $\text{La}_{0.1}\text{Dy}_x\text{Sr}_{1-1.25(0.1+x)}\text{TiO}_3$ ceramics [62].

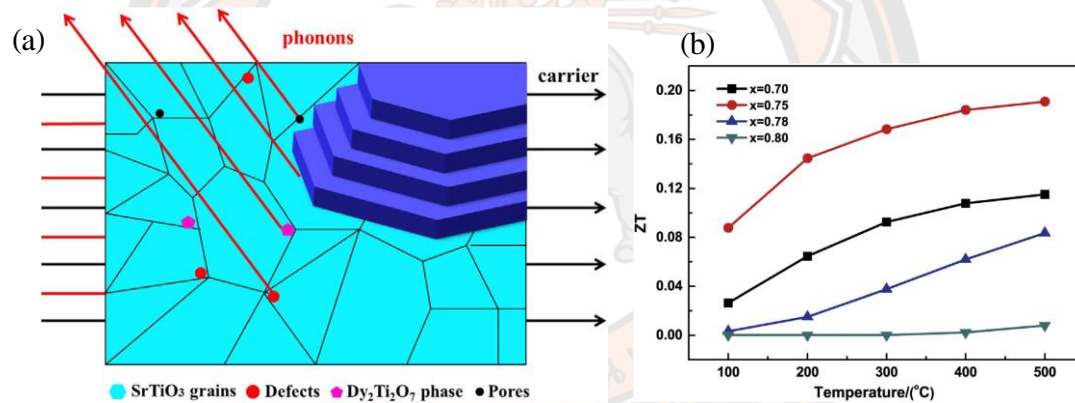


Figure 32 (a) Schematic diagram of the scattering mechanism for the non-stoichiometric samples with step-like microstructure and (b) Temperature dependence of the ZT for the $\text{La}_{0.1}\text{Dy}_{0.1}\text{Sr}_x\text{TiO}_3$ ceramics[63].

Han, J., et al. (2017) used a sol-gel method synthesized $\text{La}_{0.1}\text{Dy}_{0.1}\text{Sr}_x\text{TiO}_3$ ($x = 0.80, 0.78, 0.75, 0.70$) powders, following by sintering in a reducing atmosphere of 5 vol% H_2/N_2 at 1823 K. The samples exhibited step-like microstructure, which can be effective in suppressing thermal conductivity by improving phonon scattering at internal interfaces. As the Sr-deficient content increased, the electrical conductivity of the Sr-deficient $\text{La}_{0.1}\text{Dy}_{0.1}\text{Sr}_x\text{TiO}_3$ ceramics was apparently improved. The optimal

ZT value of 0.19 for $\text{La}_{0.1}\text{Dy}_{0.1}\text{Sr}_{0.75}\text{TiO}_3$ was achieved due to the enhanced electrical conductivity and the low thermal conductivity, demonstrating the potential to improve thermoelectric properties of donor-substituted titanates through controlling point defects and microstructure. Figure 32 provides a visualization of the results [63].

Roy, P., V. Pal, and T. Maiti (2017) showed thermoelectric properties of SrTiO_3 : 15 at% Nb (STN), that was synthesized by Spark Plasma Sintering (SPS) route (fast sintering process) and sintered at 1673 K using 30 MPa pressure in Ar-atmosphere. The maximum PF was $33.21 \mu\text{W/mK}^2$ at 1229 K. The achievement of sub-micron size grains obtained in STN samples are supposed to provide more phonon scattering and consequently lower the thermal conductivity which should result in increased ZT value of Nb-doped SrTiO_3 [64].

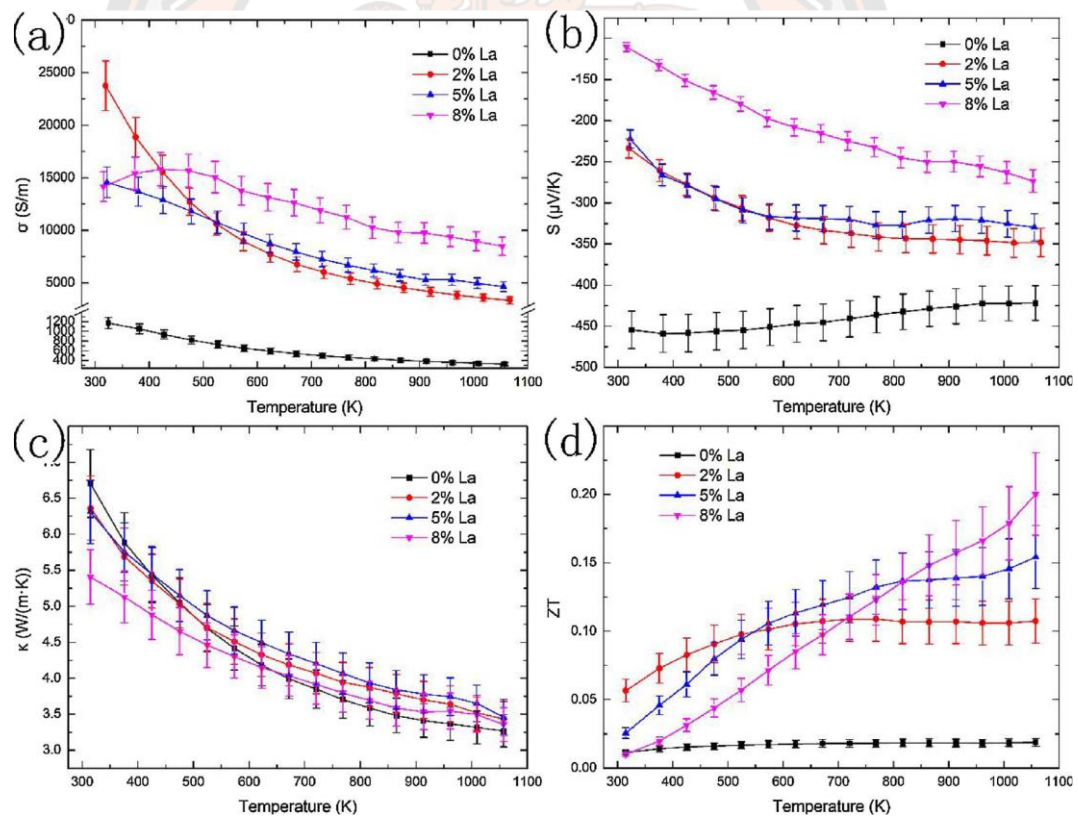


Figure 33 Temperature dependence of (a) electrical conductivity (σ), (b) Seebeck coefficient (S), (c) thermal conductivity (κ) and (d) dimensionless figure-of-merit (ZT) of the bulk SrTiO_3 samples with different La contents [65].

Liu, D., et al. (2018) reported thermoelectric properties of $\text{Sr}_{1-x}\text{La}_x\text{TiO}_3$ ($x = 0, 0.02, 0.05, 0.08$) nanoparticles prepared using mechanical alloying, then followed by carbon burial sintering. By milling process, La was successfully doped into the SrTiO_3 during the milling process and acted as an n-type dopant. The bulk samples exhibited a relatively high absolute Seebeck coefficient due to the core structure and superstructure. The ZT was observed to increase with the increasing La content and temperature. The maximum ZT value of 0.06 was observed at 300 K for $x = 0.02$ and 0.20 at 1000 K for $x = 0.08$, as shown in Figure 33. This approach for producing bulk thermoelectric materials is simple, cost-effective, and has great potential for large-scale industrial applications [65].

Park, C.-S. (2018) conducted research on mesoporous SrTiO_3 films, where Ti was substituted with group V elements (V, Nb, and Ta) to enhance the thermoelectric properties. The effective mass of the films was found to increase slightly with V substitution, whereas the use of Nb and Ta as substitutes induced an increase in the effective mass due to an increase in the electronic density of states near the Fermi level. This resulted from the increase in bond length of Nb (or Ta)-O. As a result, the use of Nb and Ta as substitutes led to an increase in the figure of merit value, which was attributed to the increase in both the effective mass and carrier concentration [66].

Srivastava, D., et al. (2018) synthesized $\text{Sr}_{0.8}\text{La}_{0.067}\text{Ti}_{0.8}\text{Nb}_{0.2}\text{O}_{3-\delta}$ ceramics with inclusions of Cu or Fe by the mixed oxide route and sintered under reducing conditions at 1700 K. The resulting products were highly dense, with Fe enhanced density (to 98% theoretical) and grain size (to 15 μm), while Cu tended to reduce both slightly. XRD and SEM analyses indicated that the material was primarily composed of cubic SrTiO_3 phase, with rutile structured minor phases and metallic inclusions along the grain boundaries. The inclusions increased carrier concentration and carrier mobility, leading to a reduction in electrical resistivity by a factor of 5 and increase in PF by 75%. Both types of metallic inclusions were beneficial, increasing the ZT from 0.25 at 1000 K for the control sample to ZT of 0.36 at 900 K for the Cu-containing samples and to 0.38 at 1000 K for the Fe-containing samples, as shown in Figure 34 [4].

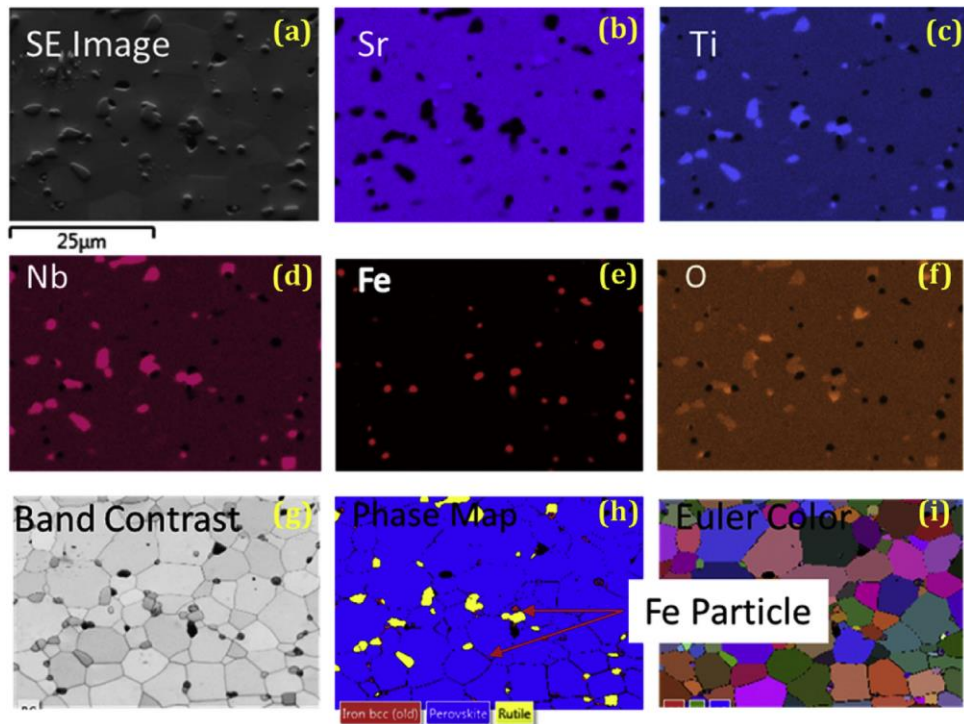


Figure 34 Micrographs and maps for samples containing Fe: (a) Backscattered electron (SE) image; (b-f) Elemental maps: (b) Sr, (c) Ti, (d) Nb, (e) Fe, (f) O; (g-i) EBSD maps: (g) Band contrast map with grain boundaries showing sharp contrast, (h) Phase distribution map of Fe particles (red) and rutile based phase (yellow) in the $\text{Sr}_{0.8}\text{La}_{0.06}\text{Ti}_{0.8}\text{Nb}_{0.2}\text{O}_3$ primary phase, (i) Euler false color maps indicating random orientation of primary phase grains [4].

2.2.3 $\text{Ca}_3\text{Co}_4\text{O}_9$ - based TE materials

Zhang, F., et al. (2013) showed thermoelectric properties of $\text{Ca}_{2.9}\text{M}_{0.1}\text{Co}_4\text{O}_9$ ($\text{M}=\text{Ca}$, Ba, La, Ag), that were prepared using citrate acid sol-gel synthesis method followed by spark plasma sintering technique (heated at 1073 K for 8 h) and was sintered by SPS at 1073 K. XRD pattern showed all samples which were found to be single-phase. The electrical resistivity was found to change due to a modification in carrier concentration, while the carrier transport process remained unaffected. However, the S was observed to deteriorate simultaneously. Through optimization, it was determined that the Ba-doped sample had the highest ZT value among the bulk samples tested, surpassing the undoped sample. Figure 35 displays the significant increase in the dimensionless figure of merit ZT 0.20 at 973 K for the $\text{Ca}_{2.9}\text{Ba}_{0.1}\text{Co}_4\text{O}_9$ [67].

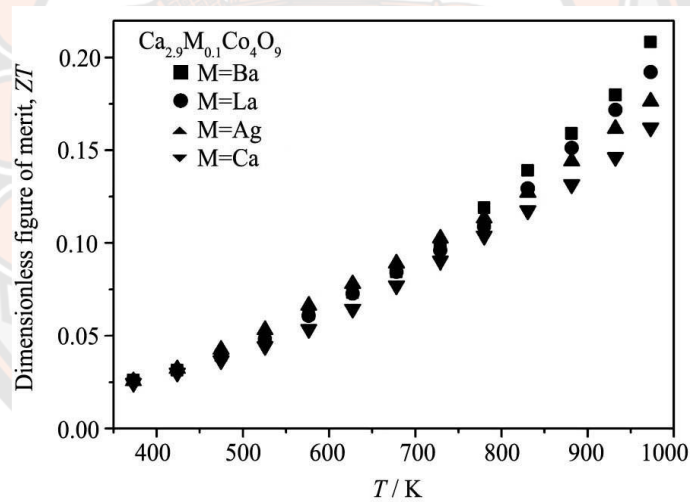


Figure 35 Dimensionless figure of merit ZT of the $\text{Ca}_{2.9}\text{M}_{0.1}\text{Co}_4\text{O}_9$ ($\text{M} = \text{Ca}$, Ba, La, Ag) bulk samples [67].

DViez, J.C., et al. (2013) synthesized $\text{Ca}_3\text{Co}_{4-x}\text{Cr}_x\text{O}_9$ polycrystalline thermoelectric ceramics with small amounts of Cr using a solid-state method. Microstructural analysis showed that all the Cr was incorporated into the $\text{Ca}_3\text{Co}_4\text{O}_9$ structure without producing any secondary phases for Cr content ≤ 0.05 . The optimal amount of Cr for Co substitution was determined based on the power factor values at 323 and 1073 K, which were found to be maximum for the 0.05 Cr-doped samples

with values of around 0.11 and 0.25 $\mu\text{W/K}^2\text{m}$, respectively. These values were about 25% higher than those obtained for undoped samples (Figure 36). Additionally, the power factor value at 1073 K was higher than the typical values obtained for samples prepared by the classical solid-state method [68].

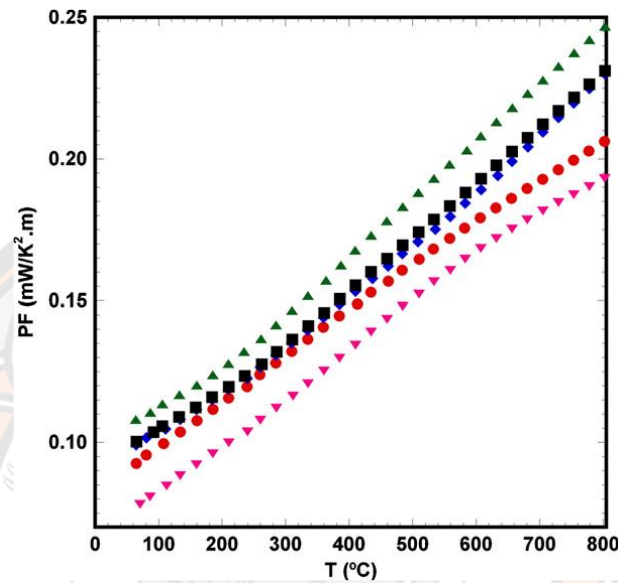


Figure 36 Temperature dependence of the power factor as a function of Cr content in $\text{Ca}_3\text{Co}_{4-x}\text{Cr}_x\text{O}_9$ samples, for $x = 0.00$ (●); 0.01 (◆); 0.03 (■); 0.05 (▲); and 0.10 (▼) [68].

Constantinescu, G. (2014) reported effect of Ga addition on Ca-deficient $\text{Ca}_3\text{Co}_4\text{O}_9$, thermoelectric properties of $\text{Ca}_{3-x}\text{Ga}_x\text{Co}_4\text{O}_9$ with $x = 0.00, 0.01, 0.03, 0.05, 0.07, 0.10, 0.12, 0.15$, and 0.17 , were synthesized using the classical solid-state method and sintered at 1183 K for 24 hours. The addition of Ga to Ca-deficient $\text{Ca}_3\text{Co}_4\text{O}_9$ samples was found to improve their thermoelectric properties, with Ga content of ≥ 0.07 leading to the production of $\text{Ca}_{3-x}\text{Ga}_x\text{Co}_4\text{O}_9$ pure phase samples and the disappearance of the $\text{Ca}_3\text{Co}_2\text{O}_6$ secondary phase. This microstructural modification resulted in a decrease in electrical resistivity due to an increase in carrier concentration and a reduction in activation energy values. The optimal Ga addition has been determined using the values of the power factor at 323 and 1073 K, which is the maximum for the 0.12 Ga-doped samples with values around 0.15 and 0.34 $\mu\text{W/K}^2\text{m}$ respectively [69].

Wu, N., et al. (2014) reported thermoelectric properties of $\text{Ca}_3\text{Co}_4\text{O}_{9+\delta}$ prepared by a conventional citric-nitrate sol-gel method and auto-combustion process. The sample was calcined at 1023 K and sintering temperatures from 973 to 1123 K, with a fixed uniaxial pressure of 50 MPa and a ramping rate of 100 K/min kept constant at 5 min. In order to examine any potential anisotropy in the transport properties, the microstructure and thermoelectric transport characteristics were evaluated along both the parallel (\parallel) and perpendicular (\perp) directions to the SPS pressure axis. Figure 37 displays the results obtained at at 1073 K, which show power factors of $506 \mu\text{W/mK}^2$ (\perp) and $147 \mu\text{W/mK}^2$ (\parallel), as well as thermal conductivities values of 2.53 W/mK (\perp) and 1.25 W/mK (\parallel). The corresponding figures-of-merit, ZT , was observed at 0.21 (\perp) and 0.13 (\parallel). Besides, the auto-combustion synthesis can be utilized for improving the thermoelectric performance of not only pure $\text{Ca}_3\text{Co}_4\text{O}_{9+\delta}$ but also doped variants of the material [70].

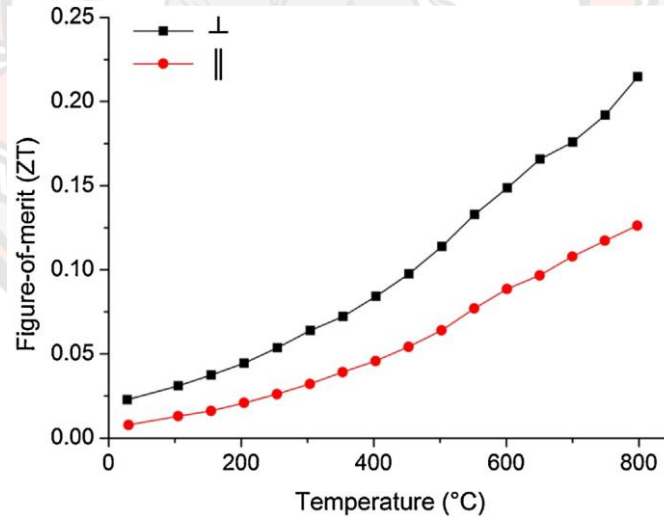


Figure 37 The temperature dependence of the ZT measured along the \perp and \parallel directions [70].

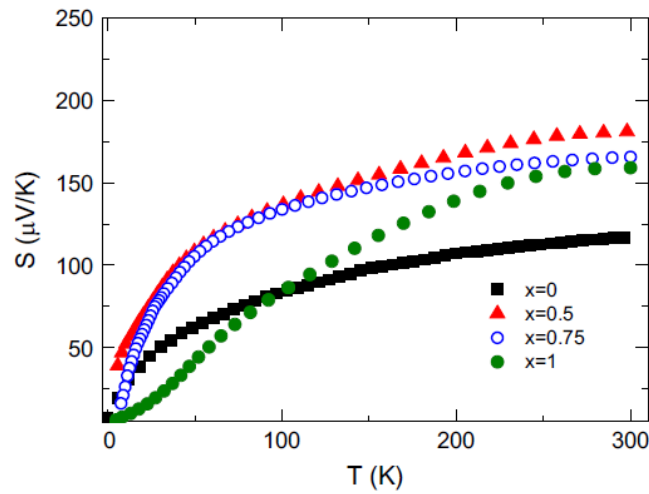


Figure 38 Temperature dependence of Seebeck coefficient (S) of $\text{Ca}_{3-x}\text{B}_x\text{Co}_4\text{O}_9$ ($x = 0, 0.5, 0.75$, and 1) [71].

Demirel, S., et al. (2014) reported structural, electrical, thermal, and thermoelectric properties of $\text{Ca}_{3-x}\text{B}_x\text{Co}_4\text{O}_9$ ($x = 0, 0.5, 0.75$, and 1) that were synthesized by the solid-state reactions, calcinated several times in $\alpha\text{-Al}_2\text{O}_3$ crucibles at 1173 K and sintered at 1173 K for 36 hours. The S was $181\text{ }\mu\text{V/K}$ at room temperature as shows in Figure 38, which is ~ 1.5 times higher than pure $\text{Ca}_3\text{Co}_4\text{O}_9$ [71].

Zhang, D., et al. (2014) investigated the impact of Cu-doping on the structure, magnetic and electrical transport characteristics of $\text{Ca}_3\text{Co}_4\text{O}_{9+\delta}$ misfit cobalt oxide system. The $\text{Ca}_3\text{Co}_{4-x}\text{Cu}_x\text{O}_{9+\delta}$ polycrystalline samples with Cu content of $x = 0, 0.1, 0.2$, and 0.4 were synthesized through a conventional solid-state reaction approach and then subjected to calcination at 1173 K for 12 hours in an air atmosphere, followed by sintered in an O_2 atmosphere at 1173 K for 12 hours. Finally, the powders were reground, pelletized, and then sintered in flowing O_2 gas at 1223 K for 36 hours. The magnetic results confirmed a rise in Co^{4+} concentration with increasing level of Cu-doping, indicating that adjusting the Co^{4+} concentration could be an effective method for enhancing the spin entropy in cobalt oxides [72].

Agilandeswari, K. and A. Ruban Kumar (2014) described the preparation of pure $\text{Ca}_3\text{Co}_4\text{O}_9$ ceramic powder through a sol-gel combustion method assisted by starch, which was then calcined at different temperatures. The XRD pattern of the

sample sintered at 1073 K for 12 hours confirmed the existence of a stable and single-phase $\text{Ca}_3\text{Co}_4\text{O}_9$ material. The SEM images displayed a microporous, sphere-like morphology with agglomerated assembled spheres, indicating excellent connectivity among the grains (Figure 39). The average diameter of these spheres was found to be in the range of 150 - 300 nm. The optical characterization of $\text{Ca}_3\text{Co}_4\text{O}_9$ ceramic revealed a band gap with an energy level of 2.10 eV. Furthermore, the material displayed a maximum electrical resistivity of 0.002 $\text{m}\Omega \text{ cm}$, which decreased to 0.0012 $\text{m}\Omega \text{ cm}$ as the temperature increased from 300 K to 473 K. Dielectric studies conducted at various temperatures, ranging from room temperature to 673 K, indicated that space charge polarization was a contributing factor to the conduction mechanism. Additionally, the study showed dielectric relaxation with an activation energy of 0.96 eV. The temperature-dependent magnetic properties indicated a ferri-paramagnetic phase transition occurring at temperatures above 50 K. The M-H curve displayed a hysteresis loop with saturation magnetization (M_s), confirming the existence of soft magnetic materials [73].

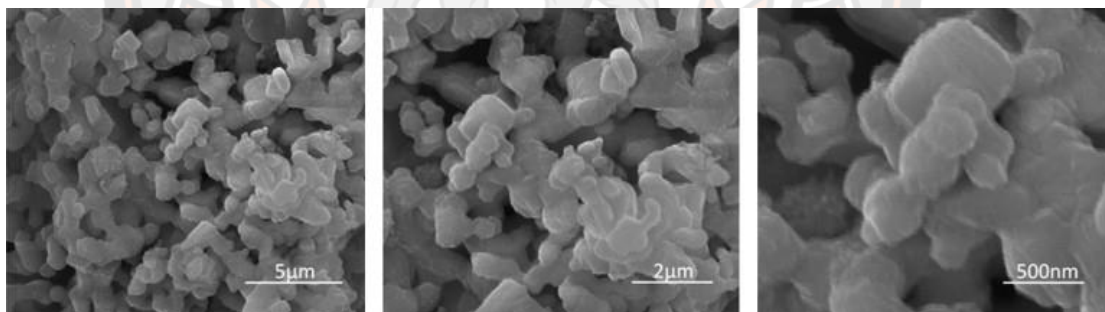


Figure 39 SEM images of $\text{Ca}_3\text{Co}_4\text{O}_9$ [73].

Demirel, S., et al. (2015) investigated the structural, electrical, thermal, and magnetic properties of $\text{Ca}_{3-x}\text{Pb}_x\text{Co}_4\text{O}_9$ (where $x = 0.0 - 0.75$) using a conventional solid-state reaction technique. The samples were calcined at 1173 K for 36 hours under an oxygen atmosphere and sintered at the same temperature for 36 hours. X-ray diffraction analysis showed that the (002) peak shifted to a lower angle with an increase in Pb content, indicating successful Pb ion doping in the $\text{Ca}_{3-x}\text{Pb}_x\text{Co}_4\text{O}_9$ structure up to 0.5. The thermopower (S) had a positive value across all temperature ranges, with a value between 113 and 200 $\mu\text{V/K}$ around room temperature. The

sample achieved a room temperature ZT value of 3.4×10^{-3} (Figure 40), which was approximately 16 times higher than that of the undoped sample [5].

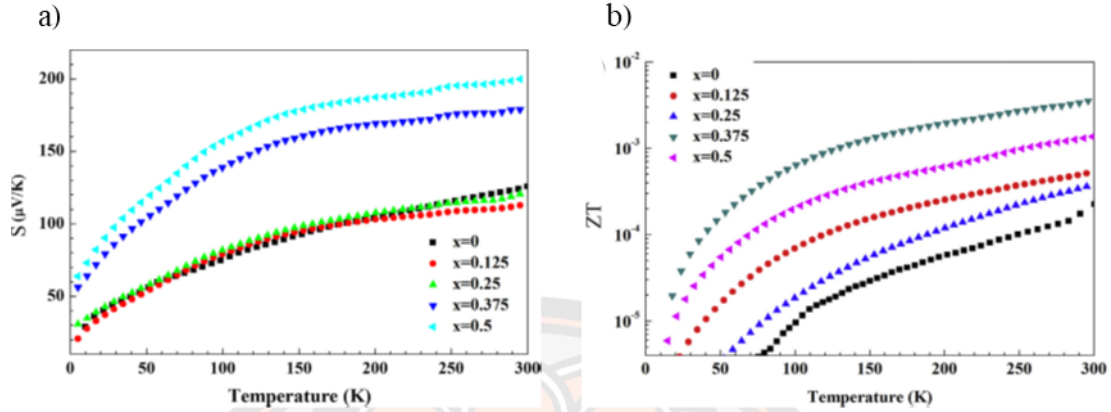


Figure 40 Temperature variation of (a) thermopower and (b) ZT for $\text{Ca}_{3-x}\text{Pb}_x\text{Co}_4\text{O}_9$ ($x = 0 - 0.5$) samples [5].

Delorme, F., et al. (2015) investigated the thermoelectric properties of $\text{Ca}_3\text{Co}_4\text{O}_9$ - Co_3O_4 composites with $x = 0, 10, 20$ and 50 vol%. The samples were prepared through solid-state reaction and sintered by spark plasma sintering. DTA analysis showed no reaction between Co_3O_4 and $\text{Ca}_3\text{Co}_4\text{O}_9$ particles during the high-temperature heat treatment. The addition of Co_3O_4 particles to the $\text{Ca}_3\text{Co}_4\text{O}_9$ matrix significantly impacted the thermoelectric properties. At high temperatures, the Seebeck coefficient was found to increase for the sample with $x = 0.5$. However, the electrical conductivity of the composite samples was reduced by a factor of two at 1000 K for $x = 0.5$. Furthermore, the thermal diffusivity was increased over the entire temperature range with an increase in Co_3O_4 content (Figure 41). As a result, the ZT values were reduced by a factor of approximately 2.5 for the sample with $x = 0.5$. These changes in thermoelectric properties may be attributed to the compressive strain on $\text{Ca}_3\text{Co}_4\text{O}_9$, caused by the mismatch in thermal expansion coefficients between $\text{Ca}_3\text{Co}_4\text{O}_9$ and Co_3O_4 [74].

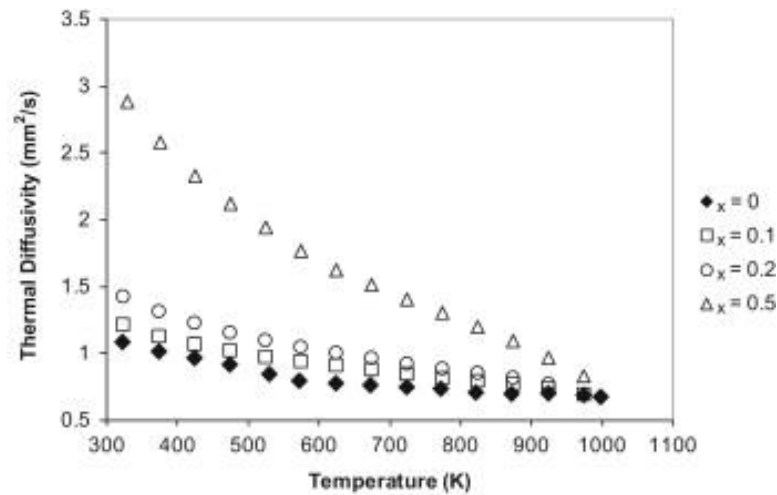


Figure 41 Temperature dependence of the thermal diffusivity as a function of the Co_3O_4 content [74].

Huang, C.S., et al. (2016) investigated the effects of dual doping with barium and praseodymium on the thermoelectric properties of $\text{Ca}_{2.8}\text{Ba}_{0.1}\text{Pr}_{0.1}\text{Co}_4\text{O}_{9+\delta}$ ($x, y = 0, 0.05, 0.1, 0.15$ and 0.2). The bulk specimens were prepared through a wet sol-gel method and spark plasma sintering, resulting in single-phase materials with modified grain orientation and bulk texture, leading to modulated electrical and thermal transport properties. The $\text{Ca}_{2.8}\text{Ba}_x\text{Pr}_y\text{Co}_4\text{O}_{9+\delta}$ ($x, y = 0.1$) bulk material samples exhibited the highest power factor values and the lowest total thermal conductivity values within the measured temperature range. At 973 K, the values reached $4620 \times 10^{-7} \text{ W/mK}$ and 1.48 W/mK , respectively, which were 14% higher and 27% lower than that of the $\text{Ca}_3\text{Co}_4\text{O}_{9+\delta}$ specimen. The bulk material also exhibited the highest thermoelectric figure of merit, reaching 0.31 at 973 K for the $\text{Ca}_{2.8}\text{Ba}_{0.1}\text{Pr}_{0.1}\text{Co}_4\text{O}_{9+\delta}$ bulk specimen due to the improved power factor and suppressed thermal conductivity (Figure 42). This figure of merit value was much higher than that of the parent specimen. The dual doping of barium and praseodymium had a positive effect on optimizing the thermoelectric performance of the titled oxide materials [20].

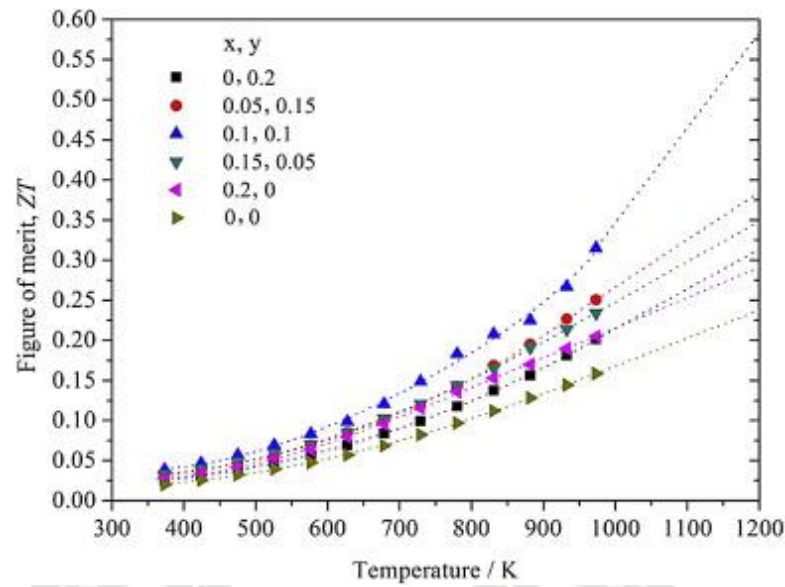


Figure 42 The ZT of the Ba and Pr dual doped $\text{Ca}_3\text{Co}_4\text{O}_{9+\delta}$ bulk specimens [20].

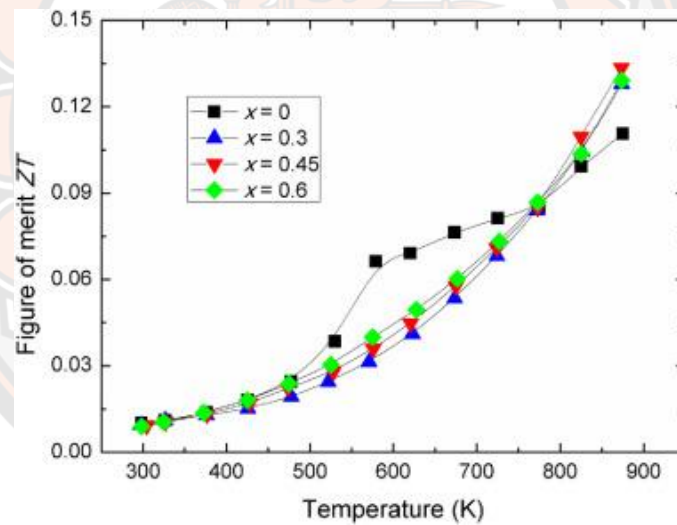


Figure 43 Temperature dependencies of ZT in the $\text{Ca}_{3-x}\text{Na}_x\text{Co}_4\text{O}_{9-x}\text{F}_x$ samples [75].

Porokhin, S., et al. (2017) investigated the thermoelectric properties of $\text{Ca}_{3-x}\text{Na}_x\text{Co}_4\text{O}_{9-x}\text{F}_x$ ($x = 0, 0.3, 0.45, 0.6$) oxide ceramics, which were prepared through a two-step solid state reaction route. The samples were calcination at 1173 K in air for 48 hours, followed by SPS process 1023 K under a pressure of 60 MPa for 5 min. Before measurements, the samples were annealed in air at 1023 K for 5 hours. The ceramics were found to be p-type semiconductors with their electrical and thermal

transport properties significantly influenced by the double substitution of Na^+ for Ca^{2+} and O^{2+} for F^+ . The addition of NaF led to a decrease in the electrical resistivity, an increase in thermal conductivity, and a slight increase in the thermopower at high temperature. The highest value of $ZT = 0.13$ was obtained for the $x = 0.45$ sample at 873 K, which is approximately 20% larger than the ZT of pure $\text{Ca}_3\text{Co}_4\text{O}_9$ (Figure 43) [75].

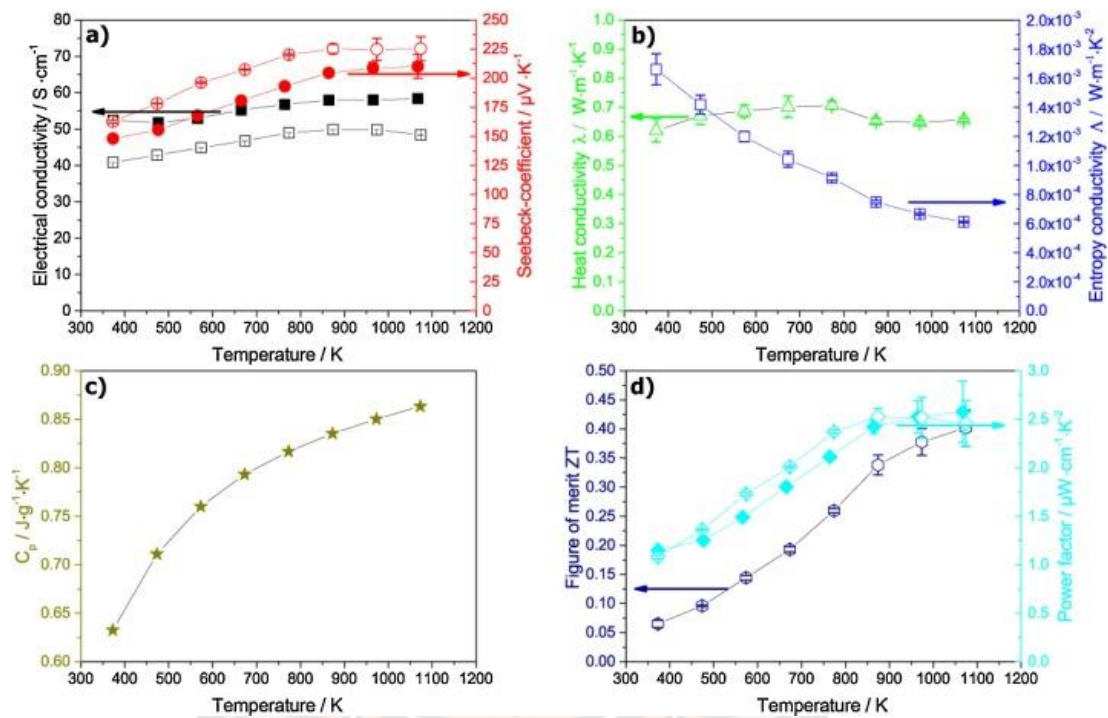


Figure 44 Thermoelectric parameters of a $\text{Ca}_3\text{Co}_4\text{O}_9$ ceramic [76].

Bittner, M., et al. (2017) reported thermoelectric properties of $\text{Ca}_3\text{Co}_4\text{O}_9$, with the samples fabricated by sol-gel synthesis and calcined for 10 hours at 1023 K with a heating and cooling rate of 3 min/K, and sintered for 10 hours at 1173 K with the same heating and cooling parameters. The $\text{Ca}_3\text{Co}_4\text{O}_9$ ceramic has a relative density of 67.7%, and its thermoelectric properties were measured in the temperature range of 373 K to 1073 K. At 1073 K, it achieved a power factor of $2.46 \mu\text{W/cm K}^2$, a low heat conductivity of 0.63 W/m K , and an entropy conductivity of $0.61 \mu\text{W/m K}^2$. The resulting figure of merit, ZT , of 0.4 from the sol-gel synthesized $\text{Ca}_3\text{Co}_4\text{O}_9$ is

the highest reported for non-doped $\text{Ca}_3\text{Co}_4\text{O}_9$ (Figure 44). The high porosity and consequently reduced thermal conductivity led to a high ZT value [76].

Jiaolian Luo, et al. (2017) successfully synthesized $\text{Ca}_3\text{Co}_4\text{O}_9$ thermoelectric material by sol-gel method. The calcination temperature of the powdery sample was 1073 K, 1123 K, 1173 K and 1273 K with the calcination time of 4 hours. The optimum sintering temperature is 1073 K. The SEM analysis results indicated that the crystal morphology consists of granulates and porous honeycomb which are closely connected. The structure of the sample is densified and uniform and the porous honeycomb increased the phonon dispersion, as well as decreased thermal conductivity. The $\text{Ca}_3\text{Co}_4\text{O}_9$ honeycomb structure can attain a good performance with broad application prospects as thermoelectric material [77].

2.2.4 Sol-Gel auto-combustion method

Xuwen, W., Z. Zhiyong, and Z. Shuixian (2001) demonstrated Nanocrystalline SrTiO_3 powder prepared by a sol-gel process. The XRD results revealed that SrTiO_3 prepared was a cubic-perovskite phase and the grain size calculated by the Scherrer formula lies in the nanometer-grade. The impurities of SrTiO_3 are reduced as temperature rises. The TEM photograph of powder treated at 1023 K for an hour gave very homogeneous grain distribution and the size was in the narrow range of 12–25 nm [78].

Klaytae, T., P. Panthong, and S. Thountom (2013) successfully synthesized nanocrystalline SrTiO_3 powder by sol-gel combustion method with the citric acid as fuel. The cubic perovskite structure of phase pure SrTiO_3 was obtained in nanometer ranges (with an average crystallite size of about 23 nm from XRD) at 773 K, along with an acid treatment process. The crystallite size was found to decrease with increasing calcined temperatures based on XRD analysis. The particles exhibited uniform and spherical shapes, as observed by SEM and TEM (Figure 45). The average particle size from TEM was estimated to be around 7.5 nm after the acid treatment process and calcination at 873 K [79].

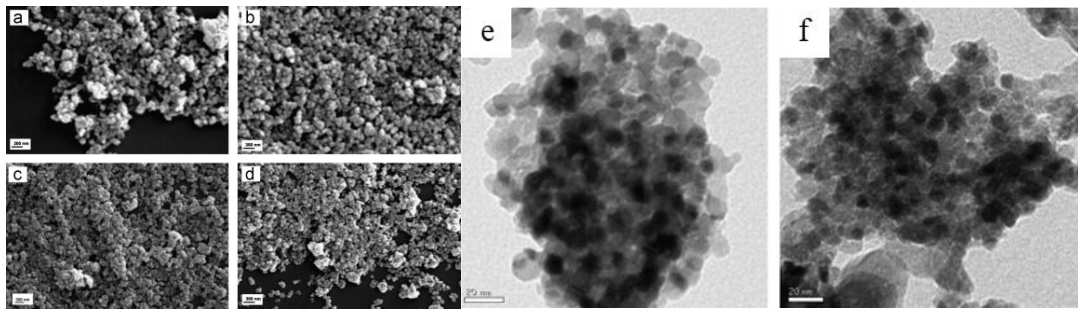


Figure 45 (a-d) SEM micrographs of SrTiO_3 at calcination temperature (a) 773 K, (b) 873 K, (c) 973 K and (d) 1073 K and (e-f) TEM micrographs of SrTiO_3 (e) before and (f) after coupled with an acid treatment process calcined at temperature of 873 K [79].

Meng, Y.Y., et al. (2014) reported magnetic properties of barium ferrite ($\text{BaFe}_{12}\text{O}_{19}$) samples that were synthesized by a sol-gel combustion technique using glycine gels prepared from metal nitrates and glycine solutions. Their findings showed that the formation of a single-phase $\text{BaFe}_{12}\text{O}_{19}$ is greatly affected by the Fe/Ba molar ratio, which is optimal at 9/1. The X-ray diffraction (XRD) patterns revealed that high calcination temperature and large glycine dosage are favorable for the formation of $\text{BaFe}_{12}\text{O}_{19}$. The morphologies of the selected powders produced at various calcination temperatures of 1173 and 1273 K were observed using scanning electron microscopy (SEM) and are presented in Figure 46. The powders calcined at 1173 K exhibited ultrafine particles with homogeneous distribution. However, at 1273 K, the micrograph showed plate-like particles of barium ferrite with varying grain sizes that agglomerate into larger ones. The TEM and size distribution analysis showed that the $\text{BaFe}_{12}\text{O}_{19}$ powders have plate-like shapes with crystallite size ranging from 55 to 110 nm. The study found that a glycine/nitrates molar ratio of 12/9 and a calcination temperature of 1173 K were optimal for achieving a high coercive force of 5750 Oe and saturation magnetization of 67.7 emu/g in the synthesized $\text{BaFe}_{12}\text{O}_{19}$ samples [80].

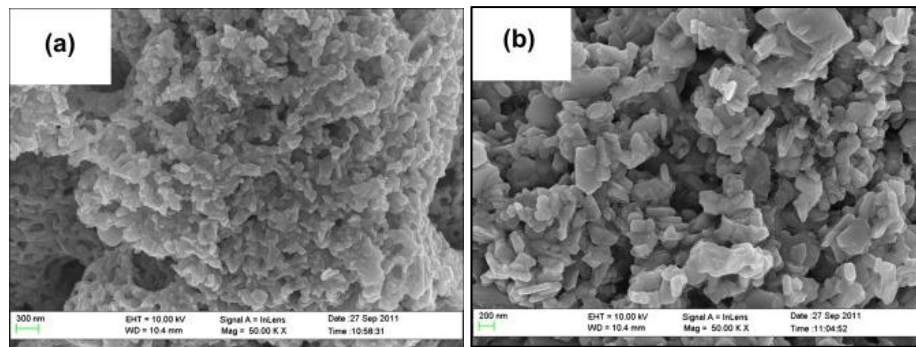


Figure 46 SEM images of the powders calcined at different temperatures for 2 h: (a) 1173 K and (b) 1273 K [80].

Thongchanthep, C. and S. Thoutom (2015) discussed the dielectric properties of $\text{Ba}_{0.7}\text{Sr}_{0.3}\text{TiO}_3$, that were prepared by the sol-gel combustion using urea as fuel. The samples were calcined at 723–1223 K for 2 hours, followed by sintering at various temperatures (1223–1623 K) for 2 hours. At the calcination temperature of 1023 K, X-ray diffraction (XRD) revealed the presence of a pure perovskite phase. The SEM showed the grain size increases corresponding with the sintering temperature, and the grains became interconnected (Figure 47). The grains had a predominantly spherical shape and their size increased with higher sintering temperatures. The average grain size ranged from 0.18 μm to 3.93 μm . Specifically, the sample sintered at 1623 K for 2 hours exhibited an impressive dielectric constant of approximately 4870 [81].

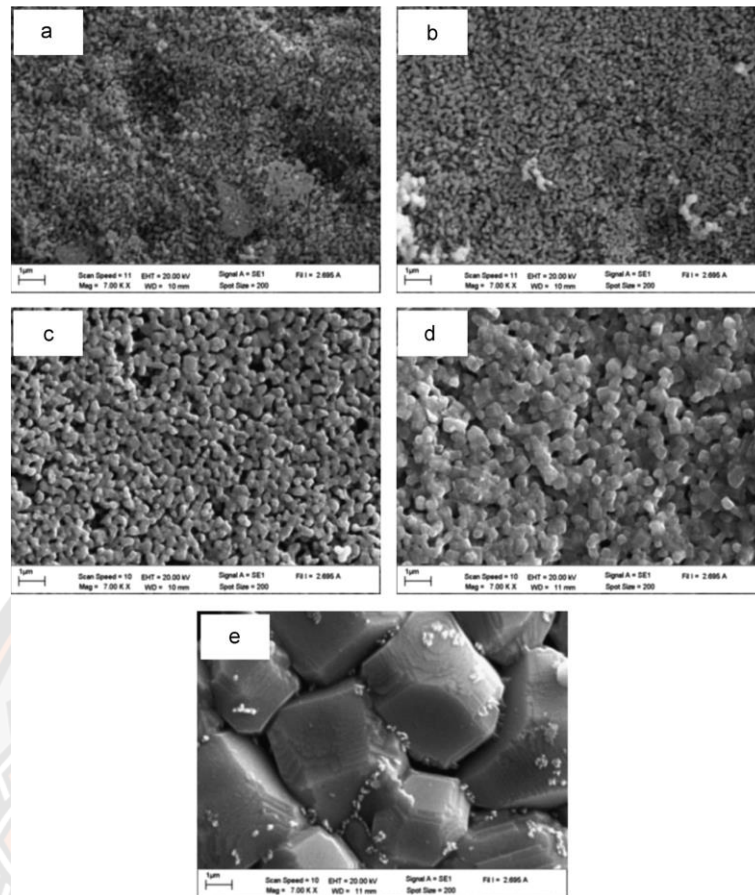


Figure 47 SEM micrographs of the $\text{Ba}_{0.7}\text{Sr}_{0.3}\text{TiO}_3$ ceramics with urea as fuel sintered at different temperatures : (a) 1223 K, (b) 1323 K, (c) 1423 K, (d) 1523 K, (e) 1623 K [81].

Alamolhoda, S., et al. (2016) synthesized NiFe_2O_4 with and without different CTAB contents by sol-gel auto combustion. According to the FESEM analysis, the addition of CTAB led to a more refined microstructure and a narrower distribution of particle sizes. Additionally, the mean crystallite sizes of the samples, as calculated by the Scherrer equation, decreased from 46 to 27 nm as the amount of CTAB increased [82].

Liu, G., et al. (2016) reported thermoelectric properties of Cu_2SnSe_3 samples that were prepared by combustion synthesis. The combustion process was three ways as combustion synthesis in the air, in vacuum or Ar atmosphere and in a high-gravity field. The findings revealed that the partial substitution of Sn with In ($\text{Cu}_2\text{Sn}_{0.95}\text{In}_{0.05}\text{Se}_3$). resulted in a significant improvement in the electrical

conductivity of the Cu_2SnSe_3 samples, as well as a reduction in thermal conductivity. When comparing the sample synthesized under a high-gravity field with the sample synthesized in a 2 MPa Ar atmosphere, the former exhibited a smaller electrical conductivity, a larger Seebeck coefficient, and a higher thermal conductivity. The maximum ZT values for the undoped and In-doped Cu_2SnSe_3 samples were 0.51 and 0.62, respectively, at 773 K, as shown in Figure 48 [29].

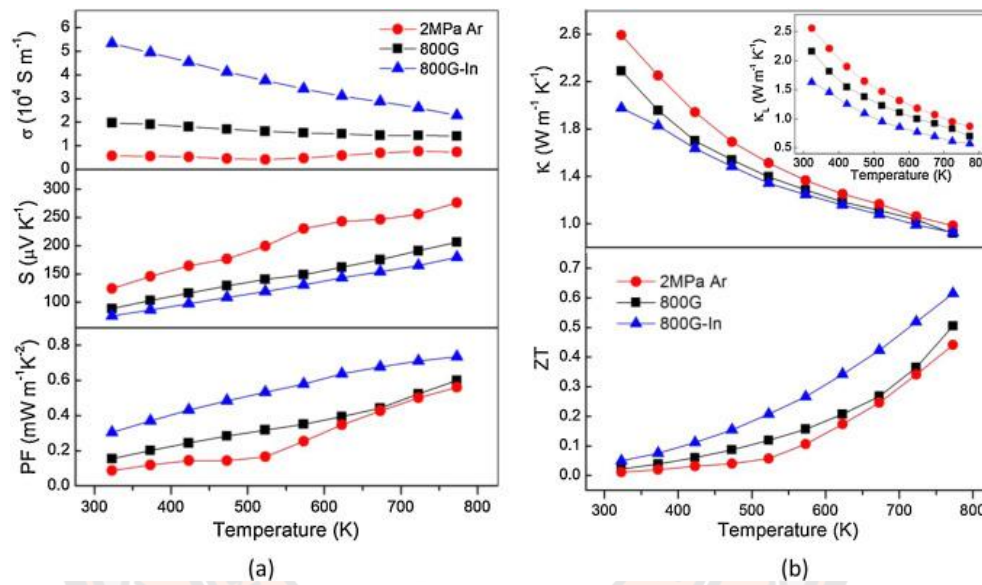


Figure 48 Thermoelectric properties of the synthesized Cu_2SnSe_3 samples [29].

Jaimeewong, P., et al. (2016) successfully synthesized Barium calcium zirconate titanate ($\text{Ba}_{0.85}\text{Ca}_{0.15}\text{Zr}_{0.1}\text{Ti}_{0.9}\text{O}_3$; BCZT) by the sol-gel auto-combustion method. To adjust the pH values to 5, 7, and 9, varying amounts of NH_4OH were added to the solution, while the mole ratio between $\text{C}_6\text{H}_8\text{O}_7$ and metal was maintained at 1:1. The results showed that an increase in pH value led to greater chemical reaction on the powder surface and tetragonality. Specifically, the optimum synthesis condition was found to be at $\text{pH} = 7$, which produced a nano-sized powder with a narrow size distribution. This suggested that a chemically neutral environment was crucial for good reactivity and well-controlled nucleation and growth of BCZT particles [83].

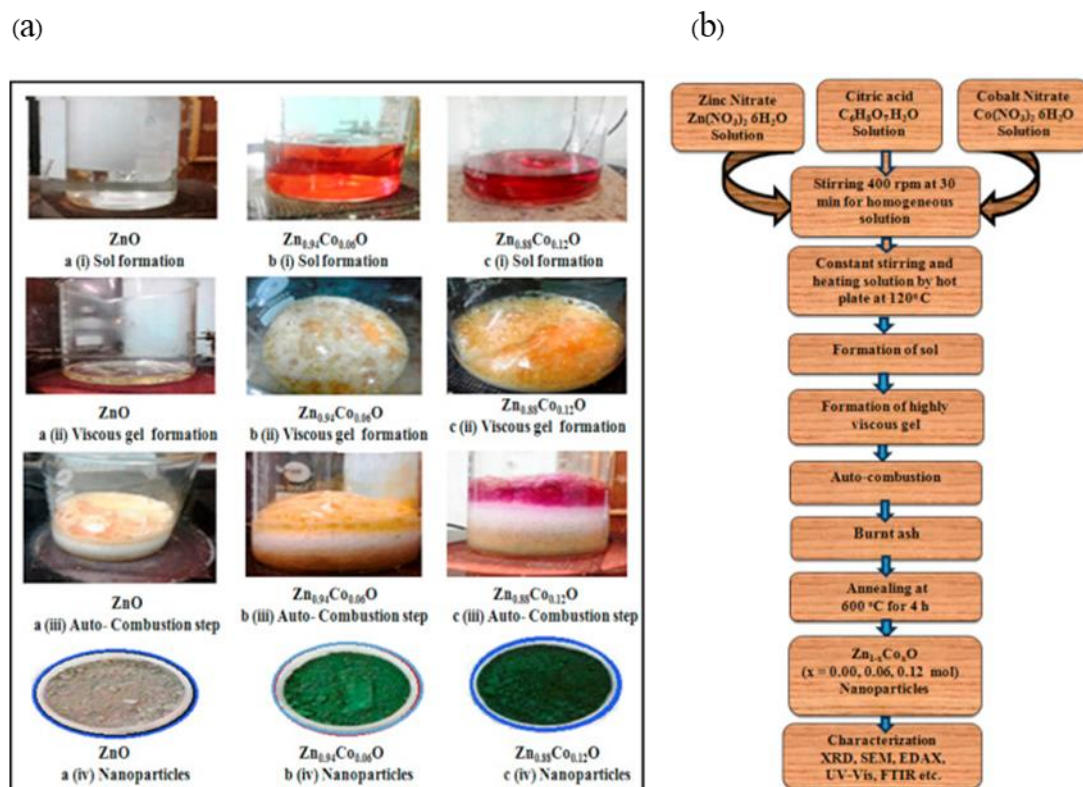


Figure 49 (a) Various stages involved in the synthesis of Zn_{1-x}Co_xO ($x = 0.00, 0.06, 0.12$ mol) nanoparticles. (b) Scheme of sol-gel auto combustion synthesis method of Zn_{1-x}Co_xO ($x = 0.00, 0.06$ and 0.12 mol) nanoparticles [84].

Birajdar, S.D., et al. (2016) described the sol-gel auto combustion method as a highly advantageous technique with many benefits over other methods. These advantages include a fast-heating rate and short reaction time, molecular-level mixing of reagents, high product purity and crystallinity, fine and narrowly distributed particle sizes, easy control of stoichiometry, and the ability to introduce dopants into the final product easily. Additionally, this method involves simple equipment and preparation processes, low processing time, low external energy consumption (as the process initiates at low temperatures) and does not require multiple steps. The sol-gel auto combustion method is particularly effective in producing nanoscale materials with high porosity and high surface area to volume ratio fine particles. The method works by initiating an exothermic reaction at low temperatures that becomes self-sustaining for a certain time interval. In their study, Birajdar et al. successfully

synthesized undoped and Co^{2+} doped ZnO nanoparticles using citric acid as a fuel with a fuel ratio based on stoichiometric proportions of metal nitrate to oxidizer ratio (1:1.11). A scheme of the sol-gel auto combustion synthesis method is depicted in Figure 49 [84].

Park, C.-S., et al. (2017) investigated the porosity effect on the thermoelectric properties of Nb-doped SrTiO_3 by controlling the surfactant concentration. Metal propionate powder was used as a precursor and Brij-S10 was used as a copolymer surfactant to prepare the mesoporous STNO. The study revealed that an increase in surfactant concentration led to enhanced carrier concentration and reduced carrier mobility, which was primarily attributed to an increase in oxygen vacancies and porosity. As a result, the STNO exhibited an enhanced Seebeck coefficient but increased electrical resistivity with increasing surfactant concentration, as shown in Figure 50. By implementing a mesoporous structure in STNO, an improved power factor was achieved due to the much larger change in the square of the Seebeck coefficient (3.6 times) compared to the change in electrical resistivity (1.6 times), as stated in reference [85].

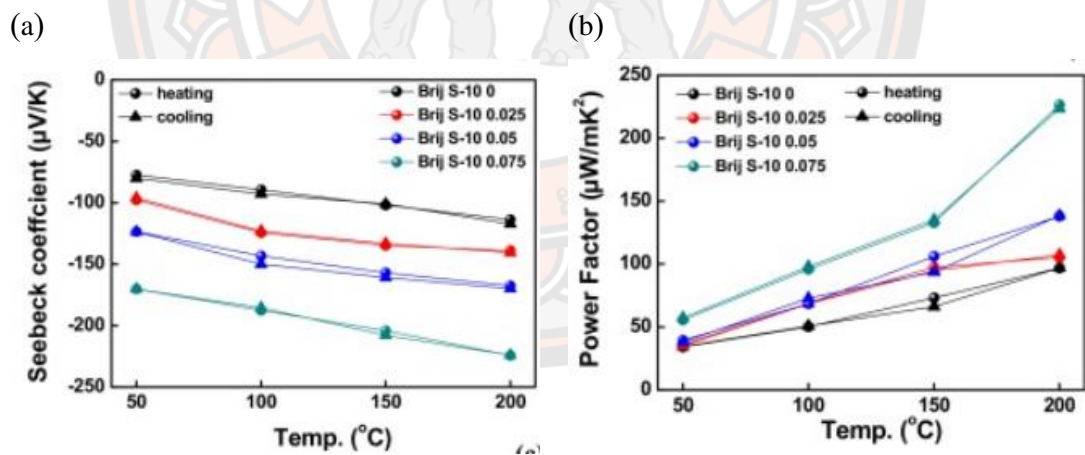


Figure 50 (a) Seebeck coefficient and (b) power factor of STNO synthesized using various surfactant concentrations [85].

Tangcharoen, T., et al. (2018) successfully synthesized nanocrystalline NiO/ZnO heterostructured composite powders using the sol-gel auto combustion method with diethanolamine (DEA) as a novel fuel. The NiO/ZnO composite powders were then calcined at a temperature of 1273 K for 4 hours. The authors investigated

the composition of different ratios of NiO and ZnO, ranging from 100/0 to 0/100, and analyzed how these ratios affected the structural, morphological, optical, and fluorescence properties of the synthesized powders. The XRD and Raman results obtained by the researchers confirmed that when the ZnO concentration in the sample was below 20%, Zn ions could fully substitute into the NiO lattice, resulting in the formation of a NiO/ZnO coupled metal oxide with no variation in the crystal phase. Additionally, SEM images showed that the morphology of the particles transformed from an irregular spherical shape of NiO to a fine cubic-like shape with an increase in ZnO concentration up to 0.5. According to the study, all the samples exhibited strong absorption in the UV region, with the maximum value reaching 90%, while an increase in ZnO concentration resulted in an improvement in reflectance in the VIS and NIR regions, up to 52% and 72%, respectively. Furthermore, in the low ZnO concentration samples, Zn atoms were found to be soluble in the rock salt phase, while Ni atoms were present in both WZ and RS phases in low NiO concentration samples, as reported by the researchers [86].

Birajdar, S.D., et al. (2018) synthesized pure ZnO and Mn-doped ZnO nanoparticles using the sol-gel auto combustion technique and sintered them at a temperature of 873 K for 6 hours. The researchers then studied the properties of these nanoparticles. The XRD pattern showed a single phase of Mn^{2+} doped ZnO with a hexagonal wurtzite structure. The average crystallite size, as determined by Scherrer's formula, was found to be in the range of 14-17 nm. The FT-IR analysis performed on the synthesized nanoparticles confirmed the presence of a Zn-O bond and the substitution of Zn^{2+} ions by Mn^{2+} ions in the crystal lattice structure. The magnetic properties of the sample were investigated using a vibrating sample magnetometer (VSM), which indicated that pure ZnO nanoparticles showed diamagnetic behavior, while Mn-doped ZnO nanoparticles exhibited paramagnetic behavior [87].

Kokare, M.K., et al. (2018) studied the structural and magnetic properties of $\text{Ni}_{0.5}\text{Co}_{0.5}\text{Nd}_x\text{Fe}_{2-x}\text{O}_4$ ($x = 0.025$ to 0.125 , in increments of 0.025). The researchers used a sol-gel auto combustion method to synthesize the samples, which were then sintered in air at a temperature of 833 K for a period of 4 hours. The XRD analysis showed that all samples exhibited the cubic spinel structure with the $\text{Fd}3\text{m}$ space group. The researchers also used FE-SEM to study the morphology and

microstructure of the samples, which showed an agglomerated grain structure. Additionally, the crystallite size of the samples was determined through TEM and found to be 41 nm, 37 nm, and 35 nm for $x = 0.025$, 0.100, and 0.125, respectively. The FTIR spectrum of samples revealed characteristic features of spinel ferrites with two prominent absorption bands at approximately 400 cm^{-1} and 600 cm^{-1} . The saturation magnetization decreased as the Nd^{3+} concentration increased from $x = 0.025$ to $x = 0.100$, but at $x = 0.125$, the saturation magnetization increased [88].

Previous research works indicate the efforts to develop thermoelectric materials in order to improve ZT to a value greater than 3. There are many ways to enhance ZT , such as material selection, optimization of thermoelectric properties and fabrication methods. The semiconductors are suitable thermoelectric materials for getting good ZT by optimizing their thermoelectric properties. For optimizing thermoelectric characteristics or properties of the materials, there are two main approaches. The first approach involves the development of bulk thermoelectric materials by alloying, doping, preparing nanostructured thermoelectric materials by reducing the material grain size and nanocomposites preparation. While the second method entails preparing nano (thin) films, based on nanotechnology. There are many fabrication methods developed for synthesizing thermoelectric materials. The widely used fabrication methods are mechanical alloying (MA), melting process, microwave irradiation, hot pressing, and spark plasma sintering (SPS). Although there have been much research and development tailored towards improving ZT , however; current advances to increase ZT to above 3 is still futile. Therefore, this research gap is the motivation and intention of the current research; to enhance ZT value of thermoelectrics oxide viz. p-type $\text{Ca}_3\text{Co}_4\text{O}_9$, and n-type SrTiO_3 , with doped oxide metal (Nb-doped SrTiO_3 , La-doped SrTiO_3 and Ag-doped $\text{Ca}_3\text{Co}_4\text{O}_9$), by sol-gel auto combustion technique.

CHAPTER III

RESEARCH METHODOLOGY

3.1 Chemical reagents and equipment

- 1) Strontium nitrate, $\text{Sr}(\text{NO}_3)_2$, ACS reagent, 99.0%, Himedia
- 2) Titanium(IV) butoxide, $\text{C}_{16}\text{H}_{36}\text{O}_4\text{Ti}$, purum $\geq 97\%$, Sigma-Aldrich
- 3) Calcium nitrate tetrahydrate, $\text{Ca}(\text{NO}_3)_2 \cdot 4\text{H}_2\text{O}$, Sigma-Aldrich
- 4) Cobalt(II) nitrate hexahydrate, $\text{Co}(\text{NO}_3)_2 \cdot 6\text{H}_2\text{O}$, Sigma-Aldrich
- 5) Lanthanum(III) nitrate hexahydrate, $\text{La}(\text{NO}_3)_3 \cdot 6\text{H}_2\text{O}$, 99%, Lobachemie
- 6) Silver Nitrate, AgNO_3 , 99%, Sigma-Aldrich
- 7) Niobium Oxide, Nb_2O_5 , 99%, Sigma-Aldrich
- 8) Citric acid monohydrate, $\text{C}_6\text{H}_8\text{O}_7 \cdot \text{H}_2\text{O}$, 99.5-102%, Lobachemie
- 9) Glycine, $\text{C}_2\text{H}_5\text{NO}_2$, Analytical reagent, 99%, Ajax FineChem
- 10) Ammonium nitrate, NH_4NO_3 , Commercial
- 11) Ethylene glycol $((\text{CH}_2\text{OH})_2)$, 99.5%, Lobachemie
- 12) Hydrochloric acid 37%, RCI Labscan
- 13) Electric balance, Ohaus, PA214, United States
- 14) Oven, Memmert, UN55, Germany
- 15) Hotplate magnetic stirrer, IKA, C-MAG HS7, Germany
- 16) High-temperature furnace, SCM, Japan
- 17) Ultrasonic cleaner, Elma, Elmasonic S 30 H, Germany
- 18) Polisher, Maruto, Doctor-lap, Japan
- 19) X-ray Diffraction (XRD), Rigaku, Ultima IV, Japan
- 20) Scanning electron microscopy with energy dispersive X-ray spectroscopy (SEM/EDX), JEOL JSM-6335F and JSM-6500F, Japan
- 21) Spectrofluorometer (PL) HORIBA, FluoroMax – 4, Japan
- 22) Spectrophotometer (UV-Vis), Hitachi, UH5300, Japan
- 23) Electrochemical Impedance Spectroscopy (EIS), Metrohm Autolab B.V., PGSTAT302N, Switzerland
- 24) Hardness tester, Matsuzawa Seiki, MMT-X, Japan

- 25) Laser flash apparatus, Netzsch, LFA-467, Germany
- 26) Thermoelectric power (TEP) measurement, Advance RIKO, ZEM-3, Japan

3.2 Methodology

The purposes of this research are to synthesize thermoelectric oxide materials, n-type (Nb-doped SrTiO₃ and La-doped SrTiO₃) and p-type (Ag-doped Ca₃Co₄O₉) by sol-gel auto combustion technique with different contents of dopant. The powder samples were characterized phase, morphology and optical properties using XRD, Raman, SEM, SEM/EDX, Luminescent and UV-vis Near IR. Investigation of photocatalytic properties by considering the decolorization of methylene blue (MB) in an aqueous solution under UV irradiation. The bulk samples were prepared by spark plasma sintering (SPS) technique. Thermoelectric properties (Seebeck coefficient, electrical resistivity, and thermal conductivity) of bulk samples were determined.

3.2.1 Synthesis and Characterize of La-doped SrTiO₃ for photocatalytic applications

Sr_{1-x}La_xTiO₃ (SLTO) nanopowders were synthesized using the sol-gel auto combustion technique. The commercial reagents strontium nitrate (Sr(NO₃)₂, Sigma-Aldrich), titanium (IV) butoxide (C₁₆H₃₆O₄Ti, Sigma-Aldrich), lanthanum(III) nitrate hexahydrate, (La(NO₃)₃·6H₂O, Loba Chemie), citric acid monohydrate (C₆H₈O₇·H₂O, Loba Chemie), ethylene glycol (C₂H₆O₂, Loba Chemie), ammonium nitrate (NH₄NO₃) and glycine (C₂H₅NO₂, Ajax FineChem) were used as the starting materials. A mixture of organic fuel was provided based on a molar ratio of glycine to citric acid of 1:2 used for the auto-combustion reaction. The mixture organic fuel to metal nitrate molar ratio was 1.5 to obtain a fuel-rich composition, achieving the high yields and best performance. Initially, stoichiometric quantities of Sr(NO₃)₂, C₁₆H₃₆O₄Ti, La(NO₃)₃·6H₂O, C₆H₈O₇·6H₂O, C₂H₅NO₂ and NH₄NO₃ were dissolved in 100 mL of deionized water with selected La mole fractions in SLTO samples with $x = 0, 0.03, 0.05, 0.07$ and 0.1 . The mixture solution was heated and constantly stirred at 80°C until a homogeneous nitrate precursor in the form of a transparent solution

was achieved, after 2 hours, at which time the ethylene glycol was added in order to enhance the forming of metal/organic gels.

The mixed solution was maintained in a heated state and constantly stirred until it transformed into a highly viscous gel. Immediately, the condensed gel was placed in an oven pre-heated to 200°C for self-ignited combustion synthesis. A dark brown precursor powder was achieved 1 hours after auto-combustion and the powder was then ground to fine particles and calcined at 900°C for 2 hours in a furnace which resulted in a white SLTO powder being produced, as shown in Figure 51.

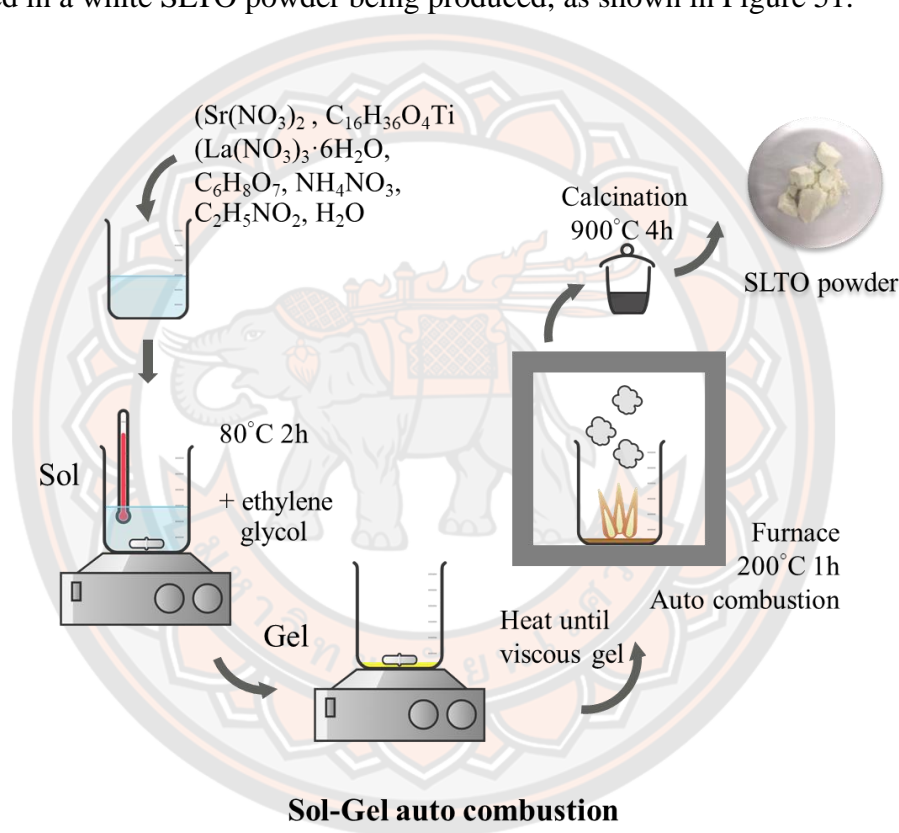
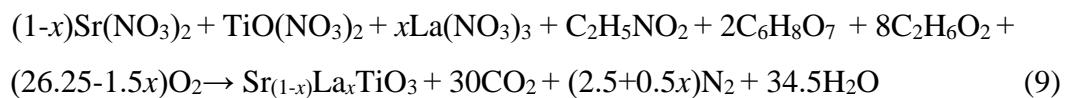
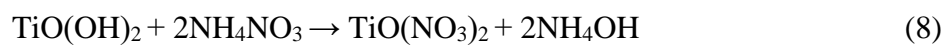
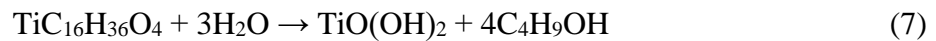


Figure 51 Scheme of synthesized La-doped SrTiO₃ by sol-gel auto combustion.

The mechanism of the sol-gel auto combustion route to prepare SLTO are as follows:



The thermal decomposition of the as-prepared SLTO sample with $x = 0$ after auto-combustion was measured by thermogravimetric/differential thermalgravimetric analysis (TG/DTG) at between 30 – 900°C in air at heating rate 10°C/min using a Perkin Elmer (Pyris 1 model). The phase analyses of the powders produced from the six fractions (with $x = 0, 0.03, 0.05, 0.07$ and 0.1) were evaluated by X-ray diffraction (XRD) with Cu-K $_{\alpha}$ radiation ($\lambda = 1.5406 \text{ \AA}$) over Bragg's angles ($2\theta, 10^{\circ} - 80^{\circ}$) at a step size of 0.02 and time/step of 0.5s. The morphologies of the particles were examined using a scanning electron microscope (FESEM, JEOL JSM-6335F) with an energy dispersive X-ray spectroscopy (EDS). Specific surface area and total pore volume of the samples were measured by Nitrogen adsorption - desorption isotherms at 77 K on a Micrometrics Surface Area and Porosity Analyzer (TriStar II 3020 model). The Brunauer–Emmett–Teller (BET) method was utilized to examine the specific surface areas. The powder samples were suspended in ethanol and sonicated for 30 min. The absorbance spectra of the sonicated ethanol suspensions were recorded at room temperature with a UV-visible-near infrared spectrophotometer (UH5300, HITACHI) in the range 275-500 nm. The Photoluminescence spectra of the samples were taken with a spectrofluorometer (FluoroMax – 4, HORIBA) using excitation wavelength (λ_{ex}) of 327 nm at room temperature.

In addition, the photocatalytic activity of the La-doped and undoped SLTO samples was investigated by considering the rate of decolorization of MB in an aqueous solution under UV irradiation. The UV lamps presented a peak wavelength (λ_p) at 253.7 nm (100-280 nm), with a net output of 108 W (18 W \times 6 tubes). The suspensions of the sample were positioned 40 cm away from the UV lamps. A suspension was prepared by dispersing 100 mg of the synthesized sample into 200 ml of 10 ppm MB. The suspension was then stirred continuously in a darkroom for 30 min to reach adsorption/desorption equilibrium. The suspension was then irradiated under UV lamps while being continuously stirred at room temperature. After initiation, 5 ml of the reaction suspension was sampled every 1 hour for 8 hours. The UV-Vis absorption of the solutions was also recorded using a UV-Vis spectrophotometer (UH5300, HITACHI) at 400-800 nm. In order to consider the effect of photocatalyst, the control sample with no SLTO photocatalyst added was

also tested under the same experiment process. The decolorization efficiency (%DE) is expressed in the following equation:

$$\%DE = \frac{C_0 - C}{C_0} \times 100 \quad (10)$$

where C_0 is the initial concentration of the MB, and C is the concentration of the MB at various times, after UV irradiation.

3.2.2 Synthesis and Characterize of La-doped SrTiO₃ for thermoelectric applications

A number of samples containing compound Sr_(1-x)La_xTiO₃ (SLTO, $x = 0, 0.01, 0.05, 0.07, \text{ and } 0.10$) were synthesized by the sol-gel auto combustion reaction. The raw materials included the commercial reagents strontium nitrate (Sr(NO₃)₂, Sigma-Aldrich), titanium (IV) butoxide (C₁₆H₃₆O₄Ti, Sigma-Aldrich), lanthanum (III) nitrate hexahydrate, (La(NO₃)₃·6H₂O, Loba Chemie), citric acid monohydrate (C₆H₈O₇·H₂O, Loba Chemie), ethylene glycol (C₂H₆O₂, Loba Chemie), ammonium nitrate (NH₄NO₃) and glycine (C₂H₅NO₂, Ajax FineChem). The sol-gel auto combustion method and the fuel ratio of auto combustion reaction followed previous work [89, 90]. The mixture solution of Sr(NO₃)₂, C₁₆H₃₆O₄Ti, La(NO₃)₃·6H₂O, C₆H₈O₇·H₂O, NH₄NO₃ and C₂H₅NO₂ in DI water was heated and continuously stirred at 80°C for 2 hours to achieved homogenous nitrate precursor in transparent solution form. To form the metal/organic gels, C₂H₆O₂ was added. The mixture solution was heated and stirred continuously until it became a viscous gel which was immediately placed in the oven, which had been warmed to 200°C, for self-ignite combustion. In 1 hours, the precursor powder was successfully auto-combusted. The powder sample was calcined at 900°C for 4 hours, which differed from previous work due to the production scale of the sample. The final products were pressed into a disk, followed by spark plasma sintering (SPS-515A, DR.SINTER LAB) in a flowing Ar atmosphere under a uniaxial pressure of 50 MPa at 1200°C for 5 minutes, as shown in Figure 52

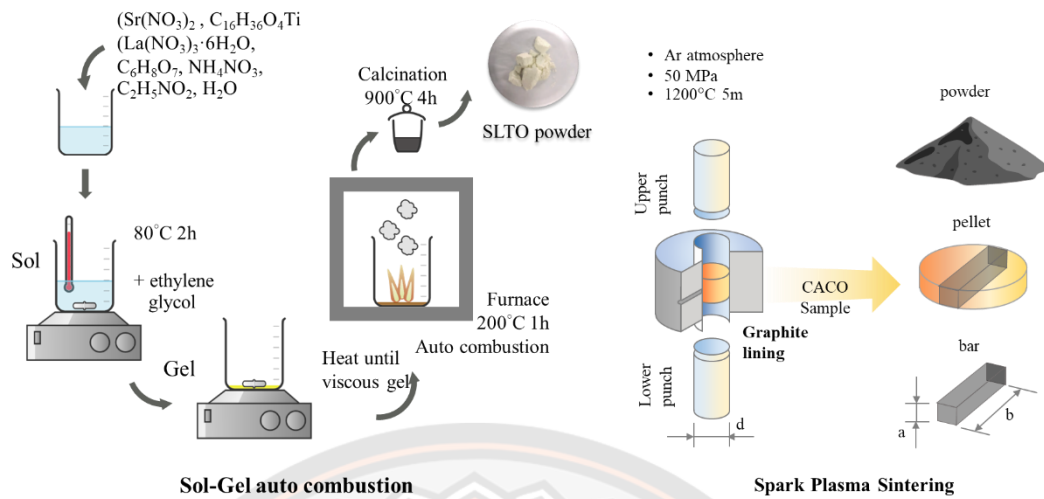


Figure 52 Scheme of synthesized La-doped SrTiO₃ by sol-gel auto combustion followed by SPS.

The phase composition of the powder and bulk samples was characterized by X-ray diffraction (XRD, Rigaku, Ultima IV) by using Cu-K α radiation ($\lambda = 1.5406 \text{ \AA}$) over Bragg's angles ($2\theta, 10^\circ - 120^\circ$) at a step size of 0.02 and the step time of 0.5s. The density (d) of the bulk samples was evaluated by the weight and dimensions of the samples. The surface morphology, microstructure and chemical compositions were determined using a scanning electron microscope (SEM, JEOL, JSM-6500F) outfitted with an energy dispersive spectrometer (EDS), which was used to investigate the ratio between Sr and La in the STO. The electrical resistivity (ρ) and Seebeck coefficients (S) of the $10 \text{ mm} \times 2 \text{ mm} \times 1 \text{ mm}$ SLTO sample were measured simultaneously in the temperature range from 375 K to 800 K by a commercial instrument (ZEM-3, Ulvac) under Ar atmosphere/vacuum. The thermal conductivity (κ) was calculated based on $\kappa = \alpha C_p d$, where α is the thermal diffusion coefficient measured by laser flash apparatus (Netzsch, LFA-467), C_p was estimated from the Dulong-Petit rule, $C_p = 3nR$, where n is the number of atom per formula unit, R is the gas constant and d is the measured density of the bulk samples. The TE properties of the SLTO sample were investigated in the temperature range from room temperature to 800 K.

3.2.3 Synthesis and Characterize of Nb-doped SrTiO₃ for photocatalytic applications

The SrTi_{1-x}Nb_xO₃ (STNO) samples with $x = 0, 0.01, 0.03, \text{ and } 0.05$ were synthesized by a new synthesis route of sol-gel auto combustion. Strontium nitrate (Sr(NO₃)₂, Sigma-Aldrich), titanium (IV) butoxide (C₁₆H₃₆O₄Ti, Sigma-Aldrich), niobium (V) chloride (NbCl₅, Sigma-Aldrich), glycine (C₂H₅NO₂, Ajax FineChem), citric acid monohydrate (C₆H₈O₇·H₂O, Loba Chemie), hydrochloric acid (HCl, RCI Labscan Limited), ammonium nitrate (NH₄NO₃, Commercial) and ethylene glycol (C₂H₆O₂, Loba Chemie) were used as starting materials. Organic fuel and extra nitrates for the auto-combustion reaction were provided from glycine and citric acid mixture with a 1:2 molar ratio and ammonium nitrate, respectively.

First, stoichiometric amounts of 1 mol of Sr(NO₃)₂, 1 mol of C₁₆H₃₆O₄Ti, 1 mol of C₂H₅NO₂, 2 mol of C₆H₈O₇·H₂O and 2.5 mol of NH₄NO₃ were dissolved in 100 ml of deionized water. Nb solution, prepared by dissolving solid NbCl₅ in concentrated HCl solution, together with selected Nb mole fractions in STNO samples with $x = 0, 0.01, 0.03 \text{ and } 0.05$, were then added to the mixture solution which was heated and constantly stirred at 80°C for 2 hours to achieve a transparent solution of homogeneous nitrate precursor. A solution with the ratio of ethylene glycol: citric acid of 4:1 was then added to enhance the formation of metal/organic gels. The mixture solution was continuously heated and stirred until it transformed into a highly viscous gel. Suddenly, the gel was put in a furnace preheated to 300°C for self-ignited combustion synthesis. A dark brown precursor product was obtained after 1 hour, which was then ground to fine particles and calcined at 1000°C for 12 hours in a furnace. A white STNO powder was successfully produced, as shown in Figure 53.

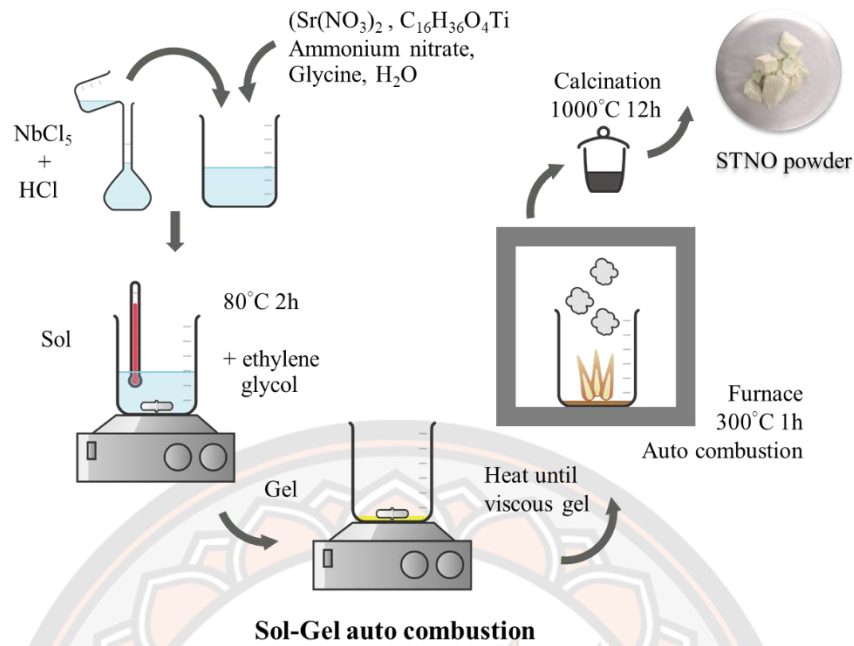
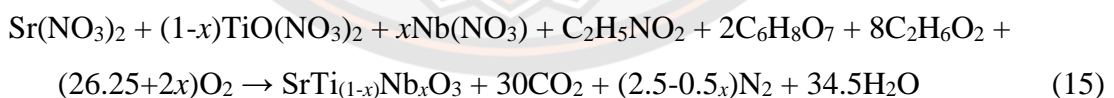
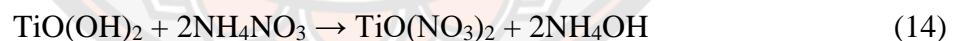
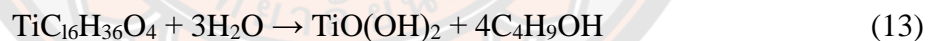
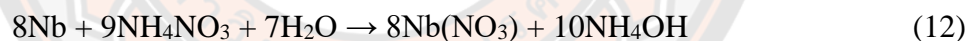


Figure 53 Scheme of synthesized Nb-doped SrTiO₃ by sol-gel auto combustion.

The mechanisms for synthesizing STNO by the sol-gel auto-combustion method are as follows:



The phase identification of the STNO powders was analyzed by X-ray diffraction (XRD) with Cu-K_a radiation ($\lambda = 1.5406 \text{ \AA}$) following Bragg's angles (2θ , $10^\circ - 80^\circ$) at a step size of 0.02 and time/step of 0.5 s. The morphologies of the particles were inspected employing a scanning electron microscope (FESEM, JEOL JSM-6335F) with energy-dispersive X-ray spectroscopy (EDS). A UV-visible-near infrared spectrophotometer (UH5300, HITACHI) was used to measure the absorbance spectra of the samples that has been suspended in ethanol and sonicated for 30 min, at

room temperature, in the range of 300 - 600 nm. Nyquist plot and Mott Schottky plot were carried out with Electrochemical Impedance Spectroscopy (EIS, PGSTAT302N, Metrohm Autolab B.V.), which was performed in 0.1M Na₂SO₄ (pH = 6) electrolyte solution under a typical three-electrode condition consisting a working electrode, a platinum wire counter electrode, and a saturated calomel reference electrode. The STNO thin film was coated on fluorine-doped tin oxide (FTO) glass for use as a working electrode. A spectrofluorometer (FluoroMax – 4, HORIBA) was used to measure the photoluminescence spectra of the samples at room temperature with the excitation wavelength (λ_{ex}) of 327 nm.

Additionally, the photocatalytic activity of the STNO powder was evaluated by the decolorization of the MB in an aqueous solution under UV irradiation with a peak wavelength (λ_p) at 253.7 nm (100-280 nm) using UV lamps with a net output of 108 W (18 W x 6 tubes). The aqueous solution used here had been prepared using 100 mg of STNO catalyst dispersed into 200 ml of 10 ppm MB at room temperature, continuously stirred in the dark for 30 min, to achieve adsorption/desorption equilibrium on the surface of the STNO photocatalytic. During this process, the aqueous solution sample was 40 cm away from the UV lamps. The solution was then continuously stirred under UV lamps for 8 h, with a 5 ml sample taken every hour during this period. Using a UV-Vis spectrophotometer (UH5300, HITACHI), the absorption spectra of the aqueous solution sample were recorded at a whole wavelength of 400-800 nm. To determine the effect of the with/without STNO catalyst, the aqueous solution without STNO was used as a control sample and tested under the same conditions. The decolorization efficiency (%DE) [89, 91] is expressed as the following equation:

$$\%DE = \frac{C_0 - C}{C_0} \times 100 \quad (16)$$

where C_0 is the concentration of the initial MB for the solution to reach adsorption/desorption equilibrium condition and C is the concentration of the MB after UV irradiation of the solution sample.

3.2.4 Synthesis and Characterize of Ag dope $\text{Ca}_3\text{Co}_4\text{O}_9$ for thermoelectric applications

The $\text{Ca}_{3-x}\text{Ag}_x\text{Co}_4\text{O}_9$ (CACO) with $x = 0, 0.1, 0.2, 0.3, 0.4$, and 0.5 was prepared by the sol-gel auto combustion method following the spark plasma sintering (SPS) technique. The calcium nitrate tetrahydrate ($\text{Ca}(\text{NO}_3)_2 \cdot 4\text{H}_2\text{O}$, Sigma-Aldrich), cobalt (II) nitrate hexahydrate ($(\text{Co}(\text{NO}_3)_2 \cdot 6\text{H}_2\text{O})$, Sigma-Aldrich), silver nitrate (AgNO_3 , Sigma-Aldrich), ammonium nitrate (NH_4NO_3 , Commercial), and glycine ($\text{C}_2\text{H}_5\text{NO}_2$, Ajax Finechem) were mixed with deionized water as starting precursor. The precursor was stirred until homogenous dissolved and was heated at 80°C kept for 2 hours. Then, ethylene glycol ($(\text{CH}_2\text{OH})_2$, RCI Labscan) was added to the precursor, kept stirring, and heated until it became viscous gel. Bring the gel into the furnace at 200°C instantly, for self-ignited combustion, and in 1 hour, the gel is completely combusted. The fine powder was calculated at 850°C for 8 hours, following spark plasma sintering at 900°C for 5 min under an Ar environment and pressure 50 MPa, as shown in Figure 54.

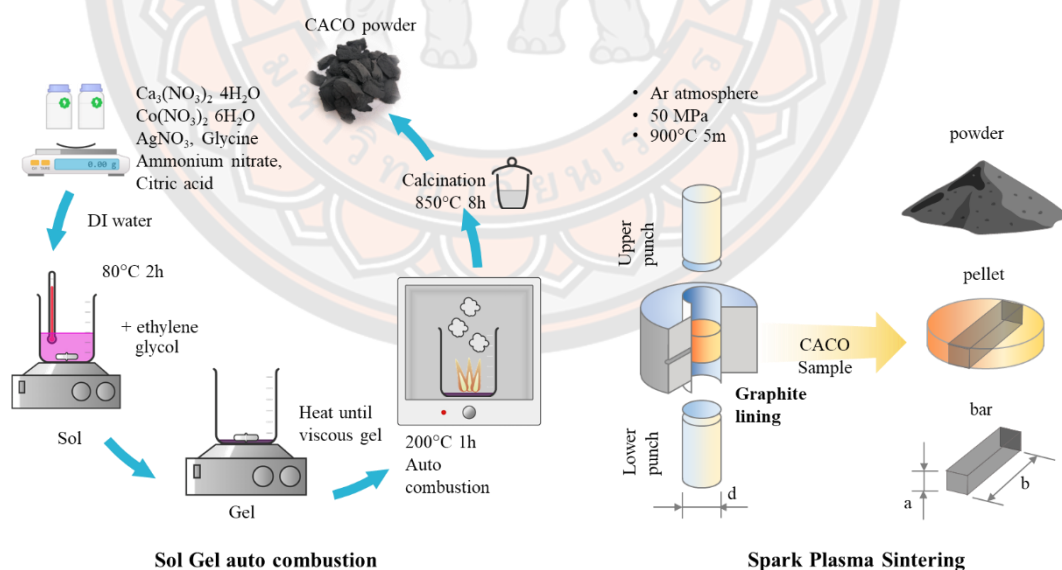


Figure 54 Scheme of synthesized Ag-doped $\text{Ca}_3\text{Co}_4\text{O}_9$ by sol-gel auto combustion followed by SPS.

The X-ray Diffraction (XRD, Rigaku Ultima IV) identified the phase composition of powder and bulk ceramic samples with Cu-K α radiation ($\lambda = 1.5406 \text{ \AA}$) over Bragg angle (2θ , $5^\circ - 80^\circ$) at a step size of 0.02 and the step time of 0.5 s. The density of bulk samples was determined by the weight and dimension of the sample. The Vickers hardness was measured by MATSUZAWA SEIKI MMT-X at room temperature. The measurements were repeated ten times for each sample, with a load of 5 N, and a loading time of 15 s. The surface and chemical compositions were investigated by a scanning electron microscope SEM (JEOL, JSM-6500F and FESEM, JEOL JSM-6335F) equipped with an energy dispersive spectrometer (EDS). The electrical resistivity (ρ) and Seebeck coefficients (S) of the CACO sample were measured in the temperature range from 450 to 950 K, with a step of 100K by ZEM3, Ulvac under He atmosphere/vacuum. The thermal conductivity (κ) was calculated based on $\kappa = \alpha C_p d$, where α is the thermal diffusion coefficient measured by laser flash apparatus (Netzsch, LFA-467) under Ar atmosphere, C_p was estimated from the Dulong-Petit rule, $C_p = 3nR$, where n is the number of atoms per formula unit, R is the gas constant and d is the measured density of the bulk samples. At temperatures ranging from 450 to 950 K, the TE characteristics of the CACO sample were investigated.

CHAPTER IV

RESULT AND DISCUSSION

4.1 La dope SrTiO₃

4.1.1 Characterization of phase, morphology, and optical properties

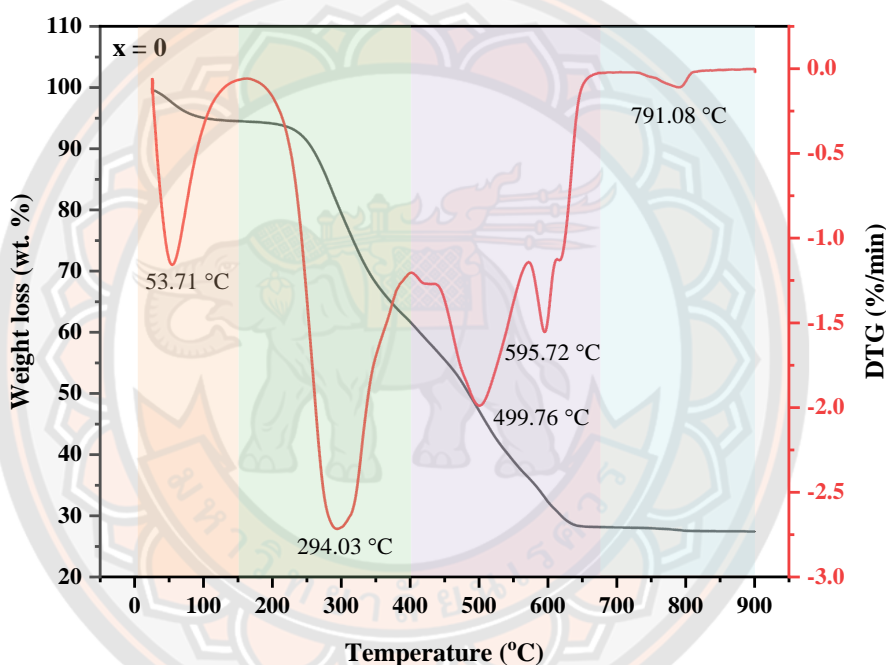


Figure 55 Weight loss (TG) and DTG curves of as-prepared SLTO ($x = 0$) precursor.

To consider the rate of decomposition, thermal stability, physical and chemical phenomena causing changes in heat/temperature, weight loss (TG) and DTG curves of as-prepared SLTO ($x = 0$) powder were determined, as shown in Figure 55. The TG-DTG curves can be divided into four stages. First, from 40 – 130°C, moisture evaporation caused weight loss of around 5%. Second, in the range of 220 – 350°C (weight loss ~ 34%), residual organics of the raw materials, such as NH_4NO_3 , $\text{C}_2\text{H}_5\text{NO}_2$, $\text{C}_6\text{H}_8\text{O}_7 \cdot \text{H}_2\text{O}$ and $\text{C}_2\text{H}_6\text{O}_2$ were decomposed. Third, about 450 – 630°C, a

further weight loss of around 33% occurs at around 450°C. This is the decomposition of *in situ* carbon residues formed during combustion reaction, and the as-prepared SLTO ($x = 0$) precursor presents as dark brown after auto combustion, probably due to the *in situ* formed carbon as an amorphous metal oxide-carbon composite [92]. As well, the decomposition of impurities, forming a pure SrTiO_3 , occurred at 791°C. In the final stage, no relative weight loss was exhibited over 800°C indicating that stable thermal characteristics of the sample had been achieved. The calcination temperature of 900°C for 2 hours was selected due to the appropriate temperature and length of calcination time, as confirmed by the XRD results.

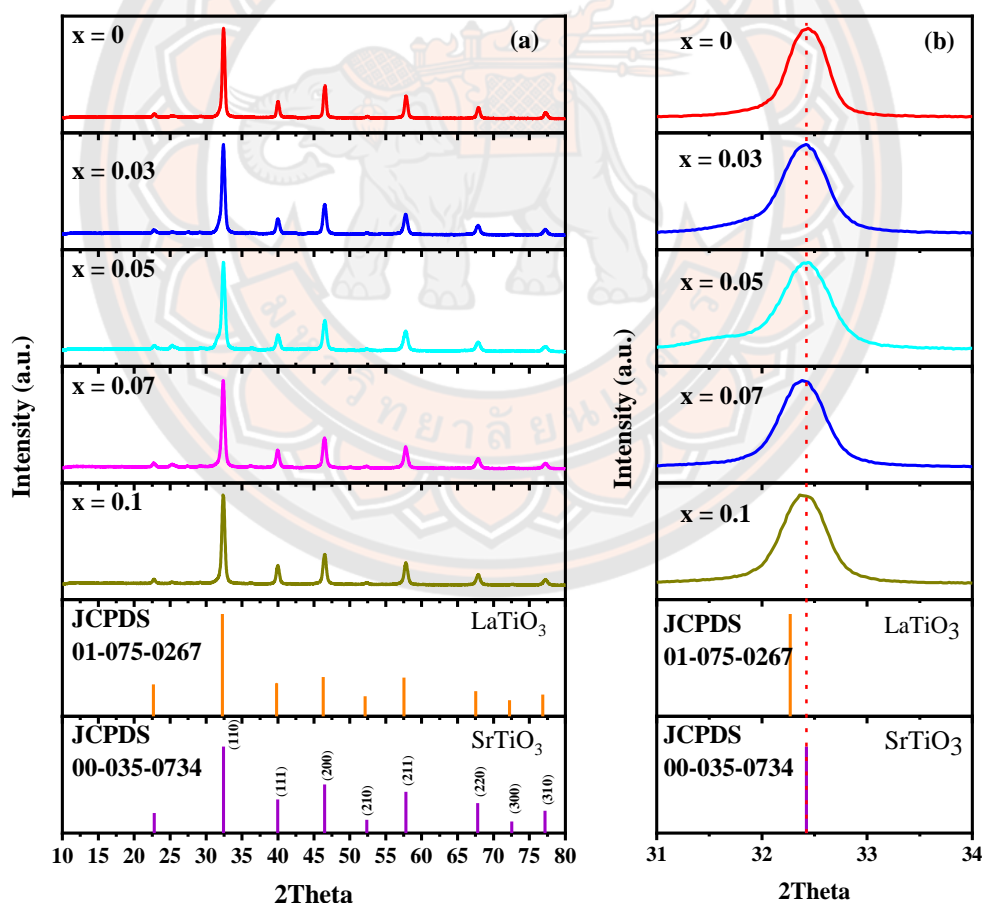


Figure 56 (a) XRD patterns of the SLTO ($x = 0, 0.03, 0.05, 0.07$ and 0.1) nanopowder (b) magnified view of the main XRD peak

The powder XRD patterns of the SLTO nanopowder with $x = 0, 0.03, 0.05, 0.07$ and 0.1 samples after calcination are presented in Figure 55(a). All the samples exhibited the dominant diffraction peak at $2\theta = 32.42^\circ, 40.05^\circ, 46.53^\circ, 57.86^\circ, 67.97^\circ$ and 77.35° corresponding to (110), (111), (200), (211), (220) and (310) planes of a cubic perovskite SrTiO_3 phase (Pm-3m) of the JCPDS no. 035-0634 [93]. The formation of other strontium and titanium compounds such as LaTiO_3 , SrO , SrO_2 , TiO , and TiO_3 were not detected in this analysis. This indicates that all the samples are identified as a single cubic perovskite SrTiO_3 structure. Figure 56(b) presents the magnified main XRD pattern of all the samples at the 2θ range between 31° and 34° according to the (110) plane. The position of the (110) peak was found to shift slightly toward the lower 2θ angles as the amount of La content increased. This is a result of the substitution of the smaller ionic radius of Sr^{2+} (1.13 \AA) by the larger ionic radius of La^{3+} (1.15 \AA) [94] which is consistent with Bragg's law equation: $n\lambda = 2d\sin\theta$ where n is a positive integer and λ is a wavelength of the incident wave. According to a previous study on lattice expansion and local lattice distortion in La-doped SrTiO_3 single crystals [95], the lattice parameter of the SLTO sample increases with increasing the La content. A similar finding was found in [94] for three-dimensional porous La-doped SrTiO_3 microspheres.

The Full Width at Half Maximum (FWHM) values of the XRD patterns of the SLTO nanopowder peaks was used to determine the crystallite size of the samples by Scherrer's equation:

$$D = \frac{k\lambda}{\beta \cos \theta} \quad (17)$$

where D is the average crystallite size, k is the constant as 0.9, λ is the wavelength of Cu-K α radiation (1.5406 \AA), β is the FWHM, θ is the Bragg's angle. The calculated D values of the SLTO samples are summarized in Table 2. The D of SrTiO_3 was 21 nm, while the SLTO samples with La dopant were 17.5 nm, indicating that D of SLTO decreases with La dopant. These results are probably due to the different valences of Sr^{2+} and La^{3+} ions, which lead to induced lattice defects in SLTO samples [94]. Compared to the different methods used for synthesizing the SLTO, the D of SLTO with and without La dopant are relatively lower than those of the SLTO

($x = 0 - 0.50$) nanopowders prepared by the hydrothermal method (27.62-34.46 nm) [93], the three-dimensional porous La-doped SrTiO₃ microspheres synthesized by a modified sol-gel method (96.8-180.4 nm) [94], as well as the D of (La_{0.12}Sr_{0.88})_{0.05}TiO₃ produced by spray pyrolysis (25 nm) [96], and a Sr_{0.96}La_{0.04}TiO₃ prepared by the two techniques solid state reaction (252 nm), and ultrasonic synthesis (137 nm) [97].

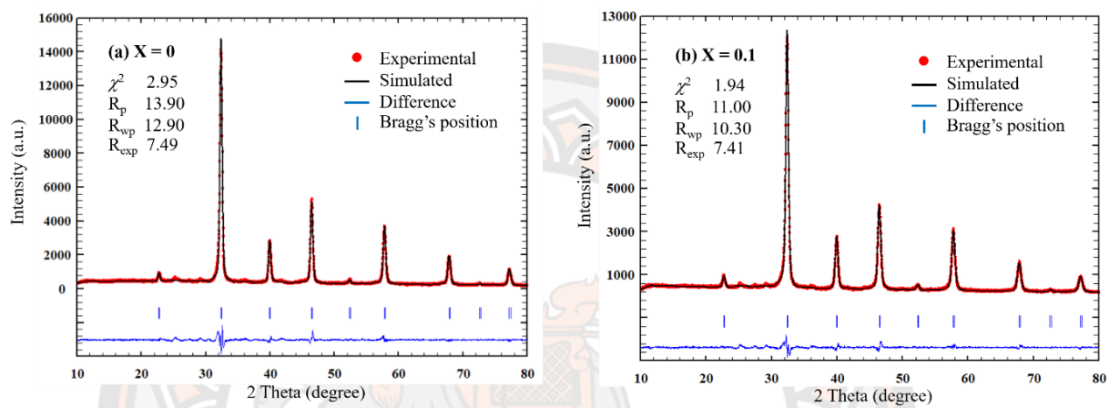


Figure 57 Typical Rietveld refinement analysis of SLTO, (a) $x = 0$ and (b) $x = 0.1$

Table 2 Lattice parameter, Chi squared (χ^2), Rietveld discrepancy factors (R_p , R_{wp} , R_{exp}) and Calculated cell density (d_{cal}) and crystallite size of SLTO ($x = 0, 0.03, 0.05, 0.07$ and 0.1)

Name	Lattice parameter $a = b = c$ (Å)	χ^2	R_p	R_{wp}	R_{exp}	d_{cal} (g/cm ³)	Crystallite sizes (nm)
JCPDS#35-0734	3.9050					5.12	
SrTiO ₃	3.9049	2.95	13.90	12.90	7.49	5.16	21.0
Sr _{0.97} La _{0.03} TiO ₃	3.9061	3.83	16.10	15.40	7.90	5.19	17.5
Sr _{0.95} La _{0.05} TiO ₃	3.9066	4.39	9.39	14.10	6.74	5.25	17.5
Sr _{0.93} La _{0.07} TiO ₃	3.9071	2.50	11.20	11.50	7.29	5.33	17.5
Sr _{0.9} La _{0.1} TiO ₃	3.9075	1.94	11.00	10.30	7.41	5.47	17.5

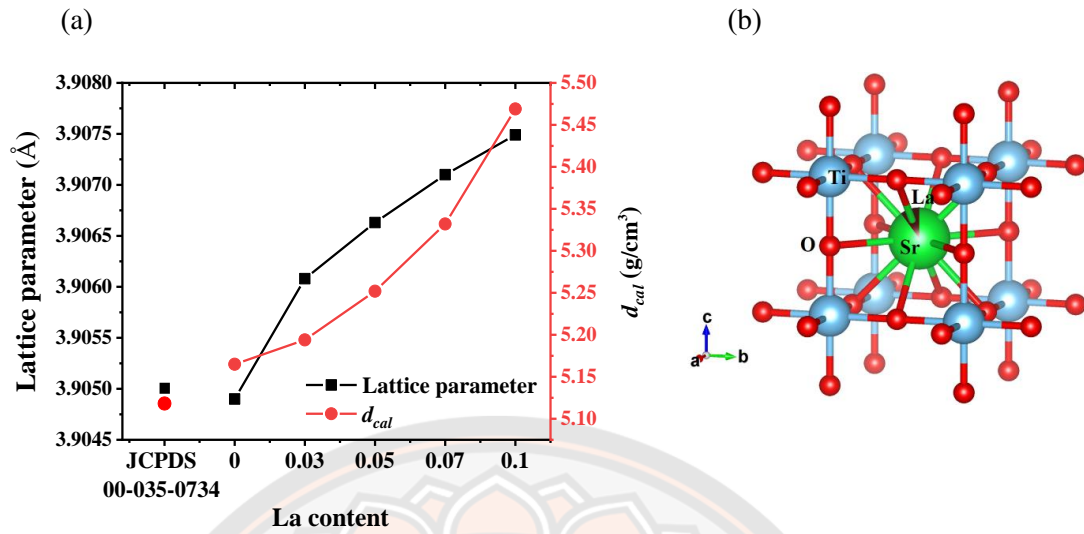


Figure 58 (a) Variation of the lattice parameter and calculated cell density (d_{cal}) of SrTiO_3 JCPDS no 00-035-0734 and SLTO ($x = 0, 0.03, 0.05, 0.07$ and 0.1) (b) The simulate structure of SLTO with $x = 0.1$.

To further consider the effect of La doping contents on the SrTiO_3 cubic perovskite structure, the Rietveld refinement method was used to analyze the experimental XRD data using the Fullprof program. The parameters of the refinement process were (1) the XRD pattern measurements, (2) the lattice constant, (3) profile half-width parameter (u , v and w), (4) atomic functional position, and (5) occupancy. The Chebyshev function was used to determine the background parameter. The diffraction peak profiles were fitted by a pseudo-Voigt function. Figure 57 shows the final output results from the Rietveld refinement analysis of the SLTO with (a) $x = 0$, (b) $x = 0.1$ for all samples shown in Table 2. It was found that all peaks of the SLTO samples fitted well with a low Chi squared (χ^2) and Rietveld discrepancy factors (R_p , R_{wp} , and $R_{exp} < 15\%$). This indicates that the refined XRD patterns were in good agreement with the experimental XRD data, corresponding with the previous study [98]. The variation of the lattice parameter ($a = b = c$) and calculated cell density (d_{cal} , g/cm³) of the SLTO sample as a function of the La content (x) is shown in Figure 58(a). The lattice parameter and d_{cal} of the undoped samples ($x = 0$) were matched with the JCPDS database ($a = b = c = 3.905 \text{ Å}$, $d_{th} = 5.12 \text{ g/cm}^3$). The lattice parameter of the doped samples increased with an increasing La content. This is due

to the substitution of the smaller ionic radius of Sr^{2+} (1.13 Å) by the larger ionic radius of La^{3+} (1.15 Å), according to the three-dimensional porous La-doped SrTiO_3 microspheres [94]. A similar trend of the changes of lattice parameters and local lattice distortion in Nb and La-doped SrTiO_3 single crystals by in-plane x-ray diffraction and first-principles calculations has been investigated [99] and [95].

The cell density of the SLTO samples was also shown to increase with increases in the La content (x) due to the substitution of the large atomic weight element (La) for the lower atomic weight element (Sr). In our research, it is found that by increasing the La dopant content the variation of the atomic weight composed in a unit cell was more considerable than the change of cell volume. The crystal structure of SLTO with $x = 0.1$ obtained from Rietveld refinement analysis is shown in Figure 58(b). With La dopant at $x = 0.1$, when considering the SLTO cubic perovskite structure, it was observed that the La^{3+} substituted in the Sr^{2+} site, with occupancy number of La^3 and Sr^{2+} , were 0.09992 (10% occupied) and 0.89258 (90% occupied).

Figure 59 shows the SEM images of SLTO ($x = 0, 0.03, 0.05, 0.07$ and 0.1) nanopowders that were prepared by the sol-gel auto combustion method and were calcined at 900°C for 2 hours. The morphology of the undoped and La-doped SLTO samples exhibited agglomerated particles of spherical shape. Each sample had a relatively homogeneous size distribution. The average particle size of all the samples were measured using the ImageJ program with 200 particles/sample, as shown in Figure 59(f). The average particle sizes of the SLTO samples were in the nano-scale range and decreased with increased the La content from 68 nm, 58 nm, 48 nm, 44 nm, and 44 nm for sample of $x = 0, 0.03, 0.05, 0.07$ and 0.1 , respectively. These values were in accordance with the crystallite size of the SLTO samples estimated by the Scherrer equation. Compared to different methods for preparing the SLTO nanopowder, the particle size of the SLTO samples synthesized by sol-gel auto combustion is smaller than other techniques, such as hydrothermal (75-125 nm) [93], SrCl_2 flux treatments (0.2–3 mm) [100]. However, this was not the case when the sol-gel combustion method used citric acid (CA) (20–30 nm) [47] or Molten salt (50-300 nm) [101].

Figure 60 shows the SEM image, EDS spectrum and mapping images of SLTO nanopowder with $x = 0.1$. The EDS spectrum (Figure 60b) and EDS mapping

images (Figure 60c-f) were measured on the spectrum area of the nanoparticles (Figure 60a). The four colors in the element map indicate the distribution of the elements Sr, Ti, O, and La, according to the qualitative property of the EDS spectrum. The EDS mapping images show that Sr, Ti, O, and La are uniform distribution on the sample surface.

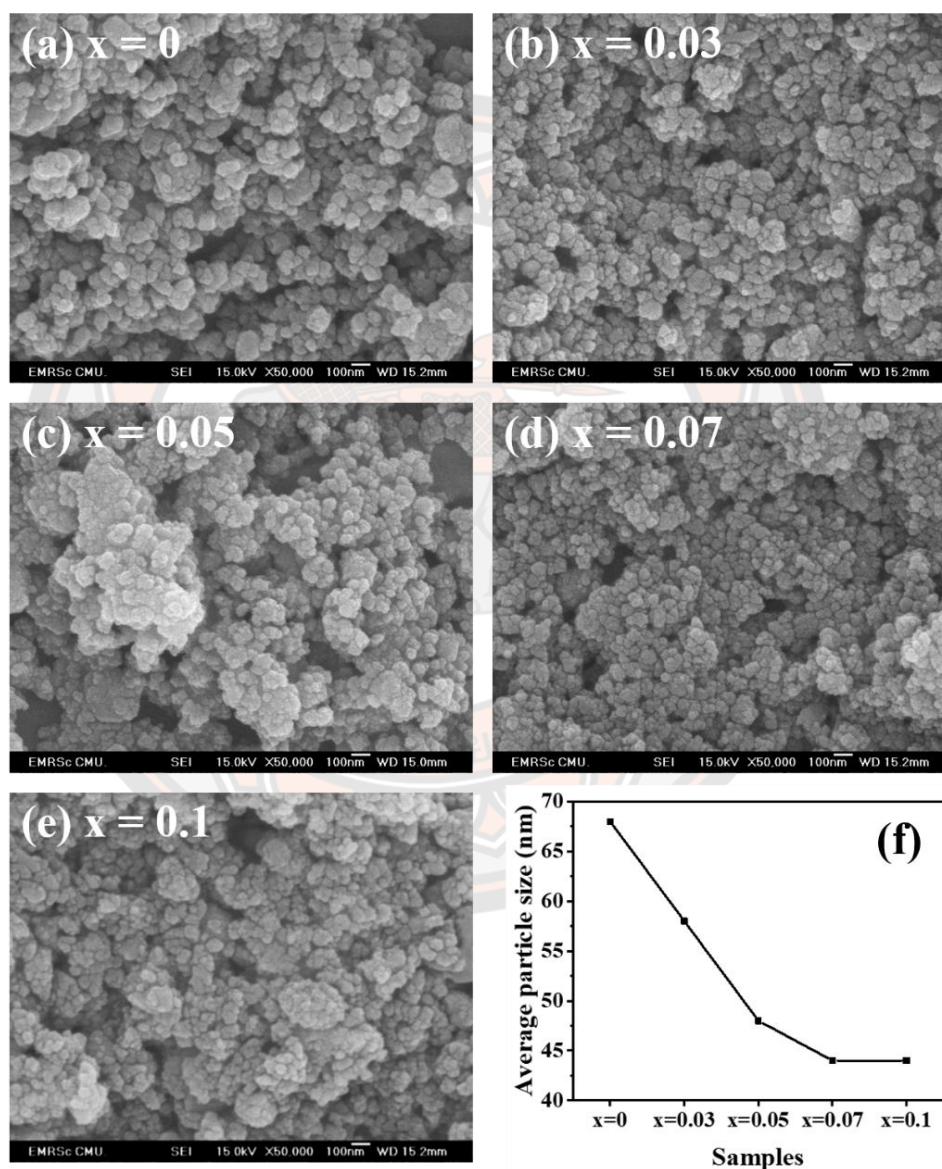


Figure 59 (a-e) SEM image and (f) the average particle size of SLTO nanopowder

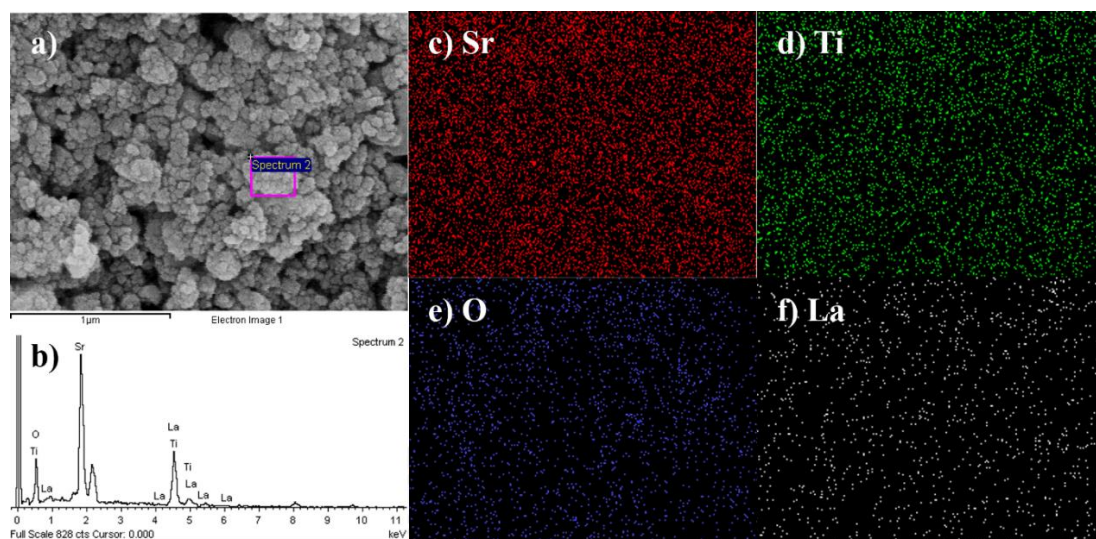


Figure 60 SEM-EDS images of the $\text{Sr}_{0.9}\text{La}_{0.1}\text{TiO}_3$ nanopowder

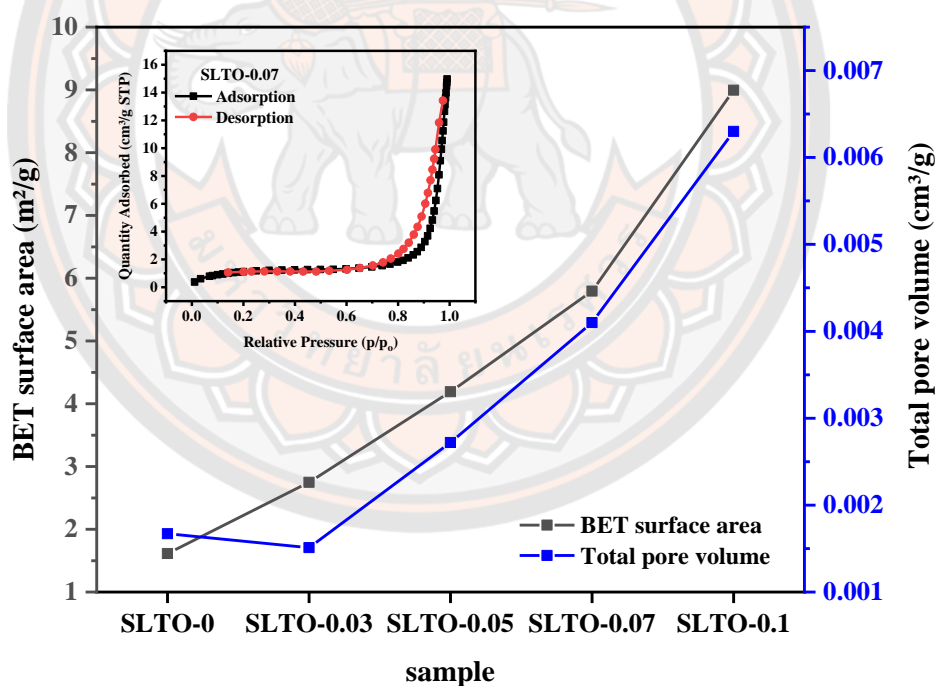


Figure 61 The specific surface area and total pore volume of the SLTO samples, (inset) the Nitrogen adsorption-desorption isotherms of typical SLTO ($x = 0.07$) sample.

Table 3 The pore distribution of the SLTO sample

SLTO-0			SLTO-0.03			SLTO-0.05			SLTO-0.07			SLTO-0.1		
Pore Width Range (nm)	BJH adsorption incremental pore volume (cm ³ /g)	Pore Width Range (nm)	BJH adsorption incremental pore volume (cm ³ /g)	Pore Width Range (nm)	BJH adsorption incremental pore volume (cm ³ /g)	Pore Width Range (nm)	BJH adsorption incremental pore volume (cm ³ /g)	Pore Width Range (nm)	BJH adsorption incremental pore volume (cm ³ /g)	Pore Width Range (nm)	BJH adsorption incremental pore volume (cm ³ /g)	Pore Width Range (nm)	BJH adsorption incremental pore volume (cm ³ /g)	
18.5-16.3	2.07E-04	18.6-16.5	4.23E-04	18.6-16.4	6.66E-04	18.4-16.2	6.19E-04	18.7-16.6	1.66E-03					
16.3-14.6	1.64E-04	16.5-14.7	3.23E-04	16.4-14.7	4.98E-04	16.2-14.4	4.57E-04	16.6-14.8	1.27E-03					
14.6-12.8	1.57E-04	14.7-13.0	3.30E-04	14.7-12.9	4.92E-04	14.4-12.6	4.24E-04	14.8-13.1	1.18E-03					
12.8-11.4	1.11E-04	13.0-11.5	2.43E-04	12.9-11.5	3.85E-04	12.6-11.2	3.45E-04	13.1-11.7	8.96E-04					
11.4-10.2	8.71E-05	11.5-10.4	2.00E-04	11.5-10.3	3.16E-04	11.2-10.1	2.41E-04	11.7-10.5	7.40E-04					
10.2-8.9	1.04E-04	10.4-9.0	2.26E-04	10.3-9.0	3.65E-04	10.1-8.7	2.73E-04	10.5-9.2	8.35E-04					
8.9-7.8	7.52E-05	9.0-7.9	1.78E-04	9.0-7.9	2.70E-04	8.7-7.7	2.07E-04	9.2-8.1	6.89E-04					
7.8-6.7	8.43E-05	7.9-6.8	1.86E-04	7.9-6.8	2.95E-04	7.7-6.6	1.43E-04	8.1-7.0	7.09E-04					
6.7-5.6	7.44E-05	6.8-5.8	1.76E-04	6.8-5.8	2.68E-04	6.6-5.5	1.24E-04	7.0-5.9	6.97E-04					
5.6-4.8	5.66E-05	5.8-5.0	1.51E-04	5.8-5.0	2.04E-04	5.5-4.7	4.05E-05	5.9-5.1	5.60E-04					
4.8-4.2	5.09E-05	5.0-4.4	1.17E-04	5.0-4.3	1.56E-04	4.7-4.1	1.60E-05	5.1-4.5	4.65E-04					
4.2-3.7	2.55E-05	4.4-3.8	9.96E-05	4.3-3.8	1.38E-04	4.1-2.3	1.40E-06	4.5-4.0	4.02E-04					
3.7-3.3	3.19E-05	3.8-3.4	9.11E-05	3.8-3.4	1.21E-04	2.3-2.0	5.15E-05	4.0-3.5	3.69E-04					
3.3-2.9	3.94E-05	3.4-3.0	9.57E-05	3.4-3.0	1.02E-04	2.0-1.7	1.26E-04	3.5-3.2	3.42E-04					
2.9-2.5	3.50E-05	3.0-2.7	8.64E-05	3.0-2.7	1.07E-04			3.2-2.8	3.28E-04					
2.5-2.2	4.61E-05	2.7-2.4	8.38E-05	2.7-2.4	9.98E-05			2.8-2.5	3.20E-04					
2.2-2.0	4.41E-05	2.4-2.1	8.74E-05	2.4-2.1	1.24E-04			2.5-2.3	3.33E-04					
2.0-1.7	7.39E-05	2.1-1.9	1.03E-04	2.1-1.8	1.27E-04			2.3-2.0	3.33E-04					
		1.9-1.8	5.05E-05	1.8-1.7	6.66E-05			2.0-1.9	1.45E-04					
		1.8-1.7	4.87E-05					1.9-1.8	1.47E-04					
								1.8-1.7	1.49E-04					

Figure 61 shows the specific surface area and total pore volume of the SLTO samples. The specific surface area of the SLTO samples was 1.6 to 8.9 m²/g, indicating that the specific surface area of the SLTO increased as the La doping content increased. This is due to the decrease in the average particle size, corresponding to the SEM images (Figure 59). Similarly, in a previous study, the specific surface area of SLTO increased with increasing the La doping [92]. The total pore volume in the SLTO samples was 0.0015 - 0.0063 cm³/g, which increased with increases in the La doping content, where the La content increase may have caused the reduced size of the mesopores [92]. The pore distribution report of the SLTO samples were shown in Table 3, which confirms that most of the total pore volume in the SLTO samples was mesopores in the range 2-50 nm [102]. Probably, the reduction in the size of the large mesopores, thereby producing small mesopore, lead to the increased total pore volume.

The inset graph shows the nitrogen adsorption-desorption isotherm of a typical SLTO ($x = 0.07$) sample, indicating that physisorption isotherms exhibit a hysteresis loop under type IV, corresponding to the IUPAC classification. In the case of type IV isotherms, the sample is characterized as mesoporous adsorbents based on monolayer-multilayer adsorption and capillary condensation, similar to the SLTO synthesized by the sol-gel combustion route [92, 103]. In the case of other SLTO samples, similar results to those for SLTO ($x = 0.07$) sample were obtained.

So, the advantage of the sol-gel auto combustion route using a mixture of glycine and citric acid as organic fuel to prepare SLTO is easy stoichiometric control, relative low ignition temperature, short time to synthesis, use of simple equipment, complete reaction, and high combustion temperature. So, it is indicated that the sol-gel auto combustion route with a mixture of organic fuels have been considered as a candidate technique for synthesis metal oxide nanoparticles under high-temperature reaction and low ignition temperature.

To investigate the optical properties of the SLTO samples, the UV-visible diffuse absorbance spectra of the samples, with $A = -\log(I/I_0)$, I_0 and I = intensity of incident and transmitted radiation, were recorded at wavelengths between 275 –500 nm at room temperature (Figure 62). Fundamentally, the absorption was applied to observe the absorption edge and energy gap, according to the electronic transition

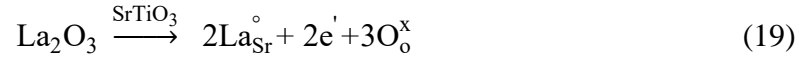
from the upper bound of the valence band to the lower bound of the conduction band [104]. The light absorption ability of all the samples exhibited a similar trend when detecting the absorption edge at 310 nm wavelength. When considering the high energy region of the absorption edge, we see that the light absorption ability is only increased by increasing the photon energy. The relationship of the absorption and incident photon energy ($h\nu$) is represented by Tauc's relation;

$$(\alpha h\nu) = A(h\nu - E_g)^n \quad (18)$$

where α denotes the absorption coefficient, A is constant, E_g is the band gap, and n depends on the type of transition. For directly allowed transitions $n = 1/2$, for the indirect allowed transitions, $n = 2$, and for direct forbidden transitions, $n = 3/2$, and indirect forbidden transitions where $n = 3$ [104, 105]. The E_g of these samples were estimated by extrapolating the linear portion of the curve to zero absorbance, shown as the inset plot of $(\alpha h\nu)^2$ vs $h\nu$ for a direct allowed transition.

The direct E_g of SrTiO₃ sample is 4.10 eV, as shown in Figure 62a. Fundamentally, the optical property of nanoparticles depends on their crystallinity, morphology, particle size, and synthesis method [106-108]. Such as E_g increases with the decreasing particle size of nanoparticles [109]. The E_g of SrTiO₃ in our study, 4.10 eV, were higher than previous reports. SrTiO₃ prepared by microwave-assisted hydrothermal was 3.5 eV with crystallite size 52 nm [106], SrTiO₃ powders synthesized by liquid-solid reaction method was 3.4 or 3.5 eV with particle size 30-108 nm [109], SrTiO₃ thin film synthesis by liquid phase deposition with 3.65-3.78 eV with varying temperature annealing [107] and with sol-gel was 3.82 eV [108]. Probably, the SrTiO₃ synthesized by the sol-gel auto combustion method provides particle size as a nanometer (Figure 59). Regarding the influence of La dopant on E_g of SLTO, as illustrated in Figure 62b-e, it was observed that the E_g slightly increased ($E_g = 4.10$ -4.12 eV) with increasing La content. This result corresponds to the findings of related SLTO materials [93, 110], that had La-doped SLTO, which also had the significant effect of relatively increasing E_g with increasing La. These results may be due to an increase of La content, leading to the formation of an oxygen vacancy state in the band gap that has the effect of shifting the Fermi level close to the conduction band, resulting in the E_g becoming larger than the undoped-SrTiO₃ [93,

111]. The increasing of oxygen vacancies is due to the reaction of the La^{3+} substitutes in Sr^{2+} site and the reducing atmosphere during the calcination process, described on Eq. 19 and Eq. 20 [65, 112].



The photocatalytic efficiencies of the SLTO samples were examined by degrading methylene blue (MB) under UV irradiation. The photocatalytic activity, in terms of the decolorization efficiency (%DE) of SLTO photocatalyst, is illustrated in Figure 63(a) which shows that the %DE of MB without a catalyst under UV irradiation slowly increases with exposure time, after 8 hours around 9%. The reaction of photocatalytic activity, showing the %DE of MB with SLTO as a catalyst, steadily increasing with exposure time and the %DE increasing with La concentration increases. After 8 hours, the %DE of the undoped SLTO sample ($x = 0$) is 39%. The %DE of the undoped-SLTO agrees with [113] in which the synthesis by the polyacrylamide gel route was reported, and which was also reported in [59] where synthesis process was by the combustion technique. Accordingly, the undoped-SLTO in the present study, applying the sol-gel auto combustion technique, can be competitive with the previous method due to the small-sized nanoparticles that have the effect of increasing the surface area for the reaction. Obviously, SLTO with $x = 0.07$ gives the highest photocatalytic efficiency around 55%, which is the optimal reaction at $x = 0.07$. La dopant greater than $x = 0.07$ is ineffective for %DE. However, because the %DE of La dopant has not investigated in the same way as in our research, these results cannot be compared with previous findings. For example, the La-doped SrTiO_3 ($\text{La}=0.5$) showed a %DE value of 80% in 100 min when an inorganic chemical ($\text{K}_2\text{Cr}_2\text{O}_7$ (Cr (VI))) was used, and the light source was a 500W Xe arc lamp [94]. Also, the co-doped SrTiO_3 (La 5%, and Cr 2%) showed the %DE of structure antibacterial medicine (Tetracycline (TC)) as 80% in 90 min with a 300 W Xe lamp light source [98].

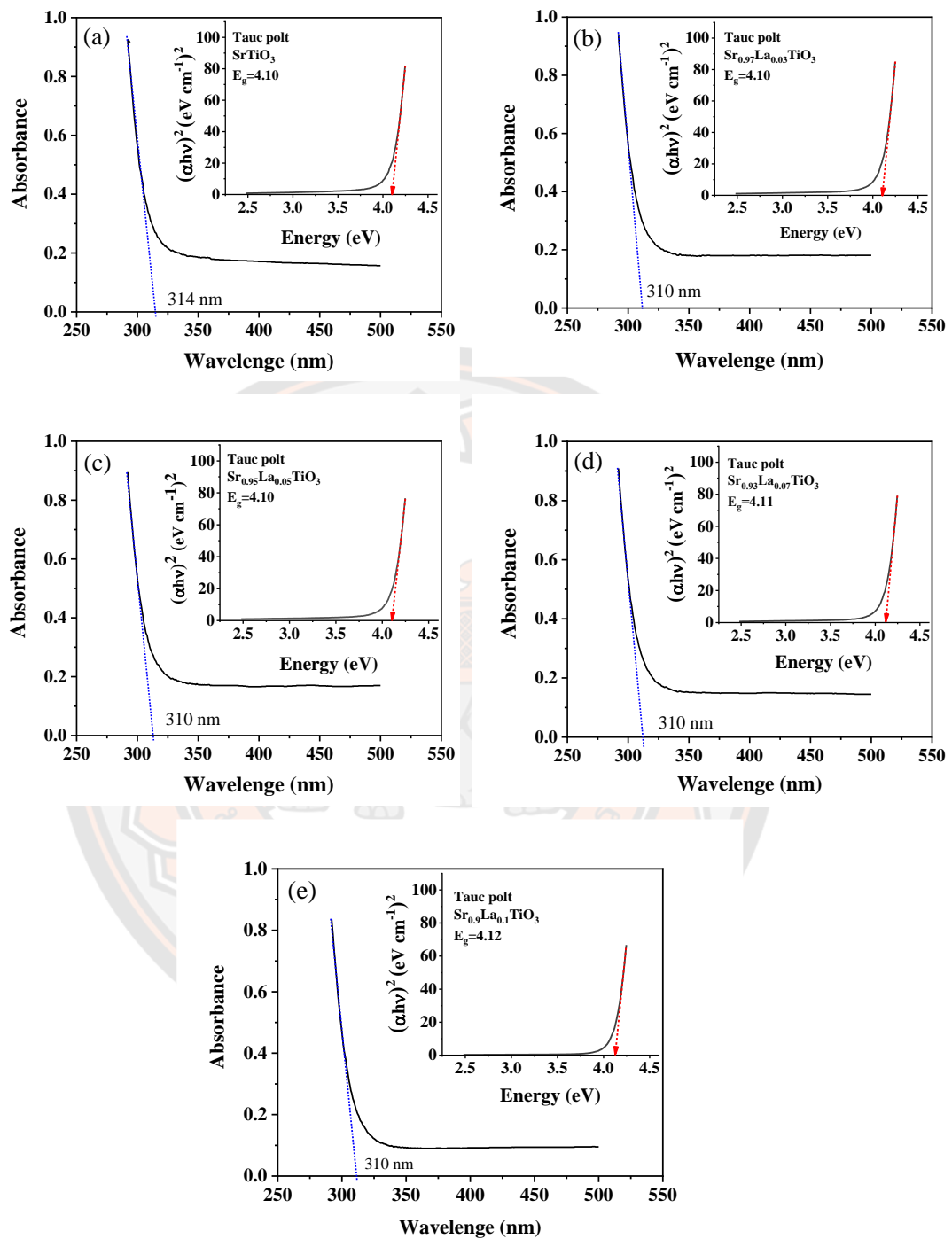


Figure 62 UV-vis spectra of the SLTO ($x = 0, 0.03, 0.05, 0.07$ and 0.1) nanopowder, together with an inset plots of $(\alpha h\nu)^2$ as a function of photon energy ($h\nu$)

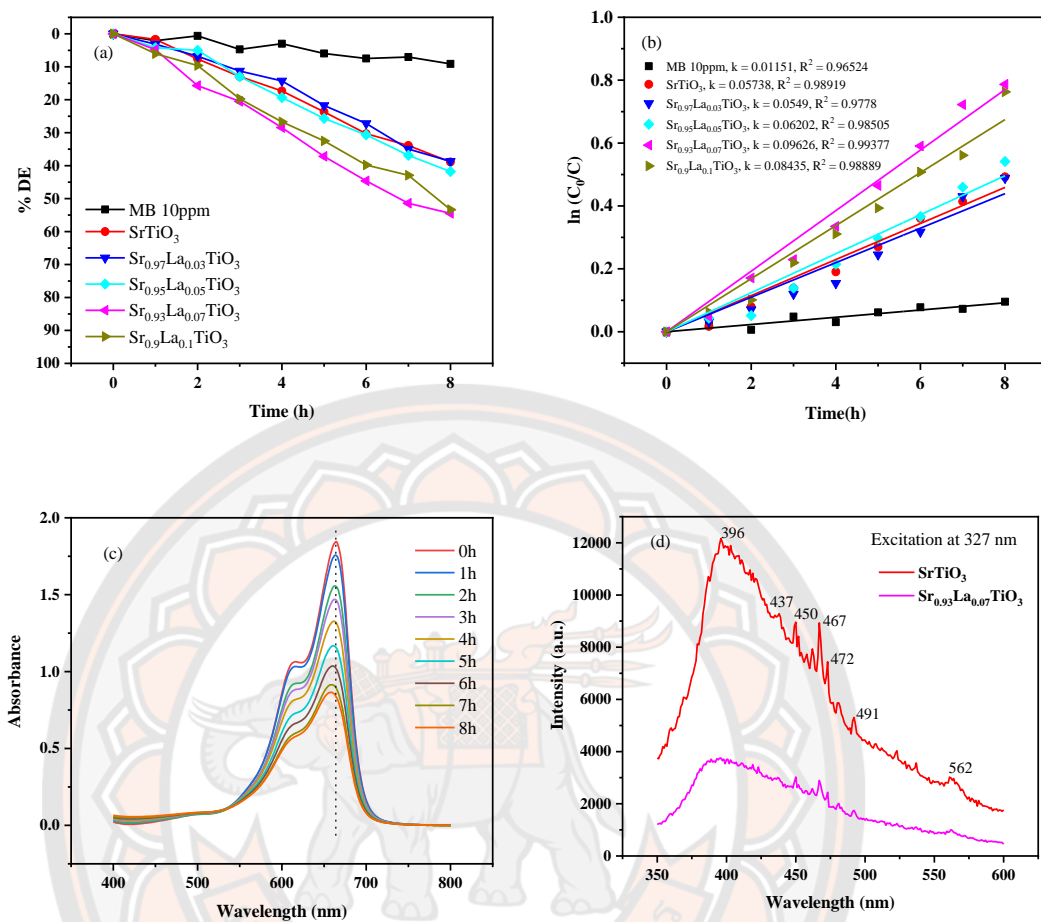


Figure 63 (a) Photocatalytic decolorization efficiency (%DE) of MB irradiated under the UV lamps (b) Pseudo-first order kinetics of the photocatalytic decolorization of MB (c) Time dependent UV-Vis spectra of MB solution for SLTO nanopowder for $x = 0.07$ and (d) Photoluminescence (PL) spectra of the SLTO nanopowders for $x = 0$ and 0.07 .

The reaction rate and physical process were studied by chemical kinetics. The reaction rate is in direct variation to the one reactant concentration. The corresponding first-order reaction kinetics constant (k) can be calculated by the equation: $\ln(C_0/C) = kt$, where C and C_0 are the real-time and initial concentrations of MB. The k value for SLTO also increased with La-dope increases, as shown in Figure 63(b). Obviously, the k value of $x = 0.07$ is the highest, corresponded to the %DE. So,

the SLTO with $x = 0.07$ has the highest of both the %DE and the first-order reaction kinetics constant.

The optimal value for La-doped SLTO as a photocatalyst reaction is $x = 0.07$, as shown in Figure 63(c) which shows the absorbance peak (λ_{\max}) of MB at different times at 664 nm. After an exposure time of 8 h, the λ_{\max} of MB continuously decreased and shifted to the lower wavelength between 664 nm to 658 nm. The λ_{\max} decreased due to decolorization of the MB and blue shift due to the stepwise removal of auxochromes (methyl or methylamine) [91]. Besides, the spectra absorbance of each SLTO samples agree with the same trends.

The SLTO samples synthesized by the sol-gel auto combustion technique have been considered to be good candidate materials for photocatalytic activity due to them having a relatively high %DE and k in terms of the amount of catalyst required and the synthesis method used, compared to previous studies.

To consider the photocatalytic activity of SLTO samples, the photoluminescence (PL) technique is used to identify the recombination of electron-holes in the semiconductor, carrier trapping, and the degree of structural order-disorder in a semiconductor. The efficiency and properties of PL on semiconductor materials depend on the synthesis process, calcination temperature, time, crystalline size, and topology of the materials [114]. Figure 63(d) shows the PL spectra of SLTO with $x = 0$ and 0.07 samples with an excitation at 327 nm wavelength at room temperature. Both of the PL spectra exhibited similar trends and peaks. The emission peaks are shown in violet, blue, and green. The centered peak emitted at 396 nm is violet colored, the peaks emitted at 437, 450, 467, 472, and 491 nm harmonize with the blue emission mainly due to Sr deficiency in the crystal structure, and the green color emission at 562 nm is due to the presence of oxygen vacancy in the SrTiO_3 lattice [114]. Moreover, the emission of PL at peak intensity was attributed to the presence of defects, as shown in Figure 64. The E_g between the Titanium $3d$ conduction band and the oxygen $2p$ valence band is 4.10 eV (Figure 62). The oxygen vacancies create a defect level below the conduction band. The emission at 396 nm was observed when the excited electrons and holes recombine through the defect level or by oxygen vacancy. Due to the electrons doped in conduction band as the result of oxygen vacancy at recombination with excited holes, the PL emission at 437 nm was

occurred. While, the spectrum emission was appeared at 467 nm, indicating that the excited holes and electrons were recombined through their trap level. The obtained PL emissions result of SLTO in the present study is a good agreement with Ref. [115]. Consequently, the PL spectra results, La-doped SLTO nanopowders, synthesized by the sol-gel auto combustion technique, has oxygen defects and local-disorder in the electrons of the SLTO material.

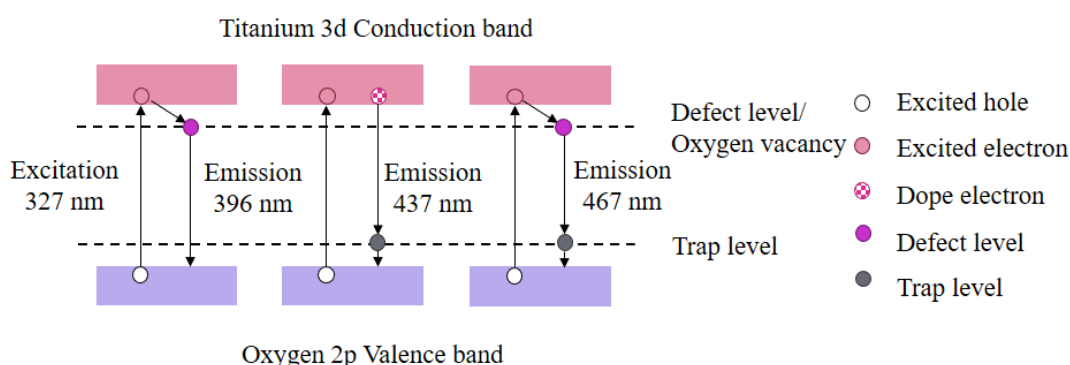
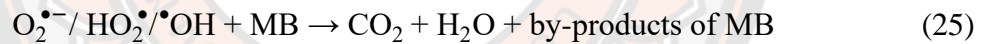


Figure 64 A schematic of the PL emissions of SLTO due to the recombination of conduction electron-valence holes.

In fundamental, there is an inverse relationship between the intensity of the PL spectra and the %DE, which shows that if the PL intensity decreases, this will result in photocatalytic activity increase due to low electron-hole recombination and low carrier recombination [116, 117]. As a result, the intensity of the PL emissions of SLTO with $x = 0$ was higher than SLTO with $x = 0.07$. This leads to electron-hole recombination of SLTO with $x = 0$ larger than SLTO with $x = 0.07$. Consequently, the SLTO with $x = 0.07$ sample exhibited the highest photocatalytic activity because La can be effective in transferring the photogenerated electrons and can also intercept the recombination of electron-hole pairs [116].

The mechanism of the photocatalytic decolorization of MB dye on the SLTO photocatalyst under the UV irradiation is shown in Figure 65. The process of photocatalytic reaction can be divided into three steps. In the first step, the photocatalysis of SLTO was excited by UV irradiation with photo-energy higher than the E_g of photocatalysis, to generate photoinduced electrons (e^-) and holes (h^+). The electron is generated from the valence band (VB) transfers to the conduction band

(CB) through valence band transition, and then holes in the valence band are generated (Eq. 21). Second, the e^- and h^+ react with O_2 and H_2O to generate high reactive hydroxyl radicals and superoxide radicals. The O_2 adsorbed on the surface of the photocatalysis is trapped e^- to form superoxide radical ($O_2^{\bullet-}$) (Eq.22), and $O_2^{\bullet-}$ radical, which further reacts with H_2O to generate the hydroperoxyl radical HO_2^{\bullet} (Eq.23). The H_2O or OH^- adsorbed on the surface of the photocatalysis are oxidized by the h^+ to generate hydroxyl radicals ($\bullet OH$) (Eq.24). Finally, the generated hydroxyl radical, hydroperoxyl radical, and superoxide radicals destructured the MB dye into CO_2 , H_2O , and by-products of MB, which could be 2-amino-5-(N-methyl formamide) benzene sulfonic acid, 2-amino-5-(methyl amino)-hydroxybenzene sulfonic acid, and benzenesulfonic acid [118] (Eq.25). To consider the by-products of MB, further characterization should be performed. The steps are written in the reaction form as follows;



The results from PL spectra (Figure 63(d)) indicate that La dopant could prevent the $e^- - h^+$ recombination in SLTO sample (Eq.21), leading to the release e^- and h^+ for further forward reactions. Hence, it can be concluded that the sol-gel auto combustion technique resulted in with/without La-doped SLTO nanopowder that leads to improved photocatalyst activity.

The SLTO synthesized by using sol-gel auto combustion with an organic fuel mixture of glycine and citric acid provides a quality nanomaterial. The synthesis process was saving energy, time, and environmentally friendly. The SLTO was small crystallite size and nanoparticle size. The band energy of SLTO slightly shifted, and the PL of SLTO emitted violet, green, and blue emission caused by oxygen vacancy on the structure after La-doped. Even though the result of %MB degradation indicates the poor photocatalytic performance of SLTO, the SLTO of our research has various advantages. Here, the SLTO prepared by sol-gel auto combustion as a photocatalyst

using MB dye under UV irradiation can fill a gap of photocatalyst activities reports, which is rarely reported. Which might be beneficial for future photocatalyst activity of the SLTO samples.

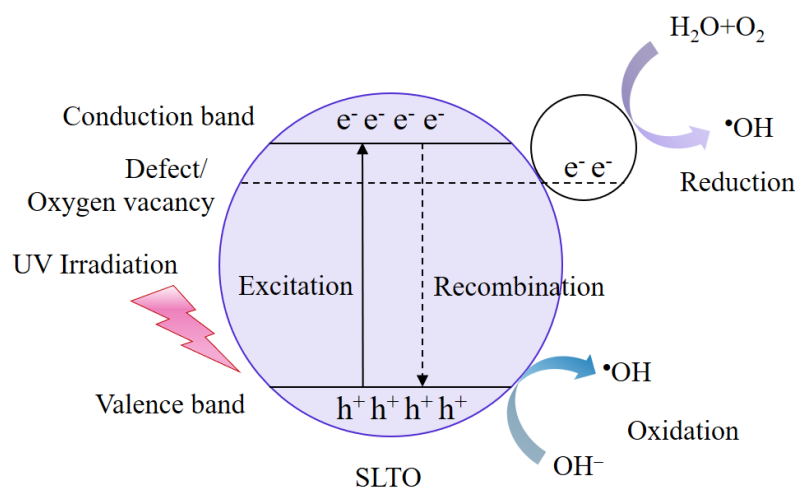


Figure 65 A schematic diagram for photocatalysis of SLTO nanopowder.

4.1.2 Characterization of thermoelectric properties

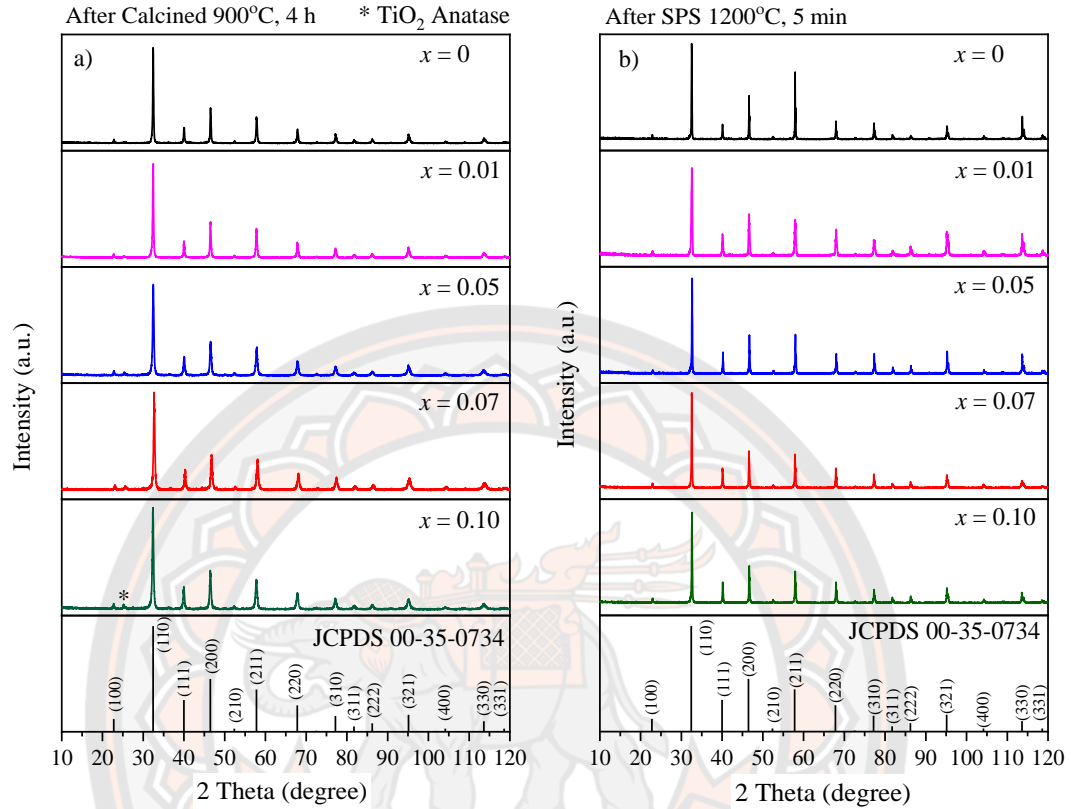


Figure 66 XRD pattern of SLTO sample with different La content ($x = 0, 0.01, 0.05, 0.07$, and 0.10): a) after calcination, and b) after SPS process

The XRD pattern of the powdered SLTO sample after calcination is shown in Figure 66(a). Almost all the samples with a peak at the $2\theta = 22.78^\circ, 32.44^\circ, 40.08^\circ, 46.54^\circ, 52.51^\circ, 57.87^\circ, 67.90^\circ, 77.26^\circ, 81.77^\circ, 86.24^\circ, 95.14^\circ, 104.17^\circ, 113.67^\circ$ belonging to (100), (110), (111), (200), (210), (211), (220), (310), (311), (222), (321), (400), (330) planes exhibited a cubic perovskite SrTiO_3 phase, that agrees with JCPDS no. 00-35-0734. Although the impurity phase (TiO_2 , anatase) at the $2\theta = 25.26^\circ$ was detected when La doping content increased, undoped STLO ($x = 0$) has no such impurities. Compared to our previous study [89], the formation of a small amount of anatase TiO_2 occurred probably due to insufficient calcination time for completely removing certain inorganic contaminants due to the scale-up preparation process. These impurity phases agree with the La-doped SrTiO_3 with $x = 0.10$ prepared by

conventional solid-state reaction followed by sintering in 5% H_2/Ar , which found TiO_2 as an impurity [119]. The XRD pattern of SLTO bulk samples is presented in Figure 66(b), together with the JCPDS no. 00-35-0734 of a cubic perovskite SrTiO_3 phase. It was found that all samples presented a pure SrTiO_3 phase, regarding the increasing temperature of the SPS process leading to entirely eliminated inorganic impurities [120, 121]. This result means that the SPS process could promote the phase change from TiO_2 to SrTiO_3 and stabilize SrTiO_3 .

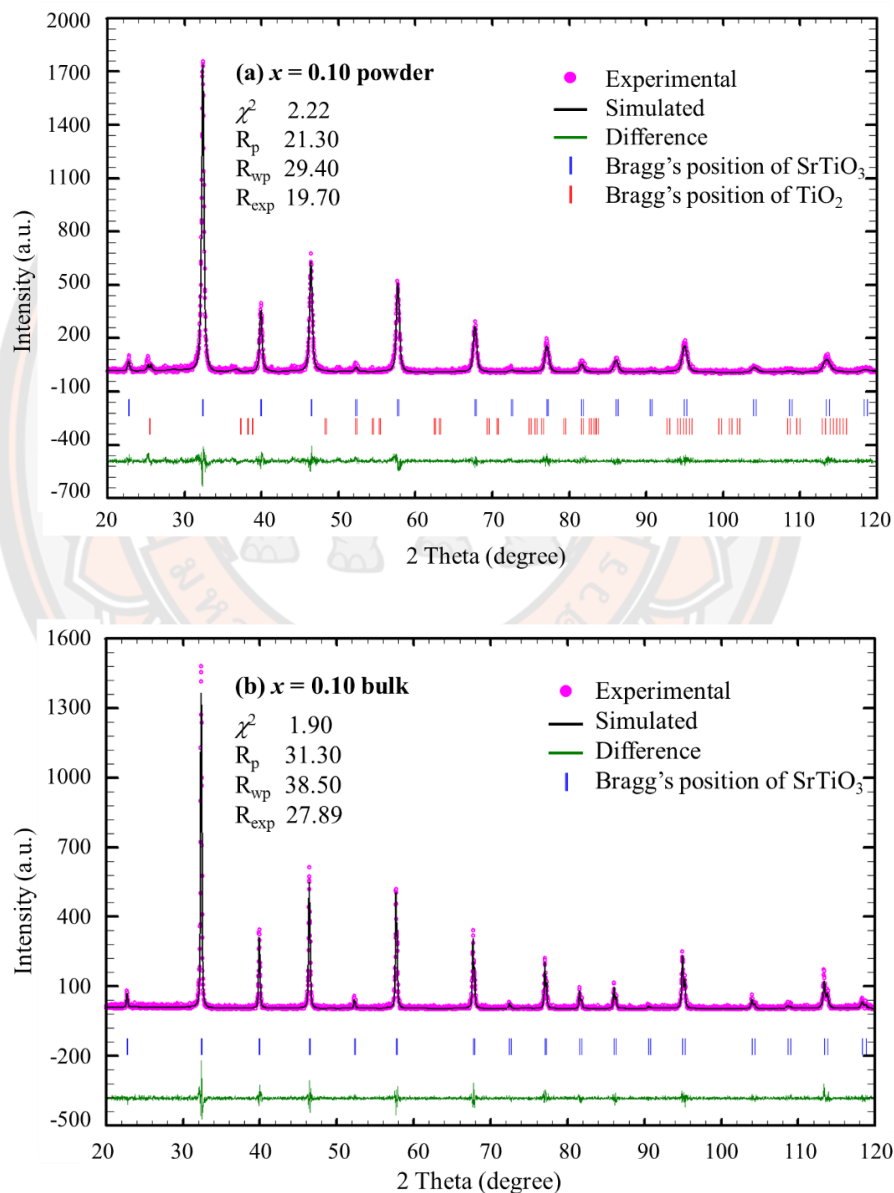


Figure 67 Typical Rietveld refinement analysis of SLTO sample for $x = 0.10$:

(a) powder and (b) bulk samples

The Rietveld refinement technique has been used to investigate the crystal structure of the composite material and unit cell information such as space group, cell location, cell orientation, and atomic distances using the Full-Prof program [89, 90]. Figure 67 illustrates the final output from the Rietveld refinement analysis undertaken in our study of the SLTO sample for $x = 0.10$, including powder and bulk samples. The quality of fit of the refinement in terms of reliability indices, including goodness-of-fit (χ^2), R -factor (R_p , R_{wp} , R_{exp}), lattice parameter and cell volume of all samples in both powder and bulk, are summarized in Table 4. The quality of fit can vary depending on the quality of the experimental data, the complexity of the crystal structure, and other factors [122]. In both cases of SLTO powder and bulk samples, as shown in Figure 67, the quality of fit indicates a good agreement between the measured and calculated intensity profiles of all samples due to the $\chi^2 < 4$. In the case of SLTO powder (Figure 67(a)), the TiO_2 with anatase phase was a contaminant in the sample. This confirms that all bulk samples are in a cubic perovskite SrTiO_3 phase with no such impurities after the SPS process.

Table 4 Chi-square (χ^2), R -factors (R_p , R_{wp} , R_{exp}), lattice parameter, cell volume, and calculated cell density (d_{cal}) of SLTO ($x = 0, 0.01, 0.05, 0.07$, and 0.10) powder and bulk.

Samples	χ^2	R_p	R_{wp}	R_{exp}	Lattice parameter $a = b = c$ (Å)	Cell volume (cm^3)	d_{cal} (g/cm^3)
JCPDS 00-035-0734					3.90500	59.550	5.120
Powder							
SLTO-0	2.35	16.30	23.90	15.61	3.90507	59.551	4.995
SLTO-0.01	2.22	16.10	23.90	16.03	3.90703	59.639	5.218
SLTO-0.05	2.25	24.00	30.60	20.39	3.90990	59.772	5.233
SLTO-0.07	2.19	20.50	37.80	25.55	3.91024	59.792	5.280
SLTO-0.10	2.22	21.30	29.40	19.70	3.91626	59.826	5.374
Bulk							
SLTO-0	2.84	42.90	46.60	27.63	3.90581	59.585	5.003
SLTO-0.01	2.30	27.30	35.70	23.56	3.90660	59.620	5.179
SLTO-0.05	2.45	22.80	31.40	20.05	3.90872	59.718	5.218
SLTO-0.07	2.09	19.20	28.40	19.61	3.90910	59.735	5.233
SLTO-0.10	1.90	31.30	38.50	27.89	3.91016	59.784	5.280

The lattice parameters obtained from the Rietveld refinement of both powder and bulk samples are presented in Table 4. The lattice parameters of undoped SLTO ($x = 0$) in our powder and bulk samples correspond to the literature data (JCPDS no. 035-0734). When the La doping contents increased, the lattice parameters of SLTO samples also increased due to lattice defects through the substitution of the larger ionic radius La^{3+} (1.15 Å) at that smaller ionic radius Sr^{2+} (1.13 Å), the difference valences of La^{3+} and Sr^{2+} ions, contain internal strain or local distortions, which was identified in previous work [89, 94, 123-125]. This occurred because the lattice parameters increased with the La content, which led to unit cell expansion of the SLTO samples. Besides, the Lattice parameter of SLTO bulk samples is relatively smaller than those of powder for the same composition as results of the sintering powders at high temperature and high pressure during SPS processing methods. As a result, the interatomic distances between the atoms in the bulk samples become smaller, and the lattice parameters decrease. The calculated unit cell density (d_{cal}) is expressed as mass of unit cell/volume of unit cell, which is obtained from the results of Rietveld refinement analysis. The d_{cal} of both the undoped SLTO powder and the bulk samples is relatively similar to the literature data. In contrast, the d_{cal} of the doped-SLTO samples increased with increasing the La content because the atomic mass of La is larger than Sr. During the SPS sintering process, the SLTO powders undergo plastic deformation and grain growth, which leads to the individual particles to fuse together and form a dense solid with a reduction in porosity and an increase in the density of the material.

Figure 68 shows the variation of the measured densities (d) and relative density ($d/d_{\text{cal}} \times 100\%$) of the SLTO bulk samples as a function of the La content (x). The d increased with increases in the La content, according to the d_{cal} , as described in Table 4. The d is very high and is above 96% of the theoretical density. The quality of d of the SLTO bulk samples synthesized by sol-gel auto combustion was achieved using the SPS process, similar to the high d (5.12 g/cm³) of La-doped SrTiO_3 prepared by combustion synthesis with post-SPS with a 5 min holding time [48].

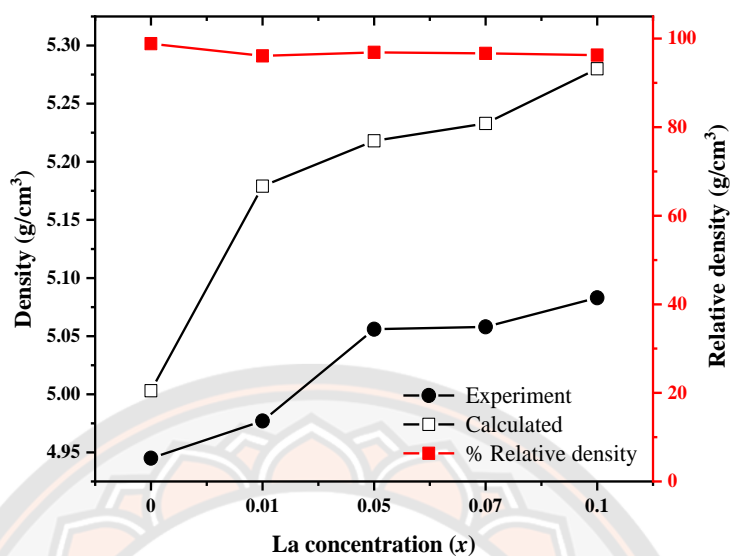


Figure 68 Variation of the measured densities (d) and relative density of SLTO bulk samples as a function of La content (x)

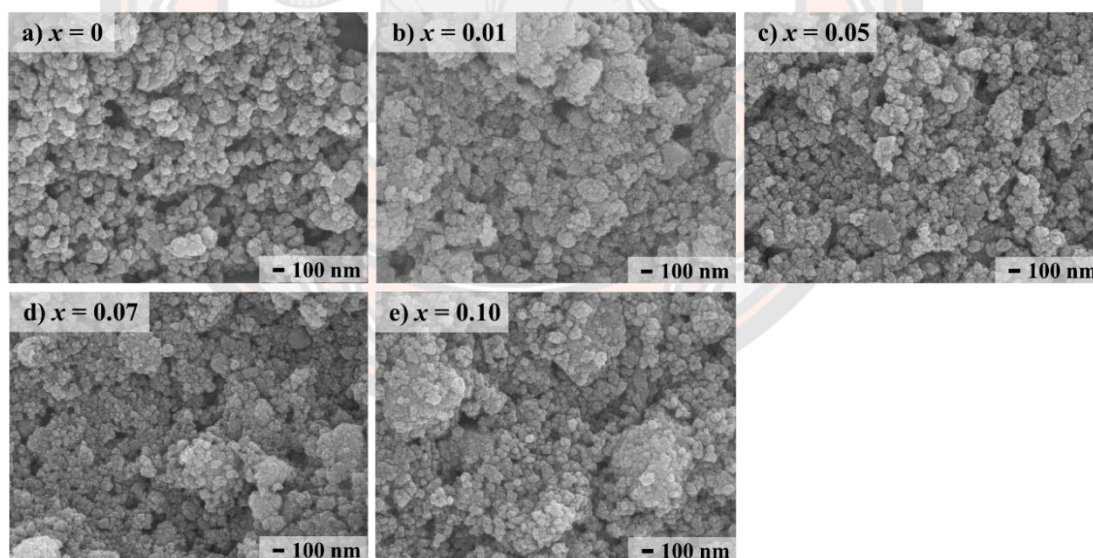


Figure 69 SEM of the SLTO powder sample with different La content ($x = 0$, 0.01, 0.05, 0.07, and 0.10)

The SEM of the SLTO powder samples with different La concentrations ($x = 0$, 0.01, 0.05, 0.07, and 0.10) are shown in Figure 69. The morphology of all the SLTO samples is a spherical shape. The particle size of the samples has a homogenous

distribution of approximately 100 nm, indicating that the La doping content had an insignificant effect on the particle size. In addition, the brightness or contrast in SEM images is observed, indicating that the surface level of the sample is not flat with the working distance (WD) of the primary electron beam during SEM measuring. The brightness area represents the hilltop of the powder location of the sample, while the dark grey area represents the valley region of the powder. These results correspond to our previous work, where the particle size slightly decreased with an increase in the La concentration [89], together with the average grain size of $\text{Sr}_{1-x}\text{La}_x\text{TiO}_3$ nanopowders [126].

The SEM and EDS mapping analysis of images of all the SLTO bulk samples are presented in Figure 70. In the SEM images, the surface of all the bulk samples is homogenous without cracks. However, numerous pores were observed on the surface of the SLTO samples with $x = 0.0, 0.01$, and 0.05 , while the SLTO samples with $x = 0.07$ and 0.1 had a smooth surface. We can surmise that the pores probably occurred after the sample was cut and polished because the SLTO samples with $x = 0.0, 0.01$, and 0.05 present a higher relative density (Figure 68), leading to high stress and hardness with a brittle composition. The EDS analysis revealed that Sr, Ti, O or La were uniformly composed and distributed on all sample surfaces. The SEM and EDS mapping analysis confirmed that all the SLTO samples were homogenous without any impurity phases, which corresponded to the XRD results. The quantitative EDS analysis indicates that the average chemical composition of all the samples was in relatively good agreement with the nominal compositions.

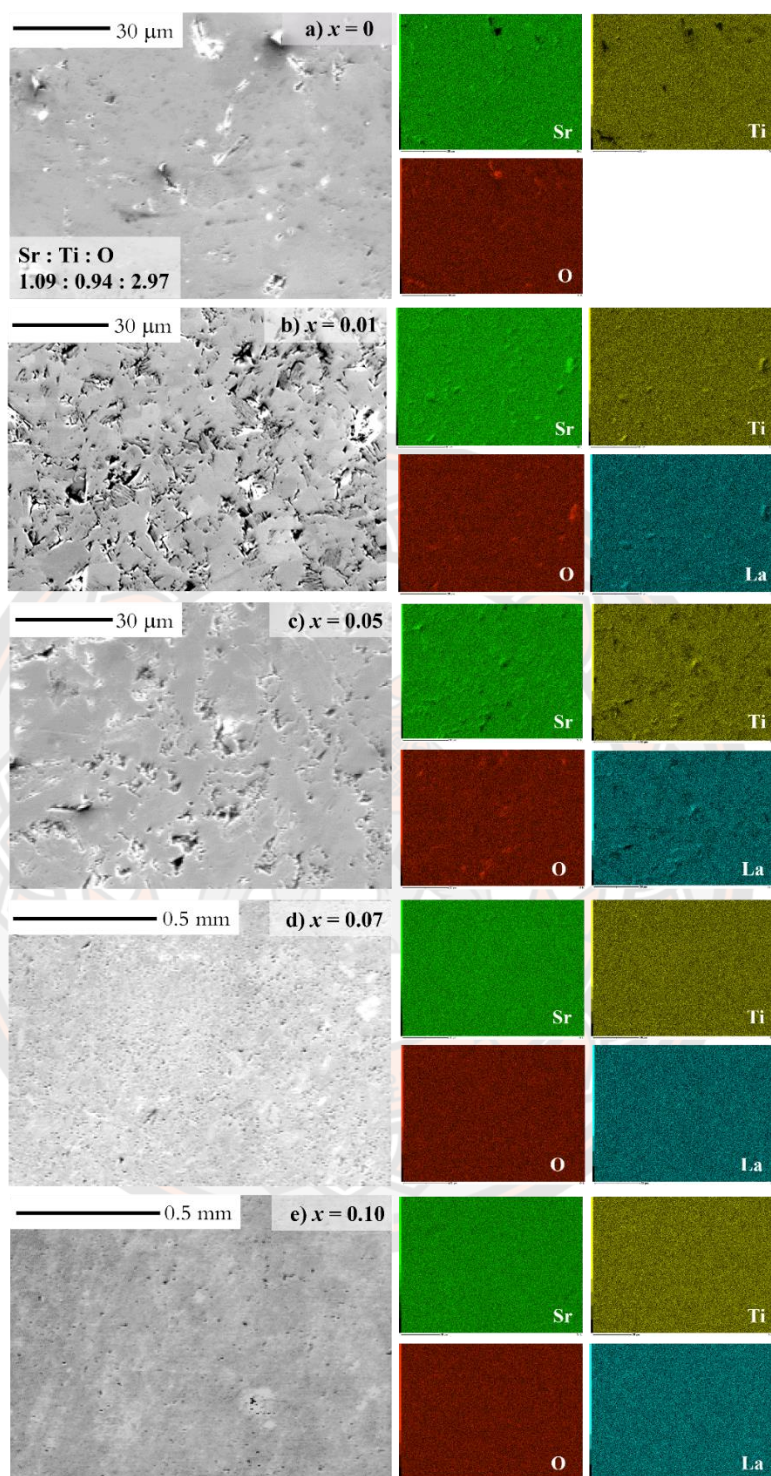


Figure 70 SEM and EDS mapping analysis of the SLTO bulk samples

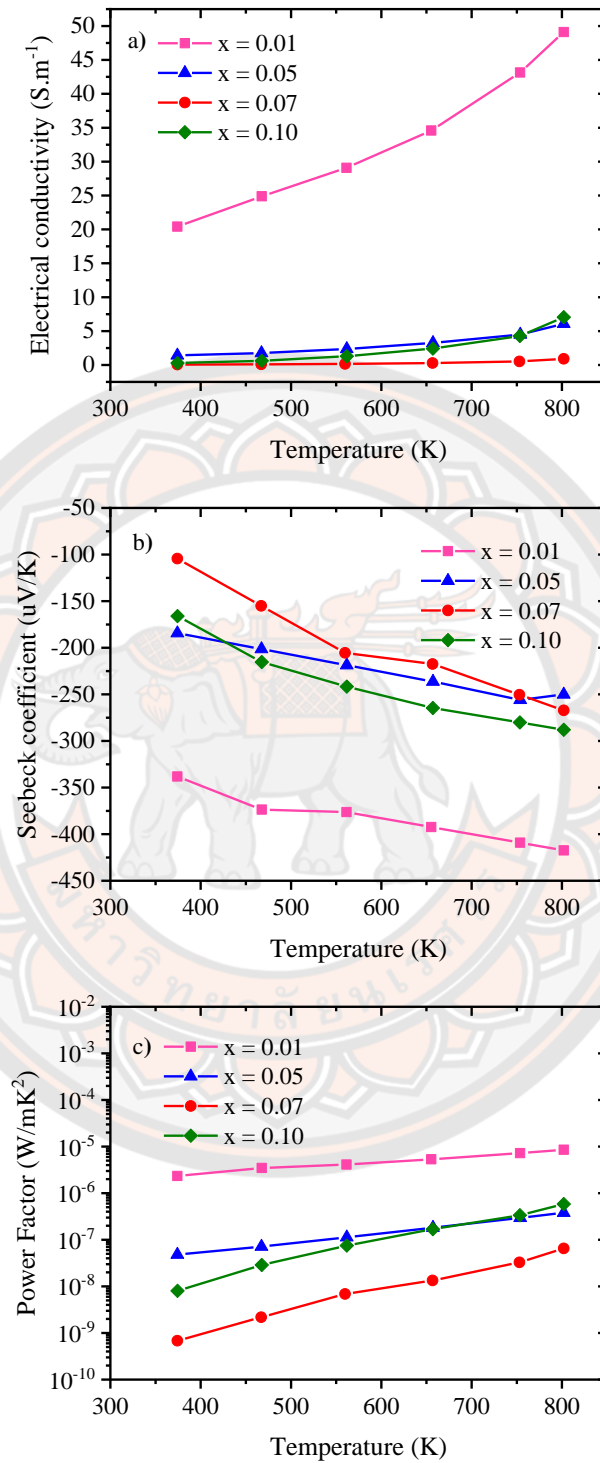
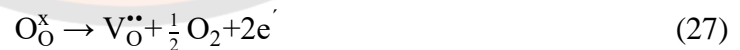
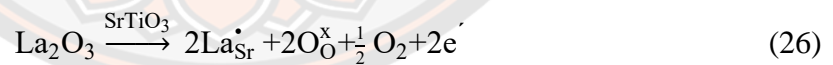


Figure 71 Temperature dependence of the electrical properties of SLTO bulk samples: (a) electrical conductivity (σ), (b) Seebeck coefficient (S), and (c) power factor ($\text{PF}, S^2\sigma$).

Figure 71 shows the temperature dependence of the electrical properties of the SLTO bulk samples. As shown in Figure 71(a), the electrical conductivity (σ) of the La-doped SLTO samples slightly increased with the temperature rise, indicating a semiconductive behaviour. Unfortunately, the undoped SLTO sample could not be measured due to the large electrical resistivity (ρ). These results showed that the σ of the SLTO sample were improved by La doping due to increasing carrier concentration (n) by introducing oxygen vacancies (Eqs. 26-28). In addition, La dopant ionized reasonably well at all doping concentrations. Particularly, the σ of the SLTO sample with $x = 0.01$ was the largest of the samples, probably due to the optimization of n and μ . Based on Eq. 28, uniform La doping can tune the n , thereby increasing the σ while reducing the μ . Therefore, it is necessary to perform the Hall measurements in order to further discuss the magnitude correlation in the electrical properties. When the La contents were larger than $x = 0.01$, lower values of σ were observed. These results may be caused by more structural distortion resulting from an increase in the La content leading to a change in the Fermi energy level, which is regularly investigated in polycrystalline and nanocrystalline materials due to decreasing the crystal size accelerating the structural distortion [51, 65, 127, 128]. The defect reaction equations are expressed with La^{3+} as a typical donor-substituted SrTiO_3 , together with σ related to n through the carrier mobility (μ) and electrical charge (e), as follows [56, 60, 65, 129]:



$$\sigma = ne\mu \quad (28)$$

The σ value of the La-doped SLTO sample was close to the order of magnitude σ of the $\text{La}_{0.08}\text{Sr}_{0.92}\text{TiO}_3$ ceramics samples prepared by a sol-gel process with different temperatures of SPS [49]. Compared to the related SLTO materials within the temperature range 300 – 600 K, these results corresponded to the 7.7 mol% La-doped SrTiO_3 nanostructured bulk produced by the SPS of chemically synthesized colloidal nanocrystals [128], nanoscale porosity of La-doped SrTiO_3 bulk [130], 10% mol% La-doped SrTiO_3 bulk with nano-scale modulation doping [131], and $\text{Sr}_{1-x}\text{La}_x\text{TiO}_3$ bulk [132].

$x\text{Gd}_x\text{TiO}_{3-\delta}$ ceramics prepared by sol-gel process and SPS [56], together with co-doped SrTiO_3 such as La-Bi co-doped SrTiO_3 ceramics [132], and 10-30 mol% La-Nb co-doped SrTiO_3 [131].

A negative Seebeck coefficient (S) value was observed for all samples, as shown in Figure 71(b), indicating that most charge carriers were electrons. These properties confirm that all the SLTO samples were typical n -type oxide TE ceramics. The absolute S ($|S|$) increased with increasing temperature. For the increase in the La content, the $|S|$ of $x = 0.01$ was the largest and reached a maximum ($417.4 \mu\text{V/K}$) at 800 K. At $x = 0.05$, those SLTO samples were lower. The $|S|$ of the related SLTO materials have been reported in the range of $165 \mu\text{V/K}$ to $250 \mu\text{V/K}$ at 1073 K [49, 54, 128-130, 132]. In most cases of metal or degenerate semiconductors (parabolic band, energy-independent scattering approximation), the S and σ will change opposite, according to the carrier concentration (n). The S is given by:

$$S = \frac{8\pi^2 k_B^2}{3eh^2} m^* T \left(\frac{\pi}{3n} \right)^{2/3} \quad (29)$$

where k_B is Boltzmann's constant, h is Planck's constant, e is the elementary charge, T is the absolute temperature, and the effective mass is m^* . However, A. Kikuchi et al. have presented that the S can also be expressed as [48]:

$$S = -\frac{k_B}{e} \left\{ r + 2 + \ln \frac{nh^3}{2(2\pi m^* k_B T)^{3/2}} \right\} \quad (30)$$

where r is the scattering factor. From Eqs. (28) and (30), it is found that the σ and S are proportional to the n . However, there are two situations where the $|S|$ may increase with increasing σ . One such situation is when the scattering of carriers is dominated by impurities or defects in the SLTO materials rather than by phonons or other scattering mechanisms. In this case, increasing the n can increase the σ while still maintaining a large $|S|$, resulting in an increase in both properties. Another situation where the $|S|$ may increase with increasing σ is when the μ increases. If the μ increases, then the σ will also increase, but the $|S|$ may also increase if the n remains relatively low. This is because the μ can affect the thermoelectric power of

the material, leading to an increase in the $|S|$. So, there are situations where the $|S|$ may increase with increasing σ . These situations may arise when the scattering of carriers is dominated by impurities or defects or when the μ increases [133-135]. Both σ and the negative S values of all the samples increased with the increase in temperature, which accords with the behaviour of an n-type semiconductor. These trends correspond to the behaviour of related SLTO samples with specific temperature ranges of 300 – 600 K, such as the $\text{Sr}_{0.9}\text{La}_{0.1}\text{TiO}_3$ ceramics [132] and nanoscale porosity of La-doped SrTiO_3 bulk [130], or other related TE materials including the $\text{Ag}(\text{Sb}_{0.97}\text{Sn}_{0.03})\text{Te}_2$ compound [136] and poly $[\text{Cu}_x(\text{Cu-ett})]$ -based organic TE material [137].

Based on the σ and S values, the power factor ($S^2\sigma$) was calculated and plotted as a function of temperature, as presented in Figure 71(c). The $S^2\sigma$ of all the samples gradually increased with increasing temperature and reached maximum values at 800 K. The SLTO sample with $x = 0.01$ exhibited a larger $S^2\sigma$ than other La content samples due to achieving a large S and σ simultaneously. The highest $S^2\sigma$ of the SLTO sample with $x = 0.01$ was $8.56 \times 10^{-6} \text{ W/mK}^2$ at 800 K, which was close to that of the $\text{Sr}_{0.9}\text{La}_{0.1}\text{TiO}_3$ ceramics [132], but lower than the $\text{Sr}_{0.92}\text{La}_{0.08}\text{TiO}_3$ ceramics prepared by SPS [49] and the $\text{Sr}_{0.9}\text{La}_{0.1}\text{TiO}_3$ ceramics [54, 132] and 20 at % La-doped SLTO ceramics [130].

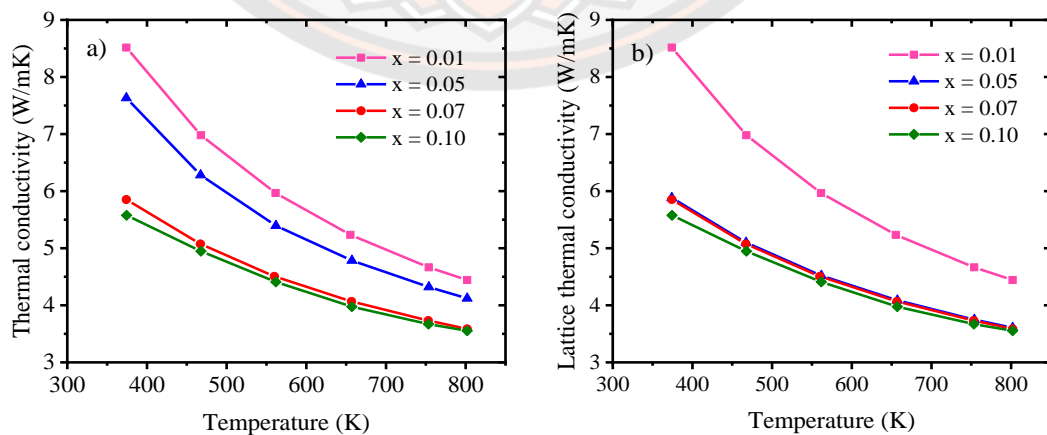


Figure 72 Temperature dependence of (a) thermal conductivity (κ) and (b) lattice thermal conductivity (κ_{lat}) of the SLTO bulk samples.

Figure 72(a) presents the temperature dependencies of thermal conductivity (κ) of the SLTO bulk samples. The κ of all the samples sharply decreased with increasing temperature, indicating that the κ comes mainly from lattice thermal conductivity (κ_{lat}). The lattice thermal conductivity (κ_{lat}) was evaluated by subtracting the electronic thermal conductivity (κ_{el}) from the thermal conductivity (κ), expressed as $\kappa_{lat} = \kappa - \kappa_{el}$. The κ_{el} was determined as $\kappa_{el} = L\sigma T$, where L is the Lorentz number ($L = 2.45 \times 10^{-8} \text{ W}\Omega\text{K}^{-2}$), σ is the electrical conductivity, and T is temperature. As shown in Figure 72(b), the κ_{el} also decreased with increasing temperature, roughly according to a T^{-1} relationship. Significantly, the reduction in κ was controlled by their reduction in κ_{lat} , which dominates κ in these SLTO ceramics. When temperature increases, the phonons are scattered by defects, grain boundaries, collision and/or impurities, which reduce the mean free path of the phonons. These trends are similar to those reported in previous reports [49, 54, 128-130, 132]. In the case of increasing the La content, the κ decreased with the increase in the La content, which is related to the σ in terms of carrier concentration, according to the electrical properties (Figure 71). The minimum κ values for all SLTO samples were 4.44 W/mK ($x = 0.01$), 3.61 W/mK ($x = 0.05$), 3.59 W/mK ($x = 0.07$), and 3.55 W/mK ($x = 0.10$), at 800K. It agrees well with the previous study for SrTiO₃ with/without doped La [54, 65, 128-130, 132, 138, 139]. The phenomenon could be explained by it being based on the different La content with the same SPS condition, which makes the large mass contrast in the lattice atoms (A-sites), indicating the mass difference between La³⁺ and Sr²⁺ was insignificantly affecting the reduction of κ . Especially, the sample with $x = 0.01$ exhibited the largest κ along the measured temperature range as the result of the largest σ (Figure 71a) and the high relative density (Figure 68).

The temperature dependence of the figures of merit (ZT) for the SLTO bulk samples with different La content is shown in Figure 73. In the whole measurement temperature range, the ZT increased with the increasing temperature, particularly where the SLTO with $x = 0.01$ steeply increased. The maximum ZT values of the SLTO sample with $x = 0.01$ was 1.5×10^{-3} at 800 K. Compared to the ZT values of La-doped SrTiO₃, the maximum ZT values of the La_{0.08}Sr_{0.92}TiO₃ prepared by

mechanical alloying was 0.20 at 1000 K [65], the $\text{La}_{0.12}\text{Sr}_{0.88}\text{TiO}_3$ prepared by conventional solid-state reaction sample exhibited maximum ZT of 0.28 at 773 K [139], a large ZT of $\text{Sr}_{0.92}\text{La}_{0.08}\text{TiO}_3$ prepared by combustion synthesis with the post-SPS process was 0.37 at 1045 K [48]. The $\text{Sr}_{1-3x/2}\text{La}_x\text{TiO}_3$ ($x = 0.15$) prepared by a solid-state reaction method with sintering in $\text{N}_2/5\% \text{H}_2$ presented the largest $ZT = 0.41$ at 973 K [129]. The $\text{Sr}_{0.09}\text{La}_{0.91}\text{TiO}_3$ synthesized by the colloidal method together with the SPS process exhibited a maximum ZT of ~ 0.37 at 973 K, which is one of the highest values for La-doped SrTiO_3 reported previously [128]. In addition, the TE properties of La-doped SrTiO_3 depend on the chemical composition, preparation, and processing condition, according to the particle sizes and grain mixtures from micro-to nanoscale [12, 129, 140]. So, the ZT of the SLTO synthesized by sol-gel auto combustion exhibited a lower value than the SLTO that was prepared by several other methods such as mechanical alloying, conventional solid-state reaction, combustion synthesis and colloidal method due to lower σ . However, our study confirmed that the La dopant could enhance the TE property of SrTiO_3 with a lower concentration than previously reported.

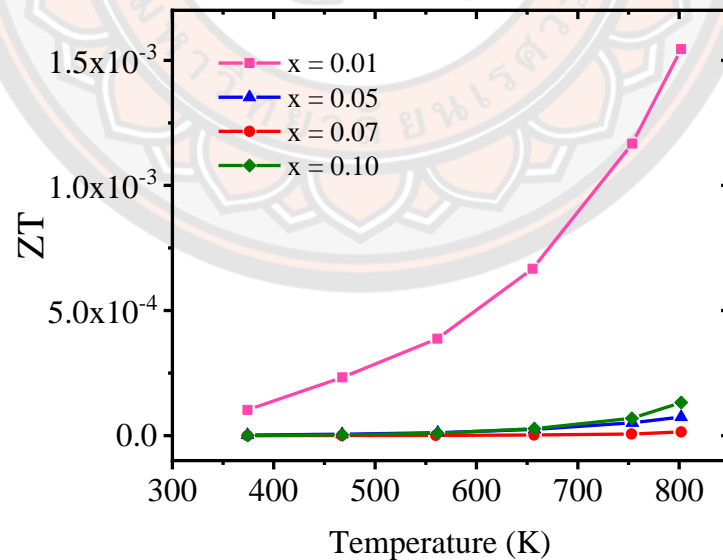


Figure 73 Temperature dependence of dimensionless figure-of-merit ZT of the bulk SLTO sample with different La concentrations.

4.2 Nb dope SrTiO₃

4.2.1 Characterization of phase, morphology, and optical properties

The XRD patterns of STNO ($x = 0, 0.01, 0.03, \text{ and } 0.05$) nanopowder after calcination at 1000°C 12 hours are presented in Figure 74(a). All samples were compared with the standard data JCPDS no. 035-0734 [141] and each showed an agreement of the main peak at $2\theta = 32.40^\circ, 40.04^\circ, 46.50^\circ, 57.87^\circ, 67.94^\circ$ and 77.27° belonging to (110), (111), (200), (211), (220) and (310) planes of a cubic perovskite STO phase (Pm-3m). This indicates that all samples were identified as pure STO without any detectable impure phase, which further confirms that a cubic perovskite STO nanocrystalline structure is retained after Nb⁵⁺ doping. In addition, the main peak belonging to the (110) plane (Figure 74(b)) shows a slight shift to a lower diffraction angle with increasing niobium doping content. This is due to the substitution of a larger radius of Nb⁵⁺ (0.64 Å) ions to the Ti⁴⁺ (0.61 Å) sites, which corresponds to Bragg's law equation: $n\lambda = 2d\sin\theta$ [142]. The crystallite size of all the STNO nanopowder was calculated using the Full Width at Half Maximum (FWHM) values of the XRD patterns from Scherer's equation (Eq. 31) [89, 106] as follows:

$$D = \frac{k\lambda}{\beta \cos\theta} \quad (31)$$

where D is the average crystallite size, k is the constant 0.9, λ is the wavelength of Cu-K_a radiation (1.5406 Å), β is the FWHM, and θ is the Braggs angle. The average crystallite size of the STNO samples calculated is shown in Table 5. The crystallite size of STO was around 23 nm and 21 nm for the STNO samples. The results indicated that there was an insignificant effect from the Nb doping content on the crystallite size of the STNO powder synthesized by the sol-gel auto-combustion method. Additionally, it was observed that the crystallite size of the STNO powders prepared in this way is relatively smaller than the crystallite size of the STO nanopowder synthesized by a modified aerogel procedure (25 nm) [143], the Sr_{0.94}Ti_{0.9}Nb_{0.1}O₃ (80 nm) synthesized by a modified glycine-nitrate process (80 nm) [46], or the STNO ($x = 0-0.03$) nanopowders prepared by the wet synthesis-sol-gel method (160-240 nm) [144].

Considering the effect of Nb doping on the STNO cubic perovskite structure, the specific structural parameters were calculated by Rietveld refinement analysis of the experimented XRD data using the Fullprof program. The refinement parameters for the process that were used included the scale factor, the background intensity, the lattice constant, profile half-width parameters (u , v , and w), functional position of the atoms, and occupancies, of the STNO sample. The background parameter was determined by the Chebyshev function. In addition, a pseudo-Voigt function was examined to fit the diffraction peak profiles of the samples.

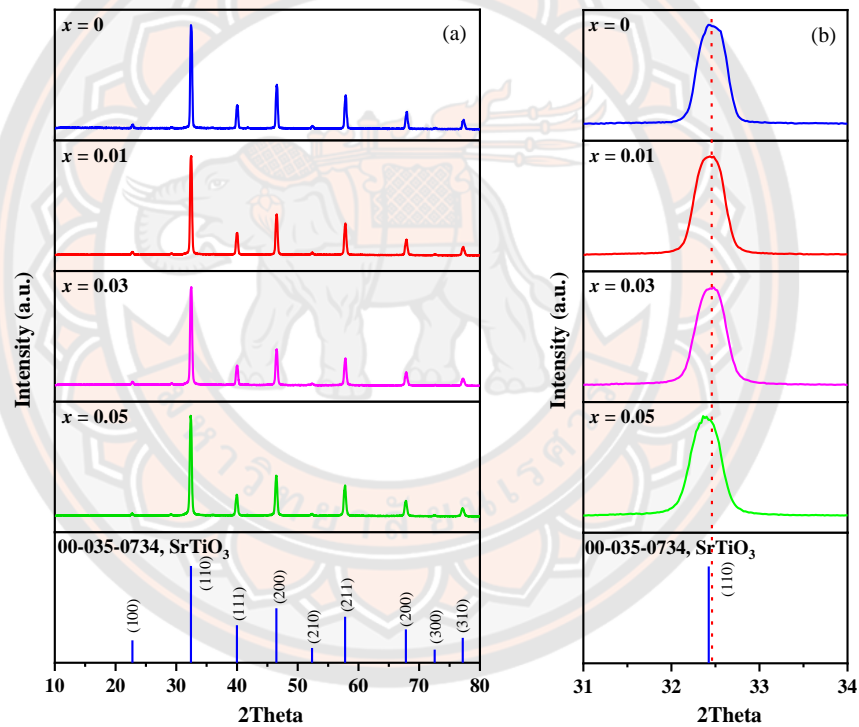


Figure 74 (a) XRD patterns of STNO powder with $x = 0, 0.01, 0.03$ and 0.05 and JCPDS of STO (b) magnified view of the main XRD peak.

Figure 75 presents the Rietveld refinement analysis results of all the STNO samples. The resultant parameters after Rietveld refinement analysis of the STNO sample and their densities are also summarized in Table 5. The peaks of the STNO samples show a good fitting with the low Chi-squared parameter ($\chi^2 < 4$) and the

Rietveld discrepancy factors (R_p , R_{wp} , $R_{exp} < 10\%$). These results show that the refined XRD patterns were in good agreement with the experimental data and good consistency with the JCPDS#35-0734 database ($a = b = c = 3.9050 \text{ \AA}$, 5.12 g/cm^3).

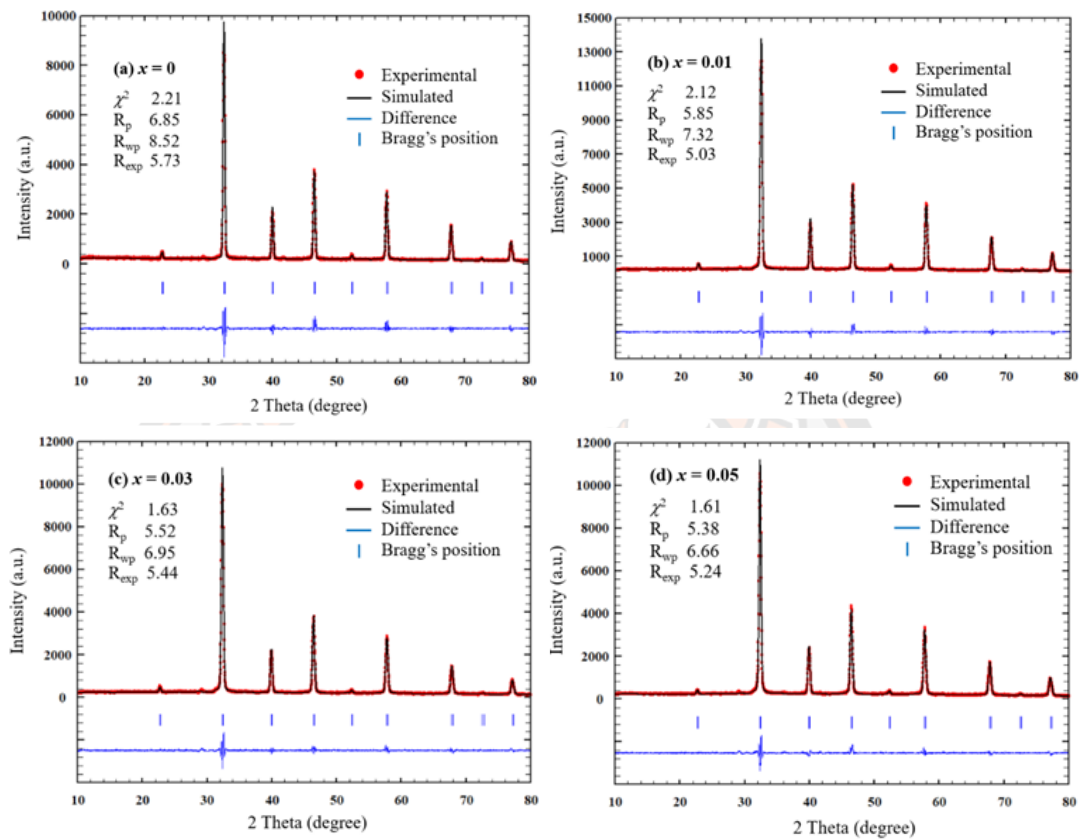


Figure 75 Rietveld refinement analysis of STNO samples: (a) $x = 0$, (b) $x = 0.01$, (c) $x = 0.03$ and (d) $x = 0.05$.

Figure 76(a) shows the lattice parameter and calculated cell density of STNO versus the Nb concentration compared with JCPDS#00-35-0734 of the STO database. The lattice parameter STNO with $x = 0$ is similar to the database and previous work: the calculation of the lattice parameter of STO (3.9050 \AA) [145]. In addition, the lattice parameter value of the undoped STNO sample was lower than that of the STO value ($3.920\text{-}3.925\text{ \AA}$), which had been prepared by the microwave-assisted hydrothermal method [106]. The result indicated that the sol-gel auto combustion provides a lattice parameter that resembles the conventional technique. The STNO with $x = 0.01\text{-}0.05$ were slightly expanded with an increase in Nb content in both

volume and the lattice parameter. The lattice parameter, density, and volume of the STNO samples exhibited a slight increase when the Nb content increased due to the substitution of Nb^{5+} (0.64 Å) ions to Ti^{4+} (0.61 Å) sites. This is in agreement with previous research on the lattice parameter and volume of Nb-doped SrTiO_3 [142, 146]. It was also found that the lattice parameter of STNO with $x = 0.01$, 0.03 and 0.05 is similar to the lattice parameter and the same trends of Nb-doped STO (3.905 – 3.918 Å) prepared by the colloidal synthetic process [147] and the (Nb, Zn) co-doped STO ceramics (3.9064-3.9069 Å) prepared by the traditional solid -state technique [141]. Figure 76 (b) shows the crystal structure of STNO with $x = 0.05$ calculated by Rietveld refinement analysis, which substituted the Nb^{5+} at the Ti^{4+} site, with occupancy numbers of Nb^{5+} and Ti^{4+} to be 0.0501 and 0.9570, respectively. The result indicated that the sol-gel auto combustion provides a lattice parameter that resembles the conventional technique.

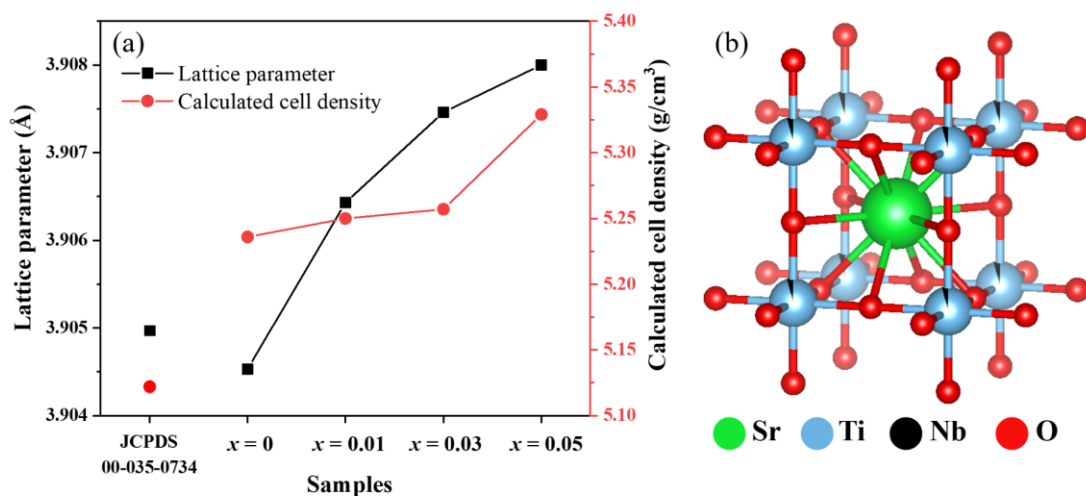


Figure 76 (a) The lattice parameter and calculated cell density (d_{cal}) of STNO nanopowder and (b) the crystal structure of STNO with $x = 0.05$ from Rietveld refinement analysis compared with SrTiO_3 database.

Table 5 Lattice parameter, Chi-squared (χ^2), Rietveld discrepancy factors (R_p , R_{wp} , R_{exp}) and Calculated cell density (d_{cal}) and crystallite size of STNO ($x = 0, 0.01, 0.03$ and 0.05)

Name	Lattice parameter $a = b = c$ (Å)	χ^2	R_p	R_{wp}	R_{exp}	d_{cal} (g/cm ³)	Crystallite sizes (nm)
JCPDS#35-0734	3.9050	-	-	-	-	5.12	
$x = 0$	3.90453	2.21	6.85	8.52	5.73	5.236	23.4
$x = 0.01$	3.90643	2.12	5.85	7.32	5.03	5.250	21.1
$x = 0.03$	3.90746	1.63	5.52	6.95	5.44	5.257	21.0
$x = 0.05$	3.90800	1.61	5.38	6.66	5.24	5.329	21.0

The SEM images of the STNO ($x = 0, 0.01, 0.03$, and 0.05) powders are shown in Figure 77. The morphology of both the undoped and the Nb-doped STNO samples presented as agglomerated particles and indeterminate shapes due to the adhesion of particles to each other by weak forces [148]. It was observed that all the samples exhibited smooth and dense surfaces with no porousness on the particles. The agglomeration of particles in the STNO sample showed more particles sticking together when the amount of Nb doping increased. The ImageJ program was used to determine the average particle size of all the samples, which measured 200 particles/sample. The average particle size of the undoped STNO was 235 nm, while the Nb-doped STNO samples with $x = 0.01, 0.03$, and 0.05 had an average particle size of 128 nm, 105 nm, and 84 nm, respectively. This indicates that the average particle size of STNO samples slightly decreased with the increase of the Nb content. These results showed that the STO nanopowders were closer and lower than others reported as being prepared by various techniques such as the flux treatment method (200-400 nm) [149]. The STNO results are also closer and lower than others reported in the literature, prepared by various techniques, such as the $\text{Sr}_{0.94}\text{Ti}_{0.9}\text{Nb}_{0.1}\text{O}_3$ powder synthesized by a modified glycine-nitrate process (100 nm) [46] and the $\text{SrTi}_{0.95}\text{Nb}_{0.05}\text{O}_3$ powders prepared by ball milling (1 μm) [150].

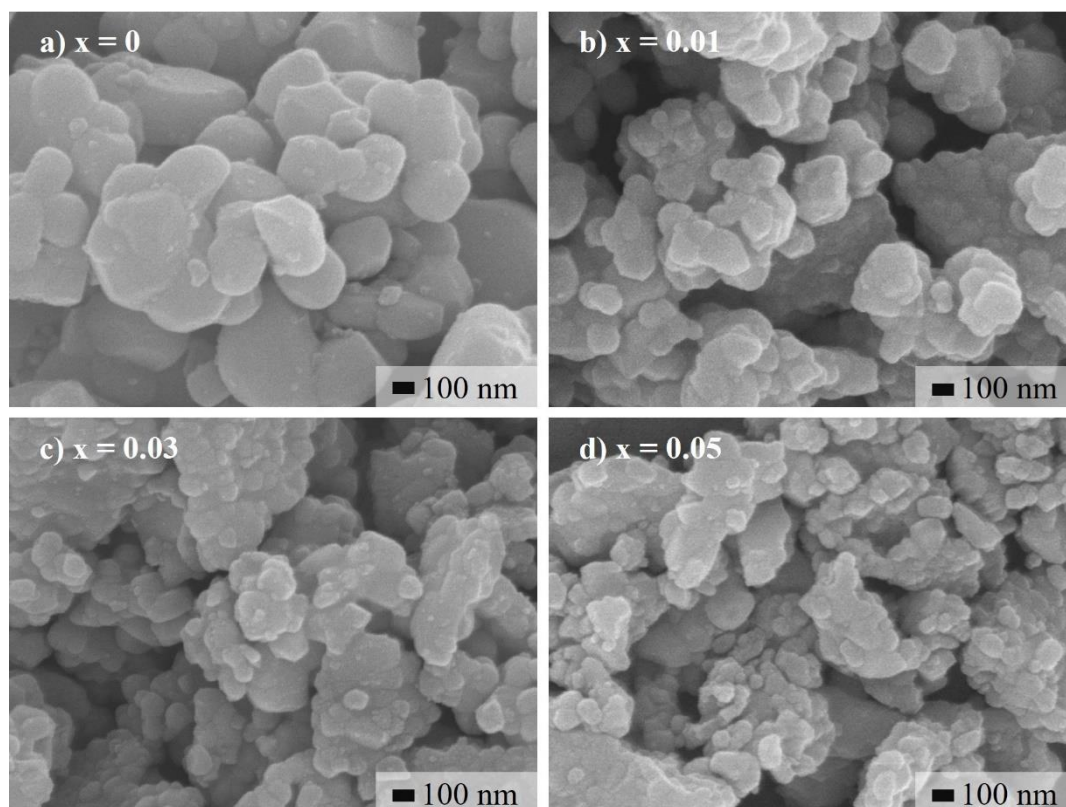


Figure 77 SEM image of STNO nanopowder: (a) $x = 0$, (b) $x = 0.01$, (c) $x = 0.03$, and (d) $x = 0.05$.

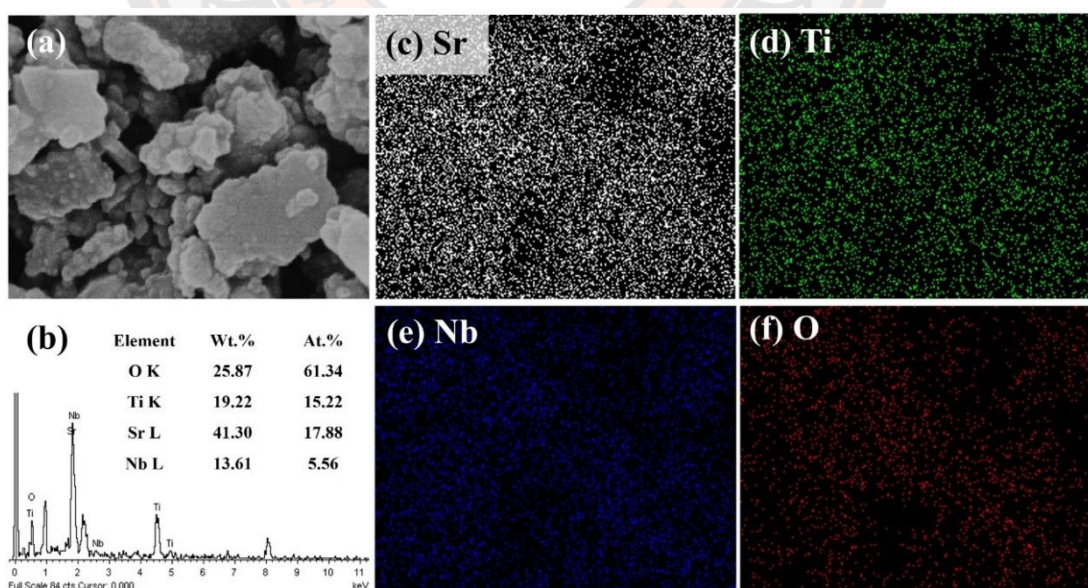


Figure 78 SEM-EDS images and spectrum of the STNO nanopowder with $x = 0.05$.

The SEM image, EDS spectrum, and mapping images of the STNO nanopowder with $x = 0.05$ are shown in Figure 78. In the EDS spectrum Figure 78(b), the signals corresponding to Sr, Ti, Nb, and O are exhibited in Figure 78(c-f). It is observed that elements Sr, Ti, Nb, and O are uniformly distributed in the STNO nanopowder. The quantitative EDS analysis confirmed that the atomic ratio of Sr, Ti, Nb, and O in STNO nanopowder with $x = 0.05$ is 1:0.85:0.31:3.43. Although the actual chemical composition was examined by EDS analysis, it was inconsistent with the nominal composition due to there being low concentrations of Nb doping, no flat surface on the selected area allowing accurate mapping analysis and measurement (different working distance of the electron beam) and the accuracy of the EDS spectrum was within $\pm 5\%$ relative to the actual value [151].

The optical properties of the STNO samples were investigated by UV-Visible spectra absorbance with Eq. (32) being recorded at wavelengths between 300 – 600 nm at room temperature (Figure 79). In a general sense, the spectra absorbance was used to observe the absorption edge and energy hole by following the movement of the electrons from the upper bound of the valence band to the lower bound of the conduction band [104]. The absorption capacity of all the samples showed a comparable trend at the absorption edge at 311 nm wavelength. In the high energy region of the absorption edge, the ability of light absorption linearly increased when the photon energy increased. The relationship of the absorption and photon energy ($h\nu$) is represented by Tauc's relation Eq. 33 [89, 152];

$$A = -\log(I/I_0) \quad (32)$$

$$(Ah\nu) = A(h\nu - E_g)^n \quad (33)$$

where I_0 is intensity of incidence, I is transmitted radiation, α denotes the absorption coefficient, A is a constant, E_g is the band gap, and n depends on the type of transition. For the directly allowed transitions, $n = 1/2$, for the indirectly allowed transitions, $n = 2$, for direct forbidden transitions, $n = 3/2$, and indirect forbidden transitions, $n = 3$ [104, 105]. The E_g of these samples was investigated by extrapolating the linear portion of the curve to zero absorbance, shown in Figure 79 as the inset plot of $(\alpha h\nu)^2$ versus $h\nu$ for a direct allowed transition. It was found that the E_g of all the STNO samples is 4.11 eV.

The optical properties of nanopowder depend on their crystallinity, particle size, and synthesis method, such as when the E_g increases with the decreasing particle size. For the undoped STNO samples, the E_g in this study was higher than reported in another research. For example, the E_g of the STO samples prepared by the microwave-assisted hydrothermal method were 3.5 ± 0.1 eV [106], and for the STO powders prepared by the liquid-solid reaction method, the E_g was 3.4 - 3.5 eV [109], and when the STO were prepared by high-temperature solid-state reaction, the direct E_g was 3.55 - 3.67 eV [153]. In addition, the STO samples that had a cubic structure showed a higher E_g than STO prepared by the topotactic, with rodlike and cubic samples exhibiting E_g of 3.0 and 3.04 eV [154]. On the other hand, for Nb-doped STNO samples, the doping usually affects the E_g value, such as the E_g of Al-doped STO (3.45 eV) being better than the undoped STO (3.30 eV), where both of them were prepared by solid-state reaction [155]. Unfortunately, in our research, the E_g of the STNO was not changed at varying concentrations of Nb-doped. This may have been due to the low concentration of Nb-doped that we used.

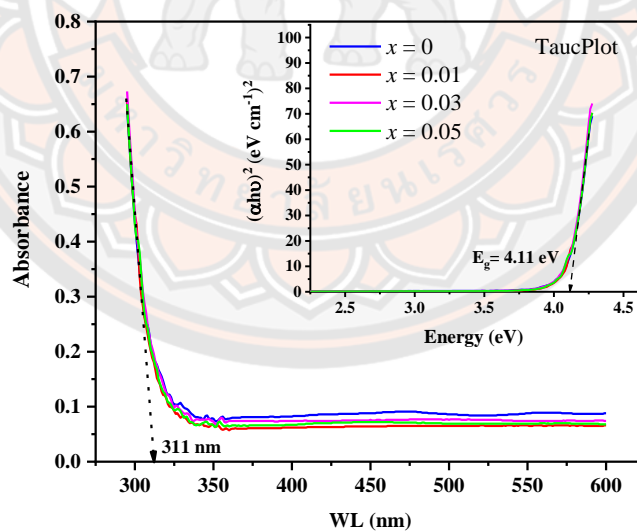


Figure 79 UV-vis spectra of the STNO samples ($x = 0, 0.01, 0.03$ and 0.05) and inset plots of $(\alpha h\nu)^2$ as a function of photon energy ($h\nu$).

Generally, the decolorization of dye is used to determine the effectiveness of a photocatalytic reaction. The decolorization efficiency (%DE) follows Eq. (34);

$$\%DE = \frac{C_0 - C}{C_0} \times 100 \quad (34)$$

where C_0 is the concentration of the initial MB for the solution to reach adsorption/desorption equilibrium condition and C is the concentration of the MB after UV irradiation of the solution sample.

Figure 80(a) presents the % DE of MB by STNO with $x = 0, 0.01, 0.03$, and 0.05 as the photocatalyst under a UV light. The photolysis tests showed a slight change in the concentration of MB of not more than 10%, which is within the acceptable value range. The photocatalytic activities of STNO with $x = 0, 0.01, 0.03$ and 0.05 increased with higher Nb content. The % DE of MB for all STNO increased hourly until 8 hours; the % DE using STNO with $x = 0$ and 0.01 was similar at around 20%, while $x = 0.03$ and 0.05 were similar at around 50%. The factors affecting photocatalytic efficiency are crystallinity, crystal structure, and particle size of the material [115]. The results indicated that the concentration of Nb dopant leads to increased photocatalytic activity of the Nb-doped STNO due to the smallest particle size providing a larger active reaction site and empowering the adsorption of more MB on the STNO photocatalyst surface, indicating that photocatalytic efficiency reached a maximum at the highest level of Nb, $x = 0.05$.

The rate of reaction can be specified by chemical kinetics. The first-order reaction kinetics constant (k) is determined using the Eq. 35 [152]:

$$kt = \ln C_0 / C \quad (35)$$

where C and C_0 are the real-time and initial concentrations of MB. The k value for STNO also increased with Nb doping content increases, as shown in Figure 80(b). Obviously, for STNO with $x = 0$ and 0.01 , the k value is similar at around 0.033-0.034. With $x = 0.03$ and 0.05 the k values are similar at 0.076-0.079, according to the %DE shown in Figure 80(a). The great value for Nb-doped STNO as a photocatalysis reaction was in the STNO sample with $x = 0.05$, as shown in Figure 80(c). The absorption peak (λ_{\max}) of MB was at 663nm. After 8h, the λ_{\max} of MB continuously decreased and shifted to the lower wavelength from 663nm to 656 nm. The blue shift

is due to the stepwise removal of methyl or methylamine, and the decolorization of the MB, which results in the λ_{max} of the MB decreasing [91]. For all SNTNO samples, the spectra absorbance follows the same trends.

Photoluminescence is widely used to characterize the optical properties of semiconductors. The electrons of the semiconductor substance are stimulated by the photon absorbance, where its electrons move to a higher energy state from a lower energy state, after which there is a relaxation phase during which photons are again emitted or released. The interval between the absorption and emission phases of the photons may vary depending on the substance. Most UV light absorbers emit light in the visible range so that colors can be seen in these substances. The photoluminescence of all our STNO samples, after excitation at 327 nm in the range of 350-600 nm at room temperature, is shown in Figure 80(d). The emission peaks of all the samples are similar trends, 397, 438, 450, 466, 479, 491, and 562 nm, indicated in violet, blue, and green. The high-intensity emission band at 397 nm indicates high electron-hole recombination [156]. The peak emission at 395 nm indicates that the violet colours are due to shallow surface defects [106]. Also, peak emissions at 438, 450, 466, 479, and 491 nm, are blue due to Sr deficiency in the crystal structure, and the peaks emitted at 562 nm, showing as green emissions, are caused by oxygen vacancy in the STO lattice, according to the previous study [114]. Moreover, the photoluminescence emission intensity related to the recombination of charge carriers in a semiconductor can be used to explain the photocatalytic activity of the photocatalyst. From Figure 80(d), the photoluminescence emission intensity of Nb-doped STNO nanopowder is lower than the undoped STNO sample ($x = 0$), indicating lower electron-hole pair recombination and photocatalytic reaction enhancement. Remarkable, the result of the photoluminescence emission intensity of the Nb-doped STNO with $x = 0$ and 0.01 are nearly closed, while $x = 0.03$ and 0.05 are closed together with lower than those of $x = 0$ and 0.01. It is indicated that the photoluminescence emission intensity of the Nb-doped STNO corresponds to the photocatalytic efficiency of the sample, as shown in Figure 80(a).

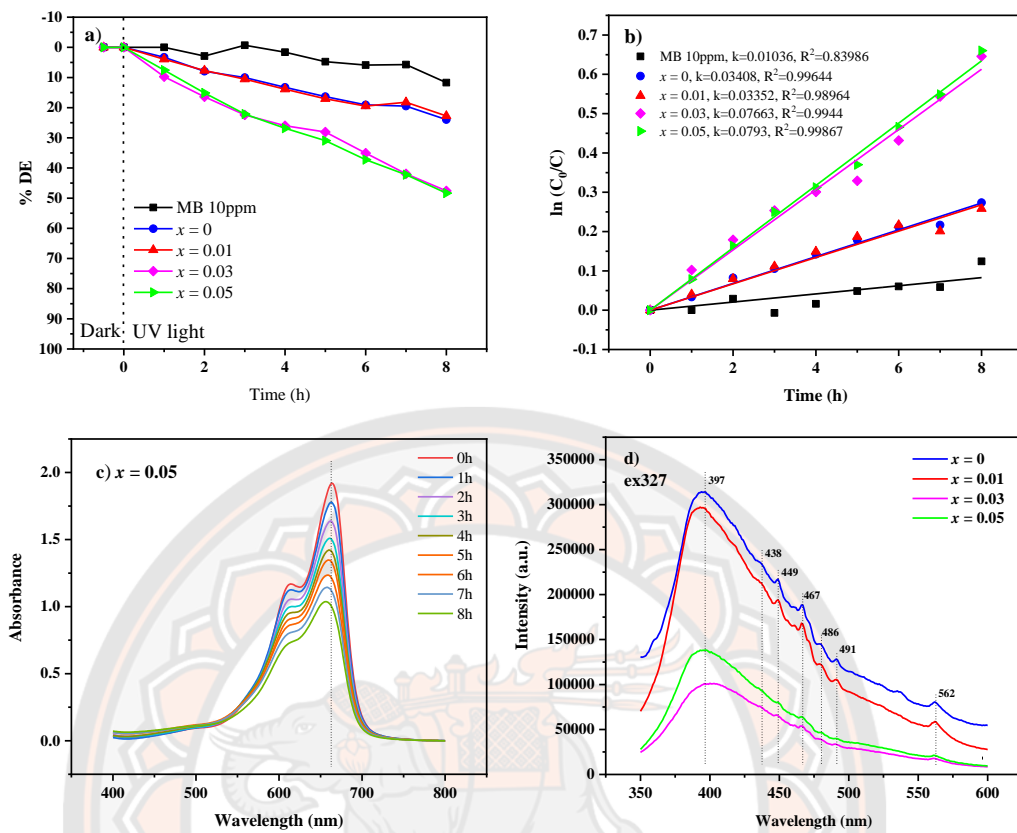


Figure 80 (a) The photocatalytic decolorization efficiency (%DE) of MB irradiated beneath the UV lamp (b) The Pseudo-first order kinetics of photocatalytic decolorization of MB (c) Time-dependent absorption spectra of MB solution using STNO photocatalyst with $x = 0.05$ (d) photoluminescence spectra of the STNO sample with $x = 0$ and 0.05 .

The Nyquist plot from the Electrochemical Impedance Spectroscopy (EIS) is used to analyse the charge carrier migration of photoelectrode in a three-electrode system. The semicircle accords to the charge transfer resistance at the photoelectrode interface R_{Ω} , which is the solution resistance. This is estimated by the x -intercept of the Nyquist plot and describes the overall resistance between the photoelectrode and the electrolyte. Figure 81 shows a Nyquist plot of all the STNO samples, using an Autolab PGSTAT302N at an applied potential of 1 V_{ref} at pH 6 (Na_2SO_4 electrolyte 0.1M) and the frequency range from 1 – 1000 Hz and amplitude of 0.01. The

experimental data are compared with the simulation data by fitting the experimental data by the equivalent circuit, as shown in the inset of Figure 81. The simulations were performed, with the impedance values being 5260.82 Ω for $x = 0$, 4827.40 Ω for $x = 0.01$, 4320.14 Ω for $x = 0.03$, and 1712.73 Ω for $x = 0.05$. The equivalent circuit of all STNO samples is shown in the inset of Figure 81. The smaller semicircle in the Nyquist plots is for increases in the Nb concentration, suggesting that the highest level of effective charge transfer efficiency occurs at higher Nb content but not at low Nb content or without doping [157-159].

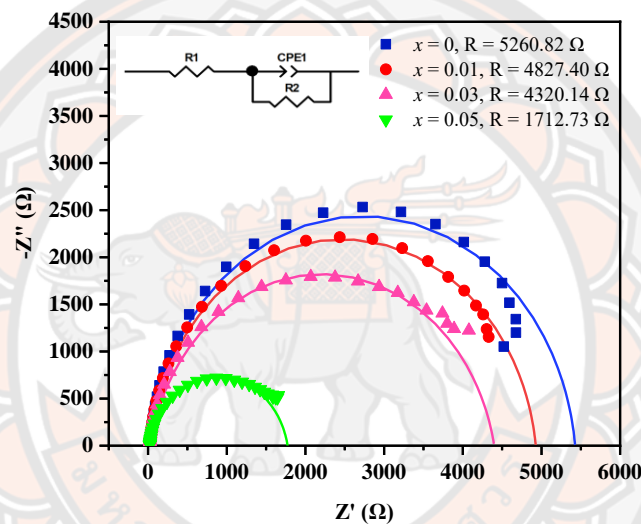


Figure 81 Experimental data and simulation of EIS Nyquist plot of STNO photocatalyst sample.

The Mott-Schottky plots of STNO samples were carried out with the EIS that measures an electrochemical interface as its DC voltage changes and with a fixed frequency. The graph can be plotted by the voltage and capacitance and are used to characterize the flat band potential and understand the charge transport in STNO. So, to consider the donor density (N_D) and the flat band potential (V_{fb}) of STNO photoelectrode, a Mott-Schottky analysis was performed. Depending on the depletion layer model, the capacitance of the semiconductor space charge layer (C_{SC}) is based on the applied potential (V_{appl}). The Mott-Schottky equation are expressed in equation 36 [147]:

$$(1/C)^{-2} = (2/\epsilon_r \epsilon_0 e N_D)(V_{\text{appl}} - V_{\text{fb}} - k_b T/e) \quad (36)$$

where e is the charge of the electron, ϵ_r is the semiconductor dielectric constant, ϵ_0 is the vacuum permittivity, T is the absolute temperature, and k_b is the Boltzmann constant (1.38×10^{-23} J/K).

Figure 82 shows the Mott-Schottky plot of the STNO samples from the EIS spectroscopy analysis (Autolab PGSTAT302N) by applying the potential range of 1.2 – 2.0 V at pH = 6 (Na₂SO₄ electrolyte 0.1M) at a 1000 Hz frequency. The Mott-Schottky curves for all samples demonstrated a positive slope, indicating their n -type character similar to that reported in the literature [147, 160, 161]. The flat band potentials (V_{fb}) determined from the x -intercepts of the curves are -0.10, -0.18, -0.25 and -0.30 V for STNO samples with $x = 0, 0.01, 0.03$ and 0.05 , respectively. The applied potential in NHE scale (E_{NHE}) was calculated by the following equation:

$$E_{\text{NHE}} = E_{\text{Ag/AgCl}} + 0.21 \quad (37)$$

Accordingly, the V_{fb} values of STNO samples with $x = 0, 0.01, 0.03$ and 0.05 are 0.11, 0.03, -0.04 and -0.11 (vs.NHE), respectively. It was found that the V_{fb} values for STO and STNO samples were shifted towards negative value when Nb content increased, favoured its better photocatalytic activity. As a rule of thumb, a conduction band potential (E_{cb}) of n -type semiconductor is more negative by -0.1 eV than E_{fb} level [162]. Therefore, E_{cb} of STNO samples with $x = 0, 0.01, 0.03$ and 0.05 could be determined as 0.01, -0.07, -0.14 and -0.21 (vs.NHE), respectively. For the valence band potentials (E_{vb}) of the STNO samples is a result from combining the E_{cb} with the E_g values. Thus, the E_{vb} of the STNO samples are 4.12 V (vs.NHE) for $x = 0$, 4.04 V (vs.NHE) for $x = 0.01$, 3.97 V (vs.NHE) for $x = 0.03$, and 3.90 V (vs.NHE) for $x = 0.05$. This result indicates in Figure 83 cooperate with the mechanism of photocatalysis process.

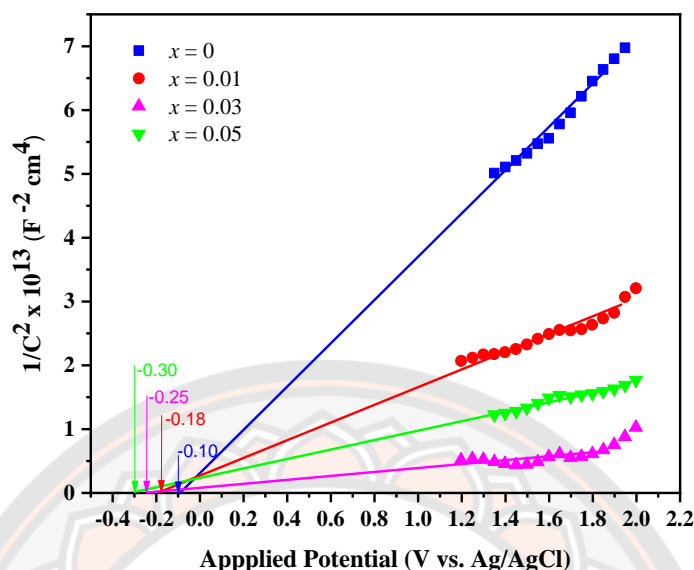


Figure 82 A Mott-Schottky plot of STNO nanopowder.

Thereby, the E_{cb} of the STNO samples are 0.01 V (vs.NHE) for $x = 0$, -0.07 V (vs.NHE) for $x = 0.01$, -0.14 V (vs.NHE) for $x = 0.03$, and -0.21 V (vs.NHE) for $x = 0.05$. The mechanism of photocatalytic decolorization of MB dye on STNO photocatalyst under UV irradiation is shown in Figure 83. The process of photocatalysis reaction can be partitioned into three steps. First, the photocatalysis of STNO is energized by UV light with photo-energy higher than the E_g of the photocatalysis to create photoinduced electrons (e^-) and gaps (h^+). The electron is produced when electrons from the valence band (VB) move to the conduction band (CB), during which process gaps within the valence band are produced (Eq. 38). Next, the e^- and h^+ respond with O_2 and H_2O (or OH^-) to produce highly receptive hydroxyl radicals (OH^\bullet) and superoxide radicals ($O_2^{\bullet-}$). The H_2O or OH^- that are adsorbed on the surface of the photocatalysis are oxidized by the h^+ to create OH^\bullet (Eq.39). The O_2 accompanying the adsorption on the surface by the photocatalysis reacts with e^- to generate the $O_2^{\bullet-}$ (Eq.40). In a further step, $O_2^{\bullet-}$ reacts with H_2O to produce hydroperoxyl radical (HO_2^\bullet) (Eq.41). Finally, these hydroxyl radicals, superoxide radicals and hydroperoxyl radicals decompose the MB dye into CO_2 , H_2O and degraded products of MB, which could be 2-amino-5-(NN-methylformamide)

benzene sulfonic acid, 2-amino-5-(methylamino)-hydroxybenzene sulfonic acid, and benzenesulfonic acid [118] (Eq.42). This entire process can be summarized in the following equations:

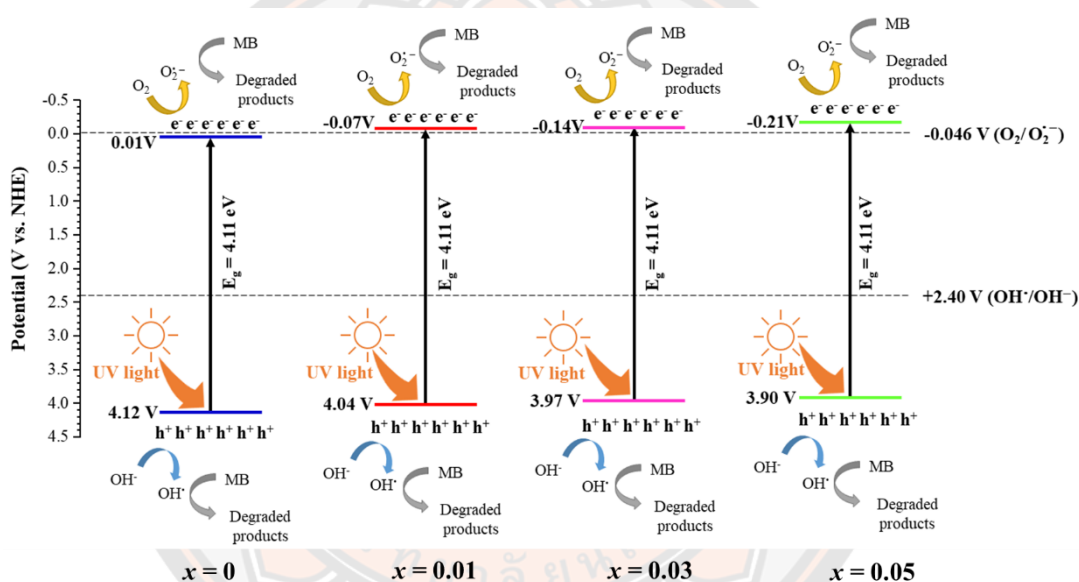
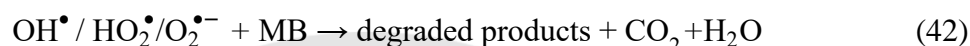
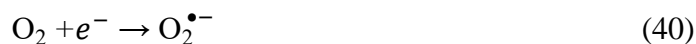


Figure 83 The charge transfer and photocatalytic mechanism of STNO nanopowder.

Based on the above mechanisms, there are three reasons for the occurrence of the outstanding photocatalytic activity of the STNO samples. Firstly, the particle size of the Nb-doped STNO samples prepared by the sol-gel auto-combustion method provides a nanosized particle, and the particle size decreases with increasing Nb doping content. Secondly, the smaller semicircle of the Nyquist plots Nb concentration increases, suggesting a higher electron transfer conductivity. Finally, the E_{cb} calculated from the Mott-Schottky equation of the STNO samples is more negative than the reduction potential of $\text{O}_2/\text{O}_2^{\bullet-}$ (-0.046 V vs. NHE) [162], and the E_{vb}

of the STNO samples are more positive than the reduction potential of $\text{OH}^\bullet/\text{OH}^-$ (+2.40 V *vs.* NHE) [162], so has a good oxidation ability to degrade the organic pollutants [163]. Therefore, the Nb-doped STNO sample with $x = 0.05$ has the smallest particle size, the lowest semicircle of the Nyquist plots, and the lowest E_{cb} and E_{vb} calculated from the Mott-Schottky equation. These results for the STNO sample with $x = 0.05$ indicate the highest %DE of photocatalytic activity.

Table 6 illustrates the decolorization of MB in an aqueous solution under a UV source as identified in previous research [59, 113]. When comparing our results with that previous research, it was found that the photocatalytic activity of undoped STNO was lower than STO. This was due to the larger particle sizes and the undoped STNO having no porous structures. Comparing the photodecolorization efficiency of MB under UV-visible irradiation with several other methods [91, 115, 164], the photocatalytic activity of undoped STNO was less than STO synthesized by those methods (also illustrated in Table 6).

The photocatalytic activity of metal-doped STNO (Table 6) could not be directly compared to our research due to different conditions of the photocatalytic system such as light source intensity, amount of photocatalytic loading, and the concentration of dye. However, no report on the photodecolorization efficiency of MB using Nb-doped STNO as photocatalysts under UV irradiation has been found. In our study, the Nb content was significantly enhanced the photocatalytic activities of STNO nanopowder.

Table 6 The summary of the photodecolorization efficiency (%DE) of several dyes using undoped-STO and metal-doped STO photocatalysts with different preparation methods, light sources, and photocatalytic conditions.

Photocatalyst	Preparation method	Light sources	Types of dye	Photocatalytic conditions			Ref.
				Photocatalyst Loading	Initial Concentration	Reaction Time	
SrTiO ₃	Polyacrylamide gel route	20W Mercury lamp (UV)	CR	1000 mg/L	10 ppm	10 h	[113]
			RhB				35%
			MO				33%
			MB				53%
SrTiO ₃	Combustion	30W UV	MB	200 mg/L	31.98 ppm	70 min	[59]
SrTiO ₃ B-SrTiO ₃	Facile solvothermal	Visible light	MB	500 mg/L	10 ppm	120 min	[164]
							70.3%
SrTiO ₃ G-N-STO ₃	Amino acids as dopants source and surface area promoters	UV-Visible irradiation	MB	200 mg/L	5 ppm	180 min	[91]
						90 min	100%
STO-P STO-20	Ball milled for different time	125 W UV-Visible irradiation	MB	1000 mg/L	3.19 ppm	210 min	[115]
						150 min	100%
La dope SrTiO ₃ (La=0.5)	Sol-gel	500W Xe arc lamp	K ₂ Cr ₂ O ₇ (Cr (VI))	1000 mg/L	20 ppm	100 min	[94]
SrTiO ₃ (La,Cr)-6 V doped SrTiO ₃	Sol-gel hydrothermal Electrospinning and thermal diffusion	300W Xe lamp 175 W mercury lamp	Tetracycline (TC) MO	500 mg/L 300 mg/L	20 ppm 10 ppm	90 min 75 min	[98] [165]
La-Fe co-doped SrTiO ₃	Solid state reaction	Visible light	MO	600 mg/L	5 ppm	150 min	[166]
SrTiO ₃ Nb-dope SrTiO ₃ (Nb=0.05)	Sol-gel auto combustion	108W UV	MB	500 mg/L	10 ppm	8 h	This study
							55%

4.3 Ag dope $\text{Ca}_3\text{Co}_4\text{O}_9$

4.3.1 Characterization of thermoelectric properties

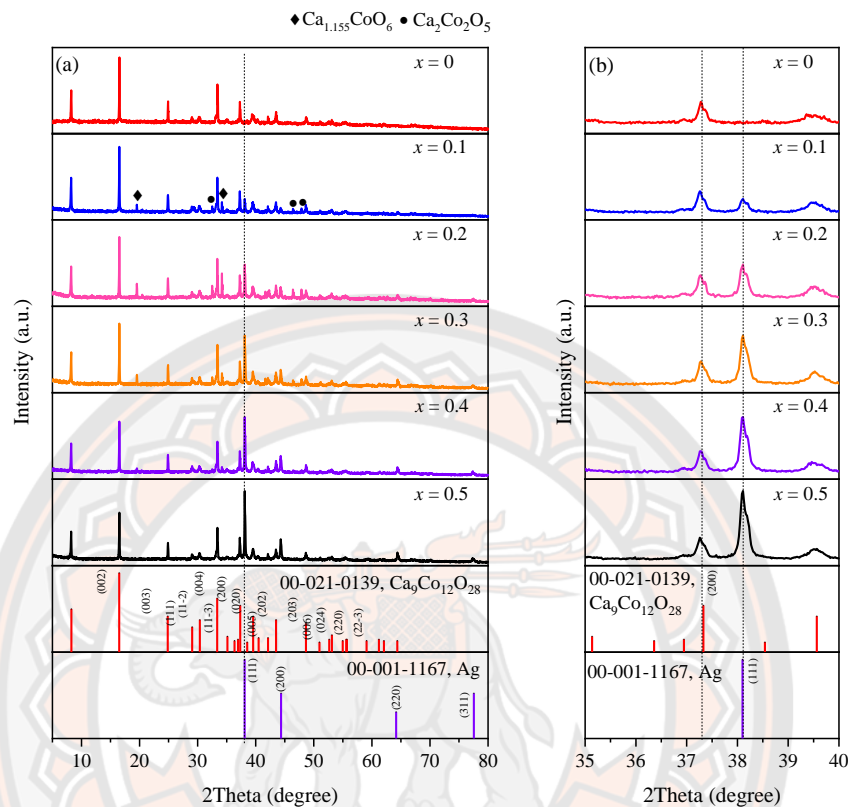


Figure 84 (a) The XRD pattern of the Ag addition $\text{Ca}_3\text{Co}_4\text{O}_9$ ($x = 0, 0.1, 0.2, 0.3, 0.4$, and 0.5) powder sample (b) magnified view of the main XRD peak

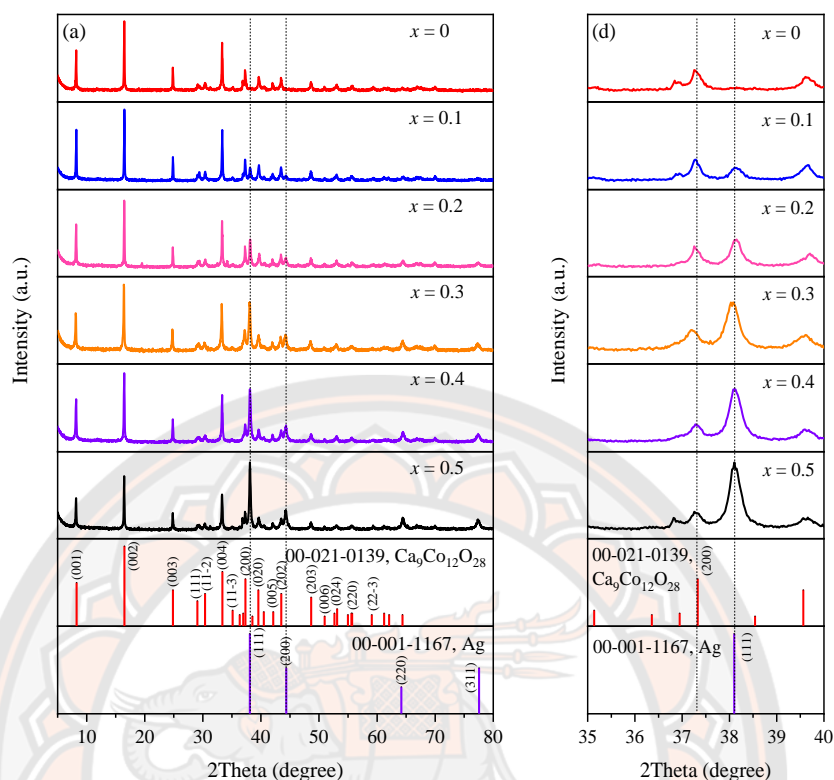


Figure 85 (a) The XRD pattern of the Ag addition $\text{Ca}_3\text{Co}_4\text{O}_9$ ($x = 0, 0.1, 0.2, 0.3, 0.4$, and 0.5) bulk sample, and (b) magnified view of the main XRD peak.

The structure of $\text{Ca}_3\text{Co}_4\text{O}_9$ can be represented as $[\text{Ca}_2\text{CoO}_3][\text{CoO}_2]$ b1/b2 with the misfit-layered structure. The b1 refers to the b-axis length of the Ca_2CoO_3 component, while b2 refers to the b-axis length of the CoO_2 component [167]. This compound exhibits a layered crystal structure, where the CoO_2 layers characterized as hexagonal (H) with CdI_2 -type arrangement, and the Ca_2CoO_3 layers are described as having a rock-salt (RS) configuration with a NaCl-type arrangement. These layers are arranged alternately along the c-axis [168].

The X-ray diffraction pattern (XRD) of the powder and bulk samples is shown in Figure 84 and Figure 85. The diffraction peak observed for all samples can be indexed in the misfit layer $\text{Ca}_3\text{Co}_4\text{O}_{9+\delta}$ by comparing with $\text{Ca}_9\text{Co}_{12}\text{O}_{28}$ (JCPDS No.00-21-0139) [169]. In the powder sample with Ag-addition, three impurity phases can be observed: $\text{Ca}_2\text{Co}_2\text{O}_5$ (marked •, JCPDS No.00-037-0668 [170]), $\text{Ca}_{1.155}\text{CoO}_6$

(marked ♦, CIF No. 7046676 [171]), and diffraction peaks at 38.2° , 44.38° , 64.21° , and 77.57° corresponding to Ag metallic with (111), (200), (220), and (311) plan, respectively. Increased Ag content resulted in increases in these four diffraction peaks [172], but increased Ag content resulted in decreases in the other two impurity phases, as shown in Figure 84(a). The peak at 37.3° corresponds to $\text{Ca}_9\text{Co}_{12}\text{O}_{28}$ with (200) plan, indicating a slightly lower shift in the case of the small addition of Ag ($x = 0.1$), as shown in Figure 84(b). This lower shift in the XRD peak is caused by the substitution of the larger ionic radius of Ag^+ (1.26 \AA) compared to Ca^{2+} (0.99 \AA) [173]. When the Ag-addition level increased, the peak at 37.3° did not change, even though the four peaks of the Ag metallic phase increased. The lattice structure has a limited number of Ca sites that Ag can occupy, so once that capacity is reached, unused Ag will remain separate outside the structure [173].

In the bulk sample, found that the impurity phase disappears after the SPS process, as shown in Figure 85(a). The XRD pattern indicated the lower shift at 37.3° peak that corresponds to $\text{Ca}_9\text{Co}_{12}\text{O}_{28}$ with (200) plan and the increase of the Ag metallic phase with the Ag-addition level increase as shown in Figure 85(b). These phenomena indicate the bulk sample found the effects of doping and inclusion in the same powder sample.

Using the TOPAS program, the Rietveld refinement approach has been utilized to examine the crystal structure of the composite material as well as unit cell data such as the space group, cell location, cell orientation, and atomic distances [90]. Figure 86 shows the final output from the Rietveld refinement of the CACO bulk sample, and the results for all samples are shown in Table 7. The reliability indices for the refinement's quality of fit are summarized, including goodness-of-fit (χ^2), R-factor (R_p , R_{wp} , R_{exp}), lattice parameter, and cell volume for all bulk samples. The results of all samples indicate that the $\chi^2 < 4$ and R_p , R_{wp} , $R_{exp} < 10$, show good agreement between the measured and calculated data [174].

The lattice parameters of the bulk CACO sample with Ag-addition were found to slightly increase with few additions ($x = 0.1 - 0.3$) which occur because the larger ionic radius of the Ag^+ (1.26 \AA) substitutes Ca^{2+} (0.99 \AA) site [173] at the Ca_2CoO_3 layer of the $\text{Ca}_3\text{Co}_4\text{O}_9$ structure, that supports the XRD result. After further Ag-

additions ($x = 0.4 - 0.5$) the lattice parameter does not change, because the Ag particle cannot substitute at Ca site of the CACO structure.

The occupancy site of atoms of the CACO bulk samples is indicated in Table 7. The CACO sample had two layers of Ca_2CoO_3 and CoO_2 . The effect of the Ag substitution and addition occurs on the Ca_2CoO_3 layer. Considering the occupancy site on the CACO sample when the Ag particle was added to the structure. The occupancy site of Ag was increased in the sample with $x = 0.1 - 0.2$ and constantly in the sample with $x = 0.3 - 0.5$. While the occupancy site of Ca was decreased in the sample with $x = 0.1 - 0.2$ and constantly when the sample as $x = 0.3 - 0.5$. The resultant occupancy site of atoms confirms the effect of Ag doping and Ag-addition on the CACO sample. The changing of the occupancy site of the CACO sample corresponds to the lattice parameter value.

Additionally, Table 7 shows the percentage of the phase of the CACO sample after refinement. The percentage of $\text{Ca}_2\text{Co}_2\text{O}_3$ and CoO_2 increased when Ag addition. Then decreased when Ag increased due to the Ca:Co ratio decreasing as a result of the Ag-addition. The percentage of the Ag phase increased when the Ag-addition increased, which corresponds with the chemical composition added to the experiment. The addition of Ag to $\text{Ca}_3\text{Co}_4\text{O}_9$ may cause limitations in substitution phenomena. Specifically, increasing amounts of Ag results in a limitation to substitute at the Ca site, causing the dispersion of Ag particles throughout the system structure. That the Rietveld refinement result corresponds to the XRD result.

These phenomena correspond to the previous research, the relationship between the doping amount and the extent of the substitution of Ag for Ca was reported, and it was found that doping amounts to $x \leq 0.15$ leads to the successful substitution of Ag. However, for doping amounts greater than $x > 0.15$, excessive Ag was observed as an isolated metallic substance, indicating a limit to the amount of Ag that can be substituted for Ca [175]. The result agrees with the previous report, the Ag-addition $\text{Ca}_3\text{Co}_4\text{O}_9$ (x , wt% = 0, 1, 2, 3, 4, and 5) by the sol-gel nitrates route and the two-step sintering process, there is no presence of the Ag within the structure of the $\text{Ca}_3\text{Co}_4\text{O}_9$ cell [172]. The $\text{Ca}_{3-x}\text{Ag}_x\text{Co}_4\text{O}_9$ (x , = 0.05, 0.1, 0.2, 0.3, and 0.5) was prepared by the sol-gel method with spontaneous combustion following cold isostatic pressing (CIP), that reported the Ag substituted the $\text{Ca}_3\text{Co}_4\text{O}_9$ at amount of Ag less

than 0.2 and cannot substituted the $\text{Ca}_3\text{Co}_4\text{O}_9$ at amount of $\text{Ag} = 0.3\text{-}0.5$ [173]. The Ag-doped or/and Ag-added $\text{Ca}_3\text{Co}_4\text{O}_9$ prepared by a cold-pressing technique, the results indicated the Ag particle, both substitution and inclusion between cobaltite grains [176].

Table 7 Chi-square (χ^2), R-factors (R_p , R_{wp} , R_{exp}), lattice parameter, occupancy, and percentage of phase refinement for the CACO bulk sample.

Sample (x)	0	0.1	0.2	0.3	0.4	0.5
R-factors						
χ^2	1.17	1.14	1.1	1.04	1.09	1.04
R_{exp}	3.35	3.35	2.52	3.39	3.45	3.47
R_{wp}	3.93	3.83	3.52	3.54	3.78	3.61
R_p	2.97	2.98	3.86	2.73	2.92	2.8
Lattice parameter						
a (Å)	4.8339	4.8339	4.8339	4.8339	4.8339	4.8339
b_1 (Å) (Ca_2CoO_3)	4.5467	4.5536	4.5597	4.5599	4.5591	4.5594
b_2 (Å) (CoO_2)	2.8250	2.8262	2.8254	2.8262	2.8253	2.8234
c (Å)	10.8436	10.8436	10.8436	10.8436	10.8436	10.8436
β	98.14	98.14	98.14	98.14	98.14	98.14
b_1/b_2	1.609	1.611	1.614	1.614	1.614	1.615
Occupancy						
Subsystem 1 (Ca_2CoO_3)						
Ag1		0.1004	0.2007	0.204	0.1955	0.1995
Ag2		0.1005	0.2007	0.2009	0.1956	0.1995
Ca1	0.9994	0.9004	0.8007	0.8045	0.7955	0.7996
Ca2	0.9994	0.9004	0.8007	0.8019	0.7956	0.7996
Co1	0.9997	0.9999	1.0000	0.9998	1.0020	0.9999
O1	0.9993	0.9979	0.9987	0.9967	0.9999	0.9985
O2	0.9988	0.9958	0.9991	0.9984	0.9998	0.9967
O3	0.9982	0.9956	1.0010	0.9930	0.9996	0.9965
Subsystem 2 (CoO_2)						
Co2	0.9999	1.0010	1.0010	1.0010	1.0040	1.0000
O4	0.9941	0.9713	0.9989	0.9996	0.9673	1.0020
O5	0.9978	0.9540	0.9974	0.9997	0.9999	1.0020
Percentage of phase refinement						
Subsystem 1 (Ca_2CoO_3)	64.54	69.13	67.15	68.78	65.80	64.07
Subsystem 2 (CoO_2)	35.46	29.83	30.32	27.64	30.04	29.66
Addition (Ag)		1.04	2.52	3.58	4.15	6.27

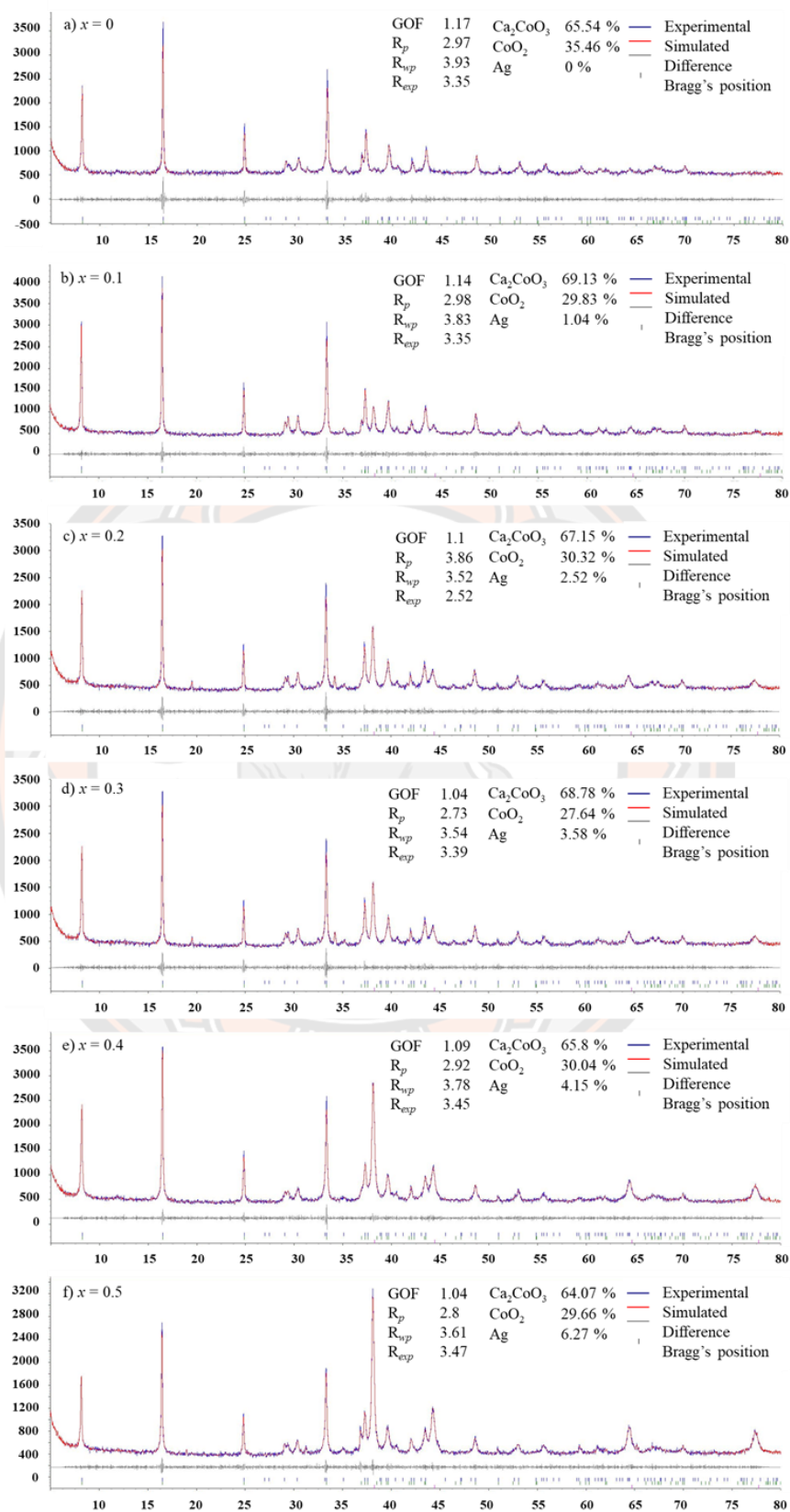


Figure 86 Rietveld refinement analysis of CACO bulk sample.

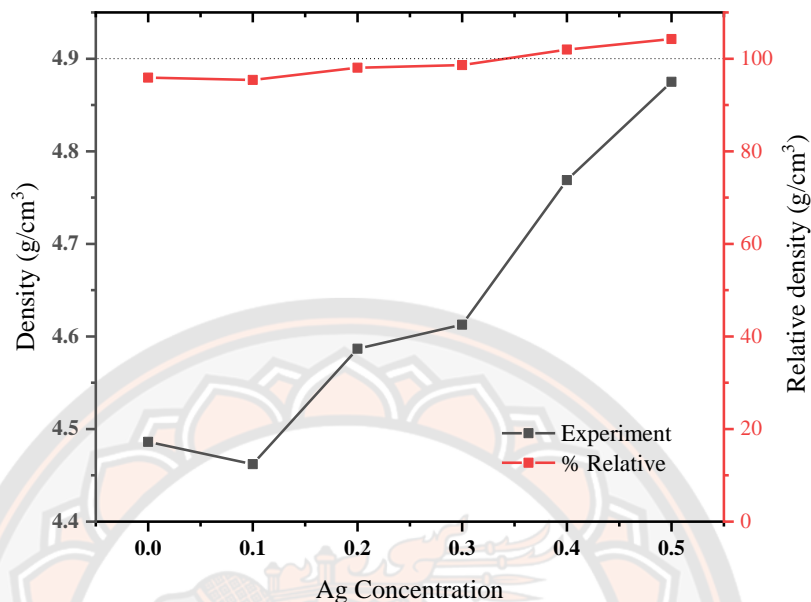


Figure 87 The measured densities (d) and relative density of CACO bulk sample.

Figure 87 shows the measured densities (d) of the CACO bulk sample. The density of the CACO sample ranged from 4.5 g/cm³ to 4.9 g/cm³. The density of the sample without Ag-addition was slightly close to the sample with Ag-addition at $x = 0.01$, after that the density of the CACO sample increased with the increases in Ag-addition. The relative density of all samples was very high, exceeding 96% of the theoretical density of 4.677 g/cm³ [172, 177, 178]. For the sample with $x = 0.4 - 0.5$, the relative density of the bulk sample was over 100%, as shown by the dotted line in Figure 87. Because the Ag particles did not completely substitute at the Ca site, which resulted in an Ag distribution in intergranular regions. The mass of the unit cell is the mass of the Ca₃Co₄O₉ together with the Ag, which resulted in the relative density of the sample being over 100%. Furthermore, when the Ag content was increased the experimental density increased, in agreement with the XRD patterns, and Rietveld refinement analysis.

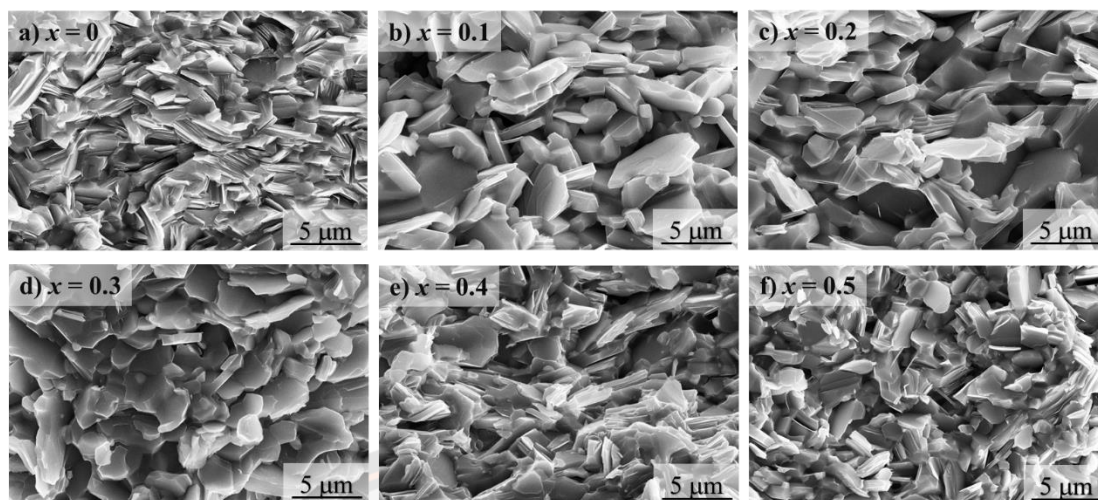


Figure 88 Fractured cross-section SEM images of the CACO bulk sample with different Ag content.

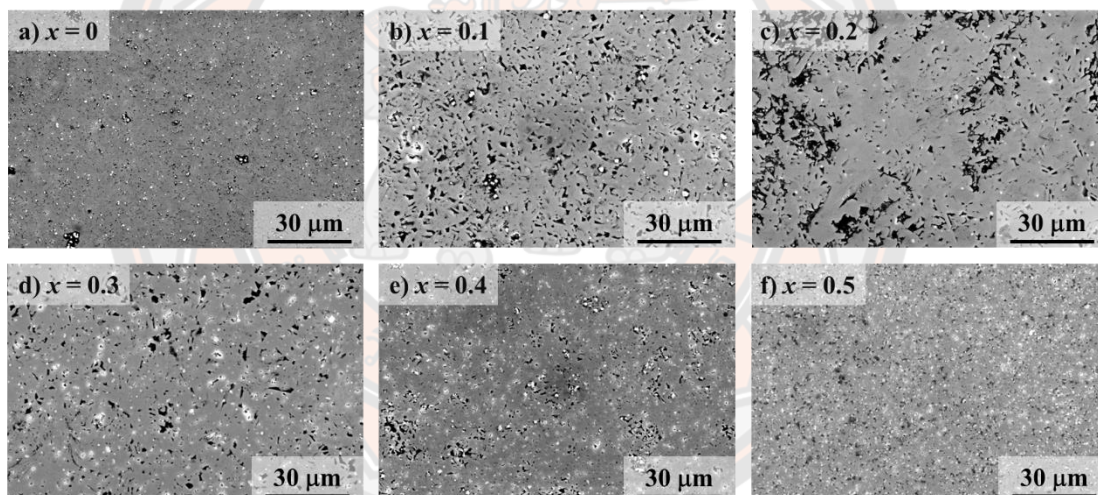


Figure 89 The surface SEM images of the CACO bulk sample with different Ag content.

The SEM of the CACO bulk sample with different Ag-additions is shown in Figure 88 and Figure 89. The fractured cross-section SEM images of the CACO sample show a layer-stacking (Figure 88) characteristic with an irregular shape that results in the CACO bulk sample showing roughly surface. The arrangement of layer stacking in the bulk sample of the CACO sample was observed to be randomly oriented. In the sample with $x = 0.1 - 0.2$, the grain size was increased, after that when with $x = 0.3 - 0.5$ the grain size slightly decreased as shown in Figure 88. These could

be due to the effect of both Ag-doped and Ag-added on the CACO sample. Typically, the pore spaces are usually attached to grain boundaries at the triple points or on the intergranular planes [179]. The large pore spaces resulting from the large grain size as shown in Figure 89, demonstrates the roughly on-surface sample.

Additionally, the relationship between grain size and density is that the grain size increases, and there is more space between grains, resulting in a lower density, as shown in sample $x = 0.1$. Moreover, materials with larger grain sizes, have more grain boundaries (the interfaces between adjacent grains) that can act as sites for deformation and cracking. This can make it easier for the material to deform and result in lower hardness values [180]. As shown in sample $x = 0.1$, the biggest grain size and lowest Vickers hardness value.

The SEM-EDS mapping analysis of the CACO bulk sample without Ag-addition ($x = 0$) showed that the elements of Ca, Co, and O had a uniform and homogeneous distribution on the sample surface (Figure 90(a)). However, with increasing levels of Ag-addition, the chemical distributions of Ca, Co, O, and Ag are no longer uniform. Specifically, the concentration of Ag particles increased and was distributed in the grain boundaries of the sample, as illustrated in Figure 90(b-c) for the CACO sample with $x = 0.1$. This is consistent with previous research that observed Ag particles at the grain boundaries of $\text{Ca}_3\text{Co}_4\text{O}_9$ samples using a solution chemical process [181]. The quantitative EDS analysis presented that the average chemical composition of all samples was in relatively good agreement with the nominal compositions. Moreover, SEM-EDS results agree with the XRD result, discussed previously, which showed a slight decrease of the peak at 37.3° of $\text{Ca}_3\text{Co}_4\text{O}_9$ phase content and an increase of the Ag phase.

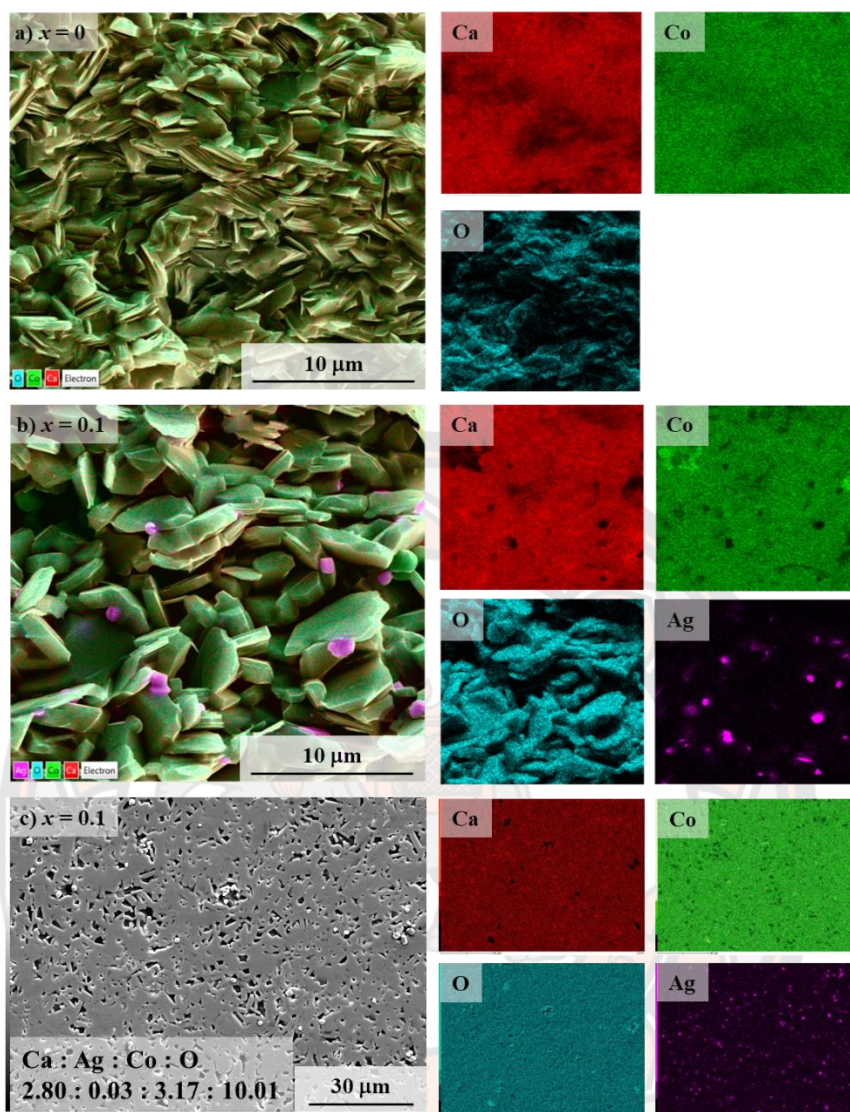


Figure 90 (a-b) Fractured cross-section and (c) surface SEM and EDS mapping analysis of the CACO bulk samples

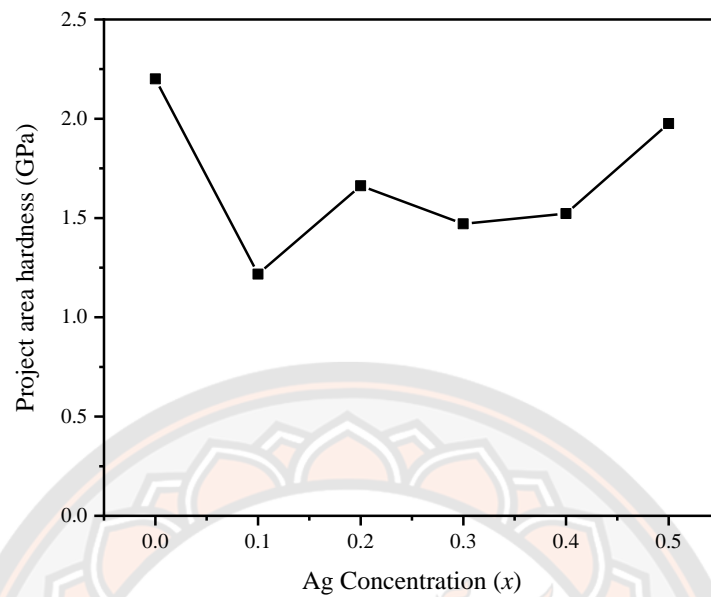


Figure 91 The Vickers hardness result of the CACO sample

The Vickers indentation tests were utilized to ascertain both hardness and fracture toughness. The Vickers hardness result of the CACO sample (Figure 91) ranged from 1.28 - 2.25 GPa. Interestingly, the Vickers hardness of the CACO sample with the Ag-addition as $x = 0.1$ was slightly lower than the sample without the Ag-addition. After that, the Vickers hardness tends to increase with increased Ag-addition. Because of the grain boundary effect, the indentation hardness increases with increasing indentation depth [180]. According to the Hall-Petch relationship, the hardness of polycrystalline ceramics is known to increase with smaller grain sizes [182]. The lowest Vickers hardness of the CACO sample ($x = 0.1$) relates to the biggest grain size that is shown in the SEM image. In materials with larger grain sizes, there are more grain boundaries, and the interfaces between adjacent grains can act as sites for deformation and cracking. This can result in lower hardness values.

Even though the CACO sample ($x = 0.1$) exhibited the lowest Vickers hardness and density due to its larger grain size. However, it is important to note that Vickers hardness is not directly linked to density. Vickers hardness primarily relates to the interaction between grain size and hardness, whereas density is an independent property representing the mass per unit volume of the material.

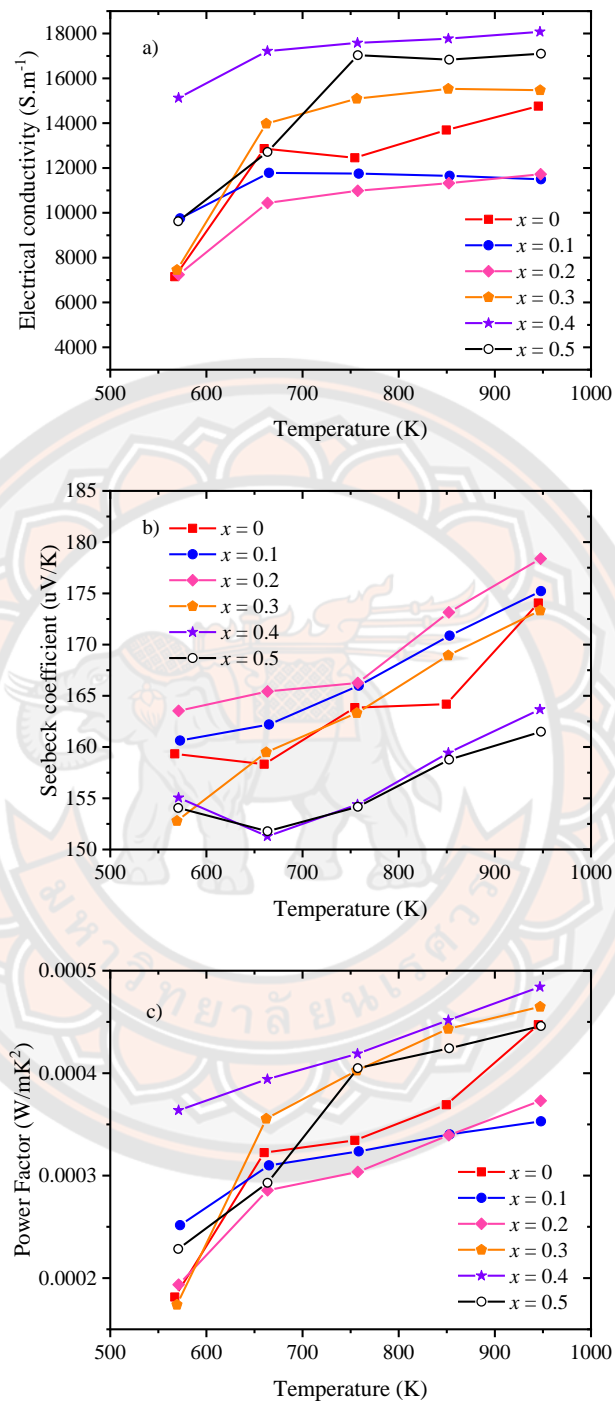


Figure 92 Temperature dependence of the electrical properties of CACO bulk samples: (a) electrical conductivity (σ), (b) Seebeck coefficient (S), and (c) power factor (PF , $S^2\sigma$).

Figure 92(a) shows the temperature dependence of the electrical properties of the CACO sample. The electrical conductivity (σ) of the sample increased with temperature, indicating a semiconductive behavior. The CACO sample indicated fluctuating electrical conductivity. For $x = 0.1$ and 0.2 , lower than without doping, whereas, for $x = 0.3$ and 0.4 , it higher than $x = 0$. The highest conductivity (180 S/cm) was observed at 950 K for $x = 0.4$ and then decreased at $x > 0.4$. This could be due to the effect of the Ag-doped and Ag-added in the CACO sample. As well, the σ increase can be attributed to the presence of Ag filling the spaces between the grains [172].

In comparison with previous research, the σ of the CACO sample with $x = 0$ was found to be higher than those of $\text{Ca}_3\text{Co}_4\text{O}_9$, and the sample was synthesized using a sol-gel method and was subjected to SPS, which resulted in a high σ of 118 S/cm at 973 K. This value was compared to the σ of a sample prepared using conventional sintering (CS), which was found to be 34 S/cm at 973 K [183]. For $x = 0.3$ and $x = 0.4$, the σ increased with Ag-doped. This increase was in agreement with [173] where it was indicated that the σ increased with an increase in Ag-addition.

However, the σ decreased at $x = 0.5$, which was still higher than the σ at the same concentration reported in the previous study. In that study, the σ of the $\text{Ca}_{3-x}\text{Ag}_x\text{Co}_4\text{O}_9$, prepared by the sol-gel method with spontaneous combustion and cold isostatic pressing, was 66.2 S/cm ($x = 0.5$) at 673 K [173].

Ag-addition, formed by the sol-gel auto combustion following SPS, indicates both doped and added forms in the CACO sample. The results obtained from XRD, Rietveld refinement, and EDS mapping also confirmed that Ag particles were present in both doped and added forms in the CACO sample, proving that both Ag doping and Ag-addition affected the σ of the CACO sample. Normally, Ag doping can increase the σ of the CACO by introducing additional charge carriers into the lattice. This results in an increase in the concentration of charge carriers, which can enhance the σ of CACO [175, 176, 184]. However, the σ of the CACO sample with $x = 0.1$ and 0.2 was lower than at $x = 0$. This probably due to the optimization of η and μ , following equation (43) [185]

$$\sigma = \eta e \mu \quad (43)$$

where σ is electrical conductivity, η is carrier concentration, e is electrical charge, and μ is carrier mobility. Based on equation 43, the Ag-doped may produce defects in the crystal structure that reduced the σ , following the reported [186]. Moreover, reducing in σ can be cause by energy levels within the band gap of the material, that can trap charge carriers [187]. However, the Hall measurements must be measured to confirm and discuss the electrical properties further.

Ag-addition can improve the electrical contact between the CACO grains. This is because Ag nanoparticles have high σ and can fill in the gaps between the grains (as shown in EDS mapping), creating a continuous conductive path. This reduces the contact resistance between the grains, which can increase the σ of the material [176]. The Ag nanoparticles, by filling in the gaps between the grains, act as scattering centers for electrons moving through the Ag particles, thereby improving σ by enhancing the transportation of the electrons [184].

The Seebeck coefficient (S) of all the CACO samples was found to be positive, which is a characteristic of p-type oxide thermoelectric (TE) materials. This was confirmed by the data shown in Figure 92(b). The addition of Ag increased the Seebeck coefficient of the CACO samples, with the highest value of 178 $\mu\text{V/K}$ observed at $x = 0.2$. However, the Seebeck coefficient began to decrease when the Ag concentration reached $x > 0.2$. This behavior is similar to the behavior that occurs in $\text{Ca}_{3-x}\text{Ag}_x\text{Co}_4\text{O}_9$ ceramics that were synthesized by the sol-gel method combined with spontaneous combustion and cold isostatic pressing, which also showed S decreasing at the same level of Ag doping [173].

Normally, the S of the material can be enhanced by increasing the Ag doping level [173]. However, it is essential to note that beyond a certain substitution limit, excessive Ag can have a detrimental effect and reduces the S [172, 175]. For Ag levels greater than 0.2, there is a strong correlation with the electrons. This is likely the reason behind this phenomenon, which cannot be explained by traditional theory [173]. The mobility of the carrier should be a significant factor in the alteration of the Seebeck coefficient in this material system, which can be mathematically represented by equation (44) [175, 188]

$$S(T) = \frac{C_e}{n} + \frac{\pi^2 k_B^2 T}{3e} \left[\frac{\partial \ln \mu(\varepsilon)}{\partial \varepsilon} \right]_{\varepsilon=E_F} \quad (44)$$

where n is the carrier concentration, $\mu(\varepsilon)$ is the carrier mobility, C_e is the heat capacity, and k_B is the Boltzmann coefficient.

In the case of the Ag-doped, the S is influenced by both the carrier concentration and carrier mobility. When the Ca^{2+} is replaced by the Ag^+ , the carrier concentration may increase, and the mobility of the carrier may change as well. Despite the inverse relationship between the carrier concentration and the first part of Eq.44, the experimental results indicate that the S increased as the Ag doping level increased. Thus, it can be inferred that the alteration in the carrier mobility is the primary factor behind the increase in the Seebeck coefficient with the Ag content ($x \leq 0.2$), rather than the carrier concentration. Therefore, to further discuss the electrical properties, the Hall measurements must be carried out.

In the case of the Ag-added, the extra Ag^+ cannot completely replace Ca^{2+} but exists in the form of an Ag substance that results in decreased S due to the inclusion of the charge carriers of the Ag and the CACO sample. The S can be expressed by equation (45) [173, 175].

$$S = \sum_i \left(\frac{\sigma_i}{\sigma} \right) S_i \quad (45)$$

where σ_i is the partial electrical conductivity and S_i is the partial thermoelectric power. The S of the Ag and the CACO sample can be expressed by equation (46)

$$S = \frac{\sigma_{\text{Ca}_3\text{Co}_4\text{O}_9}}{\sigma_{\text{Ca}_3\text{Co}_4\text{O}_9} + \sigma_{\text{Ag}}} S_{\text{Ca}_3\text{Co}_4\text{O}_9} + \frac{\sigma_{\text{Ag}}}{\sigma_{\text{Ca}_3\text{Co}_4\text{O}_9} + \sigma_{\text{Ag}}} S_{\text{Ag}} \quad (46)$$

When the conduction mechanism of the Ag-addition is via electrons, S is low [173, 181]. This leads to a noticeable reduction in the S of the CACO sample, with a significant decrease observed as Ag doping levels are greater than 0.2.

The Seebeck coefficient of the CACO sample can be influenced by both Ag doping and Ag-addition. Ag doping leads to increased concentrations of charge carriers and σ which can change the electronic structure of CACO [67], which can affect the Seebeck coefficient. Ag-addition can improve the electrical contact between the material grains, reducing the contact resistance and increasing the σ .

Additionally, in case of doping, the Ag nanoparticles can act as scattering centers for electrons, enhancing electron transport and increasing σ , leading to an increase in the S [176]. However, agglomerated Ag particles can bypass the carrier mechanisms and neutralize the thermoelectric voltage generated by CACO gains, leading to a reduction in the S value [181]. This decrease in S is caused by an increase in carrier concentration.

The power factor ($S^2\sigma$) was calculated and plotted as a function of temperature, using the σ and S values, as presented in Figure 92(c). The $S^2\sigma$ of all the samples gradually increased with increasing temperature. The $S^2\sigma$ reached a maximum value of $484 \mu\text{W/mK}^2$ at 950 K for $x = 0.4$. Over the temperature range 450 K to 950 K, the $S^2\sigma$ values decreased with $x = 0.1 - 0.2$, then increased with $x = 0.3 - 0.4$, but decreased when $x = 0.5$. The improved power factor was due to enhanced electrical conductivity [168]. This phenomenon also agrees with the previous study [169]. The $S^2\sigma$ of our result is higher than previous research where, for example, Ag-addition $\text{Ca}_3\text{Co}_4\text{O}_9$ was prepared by the sol-gel route via nitrates, following the two-step sintering process [172]. This demonstrates that Ag^+ doping, as well as Ag-addition, can raise the power factor [176].

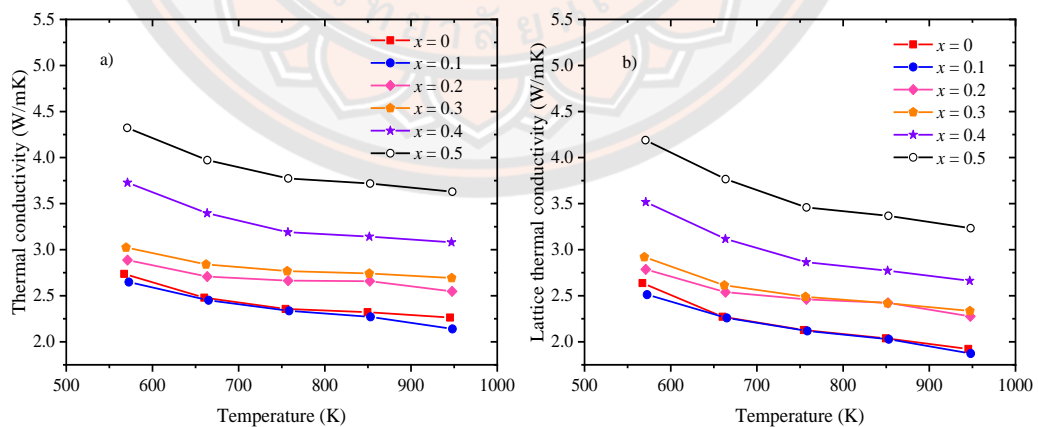


Figure 93 Temperature dependence of (a) thermal conductivity (κ) and (b) lattice thermal conductivity (κ_{lat}) of the CACO bulk samples.

The relationship between thermal conductivity (κ) and lattice thermal conductivity (κ_{lat}), following the equation $\kappa_{lat} = \kappa - \kappa_{el}$. The κ_{lat} value was computed by subtracting the electronic thermal conductivity (κ_{el}) from κ . To determine the κ_{el} , the equation $\kappa_{el} = L\sigma T$ was used, where L is the Lorentz number ($L = 2.45 \times 10^{-8} \text{ W}\Omega\text{K}^{-2}$), σ represents electrical conductivity, and T represents temperature. The temperature dependence of κ and κ_{lat} of the CACO bulk samples are illustrated in Figure 93. With an increase in temperature, the κ of all the samples decreased, indicating that the κ of CACO sample is dominated by κ_{lat} . As illustrated in Figure 93(b), The κ_{lat} also decreases with an increase in temperature, following a T^{-1} relationship.

The κ value of the CACO sample with $x = 0$ was 2.26 W/mK at 950K was both lower and higher than previous reports with different preparation methods. For example, values of 1.3 W/mK at 773 K (Sol-gel following SPS) were reported by [189], 2.1 W/mK at 773 K (Sol-gel following SPS) [20], 2.4 W/mK at 933 K (CIP) [190], 2.5 W/mK at 933 K (SPS) [190], and 2.9 W/mK at 973 K [191]. The κ value of the CACO sample was increased when Ag-addition increased. The lowest κ was 2.13 W/mK at 950 K for $x = 0.1$, which is close to $x = 0$. At $x > 0.1$, the result indicated an unexpectedly high κ with increased Ag content. The highest value of κ was 3.62 W/mK at 950 K for $x = 0.5$.

The reduction in κ was primarily due to a decrease in κ_{lat} , which dominates the κ value in the sample CACO ceramics. The significant observation is that the increase in temperature causes phonons to come across imperfections such as defects, collisions, grain boundaries, or impurities, which ultimately reduce the phonon mean free path [192]. The κ of a material can be influenced by its microstructure and crystal defects, which may vary based on the synthesising method used. Additionally, the microstructure and crystal defects can also be affected by factors such as temperature, time, pressure, and environmental conditions during the synthesis process, which can have a subsequent impact on the κ of material [193].

To improve the thermoelectric property, the κ should be low. Normally, element doping on $\text{Ca}_3\text{Co}_4\text{O}_9$ results in a decrease in κ [194], such as Ba and Pr dual-doping $\text{Ca}_3\text{Co}_4\text{O}_9$ prepared by sol-gel following SPS, that reduced κ from 2.2 to 1.5

W/mK at 973 K [20]. The value of κ decreased with increasing Ag doping. For example, with $\text{Ca}_{3-x}\text{Ag}_x\text{Co}_4\text{O}_{9+\delta}$ synthesized by the sol–gel method followed by SPS, κ reduced from 2.2 to 2.05 W/mK at 973K [169]. However, our resultant κ value of the CACO sample is not congruent with other reports. This difference can be explained by the Ag excess at the grain boundary, due to increased Ag-addition, causing the increase in the κ value, as shown in Figure 90. The rise in thermal conductivity signifies that the presence of Ag among cobaltite grains serves a dual purpose: it diminishes carrier scattering while also making a substantial contribution to phonon conductivity [176].

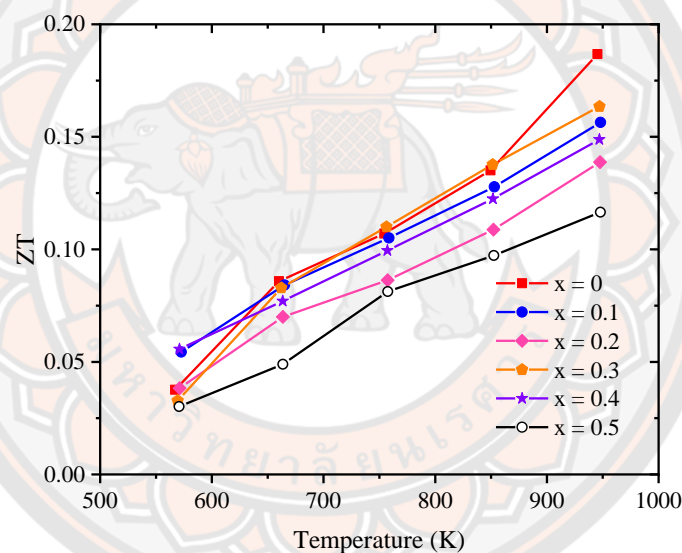


Figure 94 Temperature dependence of dimensionless figure-of-merit ZT of the bulk CACO sample with different La concentrations.

Figure 94 illustrates the temperature dependence of the figures of merit (ZT) for the CACO bulk samples with Ag-addition. In the whole measurement temperature range, the ZT value of the CACO samples increased with increasing temperature and reached a maximum of 0.18 at 950 K for $x = 0$. This value of ZT is higher than the $\text{Ca}_3\text{Co}_4\text{O}_9$ (0.05 at 650K) prepared by the sol–gel method combined with spontaneous combustion and cold isostatic pressing [173].

The result of increasing the Ag-addition was unexpectedly low ZT with increased Ag content, was 0.15 for $x = 0.1$, 0.13 for $x = 0.2$, 0.16 for $x = 0.3$, 0.14 for $x = 0.4$, and 0.11 for $x = 0.5$ at 950 K. The ZT of the CACO sample with Ag lower than the CACO sample without Ag. The ZT of CACO sample was decreased when the $x = 0.1 - 0.2$, followed by an increase at $x = 0.3$ and another decrease at $x = 0.4 - 0.05$, due to changes in power factor linked to the σ . Despite a higher power factor at $x = 0.4$ compared to $x = 0.3$, the ZT did not increase because the $x = 0.4$ sample had lower σ and higher κ . Also, the Ag level increased, the ZT value of the CACO sample decreased, due to the limit of doping. Some of the Ag particles can be substituted at the Ca site, while others are distributed in the gap between the grains. This is the effect of Ag-doped and Ag-added on the CACO sample which led to fluctuations in the electrical conductivity and increased thermal conductivity.

The ZT value of the CACO with increased Ag level decreased. These effects resulted in a maximum ZT of 0.18 at 950 K for $x = 0$. Table 8 illustrates the thermoelectric properties of doped/addition $\text{Ca}_3\text{Co}_4\text{O}_9$ with different preparation methods. When compared to our results with that previous research, it was found that the thermoelectric properties of undoped CACO using sol-gel auto combustion can competition of previous research.

Table 8 The summary of the thermoelectric properties of dope/addition $\text{Ca}_3\text{Co}_4\text{O}_9$ with different preparation methods.

Materials	Preparation method	σ (S/m)	S ($\mu\text{V/K}$)	PF ($\mu\text{W/mK}^2$)	K (W/mk)	ZT	Temperature (K)	Ref
$\text{Ca}_3\text{Co}_4\text{O}_9$	Homogeneous precipitation and pressure sintering technique	120	185	409			900	[168]
$\text{Ca}_3\text{Co}_4\text{O}_9$	Sol-gel following SPS	9,866	161		1.22	0.16	1073	[189]
$\text{Ca}_{2.9}\text{Ag}_{0.1}\text{Co}_4\text{O}_9$	Sol-gel following SPS		160		2.50	0.18	973	[67]
$\text{Ca}_{2.8}\text{Ag}_{0.2}\text{Co}_4\text{O}_9$	Sol-gel combined with spontaneous combustion and cold isostatic pressing	64	172.7		0.76	0.17	673	[173]
$\text{Ca}_{2.88}\text{Ag}_{0.15}\text{Co}_4\text{O}_9$	Pulsed laser deposition		171	730			705	[175]
$\text{Ca}_{2.97}\text{Ag}_{0.03}\text{Co}_4\text{O}_9 + \delta$	Sol-gel following SPS		200	458	2.07	0.23	973	[169]
$\text{Ca}_{2.98}\text{Tb}_{0.01}\text{Ag}_{0.01}\text{Co}_4\text{O}_9$	Sol-gel following SPS		176	330	1.62	0.22	1073	[186]
$(\text{Ca}_{0.87}\text{Ag}_{0.1}\text{La}_{0.03})_3\text{Co}_4\text{O}_9$	Solid-state reaction and cold uniaxially pressed		182.3	190	1.13	0.18	1073	[187]
$\text{Ca}_3\text{Co}_4\text{O}_9 + 10\text{ wt. \% Ag}$	Sol-gel nitrates route and two-step sintering		220	430			1073	[172]
$\text{Ca}_{2.7}\text{Ag}_{0.3}\text{Co}_4\text{O}_9/10\text{ wt. \% Ag}$	a cold-pressing and traditional sintered		194.8	883	2.52	0.5	1000	[176]
$\text{Ca}_{2.9}\text{Cd}_{0.1}\text{Co}_4\text{O}_{9+\delta} + 10\text{ wt. \% Ag}$	Solid-state reaction and hot-pressing	245	190	880	2.75	0.31	950	[184]
$\text{CACO}, x = 0$	Sol-gel auto combustion following SPS	14,760	174	447	2.26	0.18	950	This study

CHAPTER V

CONCLUSION AND RECOMMENDATION

5.1 Conclusion

In the study, various materials were successfully synthesized using the sol-gel auto combustion technique and their properties were evaluated.

First, SLTO nanopowders with different La content showed good photocatalytic activity in decolorizing methylene blue under UV irradiation. XRD analysis revealed a pure phase cubic perovskite with decreased crystallite sizes as La content increased, while SEM-EDS images showed a decrease in particle sizes and good element distribution. The band gap slightly increased with increasing La content, causing oxygen vacancy. The optimal La content for photocatalytic activity was $x = 0.07$. The sol-gel auto combustion technique resulted in comparable phase, size, and photocatalytic properties to conventional methods.

Similarly, high-density SLTO bulk ceramics were synthesized using the sol-gel auto-combustion method, followed by the SPS process. The electrical conductivity and negative Seebeck coefficient increased with temperature, indicating n-type semiconductor behavior, while thermal conductivity primarily came from lattice thermal conductivity. ZT values increased with increasing temperature, with the highest value observed in SLTO with $x = 0.01$ at 800 K. However, the ZT values were lower than reported in previous studies due to lower electrical conductivity, possibly due to preparation and processing conditions.

Additionally, STNO nanopowder with varying Nb content showed improved photocatalytic efficiency by decreasing electron-hole pair recombination and charge transfer resistance. STNO nanopowder with $x = 0.05$ showed optimal photocatalytic activity for decolorization of MB under UV irradiation. Overall, the structural, optical, and electrochemical properties of STNO nanopowder synthesized by the sol-gel auto-combustion technique enhanced photocatalytic activity.

Finally, the synthesis of high-density CACO bulk material using sol-gel auto combustion, followed by SPS technique, showed the presence of Ag metallic and non-

uniform distribution at grain boundaries when Ag was added. The p-type oxide TE materials showed a maximum ZT value of 0.18 at 950 K for $x = 0$, which is higher than for other $\text{Ca}_3\text{Co}_4\text{O}_9$ materials due to the improved process used in this study. However, the thermal conductivity increased with Ag content, resulting in a decrease in the ZT value.



REFERENCES

1. Aswal DK, Basu R, Singh A. Key issues in development of thermoelectric power generators: High figure-of-merit materials and their highly conducting interfaces with metallic interconnects. *Energy Conversion and Management*. 2016;114:50-67.
2. Zevenhoven R, Beyene A. The relative contribution of waste heat from power plants to global warming. *Energy*. 2011;36(6):3754-62.
3. Gayner C, Kar KK. Recent advances in thermoelectric materials. *Progress in Materials Science*. 2016;83:330-82.
4. Srivastava D, Norman C, Azough F, Schafer MC, Guilmeau E, Freer R. Improving the thermoelectric properties of SrTiO₃-based ceramics with metallic inclusions. *Journal of Alloys and Compounds*. 2018;731:723-30.
5. Demirel S, Altin E, Oz E, Altin S, Bayri A. An enhancement ZT and spin state transition of Ca₃Co₄O₉ with Pb doping. *Journal of Alloys and Compounds*. 2015;627:430-7.
6. He J, Liu Y, Funahashi R. Oxide thermoelectrics: The challenges, progress, and outlook. *Journal of Materials Research*. 2011;26(15):1762-72.
7. Ohta H, Sugiura K, Koumoto K. Recent Progress in Oxide Thermoelectric Materials: p-Type Ca₃Co₄O₉ and n-Type SrTiO₃⁻. *Inorganic Chemistry*. 2008;47(19):8429-36.
8. Sun R, Li D, Li L, Zhang J, Wang Q, Qin X. Preparation and thermoelectric properties of rare-earth-metal-doped SrO(SrTiO₃)_n oxides. *Procedia Engineering*. 2012;27:103-8.
9. Koumoto K, Wang Y, Zhang R, Kosuga A, Funahashi R. Oxide Thermoelectric Materials: A Nanostructuring Approach. *Annual Review of Materials Research*. 2010;40(1):363-94.
10. Jiamprasertboon A, Okamoto Y, Hiroi Z, Siritanon T. Thermoelectric properties of Sr and Mg double-substituted LaCoO₃ at room temperature. *Ceramics International*. 2014;40(8, Part B):12729-35.
11. Yin Y, Tudu B, Tiwari A. Recent advances in oxide thermoelectric materials and modules. *Vacuum*. 2017;146:356-74.
12. Fergus JW. Oxide materials for high temperature thermoelectric energy conversion. *Journal of the European Ceramic Society*. 2012;32(3):525-40.
13. Sun J, Singh DJ. Thermoelectric properties of n-type SrTiO₃. *APL Materials*. 2016;4(10):104803.
14. Zou D, Liu Y, Xie S, Lin J, Li J. Effect of strain on thermoelectric properties of SrTiO₃: First-principles calculations. *Chemical Physics Letters*. 2013;586:159-63.
15. Ohta H, Kim S, Mune Y, Mizoguchi T, Nomura K, Ohta S, et al. Giant thermoelectric Seebeck coefficient of a two-dimensional electron gas in SrTiO₃. *Nature Materials*. 2007;6(2):129-34.
16. Jeric M, de Boor J, Jancar B, Ceh M. An enhanced thermoelectric figure of merit for Sr(Ti_{0.8}Nb_{0.2})O₃ based on a Ruddlesden–Popper-polytype-induced microstructure. *Journal of the European Ceramic Society*. 2016;36(5):1177-82.
17. Koumoto K, Funahashi R, Guilmeau E, Miyazaki Y, Weidenkaff A, Wang Y, et al. Thermoelectric Ceramics for Energy Harvesting. 2012;96 (1):1-23.

18. Schulz T, Topfer J. Thermoelectric properties of $\text{Ca}_3\text{Co}_4\text{O}_9$ ceramics prepared by an alternative pressure-less sintering/annealing method. *Journal of Alloys and Compounds*. 2016;659:122-6.
19. Demirel S, Altin S, Aksan MA. Low Temperature Magnetic Behavior of $\text{Ca}_3\text{Co}_4\text{O}_x$ Polycrystalline Material. *Journal of Superconductivity and Novel Magnetism*. 2013;26(5):1617-20.
20. Huang CS, Zhang FP, Zhang X, Lu QM, Zhang JX, Liu ZY. Enhanced thermoelectric figure of merit through electrical and thermal transport modulation by dual-doping and texture modulating for $\text{Ca}_3\text{Co}_4\text{O}_{9+\delta}$ oxide materials. *Journal of Alloys and Compounds*. 2016;687:87-94.
21. Walia S, Balendhran S, Nili H, Zhuiykov S, Rosengarten G, Wang QH, et al. Transition metal oxides – Thermoelectric properties. *Progress in Materials Science*. 2013;58(8):1443-89.
22. Mohanraman R, Lan T-W, Hsiung T-C, Amada D, Lee P-C, Ou M-N, et al. Engineering Nanostructural Routes for Enhancing Thermoelectric Performance: Bulk to Nanoscale. *Frontiers in chemistry*. 2015;3:63-.
23. Feng B, Li G, Pan Z, Hou Y, Zhang C, Jiang C, et al. Effect of Ba and Pb dual doping on the thermoelectric properties of BiCuSeO ceramics. *Materials Letters*. 2018;217:189-93.
24. Li J, Sui J, Pei Y, Barreteau C, Berardan D, Dragoe N, et al. A high thermoelectric figure of merit $ZT > 1$ in Ba heavily doped BiCuSeO oxyselenides. *Energy and Environmental Science*. 2012;5(9):8543-7.
25. Wang N, Han L, He H, Ba Y, Koumoto K. Effects of mesoporous silica addition on thermoelectric properties of Nb-doped SrTiO_3 . *Journal of Alloys and Compounds*. 2010;497(1):308-11.
26. Ohta S, Nomura T, Ohta H, Hirano M, Hosono H, Koumoto K. Large thermoelectric performance of heavily Nb-doped SrTiO_3 epitaxial film at high temperature. *Applied Physics Letters*. 2005;87(9):092108.
27. Ohta S, Ohta H, Koumoto K. Grain Size Dependence of Thermoelectric Performance of Nb-Doped SrTiO_3 Polycrystals. *Journal of the Ceramic Society of Japan*. 2006;114(1325):102-5.
28. Ohta S, Nomura T, Ohta H, Koumoto K. High-temperature carrier transport and thermoelectric properties of heavily La- or Nb-doped SrTiO_3 single crystals. *Journal of Applied Physics*. 2005;97(3):034106.
29. Liu G, Chen K, Li J, Li Y, Zhou M, Li L. Combustion synthesis of Cu_2SnSe_3 thermoelectric materials. *Journal of the European Ceramic Society*. 2016;36(6):1407-15.
30. Niu G, Saint-Girons G, Vilquin B. Chapter 18 - Epitaxial systems combining oxides and semiconductors A2 - Henini, Mohamed. *Molecular Beam Epitaxy*. Oxford: Elsevier; 2013. p. 451-75.
31. Specchia S, Galletti C, Specchia V. Solution Combustion Synthesis as intriguing technique to quickly produce performing catalysts for specific applications. In: Gaigneaux EM, Devillers M, Hermans S, Jacobs PA, Martens JA, Ruiz P, editors. *Studies in Surface Science and Catalysis*. 175: Elsevier; 2010. p. 59-67.
32. Xanthopoulou G, Vekinis G. An overview of some environmental applications of self-propagating high-temperature synthesis. *Advances in Environmental Research*. 2001;5(2):117-28.

33. Marques AC. Sol-gel process: an overview. USA2007 [cited 2018 20 May]. Available from: https://www.lehigh.edu/imi/teched/LecBasic/Marques_Sol_gel.pdf.
34. Poth J, Haberkorn R, Beck HP. Combustion-synthesis of SrTiO_3 Part I. synthesis and properties of the ignition products. *Journal of the European Ceramic Society*. 2000;20(6):707-13.
35. Aruna ST, Mukasyan AS. Combustion synthesis and nanomaterials. *Current Opinion in Solid State and Materials Science*. 2008;12(3):44-50.
36. Hamid Elsheikh M, Shnawah DA, Sabri MFM, Said SBM, Haji Hassan M, Ali Bashir MB, et al. A review on thermoelectric renewable energy: Principle parameters that affect their performance. *Renewable and Sustainable Energy Reviews*. 2014;30:337-55.
37. Ohtaki M. Oxide Thermoelectric Materials for Heat-to-Electricity Direct Energy Conversion. 九州大学グローバルCOEプログラム新炭素資源学ニューズレター. 2010;3:10-5.
38. Li J-F, Liu W-S, Zhao L-D, Zhou M. High-performance nanostructured thermoelectric materials. *Npg Asia Materials*. 2010;2:152-8.
39. Liu W, Yan X, Chen G, Ren Z. Recent advances in thermoelectric nanocomposites. *Nano Energy*. 2012;1(1):42-56.
40. Chen Z-G, Han G, Yang L, Cheng L, Zou J. Nanostructured thermoelectric materials: Current research and future challenge. *Progress in Natural Science: Materials International*. 2012;22(6):535-49.
41. Alam H, Ramakrishna S. A review on the enhancement of figure of merit from bulk to nano-thermoelectric materials. *Nano Energy*. 2013;2(2):190-212.
42. Fitriani, Ovik R, Long BD, Barma MC, Riaz M, Sabri MFM, et al. A review on nanostructures of high-temperature thermoelectric materials for waste heat recovery. *Renewable and Sustainable Energy Reviews*. 2016;64:635-59.
43. Wang H, Su W, Liu J, Wang C. Recent development of n-type perovskite thermoelectrics. *Journal of Materiomics*. 2016;2(3):225-36.
44. Li Z, Xiao C, Zhu H, Xie Y. Defect Chemistry for Thermoelectric Materials. *Journal of the American Chemical Society*. 2016;138(45):14810-9.
45. He J, Tritt TM. Advances in thermoelectric materials research: Looking back and moving forward. *Science*. 2017;357(6358).
46. Blennow P, Hansen KK, Wallenberg LR, Mogensen M. Synthesis of Nb-doped SrTiO_3 by a modified glycine-nitrate process. *Journal of the European Ceramic Society*. 2007;27(13):3609-12.
47. Liu S, Xiu Z, Liu Ja, Xu F, Yu W, Yu J, et al. Combustion synthesis and characterization of perovskite SrTiO_3 nanopowders. *Journal of Alloys and Compounds*. 2008;457(1):L12-L4.
48. Kikuchi A, Okinaka N, Akiyama T. A large thermoelectric figure of merit of La-doped SrTiO_3 prepared by combustion synthesis with post-spark plasma sintering. *Scripta Materialia*. 2010;63(4):407-10.
49. Shang P-P, Zhang B-P, Li J-F, Ma N. Effect of sintering temperature on thermoelectric properties of La-doped SrTiO_3 ceramics prepared by sol-gel process and spark plasma sintering. *Solid State Sciences*. 2010;12(8):1341-6.
50. Wang HC, Wang CL, Su WB, Liu J, Zhao Y, Peng H, et al. Enhancement of thermoelectric figure of merit by doping Dy in $\text{La}_{0.1}\text{Sr}_{0.9}\text{TiO}_3$ ceramic. *Materials*

- Research Bulletin. 2010;45(7):809-12.
51. Wang HC, Wang CL, Su WB, Liu J, Peng H, Sun Y, et al. Synthesis and thermoelectric performance of Ta doped $\text{Sr}_{0.9}\text{La}_{0.1}\text{TiO}_3$ ceramics. *Ceramics International*. 2011;37(7):2609-13.
 52. Wang H, Wang C. Thermoelectric properties of Yb-doped $\text{La}_{0.1}\text{Sr}_{0.9}\text{TiO}_3$ ceramics at high temperature. *Ceramics International*. 2013;39(2):941-6.
 53. Wang Y, Zhang X, Shen L, Bao N, Wan C, Park N-H, et al. Nb-doped grain boundary induced thermoelectric power factor enhancement in La-doped SrTiO_3 nanoceramics. *Journal of Power Sources*. 2013;241:255-8.
 54. Hanbo LI, Ganhong Z, Zhenxiang DAI, Zhenheng Y, Haiqiu W, Yongqing MA. Thermoelectric properties of $\text{Sr}_{0.9}\text{La}_{0.1}\text{TiO}_3$ and $\text{Sr}_{2.7}\text{La}_{0.3}\text{Ti}_2\text{O}_7$ with 15% Ag addition. *Journal of Rare Earths*. 2014;32(4):314-9.
 55. Buscaglia MT, Maglia F, Anselmi-Tamburini U, Marre D, Pallecchi I, Ianculescu A, et al. Effect of nanostructure on the thermal conductivity of La-doped SrTiO_3 ceramics. *Journal of the European Ceramic Society*. 2014;34(2):307-16.
 56. Li L, Liu Y, Qin X, Li D, Zhang J, Song C, et al. Enhanced thermoelectric performance of highly dense and fine-grained $(\text{Sr}_{1-x}\text{Gd}_x)\text{TiO}_{3-\delta}$ ceramics synthesized by sol-gel process and spark plasma sintering. *Journal of Alloys and Compounds*. 2014;588:562-7.
 57. Wang J, Ye X, Yaer X, Zhang B, Ma W, Miao L. High thermoelectric performance of niobium-doped strontium titanate bulk material affected by all-scale grain boundary and inclusions. *Scripta Materialia*. 2015;99:25-8.
 58. Chen C, Zhang T, Donelson R, Tan TT, Li S. Effects of yttrium substitution and oxygen deficiency on the crystal phase, microstructure, and thermoelectric properties of $\text{Sr}_{1-1.5x}\text{Y}_x\text{TiO}_{3-\delta}$ ($0 \leq x \leq 0.15$). *Journal of Alloys and Compounds*. 2015;629:49-54.
 59. Saito G, Nakasugi Y, Sakaguchi N, Zhu C, Akiyama T. Glycine-nitrate-based solution-combustion synthesis of SrTiO_3 . *Journal of Alloys and Compounds*. 2015;652:496-502.
 60. Qin M, Gao F, Wang M, Zhang C, Zhang Q, Wang L. Fabrication and high-temperature thermoelectric properties of Ti-doped $\text{Sr}_{0.9}\text{La}_{0.1}\text{TiO}_3$ ceramics. *Ceramics International*. 2016;42(15):16644-9.
 61. Iyasara AC, Schmidt WL, Boston R, Sinclair DC, Reaney IM. La and Sm Co-doped $\text{SrTiO}_{3-\delta}$ Thermoelectric Ceramics. *Materials Today: Proceedings*. 2017;4(12):12360-7.
 62. Han J, Sun Q, Song Y. Enhanced thermoelectric properties of La and Dy co-doped, Sr-deficient SrTiO_3 ceramics. *Journal of Alloys and Compounds*. 2017;705:22-7.
 63. Han J, Sun Q, Li W, Song Y. Microstructure and thermoelectric properties of $\text{La}_{0.1}\text{Dy}_{0.1}\text{Sr}_x\text{TiO}_3$ ceramics. *Ceramics International*. 2017;43(7):5557-63.
 64. Roy P, Pal V, Maiti T. Effect of Spark Plasma Sintering (SPS) on the thermoelectric properties of SrTiO_3 :15at% Nb. *Ceramics International*. 2017;43(15):12809-13.
 65. Liu D, Zhang Y, Kang H, Li J, Chen Z, Wang T. Direct preparation of La-doped SrTiO_3 thermoelectric materials by mechanical alloying with carbon burial sintering. *Journal of the European Ceramic Society*. 2018;38(2):807-11.
 66. Park C-S, Hong M-H, Cho HH, Park H-H. Enhancement of Seebeck coefficient of mesoporous SrTiO_3 with V-group elements V, Nb, and Ta substituted for Ti. *Journal of the European Ceramic Society*. 2018;38(1):125-30.

67. Zhang F, Lu Q, Li T, Zhang X, Zhang J, Song X. Preparation and thermoelectric transport properties of Ba-, La- and Ag-doped $\text{Ca}_3\text{Co}_4\text{O}_9$ oxide materials. *Journal of Rare Earths*. 2013;31(8):778-83.
68. Diez JC, Torres MA, Rasekh S, Constantinescu G, Madre MA, Sotelo A. Enhancement of $\text{Ca}_3\text{Co}_4\text{O}_9$ thermoelectric properties by Cr for Co substitution. *Ceramics International*. 2013;39(6):6051-6.
69. Constantinescu G, Madre MA, Rasekh S, Torres MA, Diez JC, Sotelo A. Effect of Ga addition on Ca-deficient $\text{Ca}_3\text{Co}_4\text{O}_y$ thermoelectric materials. *Ceramics International*. 2014;40(4):6255-60.
70. Wu N, Holgate TC, Van Nong N, Pryds N, Linderroth S. High temperature thermoelectric properties of $\text{Ca}_3\text{Co}_4\text{O}_{9+\delta}$ by auto-combustion synthesis and spark plasma sintering. *Journal of the European Ceramic Society*. 2014;34(4):925-31.
71. Demirel S, Avci S, Altin E, Altin S, Yakinci ME. Enhanced thermoelectric properties induced by chemical pressure in $\text{Ca}_3\text{Co}_4\text{O}_9$. *Ceramics International*. 2014;40(4):5217-22.
72. Zhang D, Mi X, Wang Z, Tang G, Wu Q. Suppression of the spin entropy in layered cobalt oxide $\text{Ca}_3\text{Co}_4\text{O}_{9+\delta}$ by Cu doping. *Ceramics International*. 2014;40(8, Part A):12313-8.
73. Agilandewari K, Ruban Kumar A. Synthesis, characterization, temperature dependent electrical and magnetic properties of $\text{Ca}_3\text{Co}_4\text{O}_9$ by a starch assisted sol-gel combustion method. *Journal of Magnetism and Magnetic Materials*. 2014;364:117-24.
74. Delorme F, Diaz-Chao P, Guilmeau E, Giovannelli F. Thermoelectric properties of $\text{Ca}_3\text{Co}_4\text{O}_9\text{-Co}_3\text{O}_4$ composites. *Ceramics International*. 2015;41(8):10038-43.
75. Porokhin S, Shvanskaya L, Khovaylo V, Vasiliev A. Effect of NaF doping on the thermoelectric properties of $\text{Ca}_3\text{Co}_4\text{O}_9$. *Journal of Alloys and Compounds*. 2017;695:2844-9.
76. Bittner M, Helmich L, Nietschke F, Geppert B, Oeckler O, Feldhoff A. Porous $\text{Ca}_3\text{Co}_4\text{O}_9$ with enhanced thermoelectric properties derived from Sol-Gel synthesis. *Journal of the European Ceramic Society*. 2017;37(13):3909-15.
77. Jiaolian Luo, Weifu Cen, Wenjing Zhang, Ping Zou, Peng Tang, Cheng Cen, et al. The sol-gel method synthetics and the thermoelectric properties analyze of $\text{Ca}_3\text{Co}_4\text{O}_9$. *AIP Conference Proceedings*. 2017;1794(1):020012.
78. Xuewen W, Zhiyong Z, Shuixian Z. Preparation of nano-crystalline SrTiO_3 powder in sol-gel process. *Materials Science and Engineering: B*. 2001;86(1):29-33.
79. Klaytae T, Panthong P, Thoutom S. Preparation of nanocrystalline SrTiO_3 powder by sol-gel combustion method. *Ceramics International*. 2013;39:S405-S8.
80. Meng YY, He MH, Zeng Q, Jiao DL, Shukla S, Ramanujan RV, et al. Synthesis of barium ferrite ultrafine powders by a sol-gel combustion method using glycine gels. *Journal of Alloys and Compounds*. 2014;583:220-5.
81. Thongchanthep C, Thoutom S. The synthesis of $\text{Ba}_{0.7}\text{Sr}_{0.3}\text{TiO}_3$ ceramics prepared by sol-gel combustion method with urea as fuel. *Ceramics International*. 2015;41:S95-S9.
82. Alamolhoda S, Mirkazemi SM, Shahjooyi T, Benvidi N. Effect of Cetyl trimethylammonium bromide (CTAB) amount on phase constituents and magnetic properties of nano-sized NiFe_2O_4 powders synthesized by sol-gel auto-combustion method. *Journal of Alloys and Compounds*. 2015;638:121-6.

83. Jaimeewong P, Promsawat M, Jiansirisomboon S, Watcharapasorn A. Influence of pH values on the surface and properties of BCZT nanopowders synthesized via sol-gel auto-combustion method. *Surface and Coatings Technology*. 2016;306:16-20.
84. Birajdar SD, Bhagwat VR, Shinde AB, Jadhav KM. Effect of Co^{2+} ions on structural, morphological and optical properties of ZnO nanoparticles synthesized by sol-gel auto combustion method. *Materials Science in Semiconductor Processing*. 2016;41:441-9.
85. Park C-S, Hong M-H, Cho HH, Park H-H. Effect of mesoporous structure on the Seebeck coefficient and electrical properties of $\text{SrTi}_{0.8}\text{Nb}_{0.2}\text{O}_3$. *Applied Surface Science*. 2017;409:17-21.
86. Tangcharoen T, Klysubun W, Kongmark C. Synthesis of nanocrystalline NiO/ZnO heterostructured composite powders by sol-gel auto combustion method and their characterizations. *Journal of Molecular Structure*. 2018;1156:524-33.
87. Birajdar SD, Alange RC, More SD, Murumkar VD, Jadhav KM. Sol-gel Auto Combustion Synthesis, Structural and Magnetic Properties of Mn doped ZnO Nanoparticles. *Procedia Manufacturing*. 2018;20:174-80.
88. Kokare MK, Jadhav NA, Kumar Y, Jadhav KM, Rathod SM. Effect of Nd^{3+} doping on structural and magnetic properties of $\text{Ni}_{0.5}\text{Co}_{0.5}\text{Fe}_2\text{O}_4$ nanocrystalline ferrites synthesized by sol-gel auto combustion method. *Journal of Alloys and Compounds*. 2018;748:1053-61.
89. Nunocha P, Kaewpanha M, Bongkarn T, Phuruangrat A, Suriwong T. A new route to synthesizing La-doped SrTiO_3 nanoparticles using the sol-gel auto combustion method and their characterization and photocatalytic application. *Materials Science in Semiconductor Processing*. 2021;134:106001.
90. Nunocha P, Kaewpanha M, Bongkarn T, Eiad-Ua A, Suriwong T. Effect of Nb doping on the structural, optical, and photocatalytic properties of SrTiO_3 nanopowder synthesized by sol-gel auto combustion technique. *Journal of Asian Ceramic Societies*. 2022;10(3):583-96.
91. Konstas P-S, Konstantinou I, Petrakis D, Albanis T. Development of SrTiO_3 Photocatalysts with Visible Light Response Using Amino Acids as Dopant Sources for the Degradation of Organic Pollutants in Aqueous Systems. *Catalysts*. 2018;8(11):528.
92. Sukpanish P, Lertpanyapornchai B, Yokoi T, Ngamcharussrivichai C. Lanthanum-doped mesostructured strontium titanates synthesized via sol-gel combustion route using citric acid as complexing agent. *Materials Chemistry and Physics*. 2016;181:422-31.
93. Songwattanasin P, Karaphun A, Phokha S, Hunpratub S, Maensiri S, Amornkitbamrung V, et al. Influence of La concentration on structural, morphological, optical and magnetic properties of $\text{Sr}_{1-x}\text{La}_x\text{TiO}_3$ nanopowders. *Physica B: Condensed Matter*. 2019;571:213-21.
94. Yang D, Zou X, Sun Y, Tong Z, Jiang Z. Fabrication of three-dimensional porous La-doped SrTiO_3 microspheres with enhanced visible light catalytic activity for Cr(VI) reduction. *Frontiers of Chemical Science and Engineering*. 2018;12(3):440-9.
95. Kobayashi S, Ikuhara Y, Mizoguchi T. Lattice expansion and local lattice distortion in Nb- and La-doped SrTiO_3 single crystals investigated by x-ray diffraction and

- first-principles calculations. *Physical Review B*. 2018;98(13).
96. Loland TE, Sele J, Einarsrud M-A, Vullum PE, Johnsson M, Wiik K. Thermal Conductivity of A-Site Cation-Deficient La-Substituted SrTiO₃ Produced by Spark Plasma Sintering. *Energy Harvesting and Systems*. 2015;2(1-2).
 97. Chaves AS, de Andrade Raponi O, Gelfuso MV, Thomazini D. Pure and Doped SrTiO₃ Powders Obtained by Ultrasonic Synthesis. *Materials Science Forum*. 2016;869:3-7.
 98. Jiang J, Jia Y, Wang Y, Chong R, Xu L, Liu X. Insight into efficient photocatalytic elimination of tetracycline over SrTiO₃(La,Cr) under visible-light irradiation: The relationship of doping and performance. *Applied Surface Science*. 2019;486:93-101.
 99. Kittel C. *Introduction to Solid State Physics*. eighth ed. John Wiley & Sonc: USA; 2005.
 100. Ham Y, Hisatomi T, Goto Y, Moriya Y, Sakata Y, Yamakata A, et al. Flux-mediated doping of SrTiO₃ photocatalysts for efficient overall water splitting. *Journal of Materials Chemistry A*. 2016;4(8):3027-33.
 101. Leite MM, Vichi FM. Influence of synthesis route on the morphology of SrTiO₃ particles. *MRS Proceedings*. 2013;1552:51-7.
 102. Sonwane CG, Bhatia SK. Characterization of Pore Size Distributions of Mesoporous Materials from Adsorption Isotherms. *The Journal of Physical Chemistry B*. 2000;104(39):9099-110.
 103. Shen H, Lu Y, Wang Y, Pan Z, Cao G, Yan X, et al. Low temperature hydrothermal synthesis of SrTiO₃ nanoparticles without alkali and their effective photocatalytic activity. *Journal of Advanced Ceramics*. 2016;5(4):298-307.
 104. Suriwong T, Thongtem T, Thongtem S. Thermoelectric and optical properties of CuAlO₂ synthesized by direct microwave heating. *Current Applied Physics*. 2014;14(9):1257-62.
 105. Agilandeswari K, Ruban kumar A. Optical, electrical properties, characterization and synthesis of Ca₂Co₂O₅ by sucrose assisted sol gel combustion method. *Advanced Powder Technology*. 2014;25(3):904-9.
 106. Souza AE, Santos GTA, Barra BC, Macedo WD, Teixeira SR, Santos CM, et al. Photoluminescence of SrTiO₃: Influence of Particle Size and Morphology. *Crystal Growth & Design*. 2012;12(11):5671-9.
 107. Gao Y, Masuda Y, Koumoto K. Band Gap Energy of SrTiO₃ Thin Film Prepared by the Liquid Phase Deposition Method. *J Korean Ceram Soc*. 2003;40(3):213-0.
 108. Xu K, Yao M, Chen J, Zou P, Peng Y, Li F, et al. Effect of crystallization on the band structure and photoelectric property of SrTiO₃ sol-gel derived thin film. *Journal of Alloys and Compounds*. 2015;653:7-13.
 109. Posadas AB, Lin C, Demkov AA, Zollner S. Bandgap engineering in perovskite oxides: Al-doped SrTiO₃. *Applied Physics Letters*. 2013;103(14):142906.
 110. Park N-H, Dang F, Wan C, Seo W-S, Koumoto K. Self-originating two-step synthesis of core-shell structured La-doped SrTiO₃ nanocubes. *Journal of Asian Ceramic Societies*. 2018;1(1):35-40.
 111. Li F, Yu K, Lou L-L, Su Z, Liu S. Theoretical and experimental study of La/Ni co-doped SrTiO₃ photocatalyst. *Materials Science and Engineering: B*. 2010;172(2):136-41.
 112. Shang P-P, Zhang B-P, Liu Y, Li J-F, Zhu H-M. Preparation and Thermoelectric

- Properties of La-Doped SrTiO₃ Ceramics. *Journal of Electronic Materials*. 2010;40(5):926-31.
113. Xian T, Yang H, Dai JF, Wei ZQ, Ma JY, Feng WJ. Photocatalytic properties of SrTiO₃ nanoparticles prepared by a polyacrylamide gel route. *Materials Letters*. 2011;65(21-22):3254-7.
 114. Padmini E, Ramachandran K. Investigation on versatile behaviour of Cd doped SrTiO₃ perovskite structured compounds. *Solid State Communications*. 2019;302:113716.
 115. Kumar V, Choudhary S, Malik V, Nagarajan R, Kandasami A, Subramanian A. Enhancement in Photocatalytic Activity of SrTiO₃ by Tailoring Particle Size and Defects. *physica status solidi (a)*. 2019;216(18):1900294.
 116. Liu Z, Ma Z. Ag-SrTiO₃/TiO₂ composite nanostructures with enhanced photocatalytic activity. *Materials Research Bulletin*. 2019;118:110492.
 117. Xu J, Wang W, Sun S, Wang L. Enhancing visible-light-induced photocatalytic activity by coupling with wide-band-gap semiconductor: A case study on Bi₂WO₆/TiO₂. *Applied Catalysis B: Environmental*. 2012;111-112:126-32.
 118. Yang C, Dong W, Cui G, Zhao Y, Shi X, Xia X, et al. Highly efficient photocatalytic degradation of methylene blue by P2ABSA-modified TiO₂ nanocomposite due to the photosensitization synergetic effect of TiO₂ and P2ABSA. *RSC Advances*. 2017;7(38):23699-708.
 119. Li X, Zhao H, Zhou X, Xu N, Xie Z, Chen N. Electrical conductivity and structural stability of La-doped SrTiO₃ with A-site deficiency as anode materials for solid oxide fuel cells. *International Journal of Hydrogen Energy*. 2010;35(15):7913-8.
 120. Rahman MYA, Samsuri SAM, Umar AA. TiO₂-SrTiO₃ composite photoanode: effect of strontium precursor concentration on the performance of dye-sensitized solar cells. *Appl Phys A*. 2019;125(1):59.
 121. Zavjalov AP, Shichalin OO, Tikhonov SA, Kosyanov DY. Features of reactive SPS of SrTiO₃-TiO₂ biphasic ceramics. *IOP Conference Series: Materials Science and Engineering*. 2021;1093(1):012034.
 122. Toby BH. R factors in Rietveld analysis: How good is good enough. *Powder Diffraction*. 2006;21(1):67-70.
 123. Janotti A, Jalan B, Stemmer S, Walle CGVd. Effects of doping on the lattice parameter of SrTiO₃. *Applied Physics Letters*. 2012;100(26):262104.
 124. Kobayashi S, Ikuhara Y, Mizoguchi T. Lattice expansion and local lattice distortion in Nb- and La-doped SrTiO₃ single crystals investigated by x-ray diffraction and first-principles calculations. *Phys Rev B*. 2018;98(13):134114.
 125. Miyauchi M, Takashio M, Tobimatsu H. Photocatalytic Activity of SrTiO₃ Codoped with Nitrogen and Lanthanum under Visible Light Illumination. *Langmuir*. 2004;20(1):232-6.
 126. Songwattanasin P, Karaphun A, Phokha S, Hunpratub S, Maensiri S, Amornkitbamrung V, et al. Influence of La concentration on structural, morphological, optical and magnetic properties of Sr_{1-x}La_xTiO₃ nanopowders. *Phys B: Condens Matter*. 2019;571:213-21.
 127. Santander-Syro AF, Copie O, Kondo T, Fortuna F, Pailhès S, Weht R, et al. Two-dimensional electron gas with universal subbands at the surface of SrTiO₃. *Nature*. 2011;469(7329):189-93.
 128. Park K, Son JS, Woo SI, Shin K, Oh M-W, Park S-D, et al. Colloidal synthesis and

- thermoelectric properties of La-doped SrTiO₃ nanoparticles. *Journal of Materials Chemistry A*. 2014;2(12):4217-24.
129. Lu Z, Zhang H, Lei W, Sinclair DC, Reaney IM. High-Figure-of-Merit Thermoelectric La-Doped A-Site-Deficient SrTiO₃ Ceramics. *Chemistry of Materials*. 2016;28(3):925-35.
 130. Ahmed AJ, Nazrul Islam SMK, Hossain R, Kim J, Kim M, Billah M, et al. Enhancement of thermoelectric properties of La-doped SrTiO₃ bulk by introducing nanoscale porosity. *Royal Society Open Science*. 2019;6(10):190870.
 131. Wang J, Zhang B-Y, Kang H-J, Li Y, Yaer X, Li J-F, et al. Record high thermoelectric performance in bulk SrTiO₃ via nano-scale modulation doping. *Nano Energy*. 2017;35:387-95.
 132. Gong C, Dong G, Hu J, Chen Y, Qin M, Yang S, et al. Effect of reducing annealing on the microstructure and thermoelectric properties of La-Bi co-doped SrTiO₃ ceramics. *J Mater Sci - Mater Electron*. 2017;28(19):14893-900.
 133. Snyder GJ, Toberer ES. Complex thermoelectric materials. *Nature Materials*. 2008;7:105-14.
 134. Heremans JP, Jovovic V, Toberer ES, Saramat A, Kurosaki K, Charoenphakdee A, et al. Enhancement of thermoelectric efficiency in PbTe by distortion of the electronic density of states. *Science*. 2008;321(5888):554-7.
 135. Zebarjadi M, Esfarjani K, Dresselhaus MS, Ren ZF, Chen G. Perspectives on thermoelectrics: from fundamentals to device applications. *Energy & Environmental Science*. 2012;5(1):5147-62.
 136. Mohanraman R, Sankar R, Chou F-C, Lee C-H, Iizuka Y, Muthuselvam IP, et al. Influence of nanoscale Ag₂Te precipitates on the thermoelectric properties of the Sn doped P-type AgSbTe₂ compound. *APL Materials*. 2014;2(9):096114.
 137. Sun Y, Sheng P, Di C, Jiao F, Xu W, Qiu D, et al. Organic Thermoelectric Materials and Devices Based on p- and n-Type Poly(metal 1,1,2,2-ethenetetrathiolate)s. *Advanced Materials*. 2012;24(7):932-7.
 138. Rahman JU, Nam WH, Van Du N, Rahman G, Rahman AU, Shin WH, et al. Oxygen vacancy revived phonon-glass electron-crystal in SrTiO₃. *Journal of the European Ceramic Society*. 2019;39(2):358-65.
 139. Shang P-P, Zhang B-P, Liu Y, Li J-F, Zhu H-M. Preparation and Thermoelectric Properties of La-Doped SrTiO₃ Ceramics. *Journal of Electronic Materials*. 2011;40(5):926-31.
 140. Li J-F, Liu W-S, Zhao L-D, Zhou M. High-performance nanostructured thermoelectric materials. *NPG Asia Mater*. 2010;2:152-8.
 141. Pan W, Cao M, Hao H, Yao Z, Yu Z, Liu H. Defect engineering toward the structures and dielectric behaviors of (Nb, Zn) co-doped SrTiO₃ ceramics. *Journal of the European Ceramic Society*. 2020;40(1):49-55.
 142. Jiao S, Yan J, Sun G, Zhao Y. Electronic structures and optical properties of Nb-doped SrTiO₃ from first principles. *Journal of Semiconductors*. 2016;37(7):072001.
 143. Demydov D, Klabunde KJ. Characterization of mixed metal oxides (SrTiO₃ and BaTiO₃) synthesized by a modified aerogel procedure. *Journal of Non-Crystalline Solids*. 2004;350:165-72.
 144. Drozd E, Kolezynski A. The structure, electrical properties and chemical stability

- of porous Nb-doped SrTiO₃ – experimental and theoretical studies. RSC Advances. 2017;7(46):28898-908.
145. Wunderlich W, Ohta H, Koumoto K. Enhanced effective mass in doped SrTiO₃ and related perovskites. *Physica B: Condensed Matter*. 2009;404(16):2202-12.
 146. Karczewski J, Bochentyn B, Gazda M, Jasinski P, Kusz B. Electrical and structural properties of Nb-doped SrTiO₃ ceramics. *Journal of Electroceramics*. 2010;24:326-30.
 147. Pinheiro AN, Firmiano EGS, Rabelo AC, Dalmaschio CJ, Leite ER. Revisiting SrTiO₃ as a photoanode for water splitting: development of thin films with enhanced charge separation under standard solar irradiation. *RSC Adv*. 2014;4(4):2029-36.
 148. Gosens I, Post JA, de la Fonteyne LJJ, Jansen EHJM, Geus JW, Cassee FR, et al. Impact of agglomeration state of nano- and submicron sized gold particles on pulmonary inflammation. *Part Fibre Toxicol*. 2010;7(1):37-.
 149. Kato H, Kobayashi M, Hara M, Kakihana M. Fabrication of SrTiO₃ exposing characteristic facets using molten salt flux and improvement of photocatalytic activity for water splitting. *Catalysis Science & Technology*. 2013;3(7):1733-8.
 150. Liu D-Q, Zhang Y-W, Kang H-J, Li J-L, Yang X, Wang T-M. Effect of Nb doping on microstructures and thermoelectric properties of SrTiO₃ ceramics. *Chinese Physics B*. 2018;27(4):047205.
 151. Newbury DE, Ritchie NWM. Is Scanning Electron Microscopy/Energy Dispersive X-ray Spectrometry (SEM/EDS) Quantitative? *Scanning*. 2013;35(3):141-68.
 152. Xia Y, He Z, Lu Y, Tang B, Sun S, Su J, et al. Fabrication and photocatalytic property of magnetic SrTiO₃/NiFe₂O₄ heterojunction nanocomposites. *RSC Advances*. 2018;8(10):5441-50.
 153. Townsend TK, Browning ND, Osterloh FE. Nanoscale Strontium Titanate Photocatalysts for Overall Water Splitting. *ACS Nano*. 2012;6(8):7420-6.
 154. Cao J, Huang X, Liu Y, Wu J, Ji Y. Enhanced photocatalytic activity of SrTiO₃ photocatalyst by topotactic preparation. *Materials Research Express*. 2016;3(11):115903.
 155. Saadetejad D, Yildirim R. Photocatalytic hydrogen production by water splitting over Au/Al-SrTiO₃. *International Journal of Hydrogen Energy*. 2018;43(2):1116-22.
 156. Muralidharan M, Anbarasu V, Elaya Perumal A, Sivakumar K. Carrier mediated ferromagnetism in Cr doped SrTiO₃ compounds. *Journal of Materials Science: Materials in Electronics*. 2015;26(9):6352-65.
 157. Wang XL, Fang WQ, Li YH, Liu P, Zhang H, Wang Y, et al. Bottom-Up Enhancement of g-C₃N₄ Photocatalytic H₂Evolution Utilising Disorder Intermolecular Interactions of Precursor. *International Journal of Photoenergy*. 2014;2014:1-8.
 158. Alamelu K, Raja V, Shiamala L, Jaffar Ali BM. Biphasic TiO₂ nanoparticles decorated graphene nanosheets for visible light driven photocatalytic degradation of organic dyes. *Applied Surface Science*. 2018;430:145-54.
 159. Li D, Shi F, Jiang D, Chen M, Shi W. CdIn₂S₄/g-C₃N₄ heterojunction photocatalysts: enhanced photocatalytic performance and charge transfer mechanism. *RSC Advances*. 2017;7(1):231-7.
 160. Cai T, Liu Y, Wang L, Zhang S, Zeng Y, Yuan J, et al. Silver phosphate-based Z-

- Scheme photocatalytic system with superior sunlight photocatalytic activities and anti-photocorrosion performance. *Applied Catalysis B: Environmental*. 2017;208:1-13.
161. Wang L, Wang Z, Wang D, Shi X, Song H, Gao X. The photocatalysis and mechanism of new SrTiO₃/TiO₂. *Solid State Sciences*. 2014;31:85-90.
 162. Chachvalvutikul A, Luangwanta T, Pattisson S, Hutchings GJ, Kaowphong S. Enhanced photocatalytic degradation of organic pollutants and hydrogen production by a visible light-responsive Bi₂WO₆/ZnIn₂S₄ heterojunction. *Applied Surface Science*. 2021;544:148885.
 163. Shenoy S, Tarafder K. Enhanced photocatalytic efficiency of layered CdS/CdSe heterostructures: Insights from first principles electronic structure calculations. *Journal of Physics: Condensed Matter*. 2020;32(27):275501.
 164. Bantawal H, Shenoy US, Bhat DK. Tuning the Photocatalytic Activity of SrTiO₃ by Varying the Sr/Ti Ratio: Unusual Effect of Viscosity of the Synthesis Medium. *The Journal of Physical Chemistry C*. 2018;122(34):20027-33.
 165. Jing P, Lan W, Su Q, Xie E. High photocatalytic activity of V-doped SrTiO₃ porous nanofibers produced from a combined electrospinning and thermal diffusion process. *Beilstein journal of nanotechnology*. 2015;6:1281-6.
 166. Abdi M, Mahdikhah V, Sheibani S. Visible light photocatalytic performance of La-Fe co-doped SrTiO₃ perovskite powder. *Optical Materials*. 2020;102:109803.
 167. Liu C-J. Thermopower of misfit-layered calcium cobaltites. *Thermoelectric Power*. 2011:327-62.
 168. Shimonishi R, Hagiwara M, Fujihara S. Fabrication of highly textured Ca₃Co₄O₉ ceramics with controlled density and high thermoelectric power factors. *Journal of the European Ceramic Society*. 2020;40(4):1338-43.
 169. Zhang FP, Zhang X, Lu QM, Zhang JX, Liu YQ, Zhang GZ. Preparation and high temperature thermoelectric properties of Ca_{3-x}Ag_xCo₄O_{9+δ} oxides. *Solid State Ionics*. 2011;201(1):1-5.
 170. Zhang J, Zheng H, Malliakas CD, Allred JM, Ren Y, Li Qa, et al. Brownmillerite Ca₂Co₂O₅: Synthesis, Stability, and Re-entrant Single Crystal to Single Crystal Structural Transitions. *Chemistry of Materials*. 2014;26(24):7172-82.
 171. Tchitchekova DS, Frontera C, Ponrouch A, Krich C, Bardé F, Palacín MR. Electrochemical calcium extraction from 1D-Ca₃Co₂O₆. *Dalton Transactions*. 2018;47(33):11298-302.
 172. Kahraman F, Madre MA, Rasekh S, Salvador C, Bosque P, Torres MA, et al. Enhancement of mechanical and thermoelectric properties of Ca₃Co₄O₉ by Ag addition. *Journal of the European Ceramic Society*. 2015;35(14):3835-41.
 173. Fan Y, Qi X, Zeng D. Enhanced Thermoelectric Properties of Ca_{3-x}Ag_xCo₄O₉ by the Sol-Gel Method with Spontaneous Combustion and Cold Isostatic Pressing. *Materials (Basel)*. 2018;11(12).
 174. Toby BH. R factors in Rietveld analysis: How good is good enough? *Powder Diffraction*. 2006;21(1):67-70.
 175. Sun T, Hng HH, Yan QY, Ma J. Effect of Ag-doping on crystal structure and high temperature thermoelectric properties of c-axis oriented Ca₃Co₄O₉ thin films by pulsed laser deposition. *Journal of Alloys and Compounds*. 2012;511(1):133-8.
 176. Wang Y, Sui Y, Cheng J, Wang X, Su W. Comparison of the high temperature thermoelectric properties for Ag-doped and Ag-added Ca₃Co₄O₉. *Journal of*

- Alloys and Compounds. 2009;477(1-2):817-21.
177. Liouy. C, Tsaiw. C, Linw. Y, Leeu. R. Synthesis of $\text{Ca}_3\text{Co}_4\text{O}_9$ and CuAlO_2 Ceramics of Thermoelectric Application Using A Reaction-Sintering Process. *Journal of the Australian Ceramic Society*. 2009;44:17-22.
 178. Amaveda H, Mora M, Dura OJ, Torres MA, Madre MA, Marinel S, et al. Drastic enhancement of mechanical properties of $\text{Ca}_3\text{Co}_4\text{O}_9$ by B_4C addition. *Journal of the European Ceramic Society*. 2021;41(1):402-8.
 179. Yan MF, Cannon RM, Bowen HK, Chowdhry U. Effect of grain size distribution on sintered density. *Materials Science and Engineering*. 1983;60(3):275-81.
 180. Jung B-b, Lee H-k, Park H-c. Effect of grain size on the indentation hardness for polycrystalline materials by the modified strain gradient theory. *International Journal of Solids and Structures*. 2013;50(18):2719-24.
 181. Xiang P-H, Kinemuchi Y, Kaga H, Watari K. Fabrication and thermoelectric properties of $\text{Ca}_3\text{Co}_4\text{O}_9/\text{Ag}$ composites. *Journal of Alloys and Compounds*. 2008;454(1-2):364-9.
 182. Nino A, Tanaka A, Sugiyama S, Taimatsu H. Indentation Size Effect for the Hardness of Refractory Carbides. *MATERIALS TRANSACTIONS*. 2010;51(9):1621-6.
 183. Liu Y, Lin Y, Shi Z, Nan CW, Shen Z. Preparation of $\text{Ca}_3\text{Co}_4\text{O}_9$ and improvement of its thermoelectric properties by spark plasma sintering. *Journal of the American Ceramic Society*. 2005;88(5):1337-40.
 184. Li W, Wang J, Poudel B, Kang HB, Huxtable S, Nozariasbmarz A, et al. Filiform Metal Silver Nanoinclusions To Enhance Thermoelectric Performance of P-type $\text{Ca}_3\text{Co}_4\text{O}_{9+\delta}$ Oxide. *ACS Applied Materials & Interfaces*. 2019;11(45):42131-8.
 185. Nunocha P, Bongkarn T, Harnwunggmoung A, Tanusilp S-a, Suriwong T. Thermoelectric properties of La-doped A-site SrTiO_3 ceramics synthesised by the sol-gel auto-combustion technique. *Materials Research Innovations*. 2023:1-10.
 186. Zheng Y, Zhang X, Xie W, Ge N, Ren Y, Wei X, et al. Thermoelectric Performance Enhancement for $\text{Ca}_3\text{Co}_4\text{O}_9$ Ceramics Co-Doped with Ag and Tb. *Journal of Electronic Materials*. 2022;51(9):4938-43.
 187. Shi Z, Zhang Y, Zhang R, Lou Z, Qin M, Zhang P, et al. Microstructure and thermoelectric performance of La-doped $(\text{Ca}_{0.9}\text{Ag}_{0.1})_3\text{Co}_4\text{O}_9$ /nano-sized Ag composite ceramics. *International Journal of Ceramic Engineering & Science*. 2019;2(1):7-16.
 188. Hira U, Han L, Norrman K, Christensen DV, Pryds N, Sher F. High-temperature thermoelectric properties of Na- and W-Doped $\text{Ca}_3\text{Co}_4\text{O}_9$ system. *RSC Advances*. 2018;8(22):12211-21.
 189. Yin T, Liu D, Ou Y, Ma F, Xie S, Li J-F, et al. Nanocrystalline Thermoelectric $\text{Ca}_3\text{Co}_4\text{O}_9$ Ceramics by Sol–Gel Based Electrospinning and Spark Plasma Sintering. *The Journal of Physical Chemistry C*. 2010;114(21):10061-5.
 190. Song M-E, Lee H, Kang M-G, Li W, Maurya D, Poudel B, et al. Nanoscale Texturing and Interfaces in Compositionally Modified $\text{Ca}_3\text{Co}_4\text{O}_9$ with Enhanced Thermoelectric Performance. *ACS omega*. 2018;3(9):10798-810.
 191. Shikano M, Funahashi R. Electrical and thermal properties of single-crystalline $(\text{Ca}_2\text{CoO}_3)_{0.7}\text{CoO}_2$ with a $\text{Ca}_3\text{Co}_4\text{O}_9$ structure. *Applied Physics Letters*. 2003;82(12):1851-3.

192. Braginsky L, Lukzen N, Shklover V, Hofmann H. High-temperature phonon thermal conductivity of nanostructures. *Physical Review B*. 2002;66(13):134203.
193. Wu X, Tang L, Hardin CL, Dames C, Kodera Y, Garay JE. Thermal conductivity and management in laser gain materials: A nano/microstructural perspective. *Journal of Applied Physics*. 2022;131(2):020902.
194. Yu J, Freer R. Calcium cobaltite, a promising oxide for energy harvesting: effective strategies toward enhanced thermoelectric performance. *Journal of Physics: Energy*. 2022;4(2):022001.





APPENDIX

มหาวิทยาลัยนครพนม

Appendix A A new route to synthesizing La-doped SrTiO₃ nanoparticles using the sol-gel auto combustion method and their characterization and photocatalytic application.

Materials Science in Semiconductor Processing 134 (2021) 106001



Contents lists available at ScienceDirect

Materials Science in Semiconductor Processing

journal homepage: www.elsevier.com/locate/mssp



A new route to synthesizing La-doped SrTiO₃ nanoparticles using the sol-gel auto combustion method and their characterization and photocatalytic application

Pornnipa Nunocha^a, Malinee Kaewpanha^a, Theerachai Bongkarn^{b,c}, Anukorn Phuruangrat^d, Tawat Suriwong^{a,c,*}

^a School of Renewable Energy and Smart Grid Technology, Naresuan University, Phitsanulok, 65000, Thailand

^b Faculty of Science, Department of Physics, Naresuan University, Phitsanulok, 65000, Thailand

^c Research Center for Academic Excellence in Applied Physics, Faculty of Science, Naresuan University, Phitsanulok, 65000, Thailand

^d Department of Materials Science and Technology, Faculty of Science, Prince of Songkla University, Hat Yai, Songkhla, 90112, Thailand

ARTICLE INFO

Keywords:

La-doped SrTiO₃
Sol-gel auto combustion
Photoluminescence
Photocatalyst
Band gap
Optical property

ABSTRACT

The Sr_{1-x}La_xTiO₃ (SLTO) nanopowder with varied La contents was successfully synthesized by a new route sol-gel auto combustion technique. The results of the X-ray Diffraction (XRD) patterns of the undoped and La-doped SLTO samples showed a pure phase with cubic perovskite structure, together with the position of the (110) peak slightly shifted toward the lower 2θ angle with increasing amounts of La dopant. The La doping increases the lattice parameter and the unit cell density due to the substitution of the larger ionic radius of La³⁺ into the smaller ionic radius of the Sr²⁺. As well, the crystallite size and particle size of the SLTO samples decreased as the La doping content increased. Specific surface area and total pore volume increased with the increase of La doping content. The band gap (E_g) was determined for the samples to be 4.10–4.12 eV. The photoluminescence (PL) at room temperature showed violet, green, and blue emissions at an excitation of 327 nm. The photocatalytic activity of SLTO, resulting from degrading methylene blue (MB) under UV irradiation, increased with increasing La content and reached a maximum at $x = 0.07$. The effect of La doping on E_g , PL, and mechanism photocatalytic activity of SLTO nanopowders, resulting from the oxygen vacancy in the SLTO structure, was also proposed and discussed. The results emphasize the significance of sol-gel auto combustion technique, which preserves the nanostructure of SLTO and improving photocatalytic activity.

1. Introduction

Strontium titanate (SrTiO₃) is a perovskite structure material with a wide range of unique properties. It was extensively studied for years because of its outstanding features and applications, including photocatalysis, energy storage, and use in sensors and fuel cells, and others due to its excellent dielectric, ferroelectric and optical properties [1]. SrTiO₃ is well known as a promising photocatalytic material for water splitting, mineralization of organic pollutants under UV irradiation and has been extensively investigated as a photocatalyst for its n-type semiconducting features, suitable energy band levels, favourable crystalline structure, tunable morphologies, and high stability. As well, SrTiO₃ has a relatively large band gap of 3.2 eV which means that it only responds to UV light which contributes only 4% of the solar spectrum. Also, the

typical photocatalysis process over a semiconductor involves the absorption of photons, band gap excitation, separation of the photoexcited electron/hole pairs, and redox reactions on the semiconductor surface.

A number of researchers have attempted to improve the photocatalytic efficiency of SrTiO₃. The recombination of photogenerated electrons and holes was reduced to improve the separation speed of photogenerated electrons and holes and to reduce the size of the nanoparticles [2,3]. One strategy used was doping. In the morphology and microstructure of the catalyst using V-doped SrTiO₃ was developed, which exhibited excellent photocatalytic activity [4]. Mn-doped SrTiO₃ has also been used for adjustment of the energy band of SrTiO₃ and the highly effective separation of photogenerated electron-hole pairs [5], and La-doped SrTiO₃ microspheres were shown to exhibit higher photocatalytic activity than the undoped SrTiO₃ [6]. Also, La-doped SrTiO₃

* Corresponding author. School of Renewable Energy and Smart Grid Technology, Naresuan University, Phitsanulok, 65000, Thailand.
E-mail address: tawats@nu.ac.th (T. Suriwong).

<https://doi.org/10.1016/j.mssp.2021.106001>

Received 15 August 2020; Received in revised form 29 May 2021; Accepted 1 June 2021

Available online 11 June 2021

1369-8001/© 2021 Elsevier Ltd. All rights reserved.

represented a high figure of merit thermoelectric [7].

To enhance photocatalytic efficiency, the process of synthesis plays an important role. For example, SrTiO₃ was produced by molten salt and glycine-nitrate-based solution combustion method [8]. SrTiO₃ nanoparticles were prepared using the microwave-assisted hydrothermal method and prepared by a polyacrylamide gel route. SrTiO₃ thin film was prepared by liquid phase deposition and a sol-gel method [9]. In 2018, La-doped SrTiO₃ (La = 0–1) samples were prepared by a modified sol-gel method [6], and in 2019, La-doped SrTiO₃ (La = 0–0.5) was synthesized by the hydrothermal method [10]. La and Cr co-doped SrTiO₃ were fabricated via the facile sol-gel hydrothermal method [11]. These techniques consume higher energy and take a longer time to complete the reaction. Also, some techniques use hazardous solvents and toxic, corrosive, and explosive precursor gases.

There are some techniques that do not have those drawbacks such as sol-gel auto combustion technique, which requires only a short time, in just minutes, to complete, uses simple equipment and technology, and is easy to accomplish at very high processing temperatures (up to 4000 °C). It also allows perfect stoichiometric control, produces high-purity, homogeneous material with particle size measured in nanometers. The sol-gel auto combustion technique is an appropriate method for the synthesis of oxide materials such as CoFe₂O₄ [12], Sr-doped LaFeO₃ [13], and SrTiO₃ [14–16]. These references reported many advantages of using synthesized material to produce quality nanomaterials. It is well known that glycine is usually selected as the organic fuel due to its high combustion temperature; i.e. it is highly exothermic, its rigorous combustion reaction, drastic decomposition, and low cost [17,18]. The heat of combustion of glycine is 13.0 kJ/g, ignition temperature is 158 °C, and decomposition temperature is 262 °C. A glycine-nitrate-based solution-combustion has been used to synthesize SrTiO₃. To remove impurities from the SrTiO₃, it was then washed with HNO₃ [8]. However, fewer exothermic fuels can be mixed with glycine to reduce the exothermicity of the combined mixture and to optimize the performance of the mixture. Citric acid, for example, which can be used to produce a less exothermic mixture, has a heat of combustion of 10.2 kJ/g, ignition temperature of 137 °C and decomposition temperature is 175 °C [17, 18]. As well, mesoporous La-doped SrTiO₃ was synthesized by sol-gel combustion within the presence of citric acid as a complexing agent [19]. Given this information from the literature, in our research, an organic fuel mixture of glycine and citric acid is used in sol-gel auto combustion. This combination has rarely been reported, and our objective was to fill this gap in the body of knowledge.

Previous studies of the photocatalytic activities of both undoped and doped SrTiO₃ used various dyes at different concentrations and light sources. The SrTiO₃ being investigated in one project used 10 ppm methylene blue (MB) and was tested under a 20 W mercury lamp [20]. Elsewhere, the SrTiO₃ had 1 ppm MB and was tested under a 30 W UV lamp [8]. Other reported research includes La-doped SrTiO₃ with 10 ppm K₂Cr₂O₇ and using a 500 W Xe lamp [6], and co-doped SrTiO₃ (La, Cr) with 20 ppm Tetracycline (TC) and a 500 W Xe lamp [11].

In our work, we synthesized Sr_{1-x}La_xTiO₃ (SLTO) with $x = 0, 0.03, 0.05, 0.07$, and 0.1 nanopowder using a new route sol-gel auto combustion technique with an organic fuel mixture of glycine and citric acid. The structure, morphology, and optical properties of SLTO samples by XRD, SEM-EDS were investigated. Due to considering the effect of La content, the optical properties of SLTO candidate were measured by applying UV-Visible and the photoluminescence technique. The photocatalyst activities of the SLTO samples using MB dye under UV irradiation were further determined, which are rarely reported.

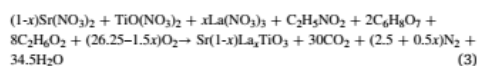
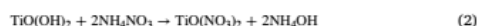
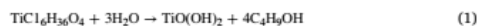
2. Experiments

Sr_{1-x}La_xTiO₃ (SLTO) nanopowders were synthesized using the sol-gel auto combustion technique. The commercial reagents strontium nitrate (Sr(NO₃)₂, Sigma-Aldrich), titanium (IV) butoxide (C₁₆H₃₆O₄Ti, Sigma-Aldrich), lanthanum (III) nitrate hexahydrate, (La(NO₃)₃·6H₂O, Loba

Chemie), citric acid monohydrate (C₆H₈O₇·H₂O, Loba Chemie), ethylene glycol (C₂H₆O₂, Loba Chemie), ammonium nitrate (NH₄NO₃) and glycine (C₂H₅NO₂, Ajax FineChem) were used as the starting materials. A mixture of organic fuel was provided based on a molar ratio of glycine to citric acid of 1:2 used for the auto-combustion reaction. The mixture organic fuel to metal nitrate molar ratio was 1.5 to obtain a fuel-rich composition, achieving the high yields and best performance. Initially, stoichiometric quantities of Sr(NO₃)₂, C₁₆H₃₆O₄Ti, La(NO₃)₃·6H₂O, C₆H₈O₇·6H₂O, C₂H₅NO₂ and NH₄NO₃ were dissolved in 100 ml of deionized water with selected La mole fractions in SLTO samples with $x = 0, 0.03, 0.05, 0.07$ and 0.1 . The mixture solution was heated and constantly stirred at 80 °C until a homogeneous nitrate precursor in the form of a transparent solution was achieved, after 2 h, at which time the ethylene glycol was added in order to enhance the forming of metal/organic gels.

The mixed solution was maintained in a heated state and constantly stirred until it transformed into a highly viscous gel. Immediately, the condensed gel was placed in an oven pre-heated to 200 °C for self-ignited combustion synthesis. A dark brown precursor powder was achieved 1 h after auto-combustion, and the powder was then ground to fine particles and calcined at 900 °C for 2 h in a furnace, which resulted in a white SLTO powder being produced.

The mechanism of the sol-gel auto combustion route to prepare SLTO are as follows:



The thermal decomposition of the as-prepared SLTO sample with $x = 0$ after auto-combustion was measured by thermogravimetric/differential thermogravimetric analysis (TG/DTG) at between 30 and 900 °C in the air at a heating rate of 10 °C/min using a PerkinElmer (Pyris 1 model). The phase analyses of the powders produced from the six fractions (with $x = 0, 0.03, 0.05, 0.07$ and 0.1) were evaluated by X-ray diffraction (XRD) with Cu-K α radiation ($\lambda = 1.5406$ Å) over Bragg's angles ($2\theta, 10^\circ$ – 80°) at a step size of 0.02 and time/step of 0.5s. The morphologies of the particles were examined using a scanning electron microscope (FESEM, JEOL JSM-6335 F) with an energy dispersive X-ray spectroscopy (EDS). Specific surface area and total pore volume of the samples were measured by Nitrogen adsorption-desorption isotherms at 77 K on a Micrometrics Surface Area and Porosity Analyzer (TriStar II 3020 model). The Brunauer–Emmett–Teller (BET) method was utilized to examine the specific surface areas. The powder samples were suspended in ethanol and sonicated for 30 min. The absorbance spectra of the sonicated ethanol suspensions were recorded at room temperature with a UV-visible-near infrared spectrophotometer (UH5300, HITACHI) in the range 275–500 nm. The photoluminescence spectra of the samples were taken with a spectrofluorometer (FluoroMax-4, HORIBA) using an excitation wavelength (λ_{ex}) of 327 nm at room temperature.

In addition, the photocatalytic activity of the La-doped and undoped SLTO samples was investigated by considering the rate of decolorization of MB in an aqueous solution under UV irradiation. The UV lamps presented a peak wavelength (λ_p) at 253.7 nm (100–280 nm), with a net output of 108 W (18 W \times 6 tubes). The suspensions of the sample were positioned 40 cm away from the UV lamps. A suspension was prepared by dispersing 100 mg of the synthesized sample into 200 ml of 10 ppm MB. The suspension was then stirred continuously in a darkroom for 30 min to reach adsorption/desorption equilibrium. The suspension was then irradiated under UV lamps while being continuously stirred at room temperature. After initiation, 5 ml of the reaction suspension was sampled every 1 h for 8 h. The UV-Vis absorption of the solutions was also recorded using a UV-Vis spectrophotometer (UH5300, HITACHI) at

400–800 nm. In order to consider the effect of photocatalyst, the control sample with no SLTO photocatalyst added was also tested under the same experiment process. The decolorization efficiency (%DE) is expressed in the following equation:

$$\%DE = \frac{C_0 - C}{C_0} \times 100 \quad (4)$$

where C_0 is the initial concentration of the MB, and C is the concentration of the MB at various times, after UV irradiation.

3. Result and discussion

To consider the rate of decomposition, thermal stability, physical and chemical phenomena causing changes in heat/temperature, weight loss (TG) and DTG curves of as-prepared SLTO precursor for $x = 0$ were determined, as shown in Fig. 1. The TG-DTG curves can be divided into four stages. First, from 40 to 130 °C, moisture evaporation caused weight loss of around 5%. Second, in the range of 220–350 °C (weight loss ~ 34%), residual organics of the raw materials, such as NH_4NO_3 , $\text{C}_2\text{H}_5\text{NO}_2$, $\text{C}_6\text{H}_8\text{O}_7 \cdot \text{H}_2\text{O}$ and $\text{C}_2\text{H}_6\text{O}_2$ were decomposed. Third, about 450–630 °C, a further weight loss of around 33% occurs at around 450 °C. This is the decomposition of *in situ* carbon residues formed during combustion reaction, and the as-prepared SLTO precursor ($x = 0$) presents as dark brown after auto combustion, probably due to the *in situ* formed carbon as an amorphous metal oxide-carbon composite [19]. As well, the decomposition of impurities, forming a pure SrTiO_3 , occurred at 781 °C. In the final stage, no relative weight loss was exhibited over 800 °C indicating that stable thermal characteristics of the sample had been achieved. So, the calcination temperature of 900 °C for 2 h was selected due to the appropriate temperature and length of calcination time, as confirmed by the XRD results.

The powder XRD patterns of the SLTO nanopowder with $x = 0, 0.03, 0.05, 0.07$ and 0.1 samples after calcination are presented in Fig. 2(a). All the samples exhibited the dominant diffraction peak at $2\theta = 32.42^\circ, 40.05^\circ, 46.53^\circ, 57.86^\circ, 67.97^\circ$ and 77.35° corresponding to (110), (111), (200), (211), (220) and (310) planes of a cubic perovskite SrTiO_3 phase (Pm-3m) of the JCPDS no. 035-0634 [10]. The formation of other strontium and titanium compounds such as LaTiO_3 , SrO , Sr_2O_3 , TiO , and TiO_2 were not detected in this analysis. This indicates that all the samples are identified as a single cubic perovskite SrTiO_3 structure. Fig. 2(b) presents the magnified main XRD pattern of all the samples at the 2θ range between 31° and 34° according to the (110) plane. The position of the (110) peak was found to shift slightly toward the lower 2θ angles as the amount of La content increased. This is a result of the substitution of

the smaller ionic radius of Sr^{2+} (1.13 Å) by the larger ionic radius of La^{3+} (1.15 Å) [6] which is consistent with Bragg's law equation: $n\lambda = 2d\sin\theta$ where n is a positive integer and λ is a wavelength of the incident wave. According to a previous study on lattice expansion and local lattice distortion in La-doped SrTiO_3 single crystals [21], the lattice parameter of the SLTO sample increases with increasing the La content. A similar finding was found in three-dimensional porous La-doped SrTiO_3 microspheres [6].

The Full Width at Half Maximum (FWHM) values of the XRD patterns of the SLTO nanopowder peaks was used to determine the crystallite size of the samples by Scherrer's equation:

$$D = \frac{k\lambda}{\beta\cos\theta} \quad (5)$$

where D is the average crystallite size, k is the constant as 0.9, λ is the wavelength of Cu-K α radiation (1.5406 Å), β is the FWHM, θ is the Bragg's angle. The calculated D values of the SLTO samples are summarized in Table 1. The D of SrTiO_3 was 21 nm, while the SLTO samples with La dopant were 17.5 nm, indicating that D of SLTO decreases with La dopant. These results are probably due to the different valences of Sr^{2+} and La^{3+} ions, which lead to induced lattice defects in SLTO samples [6]. Compared to the different methods used for synthesizing the SLTO, the D of SLTO with and without La dopant are relatively lower than those of the SLTO ($x = 0$ –0.50) nanopowders prepared by the hydrothermal method (27.62–34.46 nm) [10], the three-dimensional porous La-doped SrTiO_3 microspheres synthesized by a modified sol-gel method (96.8–180.4 nm) [6], as well as the D of $(\text{La}_{0.12}\text{Sr}_{0.88})_{0.05}\text{TiO}_3$ produced by spray pyrolysis (25 nm) [22], and a $\text{Sr}_{0.96}\text{La}_{0.04}\text{TiO}_3$ prepared by the two techniques solid-state reaction (252 nm), and ultrasonic synthesis (137 nm) [23].

To further consider the effect of La doping contents on the SrTiO_3 cubic perovskite structure, the Rietveld refinement method was used to analyze the experimental XRD data using the Fullprof program. The parameters of the refinement process were (1) the XRD pattern measurements, (2) the lattice constant, (3) profile half-width parameter (u , v and w), (4) atomic functional position, and (5) occupancy. The Chebyshev function was used to determine the background parameter. The diffraction peak profiles were fitted by a pseudo-Voigt function. Fig. 3 shows the final output results from the Rietveld refinement analysis of the SLTO with (a) $x = 0$, (b) $x = 0.1$ for all samples shown in Table 1. It was found that all peaks of the SLTO samples fitted well with a low Chi-squared (χ^2) and Rietveld discrepancy factors (R_p , R_{wp} , and $R_{exp} < 15\%$). This indicates that the refined XRD patterns were in good agreement with the experimental XRD data, corresponding with the previous study [11]. The variation of the lattice parameter ($a = b = c$) and calculated cell density (d_{cal} , g/cm^3) of the SLTO sample as a function of the La content (x) is shown in Fig. 4(a). The lattice parameter and d_{cal} of the undoped samples ($x = 0$) were matched with the JCPDS database ($a = b = c = 3.905$ Å, $d_{th} = 5.12$ g/cm^3). The lattice parameter of the doped samples increased with an increasing La content. This is due to the substitution of the smaller ionic radius of Sr^{2+} (1.13 Å) by the larger ionic radius of La^{3+} (1.15 Å), according to the three-dimensional porous La-doped SrTiO_3 microspheres [6]. A similar trend of the changes of lattice parameters and local lattice distortion in Nb and La-doped SrTiO_3 single crystals has been investigated by in-plane x-ray diffraction and first-principles calculations [21,24].

The cell density of the SLTO samples was also shown to increase with increases in the La content (x) due to the substitution of the large atomic weight element (La) for the lower atomic weight element (Sr). In our research, by increasing the La dopant content, the variation of the atomic weight composed in a unit cell was more considerable than the change of cell volume. The crystal structure of SLTO with $x = 0.1$ obtained from Rietveld refinement analysis is shown in Fig. 4(b). With La dopant at $x = 0.1$, when considering the SLTO cubic perovskite structure, it was observed that the La^{3+} substituted in the Sr^{2+} site, with

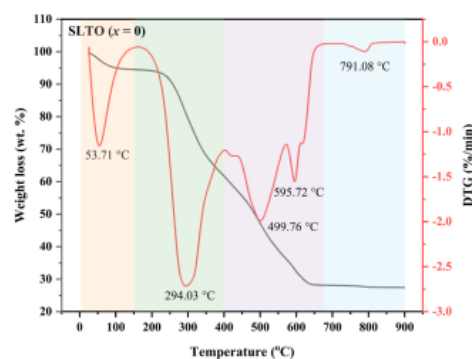


Fig. 1. Weight loss (TG) and DTG curves of as-prepared SLTO precursor for $x = 0$.

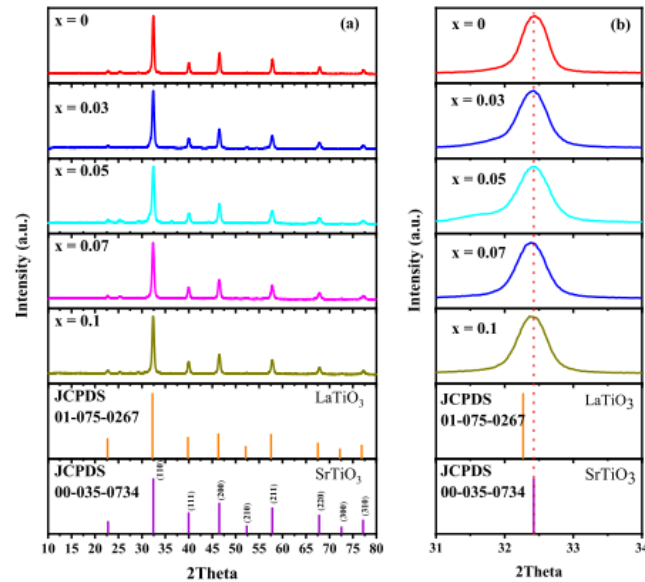


Fig. 2. (a) XRD patterns of the SLTO ($x = 0, 0.03, 0.05, 0.07$ and 0.1) nanopowder (b) magnified view of the main XRD peak.

Table 1

Lattice parameter, Chi-squared (χ^2), Rietveld discrepancy factors (R_p , R_{wp} , R_{exp}) and Calculated cell density (d_{cal}) and crystallite size of SLTO ($x = 0, 0.03, 0.05, 0.07$ and 0.1).

Name	Lattice parameter $a = b = c$ (Å)	χ^2	R_p	R_{wp}	R_{exp}	d_{cal} (g/cm ³)	Crystallite sizes (nm)
JCPDS#35-0734	3.9050					5.12	
SrTiO ₃	3.9049	2.95	13.90	12.90	7.49	5.16	21.0
Sr _{0.97} La _{0.03} TiO ₃	3.9061	3.83	16.10	15.40	7.90	5.19	17.5
Sr _{0.95} La _{0.05} TiO ₃	3.9066	4.39	9.39	14.10	6.74	5.25	17.5
Sr _{0.93} La _{0.07} TiO ₃	3.9071	2.50	11.20	11.50	7.29	5.33	17.5
Sr _{0.9} La _{0.1} TiO ₃	3.9075	1.94	11.00	10.30	7.41	5.47	17.5

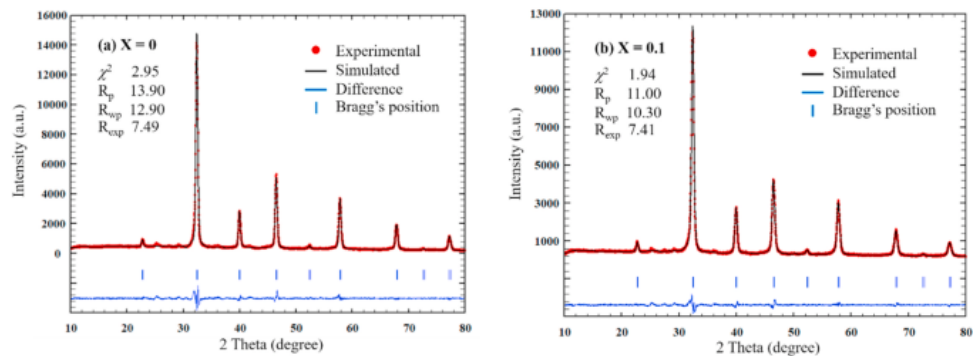


Fig. 3. Typical Rietveld refinement analysis of SLTO, (a) $x = 0$ and (b) 0.1 .

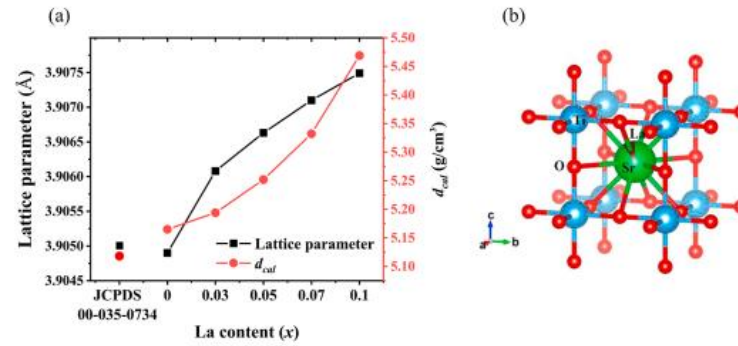


Fig. 4. (a) Variation of the lattice parameter and calculated cell density (d_{cal}) of SrTiO_3 with the JCPDS no. 00-035-0734 and SLTO ($x = 0, 0.03, 0.05, 0.07$ and 0.1) and (b) The simulate structure of SLTO with $x = 0.1$.

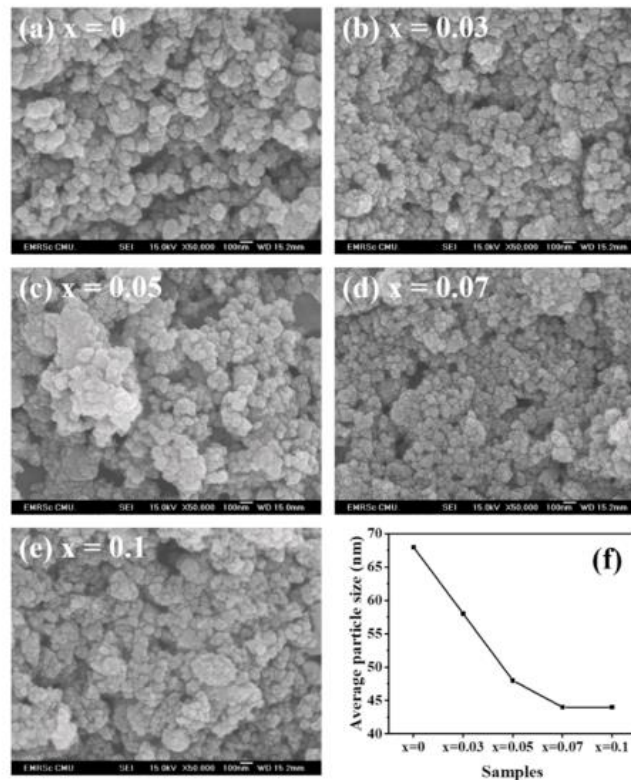


Fig. 5. a-e) SEM image and f) the average particle size of SLTO nanopowder.

occupancy number of La^{3+} and Sr^{2+} , were 0.09992 (10% occupied) and 0.89258 (90% occupied).

Fig. 5 shows the SEM images of SLTO ($x = 0, 0.03, 0.05, 0.07$ and 0.1) nanopowders that were prepared by the sol-gel auto combustion method and were calcined at 900°C for 2 h. The morphology of the undoped and La-doped SLTO samples exhibited agglomerated particles of spherical shape. Each sample had a relatively homogeneous size distribution. The average particle size of all the samples was measured using the ImageJ program with 200 particles/sample, as shown in Fig. 5 (f). The average particle sizes of the SLTO samples were in the nano-scale range and decreased with increased La content from 68 nm, 58 nm, 48 nm, 44 nm and 44 nm for sample of $x = 0, 0.03, 0.05, 0.07$ and 0.1 , respectively. These values were in accordance with the crystallite size of the SLTO samples estimated by the Scherrer equation. Compared to different methods for preparing the SLTO nanopowder, the particle size of the SLTO samples synthesized by sol-gel auto combustion is smaller than other techniques, such as hydrothermal (75–125 nm) [10], SrCl_2 flux treatments (0.2–3 nm) [25]. However, this was not the case when the sol-gel combustion method used citric acid (CA) (20–30 nm) [14] or Molten salt (50–300 nm) [26].

Fig. 6 shows the SEM image, EDS spectrum and mapping images of SLTO nanopowder with $x = 0.1$. The EDS spectrum (Fig. 6(b)) and EDS mapping images (Fig. 6(c–f)) were measured on the spectrum area of the nanoparticles (Fig. 6(a)). The four colors in the element map indicate the distribution of the elements Sr, Ti, O, and La, according to the qualitative property of the EDS spectrum. The EDS mapping images show that Sr, Ti, O, and La are uniform distribution on the sample surface.

Fig. 7 shows the specific surface area and total pore volume of the SLTO samples. The specific surface area of the SLTO samples was $1.6\text{--}8.9\text{ m}^2/\text{g}$, indicating that the specific surface area of the SLTO increased as the La doping content increased. This is due to the decrease in the average particle size, corresponding to the SEM images (Fig. 5). Similarly, in a previous study, the specific surface area of SLTO increased with increasing the La doping [19]. The total pore volume in the SLTO samples was $0.0015\text{--}0.0063\text{ cm}^3/\text{g}$, which increased with increases in the La doping content, where the La content increase may have caused the reduced size of the mesopores [19]. Probably, the reduction in the size of the large mesopores, thereby producing small

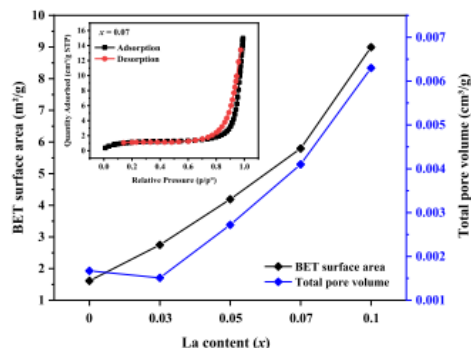


Fig. 7. The specific surface area and total pore volume of the SLTO samples, (inset) the Nitrogen adsorption-desorption isotherms of typical SLTO ($x = 0.07$) sample.

mesopore, lead to the increased total pore volume.

The inset graph shows the nitrogen adsorption-desorption isotherm of a typical SLTO sample for $x = 0.07$, indicating that physisorption isotherms exhibit a hysteresis loop under type IV corresponded to the IUPAC classification. In the case of type IV isotherms, the sample is characterized as mesoporous adsorbents based on monolayer-multilayer adsorption and capillary condensation, similar to the SLTO synthesized by the sol-gel combustion route [19,27]. In the case of other SLTO samples, similar results to those for the SLTO sample with $x = 0.07$ were obtained.

So, the advantage of the sol-gel auto combustion route using a mixture of glycine and citric acid as organic fuel to prepare SLTO nanopowder is easy stoichiometric control, relative low ignition temperature, short time to synthesis, use of simple equipment, complete reaction, and high combustion temperature. It is indicated that the sol-gel auto combustion route with a mixture of organic fuels have been considered as a candidate technique

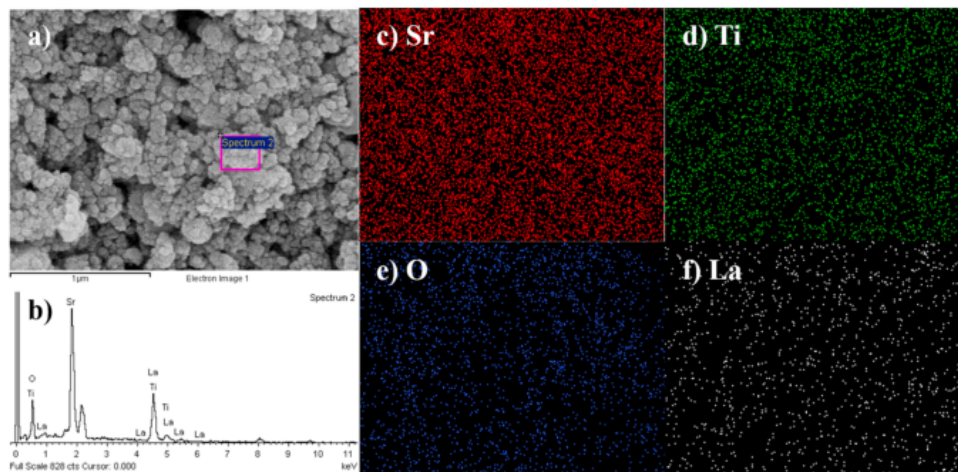


Fig. 6. SEM-EDS images of the $\text{Sr}_{0.9}\text{La}_{0.1}\text{TiO}_3$ nanopowder.

for the synthesis of metal oxide nanopowder under high-temperature reaction and low ignition temperature.

To investigate the optical properties of the SLTO samples, the UV–visible diffuse absorbance spectra of the samples, with $A = -\log(I/I_0)$, I_0 and I = intensity of incident and transmitted radiation, were recorded at wavelengths between 275 and 500 nm at room temperature

(Fig. 8). Fundamentally, the absorption was applied to observe the absorption edge and energy gap, according to the electronic transition from the upper bound of the valence band to the lower bound of the conduction band [28]. The light absorption ability of all the samples exhibited a similar trend when detecting the absorption edge at 310 nm wavelength. When considering the high energy region of the absorption

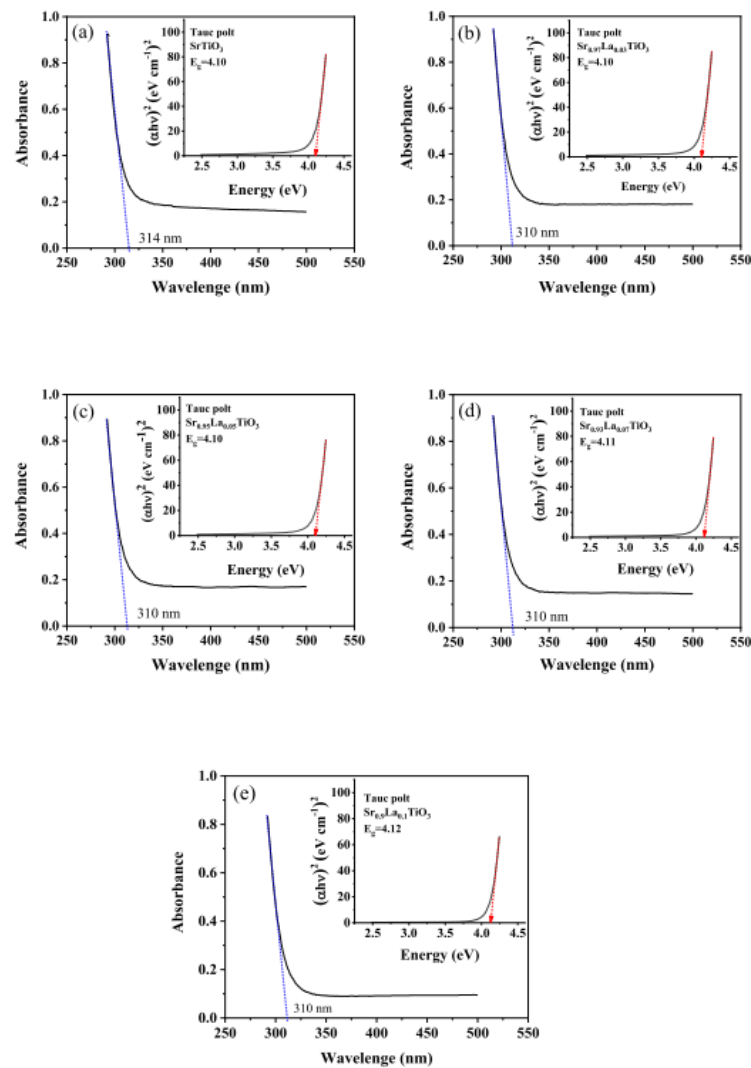


Fig. 8. UV–vis spectra of the SLTO ($x = 0, 0.03, 0.05, 0.07$ and 0.1) nanopowder, together with an inset plot of $(\alpha h\nu)^2$ as a function of photon energy ($h\nu$).

edge, we see that the light absorption ability is only increased by increasing the photon energy. The relationship of the absorption and incident photon energy ($h\nu$) is represented by Tauc's relation;

$$(\alpha h\nu) = A(h\nu - E_g)^n \quad (6)$$

where α denotes the absorption coefficient, A is constant, E_g is the band gap, and n depends on the type of transition. For direct allowed transitions $n = 1/2$, for the indirect allowed transitions, $n = 2$, and for direct forbidden transitions, $n = 3/2$, and indirect forbidden transitions where $n = 3$ [28,29]. The E_g of these samples was estimated by extrapolating the linear portion of the curve to zero absorbance, shown as the inset plot of $(\alpha h\nu)^2$ vs $h\nu$ for a direct allowed transition.

The E_g of the undoped SLTO ($x = 0$) sample is 4.10 eV, as shown in Fig. 8(a). Fundamentally, the optical property of nanoparticles depends on their crystallinity, morphology, particle size, and synthesis method, particularly [9,30–32]. The E_g of undoped SLTO sample in our study, 4.10 eV, were higher than in previous reports. SrTiO₃ prepared by microwave-assisted hydrothermal was 3.5 eV with crystallite size 52 nm [30], SrTiO₃ powders synthesized by liquid-solid reaction method was

3.4 or 3.5 eV with particle size 30–108 nm [32], SrTiO₃ thin film synthesis by liquid phase deposition with 3.65–3.78 eV with varying temperature annealing [31] and with sol-gel was 3.82 eV [9]. Probably, the SrTiO₃ synthesized by the sol-gel auto combustion method provides particle size as a nanometer (Fig. 5). Regarding the influence of La dopant on E_g of SLTO, as illustrated in Fig. 8(b)–e, it was observed that the E_g slightly increased ($E_g = 4.10$ –4.12 eV) with increasing La content. This result corresponds to the findings of related SLTO materials [10, 33], that had La-doped SLTO, which also had the significant effect of relatively increasing E_g with increasing La. These results may be due to an increase of La content, leading to the formation of an oxygen vacancy state in the band gap that has the effect of shifting the Fermi level close to the conduction band, resulting in the E_g becoming larger than the undoped-SrTiO₃ [10,34]. The increase of oxygen vacancies is due to the reaction of the La³⁺ substitutes in Sr²⁺ site and the reducing atmosphere during the calcination process, described on Eq. (7) and Eq. (8) [35,36].

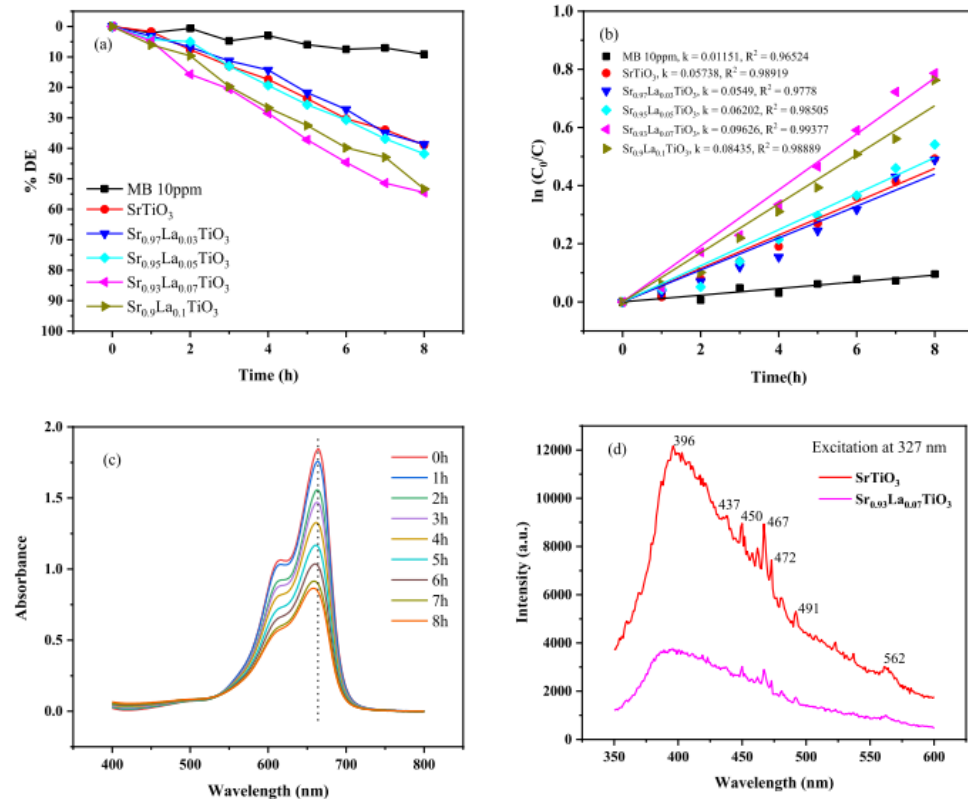


Fig. 9. (a) Photocatalytic decolorization efficiency (%DE) of MB irradiated under the UV lamps (b) Pseudo-first order kinetics of the photocatalytic decolorization of MB (c) Time dependent UV-Vis spectra of MB solution for SLTO nanopowder for $x = 0.07$ and (d) Photoluminescence (PL) spectra of the SLTO nanopowders for $x = 0$ and 0.07 .



The photocatalytic efficiencies of the SLTO samples were examined by degrading methylene blue (MB) under UV irradiation. The photocatalytic activity, in terms of the decolorization efficiency (%DE) of SLTO photocatalyst, is illustrated in Fig. 9(a) which shows that the %DE of MB without a catalyst under UV irradiation slowly increases with exposure time, after 8 h around 9%. The reaction of photocatalytic activity, showing the %DE of MB with SLTO as a catalyst, steadily increasing with exposure time and the %DE increasing with La concentration increases. After 8 h, the %DE of the undoped SLTO ($x = 0$) sample is 39%. The %DE of the undoped-SLTO agrees with SrTiO_3 in which the synthesis by the polyacrylamide gel route [20] and combustion technique [8]. Accordingly, the undoped-SLTO in the present study, applying the sol-gel auto combustion technique, can be competitive with the previous method due to the small-sized nanoparticles that increase the surface area for photocatalytic activity. Obviously, SLTO with $x = 0.07$ gives the highest photocatalytic efficiency around 55%, which is the optimal reaction at $x = 0.07$. La dopant greater than $x = 0.07$ is ineffective for %DE. However, because the %DE of La dopant has not investigated in the same way as in our research, these results cannot be compared with previous findings. For example, the La-doped SrTiO_3 (La = 0.5) showed a %DE value of 80% in 100 min when an inorganic chemical ($\text{K}_2\text{Cr}_2\text{O}_7$ (Cr (VI)) was used, and the light source was a 500 W Xe arc lamp [6]. Also, the co-doped SrTiO_3 (La 5%, and Cr 2%) showed the %DE of structure antibacterial medicine (Tetracycline (TC)) as 80% in 90 min with a 300 W Xe lamp light source [11].

The reaction rate and physical process were studied by chemical kinetics. The reaction rate is in direct variation to the one reactant concentration. The corresponding first-order reaction kinetics constant (k) can be calculated by the equation: $\ln(C_0/C) = kt$, where C and C_0 are the real-time and initial concentrations of MB. The k value for SLTO also increased with La-dope increases, as shown in Fig. 9(b). Obviously, the k value of $x = 0.07$ is the highest, corresponded to the %DE. So, the SLTO with $x = 0.07$ has the highest of both the %DE and the first-order reaction kinetics constant.

The optimal value for La-doped SLTO as a photocatalyst reaction is $x = 0.07$, as shown in Fig. 9(c), which shows the absorbance peak (λ_{max}) of MB at different times at 664 nm. After an exposure time of 8 h, the λ_{max} of MB continuously decreased and shifted to the lower wavelength between 664 nm and 658 nm. The λ_{max} decreased due to decolorization of the MB and blue shift due to the stepwise removal of auxochromes (methyl or methylamine) [37]. Besides, the spectra absorbance of each SLTO samples agrees with the same trends.

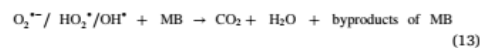
As a result, the photocatalyst activities of the SLTO samples using MB dye under UV irradiation are relatively poor due to 50% MB decolorization was achieved in a long time (8 h). However, the present study full fill a gap of knowledge on investigating the photocatalyst activities of the SLTO samples using MB dye under UV irradiation. It might be a guideline and benefit for future development of SLTO photocatalyst activity. Significantly, the sol-gel auto combustion with an organic fuel mixture of glycine and citric acid has been considered a candidate technique for preparing SLTO photocatalyst in a nano-sized product.

To consider the photocatalytic activity of SLTO samples, the photoluminescence (PL) technique is used to identify the recombination of electron-holes in the semiconductor, carrier trapping, and the degree of structural order-disorder in a semiconductor. The efficiency and properties of PL on semiconductor materials depend on the synthesis process, calcination temperature, time, crystalline size, and topology of the materials [38]. Fig. 9(d) shows the PL spectra of SLTO with $x = 0$ and 0.07 samples with an excitation wavelength (λ_{ex}) of 327 nm at room temperature. Both of the PL spectra exhibited similar trends and peaks. The emission peaks are shown in violet, blue, and green. The centered peak emitted at 396 nm is violet colored, the peaks emitted at 437, 450, 467, 472, and 491 nm harmonize with the blue emission mainly due to

Sr deficiency in the crystal structure, and the green color emission at 562 nm is due to the presence of oxygen vacancy in the SrTiO_3 lattice [38]. Moreover, the emission of PL at peak intensity was attributed to the presence of defects, as shown in Fig. 10. The E_g between the Titanium 3d conduction band and the oxygen 2p valence band is 4.10 eV (Fig. 8). The oxygen vacancies create a defect level below the conduction band. The emission at 396 nm was observed when the excited electrons and holes recombine through the defect level or by oxygen vacancy. Due to the electrons doped in the conduction band as the result of oxygen vacancy at recombination with excited holes, the PL emission at 437 nm was occurred. While, the spectrum emission was appeared at 467 nm, indicating that the excited holes and electrons were recombined through their trap level. The obtained PL emissions result of SLTO in the present study is a good agreement with SrTiO_3 prepared by ball mill for different time durations [3]. Consequently, the PL spectra results, La-doped SLTO nanopowders, synthesized by the sol-gel auto combustion technique, has oxygen defects and local-disorder in the electrons of the SLTO material.

In fundamental, there is an inverse relationship between the intensity of the PL spectra and the %DE, which shows that if the PL intensity decreases, this will result in photocatalytic activity increase due to low electron-hole recombination and low carrier recombination [39, 40]. As a result, the intensity of the PL emissions of SLTO with $x = 0$ was higher than SLTO with $x = 0.07$. This leads to electron-hole recombination of SLTO with $x = 0$ larger than SLTO with $x = 0.07$. Consequently, the SLTO with $x = 0.07$ sample exhibited the highest photocatalytic activity because La can be effective in transferring the photogenerated electrons and can also intercept the recombination of electron-hole pairs [39].

The mechanism of the photocatalytic decolorization of MB dye on the SLTO photocatalyst under UV irradiation is shown in Fig. 11. The process of photocatalytic reaction can be divided into three steps. In the first step, the photocatalysis of SLTO was excited by UV irradiation with photo-energy higher than the E_g of photocatalysis to generate photoinduced electrons (e') and holes (h^+). The electron is generated from the valence band (VB) transfers to the conduction band (CB) through valence band transition, and then holes in the valence band are generated (Eq. (9)). Second, the e' and h^+ react with O_2 and H_2O to generate high reactive hydroxyl radicals and superoxide radicals. The O_2 adsorbed on the surface of the photocatalysis is trapped e' to form superoxide radical ($\text{O}_2^{\bullet-}$) (Eq. (10)), and $\text{O}_2^{\bullet-}$ radical, which further reacts with H_2O to generate the hydroperoxyl radical $\text{H}_2\text{O}^{\bullet}$ (Eq. (11)). The H_2O or OH^{\bullet} adsorbed on the surface of the photocatalysis are oxidized by the h^+ to generate hydroxyl radicals (OH^{\bullet}) (Eq. (12)). Finally, the generated hydroxyl radical, hydroperoxyl radical, and superoxide radicals decomposed the MB dye into CO_2 , H_2O , and by-products of MB, which could be 2-amino-5-(*N*-methyl formamide) benzene sulfonic acid, 2-amino-5-(methyl amino)-hydroxybenzene sulfonic acid, and benzenesulfonic acid [41] (Eq. (13)). To consider the by-products of MB, further characterization should be performed. The steps are written in the reaction form as follows;



The results from PL spectra (Fig. 9(d)) indicate that La dopant could prevent the $\text{e}' - \text{h}^+$ recombination in SLTO sample (Eq. (9)), leading to the release e' and h^+ for further forward reactions. Hence, it can be concluded that the sol-gel auto combustion technique resulted in undoped and La-doped SLTO nanopowder that leads to improved photocatalyst activity.

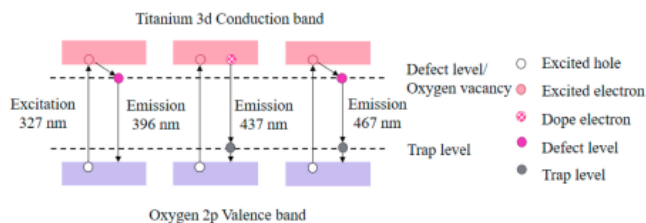


Fig. 10. A schematic of the PL emissions of SLTO due to the recombination of conduction electron-valence holes.

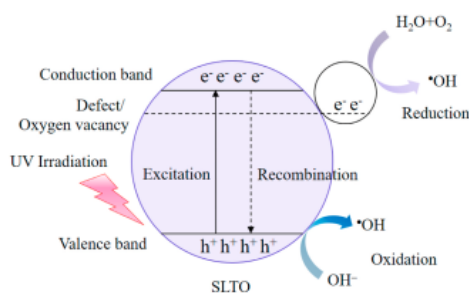


Fig. 11. A schematic diagram for photocatalysis of SLTO nanopowder.

4. Conclusion

The $\text{Sr}_{1-x}\text{La}_x\text{TiO}_3$ (SLTO) nanopowder with $x = 0, 0.03, 0.05, 0.07$, and 0.1 were successfully synthesized by a new route sol-gel auto combustion technique using a mixture of glycine and citric acid as organic fuel resulted in good photocatalyst activity with regard to the decolorization of methylene blue organic dyes under UV irradiation. XRD shows a pure phase as a cubic perovskite with a slight decrease in the crystallite sizes as La increased. The lattice parameter and density of SLTO from the Rietveld refinement technique increased when La increased. SEM-EDS images showed the effect of La dope STO increasing on nanoparticles that lead to decreased particle sizes of 44–68 nm and a good distribution of Sr, Ti, O and La elements. The band gap (E_g) slightly increased with increasing La content which causes oxygen vacancy. The SLTO with $x = 0.07$ is an optimal level for photocatalytic activity, according to the result of photoluminescence (PL) spectra. Consequently, the SLTO prepared by the sol-gel auto combustion technique with a mixture of organic fuels is comparable with that prepared by conventional methods in terms of phase, size, and photocatalytic properties.

Authorship contribution statement

Pornnipa Nunocha: Methodology, Formal analysis, Investigation, Visualization, Writing - original draft preparation. Malinee Kaewpanha: Formal analysis, Investigation. Theerachai Bongkarn: Formal analysis, Supervision. Anukorn Phurangrat: Resources, Formal analysis. Tawat Suriwong: Conceptualization, Supervision, Formal analysis, Writing - review & editing, Visualization, Project administration, Funding acquisition.

Declaration of competing interest

The authors declare that they have no known competing financial interests or personal relationships that could have appeared to influence the work reported in this paper.

Acknowledgements

This research was supported by The National Research Council of Thailand (NRCT) and Thailand Science Research and Innovation (TSRI) through the Royal Golden Jubilee Ph.D. Program (PHD/0049/2560). Furthermore, this work was made possible by a generous grant from The National Science, Research and Innovation Fund (NSRF) through Naresuan University (R2564B001). We also thank you to Assistant Prof. Dr. Sulawan Kaowphong and member's lab, Department of Chemistry, Faculty of Science, Chiang Mai University, for suggestions in the photocatalyst activity part. Many thanks also to Mr. Roy I. Morien of the Naresuan University Graduate School for his assistance in editing the English grammar, syntax, and expression in this document.

References

- [1] B.L. Phoon, C.W. Lai, J.C. Juan, P.L. Show, W.H. Chen, A review of synthesis and morphology of SrTiO_3 for energy and other applications, *Int. J. Energy Res.* 43 (2019) 5151–5174.
- [2] F. Zhang, X. Wang, H. Liu, C. Liu, Y. Wan, Y. Long, Z. Cai, Recent advances and applications of semiconductor photocatalytic technology, *Appl. Sci.* 9 (2019), 2489.
- [3] V. Kumar, S. Choudhary, V. Malik, R. Nagarajan, A. Kandasami, A. Subramanian, Enhancement in photocatalytic activity of SrTiO_3 by tailoring particle size and defects, *Phys. Status Solidi* 216 (2019), 1900294.
- [4] P. Jing, W. Lan, Q. Su, E. Xie, High photocatalytic activity of V-doped SrTiO_3 porous nanofibers produced from a combined electrospinning and thermal diffusion process, *Beilstein J. Nanotechnol.* 6 (2015) 1281–1286.
- [5] G. Wu, P. Li, D. Xu, B. Luo, Y. Hong, W. Shi, C. Liu, Hydrothermal synthesis and visible-light-driven photocatalytic degradation for tetracycline of Mn-doped SrTiO_3 nanocubes, *Appl. Surf. Sci.* 333 (2015) 39–47.
- [6] D. Yang, X. Zou, Y. Sun, Z. Tong, Z. Jiang, Fabrication of three-dimensional porous La-doped SrTiO_3 microspheres with enhanced visible light catalytic activity for Cr (VI) reduction, *Front. Chem. Sci. Eng.* 12 (2018) 440–449.
- [7] Z. Lu, H. Zhang, W. Lei, D.C. Sinclair, L.M. Reaney, High-Figure-of-Merit thermoelectric La-doped A-site-deficient SrTiO_3 ceramics, *Chem. Mater.* 28 (2016) 925–935.
- [8] G. Saito, Y. Nakasugi, N. Sakaguchi, C. Zhu, T. Akiyama, Glycine-nitrate-based solution-combustion synthesis of SrTiO_3 , *J. Alloys Compd.* 652 (2015) 496–502.
- [9] K. Xu, M. Yao, J. Chen, P. Zou, Y. Peng, F. Li, X. Yao, Effect of crystallization on the band structure and photoelectric property of SrTiO_3 sol-gel derived thin film, *J. Alloys Compd.* 653 (2015) 7–13.
- [10] P. Songwattanasin, A. Karaphum, S. Phokha, S. Hunpradub, S. Maensiri, V. Amornkithamrungs, E. Swatsitang, Influence of La concentration on structural, morphological, optical and magnetic properties of $\text{Sr}_{1-x}\text{La}_x\text{TiO}_3$ nanopowders, *Phys. B Condens. Matter* 571 (2019) 213–221.
- [11] J. Jiang, Y. Jia, Y. Wang, R. Chong, L. Xu, X. Liu, Insight into efficient photocatalytic elimination of tetracycline over $\text{SrTiO}_3(\text{La,Cr})$ under visible-light irradiation: the relationship of doping and performance, *Appl. Surf. Sci.* 486 (2019) 93–101.
- [12] V.R. Bhagwat, A.V. Humbe, S.D. More, K.M. Jadhav, Sol-gel auto combustion synthesis and characterizations of cobalt ferrite nanoparticles: different fuels approach, *Mater. Sci. Eng., B* 248 (2019), 114388.
- [13] M. Kaewpanha, T. Suriwong, W. Wamse, P. Nunocha, Synthesis and Characterization of Sr-doped LaFeO_3 perovskite by sol-gel auto-combustion method, *J. Phys. Conf.* 1259 (2019), 012017.
- [14] S. Liu, Z. Xiu, J. Liu, F. Xu, W. Yu, J. Yu, G. Feng, Combustion synthesis and characterization of perovskite SrTiO_3 nanopowders, *J. Alloys Compd.* 457 (2008) L12–L14.
- [15] S. Fuentes, R.A. Zarate, E. Chavez, P. Muñoz, D. Díaz-Droguett, P. Leyton, Preparation of SrTiO_3 nanomaterial by a sol-gel-hydrothermal method, *J. Mater. Sci.* 45 (2010) 1448–1452.

- [16] P. Panthong, T. Klaytae, K. Boonma, S. Thoutom, Preparation of SrTiO₃ nanopowder via sol-gel combustion method, *Ferroelectrics* 455 (2013) 29–34.
- [17] A.V. Saghir, S.M. Beidokhti, J.V. Khaki, A. Salimi, One-step synthesis of single-phase (Co, Mg, Ni, Cu, Zn) O High entropy oxide nanoparticles through SCS procedure: thermodynamics and experimental evaluation, *J. Eur. Ceram. Soc.* 41 (2021) 563–579.
- [18] C.-C. Hwang, T.-Y. Wu, J. Wan, J.-S. Tsai, Development of a novel combustion synthesis method for synthesizing of ceramic oxide powders, *Mater. Sci. Eng., B* 111 (2004) 49–56.
- [19] P. Sukpanish, B. Lertpanyapornchai, T. Yokoi, C. Ngamcharussrivichai, Lanthanum-doped mesostructured strontium titanates synthesized via sol-gel combustion route using citric acid as complexing agent, *Mater. Chem. Phys.* 181 (2016) 422–431.
- [20] T. Xian, H. Yang, J.F. Dai, Z.Q. Wei, J.Y. Ma, W.J. Feng, Photocatalytic properties of SrTiO₃ nanoparticles prepared by a polyacrylamide gel route, *Mater. Lett.* 65 (2011) 3254–3257.
- [21] S. Kobayashi, Y. Ikumura, T. Mizoguchi, Lattice expansion and local lattice distortion in Nb- and La-doped SrTiO₃ single crystals investigated by x-ray diffraction and first-principles calculations, *Phys. Rev. B* 98 (2018).
- [22] T.E. Lofland, J. Sele, M.-A. Einarsrud, P.E. Vullum, M. Johansson, K. Wik, Thermal conductivity of A-site cation-deficient La-substituted SrTiO₃ produced by spark plasma sintering, *Energy Harvest. Syst.* 2 (2015).
- [23] A.S. Chaves, O. de Andrade Raponi, M.V. Gelfuso, D. Thomazini, Pure and doped SrTiO₃ powders obtained by ultrasonic synthesis, *Mater. Sci. Forum* 869 (2016) 3–7.
- [24] C. Kittel, *Introduction to Solid State Physics*, eighth ed. edn, John Wiley & Sons, 2005.
- [25] Y. Ham, T. Hisatomi, Y. Goto, Y. Moriya, Y. Sakata, A. Yamakata, J. Kubota, K. Domen, Flux-mediated doping of SrTiO₃ photocatalysts for efficient overall water splitting, *J. Mater. Chem.* 4 (2016) 3027–3033.
- [26] M.M. Leite, F.M. Vichi, Influence of synthesis route on the morphology of SrTiO₃ particles, *MRS Proc.* 1552 (2013) 51–57.
- [27] H. Shen, Y. Lu, Y. Wang, Z. Pan, G. Cao, X. Yan, G. Fang, Low temperature hydrothermal synthesis of SrTiO₃ nanoparticles without alkali and their effective photocatalytic activity, *J. Adv. Ceram.* 5 (2016) 298–307.
- [28] T. Suriwong, T. Thongtem, S. Thongtem, Thermoelectric and optical properties of CuAlO₂ synthesized by direct microwave heating, *Curr. Appl. Phys.* 14 (2014) 1257–1262.
- [29] K. Agilandewari, A. Ruban kumar, Optical, electrical properties, characterization and synthesis of Ca₂Co₂O₉ by sucrose assisted sol gel combustion method, *Adv. Powder Technol.* 25 (2014) 904–909.
- [30] A.E. Souza, G.T.A. Santos, B.C. Barra, W.D. Macedo, S.R. Teixeira, C.M. Santos, A. M.O.R. Senos, L. Amaral, E. Longo, Photoluminescence of SrTiO₃: influence of particle size and morphology, *Cryst. Growth Des.* 12 (2012) 5671–5679.
- [31] Y. Gao, Y. Masuda, K. Koumoto, Band gap energy of SrTiO₃ thin film prepared by the liquid phase deposition method, *J. Kor. Ceram. Soc.* 40 (2003) 210–213.
- [32] A.B. Posadas, C. Lin, A.A. Demkov, S. Zollner, Bandgap engineering in perovskite oxides: Al-doped SrTiO₃, *Appl. Phys. Lett.* 103 (2013), 142906.
- [33] N.-H. Park, F. Dang, C. Wan, W.-S. Seo, K. Koumoto, Self-originating two-step synthesis of core-shell structured La-doped SrTiO₃ nanocubes, *Journal of Asian Ceramic Societies* 1 (2018) 35–40.
- [34] F. Li, K. Yu, L.-L. Lou, Z. Su, S. Liu, Theoretical and experimental study of La/Ni co-doped SrTiO₃ photocatalyst, *Mater. Sci. Eng., B* 172 (2010) 136–141.
- [35] P.-P. Shang, B.-P. Zhang, Y. Liu, J.-F. Li, H.-M. Zhu, Preparation and thermoelectric properties of La-doped SrTiO₃ ceramics, *J. Electron. Mater.* 40 (2010) 926–931.
- [36] D. Liu, Y. Zhang, H. Kang, J. Li, Z. Chen, T. Wang, Direct preparation of La-doped SrTiO₃ thermoelectric materials by mechanical alloying with carbon burial sintering, *J. Eur. Ceram. Soc.* 38 (2018) 807–811.
- [37] P.-S. Konstantas, I. Konstantinou, D. Petrakis, T. Albanis, Development of SrTiO₃ photocatalysts with visible light response using amino acids as dopant sources for the degradation of organic pollutants in aqueous systems, *Catalysts* 8 (2018), 528.
- [38] E. Padmini, K. Ramachandran, Investigation on versatile behaviour of Cd doped SrTiO₃ perovskite structured compounds, *Solid State Commun.* 302 (2019), 113716.
- [39] Z. Liu, Z. Ma, Ag-SrTiO₃/TiO₂ composite nanostructures with enhanced photocatalytic activity, *Mater. Res. Bull.* 118 (2019), 110492.
- [40] J. Xu, W. Wang, S. Sun, L. Wang, Enhancing visible-light-induced photocatalytic activity by coupling with wide-band-gap semiconductor: a case study on Bi₂WO₆/TiO₂, *Appl. Catal. B Environ.* 111–112 (2012) 126–132.
- [41] C. Yang, W. Dong, G. Cui, Y. Zhao, X. Shi, X. Xia, B. Tang, W. Wang, Highly efficient photocatalytic degradation of methylene blue by P2ABSA-modified TiO₂ nanocomposite due to the photosensitization synergetic effect of TiO₂ and P2ABSA, *RSC Adv.* 7 (2017) 23699–23708.

Appendix B Effect of Nb doping on the structural, optical, and photocatalytic properties of SrTiO₃ nanopowder synthesized by sol-gel auto combustion technique.

JOURNAL OF ASIAN CERAMIC SOCIETIES
2022, VOL. 10, NO. 3, 583–596
<https://doi.org/10.1080/21870764.2022.2094556>



FULL LENGTH ARTICLE

OPEN ACCESS

Effect of Nb doping on the structural, optical, and photocatalytic properties of SrTiO₃ nanopowder synthesized by sol-gel auto combustion technique

Pornnipa Nunocha^a, Malinee Kaewpanha^a, Theerachai Bongkarn^{b,c}, Apiluck Eiad-Ua^d and Tawat Suriwong^{b,c}

^aSchool of Renewable Energy and Smart Grid Technology, Naresuan University, Phitsanulok, Thailand; ^bFaculty of Science, Department of Physics, Naresuan University, Phitsanulok, Thailand; ^cResearch Center for Academic Excellence in Applied Physics, Faculty of Science, Naresuan University, Phitsanulok, Thailand; ^dCollege of Nanotechnology, King Mongkut's Institute of Technology, Bangkok, Thailand

ABSTRACT

Metal oxide photocatalyst is a promising wastewater treatment process due to its simplicity, high efficiency, and low cost, as well as being environmentally friendly and non-energy consuming. The perovskite structure material, SrTi_{1-x}Nb_xO₃ (STNO) with $x = 0, 0.01, 0.03$, and 0.05 , was successfully synthesized by the sol-gel auto-combustion method. Samples with a pure phase and cubic perovskite structure were obtained. The Rietveld refinement results showed that the lattice parameter and unit cell density increased as the Nb-doping level increased. The particle size of the STNO decreases with increasing Nb doping content. Photoluminescence was excited at 327 nm, producing violet, green, and blue emissions, while the Nb content asserts an insignificant effect on the bandgap (E_g). The Nyquist plot and Mott-Schottky analysis were used to determine the photoelectrode performance of the STNO samples. The photocatalytic activity of STNO on the decolorization of methylene blue (MB) under UV irradiation increased with increasing Nb content and optimization at $x = 0.05$, corresponding to the results obtained from photoluminescence, E_g , Nyquist plot, and Mott-Schottky analyses.

ARTICLE HISTORY

Received 13 March 2022
Accepted 22 June 2022

KEYWORDS

Nb-doped SrTiO₃; perovskite;
decolorization; energy band;
Nyquist plot; Mott-Schottky
plot

1. Introduction

The increasing world population together with the associated increase in industrial and agricultural development has resulted in the growth in the amount of organic contamination in water resources. Dyes are a major contaminant that can come from a variety of sources, including textiles, paint, paper, and plastics manufacture [1]. Photocatalysis mechanisms have been widely performed to decolorize organic pollutants in water sources due to an environmentally friendly process [2]. Semiconductor photocatalysis is a promising wastewater treatment process that is easy to use, is highly efficient and low cost. Furthermore, it is environmentally friendly, non-energy consuming, nontoxic, and nonpolluting [3]. Various semiconductor-based photocatalysts, such as TiO₂ [4], CaTiO₃ [5], SrTiO₃ [6,7], and ZnO [8], have shown improved photocatalytic activity and chemical stability.

Perovskite structure materials (ABO₃) are more effective in the application of photocatalysts, sensors, dye-sensitized solar cells (DSCC), and supercapacitors [9] due to the availability of several elements that were replaced or doped in A and B-sites to fabricate the new materials. These demonstrated excellent properties of flexibility in their chemical composition, structure, band gap, oxidation states, and valence states [10].

However, to increase the photocatalytic performance of the ABO₃, the development of perovskite oxide-based materials for photocatalytic application has been focused on band gap tuning, suppressing the recombination of photogenerated charges, and inducing the defect in the material structure [11].

Strontium titanate (SrTiO₃, STO) is an oxide ceramic which has an oxide crystal with a cubic perovskite structure. STO is also a semiconductor material with a wide band gap (E_g) with intriguing electronic, optical, magnetic, and photocatalytic properties. The electrical properties of STO are indicated by the sizable dielectric permittivity and ferroelectric phase. Furthermore, the band structure of STO is in two band gaps: direct 3.75 eV and indirect 3.2 eV [12]. Therefore, the photocatalyst properties of STO, with these outstanding features, were fascinating to study. Nanostructure, doping, and heterojunction are modification techniques of the STO based on the photocatalyst. Nanostructures are attractive because of their high specific surface area and the migration of $e^- - h^+$ on the surface in chemical reactions that occur before recombination [13]. These properties of nanostructures improve photocatalysis efficiency. Several processes for synthesizing materials result in nanoscale structures. Using doping to tune the luminescent, electronic, optical, and other physical properties leads to improved semiconductors with a wide band gap.

CONTACT Tawat Suriwong tawats@nu.ac.th School of Renewable Energy and Smart Grid Technology, Naresuan University, Phitsanulok, Thailand; Research Center for Academic Excellence in Applied Physics, Faculty of Science, Naresuan University, Phitsanulok, Thailand

© 2022 The Author(s). Published by Informa UK Limited, trading as Taylor & Francis Group on behalf of The Korean Ceramic Society and The Ceramic Society of Japan. This is an Open Access article distributed under the terms of the Creative Commons Attribution License (<http://creativecommons.org/licenses/by/4.0/>), which permits unrestricted use, distribution, and reproduction in any medium, provided the original work is properly cited.

Many publications have identified various methods for creating nanostructures and doping elements that result in greater photocatalytic efficiency. Enhanced photocatalytic activity is enabled by having a large number of pores and small particle sizes (60–80 nm) of STO produced in a two-step process; solvothermal and solid-state method [14]. The flux treatment method created the nanoparticle sizes (200–400 nm) in STO powders, leading to enhanced photocatalytic activity [15]. The photocatalyst of Cr-doped STO using a sol-gel hydrothermal method had a small grain size (18–32 nm) [16]. The band gap energy of Al-doped STO prepared by solid-state reaction (3.45 eV) was better than STO (3.30 eV) [17]. Besides, the 25–40 nm Au-doped STO nanoparticles synthesized via sol-gel synthesis gave enhanced photocatalytic efficiency [18]. The Cr-doped STO, prepared by the co-precipitation technique, enhanced the efficiency by ~4 times by degrading the Methylene Blue (MB) dye [19].

The Nb-doped STO, prepared by conventional solid-state reaction, demonstrated improved electrical and structural properties [20]. Au nanoparticles were decorated on 0.01 wt% Nb-doped STO and the impact on visible light utilization was assessed. This widened the band gap of the 0.01 wt% Nb-doped STO semiconductor, enhancing its usefulness for various energy conversion and environmental purposes [21]. $\text{SrTi}_{1-x}\text{Nb}_x\text{O}_3$ where $x = 0, 1, 2, 3$ mol%, synthesized via wet synthesis, resulted in a shift of the Fermi level [22]. Additionally, 0.1% of Nb-doped TiO_2 , was found to be the optimum level for suppressing the surface recombination [23]. Also, Nb-doped TiO_2 improved the transport of electrons [24]. MB dye was also used to investigate the decolorization of STO samples under various light sources. STO, prepared by the combustion method, also degraded MB under 30 W UV light [7]. B-STO, synthesized by facile solvothermal, was used to decolorize MB in a visible light environment [25].

Different processes can prepare STO. The synthesis method and the different doping elements can affect the structure, morphology, optical, and other properties of the STO. There are few previously published works regarding the synthesizing of STO with sol-gel auto-combustion. However, this process has the advantages of a short duration of synthesis, easy stoichiometric control, high purity, homogeneous materials, and particle size at the nanoscale [26]. In past research, Nb-doped STO has also been rarely discussed in photocatalyst applications, even though Nb-doped elements have been shown to increase photoelectrode performance and electrical properties.

Sol-gel auto-combustion can be achieved with different fuels such as glycine, citric acid, ethylene glycol, and urea. The different fuels lead to different properties, such as when using urea as a fuel, smaller particles can be achieved, or where using ethylene glycol as

a fuel can improve the magnetic properties of materials [27]. Cetyltrimethylammonium bromide, mixed with citric acid fuels in solution, used for combustion synthesis, led to a higher specific surface area [28]. Most publications use only one fuel to prepare a sample. For example, the individual samples of CoFe_2O_4 were prepared by sol-gel auto-combustion using different fuels: ethylene glycol, glycine, and urea [27]. Elsewhere, $\text{BaFe}_{12}\text{O}_{19}$ was prepared by sol-gel auto-combustion using glycine [29], and STO was prepared by sol-gel auto-combustion using citric acid [30]. However, our previous research reported a pure phase, small size as nanosized of La-doped SrTiO_3 and improved photocatalytic efficiency, using a mixture of fuel: glycine and citric acid [31].

Therefore, in our research, a mixture of glycine and citric acid was used as fuel to reduce ignition and improve the properties of the samples. We attempted to synthesize $\text{SrTi}_{1-x}\text{Nb}_x\text{O}_3$ (STNO) nanopowder by a new approach using sol-gel auto-combustion. The effect of various Nb-doped concentrations on the phase, structure, morphology, and optical properties of the STNO was characterized. The flat band potential of STNO is unknown, so a Mott–Schottky equation was used to determine it by the electrochemical impedance spectroscopy (EIS) technique. Charge transfer resistance and photocatalytic decolorization efficiency of MB dye under UV irradiation were further investigated, with the expectation of good photocatalytic activity.

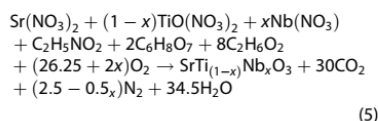
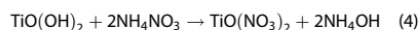
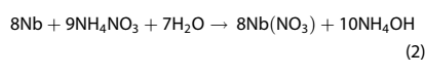
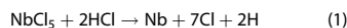
2. Experimental

The $\text{SrTi}_{1-x}\text{Nb}_x\text{O}_3$ (STNO) samples with $x = 0, 0.01, 0.03$, and 0.05 were synthesized by a new synthesis route of sol-gel auto-combustion. Strontium nitrate ($\text{Sr}(\text{NO}_3)_2$, Sigma-Aldrich), titanium (IV) butoxide ($\text{C}_{16}\text{H}_{36}\text{O}_4\text{Ti}$, Sigma-Aldrich), niobium (V) chloride (NbCl_5 , Sigma-Aldrich), glycine ($\text{C}_2\text{H}_5\text{NO}_2$, Ajax FineChem), citric acid monohydrate ($\text{C}_6\text{H}_8\text{O}_7\cdot\text{H}_2\text{O}$, Loba Chemie), hydrochloric acid (HCl, RCI Labscan Limited), ammonium nitrate (NH_4NO_3 , Commercial), and ethylene glycol ($\text{C}_2\text{H}_6\text{O}_2$, Loba Chemie) were used as starting materials. Organic fuel and extra nitrates for the auto-combustion reaction were provided from glycine and citric acid mixture with a 1:2 molar ratio and ammonium nitrate, respectively.

First, stoichiometric amounts of 1 mol of $\text{Sr}(\text{NO}_3)_2$, 1 mol of $\text{C}_{16}\text{H}_{36}\text{O}_4\text{Ti}$, 1 mol of $\text{C}_2\text{H}_5\text{NO}_2$, 2 mol of $\text{C}_6\text{H}_8\text{O}_7\cdot\text{H}_2\text{O}$ and 2.5 mol of NH_4NO_3 were dissolved in 100 ml of deionized water. Nb solution, prepared by dissolving solid NbCl_5 in concentrated HCl solution, together with selected Nb mole fractions in STNO samples with $x = 0, 0.01, 0.03$, and 0.05, were then added to the mixture solution which was heated and constantly stirred at 80°C for 2 hr to achieve a transparent solution of homogeneous nitrate precursor.

A solution with the ratio of ethylene glycol: citric acid of 4:1 was then added to enhance the formation of metal/organic gels. The mixture solution was continuously heated and stirred until it transformed into a highly viscous gel. Suddenly, the gel was put in a furnace preheated to 300°C for self-ignited combustion synthesis. A dark brown precursor product was obtained after 1 h, which was then ground to fine particles and calcined at 1000°C for 12 h in a furnace. A white STNO powder was successfully produced.

The mechanisms for synthesizing STNO by the sol-gel auto-combustion method are as follows:



The phase identification of the STNO powders was analyzed by X-ray diffraction (XRD) with Cu-K α radiation ($\lambda = 1.5406 \text{ \AA}$) following Bragg's angles (2θ , $10^\circ - 80^\circ$) at a step size of 0.02 and time/step of 0.5 s. The morphologies of the particles were inspected employing a scanning electron microscope (FESEM, JEOL JSM-6335 F) with energy-dispersive X-ray spectroscopy (EDS). A UV-visible-near infrared spectrophotometer (UH5300, HITACHI) was used to measure the absorbance spectra of the samples that have been suspended in ethanol and sonicated for 30 min, at room temperature, in the range of 300–600 nm. Nyquist plot and Mott Schottky plot were carried out with Electrochemical Impedance Spectroscopy (EIS, PGSTAT302N, Metrohm Autolab B.V.), which was performed in 0.1 M Na $_2$ SO $_4$ (pH 6) electrolyte solution under a typical three-electrode condition consisting a working electrode, a platinum wire counter electrode, and a saturated calomel reference electrode. The STNO thin film was coated on fluorine-doped tin oxide (FTO) glass for use as a working electrode. A spectrofluorometer (FluoroMax – 4, HORIBA) was used to measure the photoluminescence spectra of the samples at room temperature with the excitation wavelength (λ_{ex}) of 327 nm.

Additionally, the photocatalytic activity of the STNO powder was evaluated by the decolorization of the MB in an aqueous solution under UV irradiation with a peak wavelength (λ_p) at 253.7 nm (100–280 nm) using UV lamps with a net output of 108 W (18 W \times 6

tubes). The aqueous solution used here had been prepared using 100 mg of STNO catalyst dispersed into 200 ml of 10 ppm MB at room temperature, continuously stirred in the dark for 30 min, to achieve adsorption/desorption equilibrium on the surface of the STNO photocatalytic. During this process, the aqueous solution sample was 40 cm away from the UV lamps. The solution was then continuously stirred under UV lamps for 8 h, with a 5 ml sample taken every hour during this period. Using a UV-Vis spectrophotometer (UH5300, HITACHI), the absorption spectra of the aqueous solution sample were recorded at a whole wavelength of 400–800 nm. To determine the effect of the with/without STNO catalyst, the aqueous solution without STNO was used as a control sample and tested under the same conditions. The decolorization efficiency (%DE) [31,32] is expressed as the following equation:

$$\%DE = \frac{C_0 - C}{C_0} \times 100 \quad (6)$$

where C_0 is the concentration of the initial MB for the solution to reach adsorption/desorption equilibrium condition and C is the concentration of the MB after UV irradiation of the solution sample.

3. Result and discussion

The XRD patterns of STNO ($x = 0, 0.01, 0.03$, and 0.05) nanopowder after calcination at 1000°C 12 h are presented in Figure 1a. All samples were compared with the standard data JCPDS no. 035-0734 [33] and each showed an agreement of the main peak at $2\theta = 32.40^\circ, 40.04^\circ, 46.50^\circ, 57.87^\circ, 67.94^\circ$, and 77.27° belonging to (110), (111), (200), (211), (220), and (310) planes of a cubic perovskite STO phase (Pm-3m). This indicates that all samples were identified as pure STO without any detectable impure phase, which further confirms that a cubic perovskite STO nanocrystalline structure is retained after Nb $^{5+}$ doping. In addition, the main peak belonging to the (110) plane (Figure 1b) shows a slight shift to a lower diffraction angle with increasing niobium doping content. This is due to the substitution of a larger radius of Nb $^{5+}$ (0.64 Å) ions to the Ti $^{4+}$ (0.61 Å) sites, which corresponds to Bragg's law equation: $n\lambda = 2d\sin\theta$ [34]. The crystallite size of all the STNO nanopowder was calculated using the Full Width at Half Maximum (FWHM) values of the XRD patterns from Scherer's equation (Eq. 7) [31,35] as follows:

$$D = \frac{k\lambda}{\beta\cos\theta} \quad (7)$$

where D is the average crystallite size, k is the constant 0.9, λ is the wavelength of Cu-K α radiation (1.5406 Å), β is the FWHM, and θ is the Bragg's angle. The average crystallite size of the STNO samples calculated is shown in Table 1. The crystallite size of STO was around 23 nm and 21 nm for the STNO samples. The results indicated

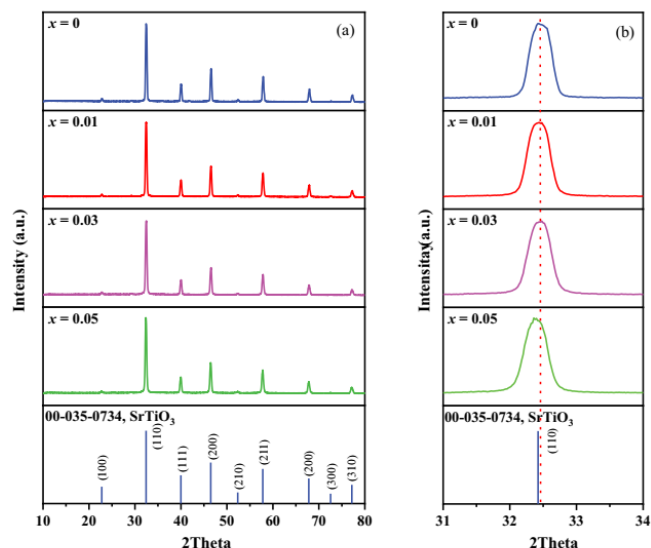


Figure 1. (a) XRD patterns of STNO powder with $x = 0, 0.01, 0.03$ and 0.05 and JCPDS of STO and (b) magnified view of the main XRD peak.

Table 1. Lattice parameter, Chi-squared (χ^2), Rietveld discrepancy factors (R_p , R_{wp} , R_{exp}) and Calculated cell density (d_{cal}) and crystallite size of STNO ($x = 0, 0.01, 0.03$, and 0.05).

Name	Lattice parameter $a=b=c$ (Å)	χ^2	R_p	R_{wp}	R_{exp}	d_{cal} (g/cm ³)	Crystallite sizes (nm)
JCPDS#35-0734	3.9050	-	-	-	-	5.12	-
$x = 0$	3.90453	2.21	6.85	8.52	5.73	5.236	23.4
$x = 0.01$	3.90643	2.12	5.85	7.32	5.03	5.250	21.1
$x = 0.03$	3.90746	1.63	5.52	6.95	5.44	5.257	21.0
$x = 0.05$	3.90800	1.61	5.38	6.66	5.24	5.329	21.0

that there was an insignificant effect of the Nb doping content on the crystallite size of the STNO powder synthesized by the sol-gel auto-combustion method. Additionally, it was observed that the crystallite size of the STNO powders prepared in this way is relatively smaller than the crystallite size of the STO nanopowder synthesized by a modified aerogel procedure (25 nm) [36], the $\text{Sr}_{0.94}\text{Ti}_{0.9}\text{Nb}_{0.1}\text{O}_3$ (80 nm) synthesized by a modified glycine-nitrate process (80 nm) [37], or the STNO ($x = 0-0.03$) nanopowders prepared by the wet synthesis-sol-gel method (160–240 nm) [22].

Considering the effect of Nb doping on the STNO cubic perovskite structure, the specific structural parameters were calculated by Rietveld refinement analysis of the experimented XRD data using the Fullprof program. The refinement parameters for the process that were used included the scale factor, the background intensity, the lattice constant, profile half-width parameters (u , v , and w), functional position of the atoms, and occupancies, of the STNO sample. The background

parameter was determined by the Chebyshev function. In addition, a pseudo-Voigt function was examined to fit the diffraction peak profiles of the samples.

Figure 2 presents the Rietveld refinement analysis results of all the STNO samples. The resultant parameters after Rietveld refinement analysis of the STNO sample and their densities are also summarized in Table 1. The peaks of the STNO samples show a good fitting with the low Chi-squared parameter ($\chi^2 < 4$) and the Rietveld discrepancy factors (R_p , R_{wp} , $R_{exp} < 10\%$). These results show that the refined XRD patterns were in good agreement with the experimental data and good consistency with the JCPDS#35-0734 database ($a = b = c = 3.9050$ Å, $d_{cal} = 5.12$ g/cm³).

Figure 3(a) shows the lattice parameter and calculated cell density of STNO versus the Nb concentration compared with JCPDS#35-0734 of the STO database. The lattice parameter STNO with $x = 0$ is similar to the database and previous work: the calculation of the lattice parameter of STO (3.9050 Å) [38]. In addition,

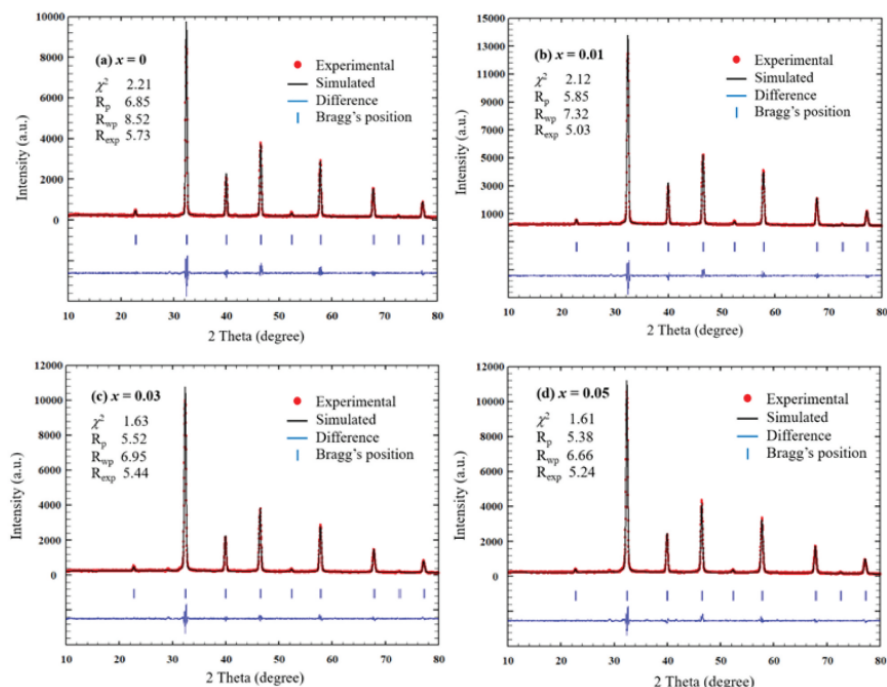


Figure 2. Rietveld refinement analysis of STNO samples: (a) $x = 0$, (b) $x = 0.01$, (c) $x = 0.03$ and (d) $x = 0.05$.

the lattice parameter value of the undoped STNO sample was lower than that of the STO value (3.920–3.925 Å), which had been prepared by the microwave-assisted hydrothermal method [35]. The result indicated that the sol-gel auto-combustion provides a lattice parameter that resembles the conventional technique. The STNO with $x = 0.01$ –0.05 were slightly expanded with an increase in Nb content in both volume and the lattice parameter. The lattice parameter, density, and volume of the STNO samples exhibited a slight increase when the Nb content increased due to the substitution of Nb^{5+} (0.64 Å) ions to Ti^{4+} (0.61 Å) sites. This is in agreement with previous research on the lattice parameter and volume of Nb-doped SrTiO_3 [20,34]. It was also found that the lattice parameter of STNO with $x = 0.01$, 0.03, and 0.05 is similar to the lattice parameter and the same trends of Nb-doped STO (3.905–3.918 Å) prepared by the colloidal synthetic process [39] and the (Nb, Zn) co-doped STO ceramics (3.9064–3.9069 Å) prepared by the traditional solid-state technique [33]. Figure 3b shows the crystal structure of STNO with $x = 0.05$ calculated by Rietveld refinement analysis, which substituted the Nb^{5+} at the Ti^{4+} site, with occupancy numbers of Nb^{5+} and Ti^{4+} to be 0.0501 and 0.9570,

respectively. The result indicated that the sol-gel auto-combustion provides a lattice parameter that resembles the conventional technique.

The SEM images of the STNO ($x = 0$, 0.01, 0.03, and 0.05) powders are shown in Figure 4. The morphology of both the undoped and the Nb-doped STNO samples presented as agglomerated particles and indeterminate shapes due to the adhesion of particles to each other by weak forces [40]. It was observed that all the samples exhibited smooth and dense surfaces with no porousness of the particles. The agglomeration of particles in the STNO sample showed more particles sticking together when the amount of Nb doping increased. The ImageJ program was used to determine the average particle size of all the samples, which measured 200 particles/sample. The average particle size of the undoped STNO was 235 nm, while the Nb-doped STNO samples with $x = 0.01$, 0.03, and 0.05 had an average particle size of 128 nm, 105 nm, and 84 nm, respectively. This indicates that the average particle size of STNO samples slightly decreased with the increase in the Nb content. These results showed that the STO nanopowders were closer and lower than others reported as being prepared by various techniques such as the flux treatment method (200–400 nm)

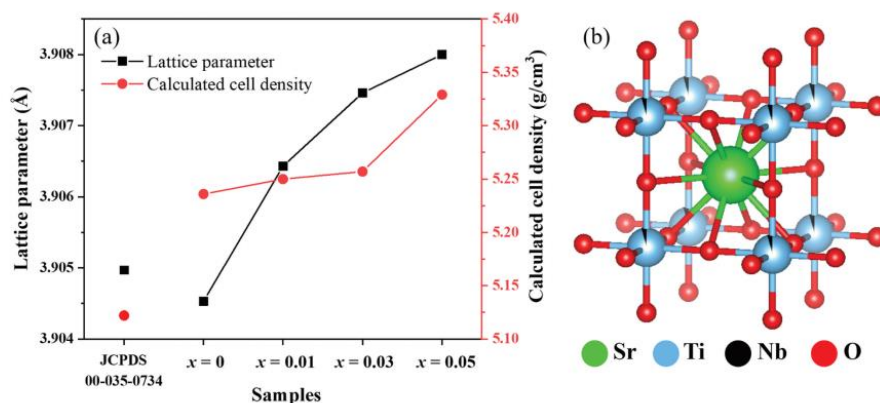


Figure 3. (a) The lattice parameter and calculated cell density (d_{cal}) of STNO nanopowder and (b) the crystal structure of STNO with $x = 0.05$ from Rietveld refinement analysis compared with SrTiO_3 database.

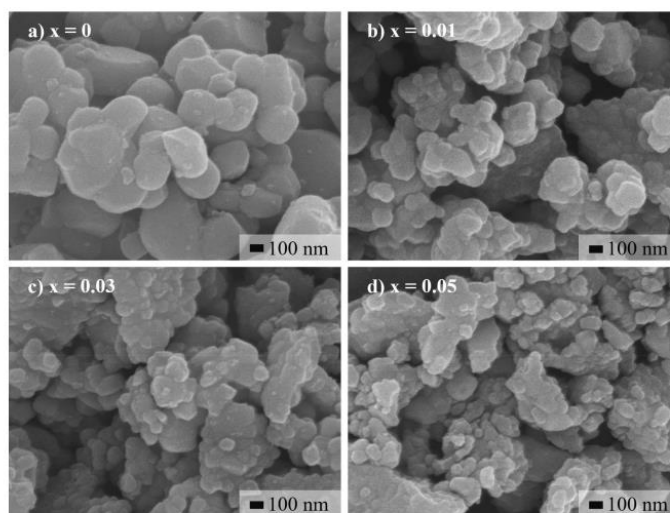


Figure 4. SEM image of STNO nanopowder: (a) $x = 0$, (b) $x = 0.01$, (c) $x = 0.03$, and (d) $x = 0.05$.

[15]. The STNO results are also closer and lower than others reported in the literature, prepared by various techniques, such as the $\text{Sr}_{0.94}\text{Ti}_{0.9}\text{Nb}_{0.1}\text{O}_3$ powder synthesized by a modified glycine-nitrate process (100 nm) [37] and the $\text{SrTi}_{0.95}\text{Nb}_{0.05}\text{O}_3$ powders prepared by ball milling (1 μm) [41].

The SEM image, EDS spectrum, and mapping images of the STNO nanopowder with $x = 0.05$ are shown in Figure 5. In the EDS spectrum Figure 5(b), the signals corresponding to Sr, Ti, Nb, and O are exhibited in

Figure 5(c-f). It is observed that elements Sr, Ti, Nb, and O are uniformly distributed in the STNO nanopowder. The quantitative EDS analysis confirmed that the atomic ratio of Sr, Ti, Nb, and O in STNO nanopowder with $x = 0.05$ is 1:0.85:0.31:3.43. Although the actual chemical composition was examined by EDS analysis, it was inconsistent with the nominal composition due to there being low concentrations of Nb doping, no flat surface in the selected area allowing accurate mapping analysis and measurement (different working distance

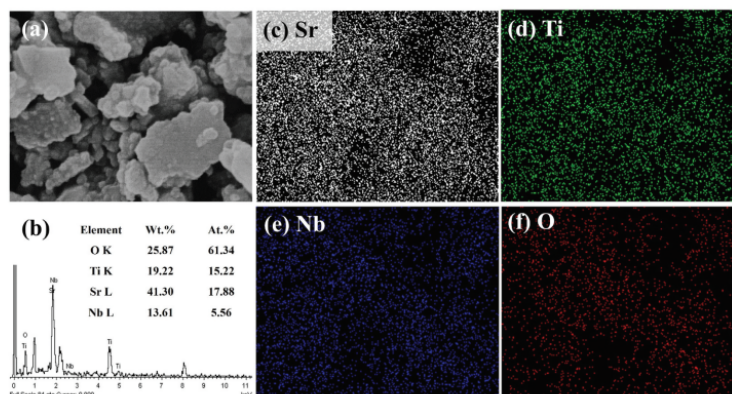


Figure 5. SEM-EDS images and spectrum of the STNO nanopowder with $x = 0.05$.

of the electron beam) and the accuracy of the EDS spectrum was within $\pm 5\%$ relative to the actual value [42].

The optical properties of the STNO samples were investigated by UV-Visible spectra absorbance with $A = -\log(I/I_0)$, with I_0 (intensity of incidence) and I (transmitted radiation) being recorded at wavelengths between 300–600 nm at room temperature (Figure 6). In a general sense, the spectra absorbance was used to observe the absorption edge and energy hole by following the movement of the electrons from the upper bound of the valence band to the lower bound of the conduction band [43]. The absorption capacity of all the samples showed a comparable trend at the absorption edge at 311 nm wavelength. In the high energy region of the absorption edge, the ability of light absorption linearly increased when the photon

energy increased. The relationship of the absorption and photon energy ($h\nu$) is represented by Tauc's relation [31,44];

$$(ah\nu) = B(h\nu - E_g)^n \quad (8)$$

where a denotes the absorption coefficient, B is a constant, E_g is the band gap, and n depends on the type of transition. For the directly allowed transitions, $n = 1/2$, for the indirectly allowed transitions, $n = 2$, for direct forbidden transitions, $n = 3/2$, and indirect forbidden transitions, $n = 3$ [43,45]. The E_g of these samples was investigated by extrapolating the linear portion of the curve to zero absorbance, shown in Figure 6 as the inset plot of $(ah\nu)^2$ versus $h\nu$ for a direct allowed transition. It was found that the E_g of all the STNO samples is 4.11 eV.

The optical properties of nanopowder depend on their crystallinity, particle size, and synthesis method, such as when the E_g increases with the decreasing particle size. For the undoped STNO samples, the E_g in this study was higher than reported in another research. For example, the E_g of the STO samples prepared by the microwave-assisted hydrothermal method were 3.5 ± 0.1 eV [35], and for the STO powders prepared by the liquid-solid reaction method, the E_g was 3.4–3.5 eV [46], and when the STO were prepared by high-temperature solid-state reaction, the direct E_g was 3.55–3.67 eV [47]. In addition, the STO samples that had a cubic structure showed a higher E_g than STO prepared by the topotactic, with rodlike and cubic samples exhibiting E_g of 3.0 and 3.04 eV [48]. On the other hand, for Nb-doped STNO samples, the doping usually affects the E_g value, such as the E_g of Al-doped STO (3.45 eV) being better than the undoped STO (3.30 eV), where both of them were prepared by solid-state reaction [17]. Unfortunately, in our research, the

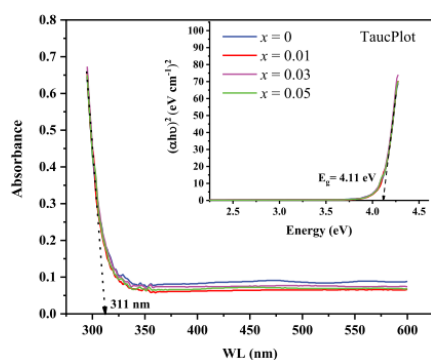


Figure 6. UV-vis spectra of the STNO samples ($x = 0, 0.01, 0.03$ and 0.05) and inset plots of $(ah\nu)^2$ as a function of photon energy ($h\nu$).

E_g of the STNO was not changed at varying concentrations of Nb-doped. This may have been due to the low concentration of Nb-doped that we used.

Generally, the decolorization of dye is used to determine the effectiveness of a photocatalytic reaction. The decolorization efficiency (%DE) follows Eq. 6. Figure 7(a) presents the %DE of MB by STNO with $x = 0, 0.01, 0.03$, and 0.05 as the photocatalyst under a UV light. The photolysis tests showed a slight change in the concentration of MB of not more than 10%, which is within the acceptable value range. The photocatalytic activities of STNO with $x = 0, 0.01, 0.03$, and 0.05 increased with higher Nb content. The %DE of MB for all STNO increased hourly until 8 h; the %DE using STNO with $x = 0$ and 0.01 was similar at around 20%, while $x = 0.03$ and 0.05 were similar at around 50%. The factors affecting photocatalytic efficiency are crystallinity, crystal structure, and particle size of the material [49]. The results indicated that the concentration of Nb dopant leads to increased photocatalytic activity of the Nb-doped STNO due to the smallest particle size providing a larger active reaction site and empowering the

adsorption of more MB on the STNO photocatalyst surface, indicating that photocatalytic efficiency reached a maximum at the highest level of Nb, $x = 0.05$.

The rate of reaction can be specified by chemical kinetics. The first-order reaction kinetics constant (k) is determined using the equation: ($kt = \ln C_0/C$) [44], where C and C_0 are the real-time and initial concentrations of MB. The k value for STNO also increased with Nb doping content increases, as shown in Figure 7(b). Obviously, for STNO with $x = 0$ and 0.01 , the k value is similar at around 0.033 – 0.034 . With $x = 0.03$ and 0.05 the k values are similar at 0.076 – 0.079 , according to the %DE shown in Figure 7(a). The great value for Nb-doped STNO as a photocatalysis reaction was in the STNO sample with $x = 0.05$, as shown in Figure 7(c). The absorption peak (λ_{max}) of MB was at 663 nm. After 8 h, the λ_{max} of MB continuously decreased and shifted to the lower wavelength from 663 nm to 656 nm. The blue shift is due to the stepwise removal of methyl or methylamine, and the decolorization of the MB, which results in

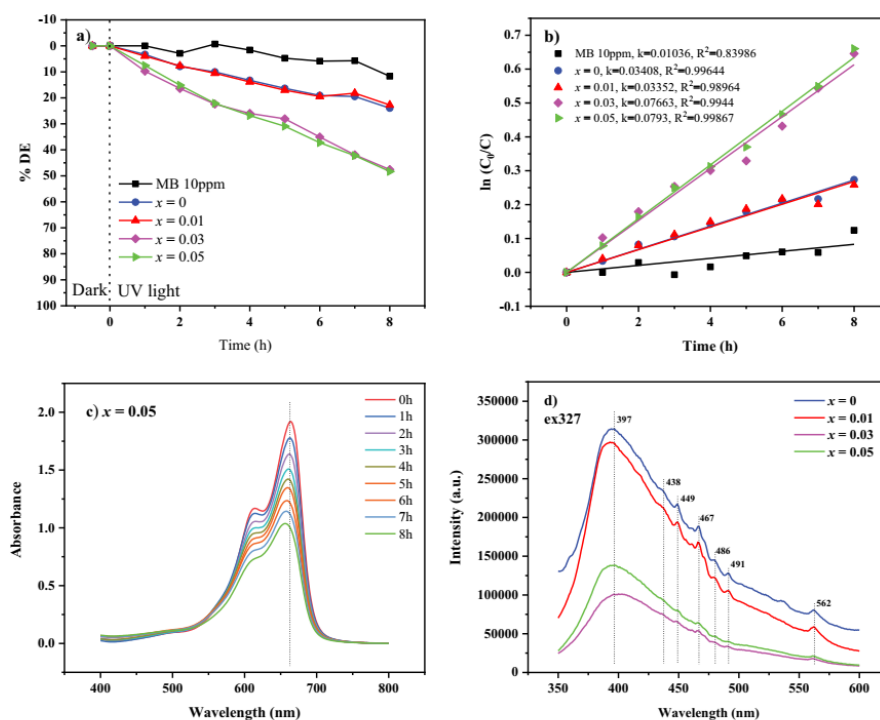


Figure 7. (a) The photocatalytic decolorization efficiency (%DE) of MB irradiated beneath the UV lamp, (b) The Pseudo-first order kinetics of photocatalytic decolorization of MB, (c) Time-dependent absorption spectra of MB solution using STNO photocatalyst with $x = 0.05$ and (d) photoluminescence spectra of the STNO sample with $x = 0$ and 0.05 .

the λ_{\max} of the MB decreasing [32]. For all SNT0 samples, the spectra absorbance follows the same trends.

Photoluminescence is widely used to characterize the optical properties of semiconductors. The electrons of the semiconductor substance are stimulated by the photon absorbance, where its electrons move to a higher energy state from a lower energy state, after which there is a relaxation phase during which photons are again emitted or released. The interval between the absorption and emission phases of the photons may vary depending on the substance. Most UV light absorbers emit light in the visible range so that colors can be seen in these substances. The photoluminescence of all our STNO samples, after excitation at 327 nm in the range of 350–600 nm at room temperature, is shown in Figure 7(d). The emission peaks of all the samples are similar trends, 397, 438, 450, 466, 479, 491, and 562 nm, indicated in violet, blue, and green. The high-intensity emission band at 397 nm indicates high electron-hole recombination [50]. The peak emission at 395 nm indicates that the violet colors are due to shallow surface defects [35]. Also, peak emissions at 438, 450, 466, 479, and 491 nm are blue due to Sr deficiency in the crystal structure, and the peaks emitted at 562 nm, showing as green emissions, are caused by oxygen vacancy in the STO lattice, according to the previous study [51]. Moreover, the photoluminescence emission intensity related to the recombination of charge carriers in a semiconductor can be used to explain the photocatalytic activity of the photocatalyst. From Figure 7(d), the photoluminescence emission intensity of Nb-doped STNO nanopowder is lower than the undoped STNO sample ($x = 0$), indicating lower electron-hole pair recombination and photocatalytic reaction enhancement. Remarkably, the result of the photoluminescence emission intensity of the Nb-doped STNO with $x = 0$ and 0.01 are nearly closed, while $x = 0.03$ and 0.05 are closed together with lower than those of $x = 0$ and 0.01. It is indicated that the photoluminescence emission intensity of the Nb-doped STNO corresponds to the photocatalytic efficiency of the sample, as shown in Figure 7(a).

The Nyquist plot from the Electrochemical Impedance Spectroscopy (EIS) is used to analyze the charge carrier migration of photoelectrode in a three-electrode system. The semicircle accords with the charge transfer resistance at the photoelectrode interface R_{ct} , which is the solution resistance. This is estimated by the x -intercept of the Nyquist plot and describes the overall resistance between the photoelectrode and the electrolyte. Figure 8 shows a Nyquist plot of all the STNO samples, using an Autolab PGSTAT302N at an applied potential of 1 V_{ref} at pH 6 (Na_2SO_4 electrolyte 0.1 M) and the frequency range from 1–1000 Hz and amplitude of 0.01. The experimental data are compared with the simulation

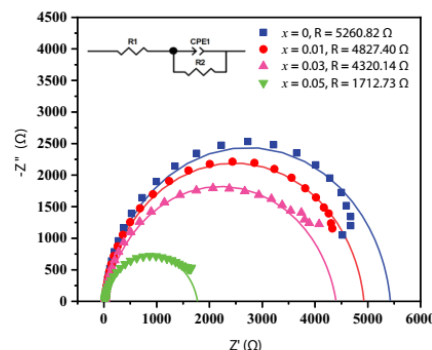


Figure 8. Experimental data and simulation of EIS Nyquist plot of STNO photocatalyst sample.

data by fitting the experimental data by the equivalent circuit, as shown in the inset of Figure 8. The simulations were performed, with the impedance values being 5260.82 Ω for $x = 0$, 4827.40 Ω for $x = 0.01$, 4320.14 Ω for $x = 0.03$, and 1712.73 Ω for $x = 0.05$. The equivalent circuit of all STNO samples is shown in the inset of Figure 8. The smaller semicircle in the Nyquist plots is for increases in the Nb concentration, suggesting that the highest level of effective charge transfer efficiency occurs at higher Nb content but not at low Nb content or without doping [52].

The Mott-Schottky plots of STNO samples were carried out with the EIS that measures an electrochemical interface as its DC voltage changes and with a fixed frequency. The graph can be plotted by the voltage and capacitance and are used to characterize the flat band potential and understand the charge transport in STNO. So, to consider the donor density (N_D) and the flat band potential (V_{fb}) of STNO photoelectrode, a Mott-Schottky analysis was performed. Depending on the depletion layer model, the capacitance of the semiconductor space charge layer (C_{sc}) is based on the applied potential (V_{appl}). The Mott-Schottky equation is expressed in equation 9 [39]:

$$(1/C)^{-2} = (2/\epsilon_r \epsilon_0 e N_D)(V_{appl} - V_{fb} - k_b T/e) \quad (9)$$

where e is the charge of the electron, ϵ_r is the semiconductor dielectric constant, ϵ_0 is the vacuum permittivity, T is the absolute temperature, and k_b is the Boltzmann constant (1.38×10^{-23} J/K).

Figure 9 shows the Mott-Schottky plot of the STNO samples from the EIS spectroscopy analysis (Autolab PGSTAT302N) by applying the potential range of 1.2–2.0 V at pH 6 (Na_2SO_4 electrolyte 0.1 M) at a 1000 Hz frequency. The Mott-Schottky curves for all samples demonstrated a positive slope, indicating their n -type character similar to that reported in the literature [39,53]. The flat band potentials (V_{fb}) determined

from the x -intercepts of the curves are -0.10 , -0.18 , -0.25 , and -0.30 V for STNO samples with $x = 0$, 0.01 , 0.03 , and 0.05 , respectively. The applied potential in NHE scale (E_{NHE}) was calculated by the following equation:

$$E_{\text{NHE}} = E_{\text{Ag/AgCl}} + 0.21 \quad (10)$$

Accordingly, the V_{fb} values of STNO samples with $x = 0$, 0.01 , 0.03 , and 0.05 are 0.11 , 0.03 , -0.04 and -0.11 (vs. NHE), respectively. It was found that the V_{fb} values for STO and STNO samples were shifted toward negative value when Nb content increased, favored its better photocatalytic activity. As a rule of thumb, a conduction band potential (E_{cb}) of n-type

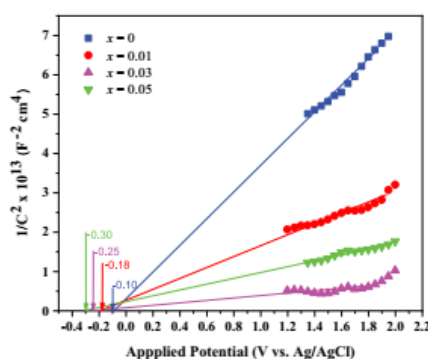


Figure 9. A Mott-Schottky plot of STNO nanopowder.

semiconductor is more negative by -0.1 eV than E_{fb} level [54]. Therefore, E_{cb} of STNO samples with $x = 0$, 0.01 , 0.03 , and 0.05 could be determined as 0.01 , -0.07 , -0.14 , and -0.21 (vs.NHE), respectively. For the valence band potentials (E_{vb}) of the STNO samples are a result from combining the E_{cb} with the E_g values. Thus, the E_{vb} of the STNO samples are 4.12 V (vs.NHE) for $x = 0$, 4.04 V (vs.NHE) for $x = 0.01$, 3.97 V (vs.NHE) for $x = 0.03$, and 3.90 V (vs.NHE) for $x = 0.05$. This result indicates in Figure 10 cooperate with the mechanism of photocatalysis process.

Thereby, the E_{cb} of the STNO samples are 0.01 V (vs. NHE) for $x = 0$, -0.07 V (vs.NHE) for $x = 0.01$, -0.14 V (vs. NHE) for $x = 0.03$, and -0.21 V (vs.NHE) for $x = 0.05$. The mechanism of photocatalytic decolorization of MB dye on STNO photocatalyst under UV irradiation is shown in Figure 10. The process of photocatalysis reaction can be partitioned into three steps. First, the photocatalysis of STNO is energized by UV light with photo-energy higher than the E_g of the photocatalysis to create photoinduced electrons (e^-) and gaps (h^+). The electron is produced when electrons from the valence band (VB) move to the conduction band (CB), during which process gaps within the valence band are produced (Eq. 11). Next, the e^- and h^+ respond with O_2 and H_2O (or OH^-) to produce highly receptive hydroxyl radicals (OH^\cdot) and superoxide radicals ($\text{O}_2^{\cdot-}$). The H_2O or OH^- that are adsorbed on the surface of the photocatalysis are oxidized by the h^+ to create OH^\cdot (Eq.12). The O_2 accompanying the adsorption on the surface by the photocatalysis reacts with e^- to generate the $\text{O}_2^{\cdot-}$ (Eq.13). In a further step, $\text{O}_2^{\cdot-}$ reacts with H_2O to

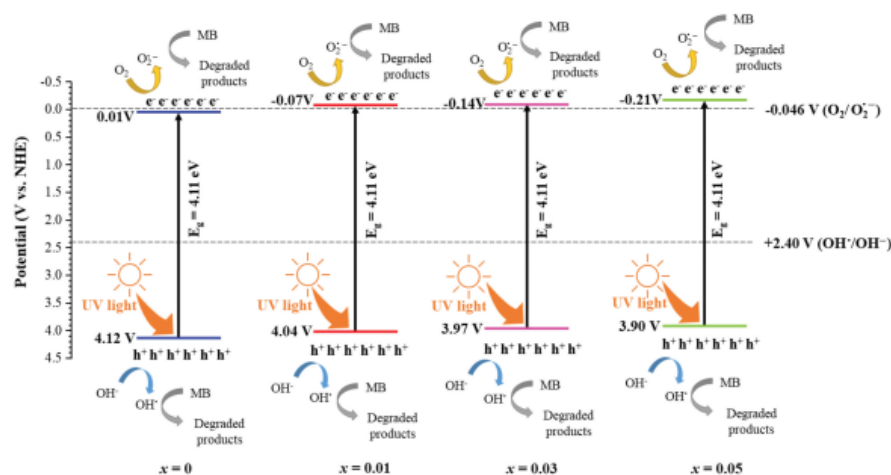
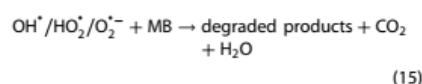
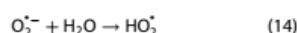
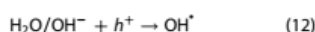
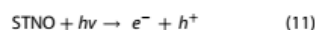


Figure 10. The charge transfer and photocatalytic mechanism of STNO nanopowder.

produce hydroperoxyl radical (HO_2^\bullet) (Eq.14). Finally, these hydroxyl radicals, superoxide radicals, and hydroperoxyl radicals decompose the MB dye into CO_2 , H_2O and degraded products of MB, which could be 2-amino-5-(*NN*-methylformamide) benzene sulfonic acid, 2-amino-5-(methylamino)-hydroxybenzene sulfonic acid, and benzenesulfonic acid [55] (Eq.15). This entire process can be summarized in the following equations:



Based on the above mechanisms, there are three reasons for the occurrence of the outstanding photocatalytic activity of the STNO samples. Firstly, the particle size of the Nb-doped STNO samples prepared by the sol-gel auto-combustion method provides a nanosized particle, and the particle size decreases with increasing Nb doping content. Secondly, the smaller semicircle of the Nyquist plots Nb concentration increases, suggesting a higher electron transfer conductivity. Finally, the E_{cb} calculated from the Mott-Schottky equation of the STNO samples is more negative than the

reduction potential of $\text{O}_2/\text{O}_2^{\bullet-}$ (−0.046 V vs. NHE) [54], and the E_{vb} of the STNO samples are more positive than the reduction potential of $\text{OH}^\bullet/\text{OH}^-$ (+2.40 V vs. NHE) [54], so has a good oxidation ability to degrade the organic pollutants [56]. Therefore, the Nb-doped STNO sample with $x = 0.05$ has the smallest particle size, the lowest semicircle of the Nyquist plots, and the lowest E_{cb} and E_{vb} calculated from the Mott-Schottky equation. These results for the STNO sample with $x = 0.05$ indicate the highest %DE of photocatalytic activity.

Table 2 illustrates the decolorization of MB in an aqueous solution under a UV source as identified in previous research [6,7]. When comparing our results with that previous research, it was found that the photocatalytic activity of undoped STNO was lower than STO. This was due to the larger particle sizes and the undoped STNO having no porous structures. Comparing the photodecolorization efficiency of MB under UV-visible irradiation with several other methods [25,32,49], the photocatalytic activity of undoped STNO was less than STO synthesized by those methods (also illustrated in Table 2).

The photocatalytic activity of metal-doped STNO (Table 2) could not be directly compared to our research due to different conditions of the photocatalytic system such as light source intensity, amount of photocatalytic loading, and the concentration of dye. However, no report on the photodecolorization efficiency of MB using Nb-doped STNO as photocatalysts under UV irradiation has been found. In our study, the Nb content was significantly enhanced the photocatalytic activities of STNO nanopowder.

Table 2. The summary of the photodecolorization efficiency (%DE) of several dyes using undoped-STO and metal-doped STO photocatalysts with different preparation methods, light sources, and photocatalytic conditions.

Photocatalyst	Preparation method	Light sources	Types of dye	Photocatalytic conditions				Ref.
				Photocatalyst Loading	Initial Concentration	Reaction Time	%DE	
SrTiO_3	Polyacrylamide gel route	20 W Mercury lamp (UV)	CR RhB MO MB	1000 mg/L	10 ppm	10 h	90% 35% 33% 53%	[6]
SrTiO_3	Combustion	30 W UV	MB	200 mg/L	31.98 ppm	70 min	65%	[7]
SrTiO_3	Facile solvothermal	Visible light	MB	500 mg/L	10 ppm	120 min	62.7%	[25]
B- SrTiO_3							70.3%	
SrTiO_3	Amino acids as dopants	UV-Visible	MB	200 mg/L	5 ppm	180 min	100%	[32]
G-N-STO3	source and surface area promoters	irradiation				90 min	100%	
STO-P	Ball milled for different time	125 W UV-Visible irradiation	MB	1000 mg/L	3.19 ppm	210 min	100%	[49]
STO-20						150 min	100%	
La-doped SrTiO_3 (La = 0.5)	Sol-gel	500 W Xe arc lamp	$\text{K}_2\text{Cr}_2\text{O}_7$ (Cr (VI))	1000 mg/L	20 ppm	100 min	84%	[57]
SrTiO_3 (La,Cr)-6	Sol-gel hydrothermal	300 W Xe lamp	Tetracycline (TC)	500 mg/L	20 ppm	90 min	80%	[58]
V-doped SrTiO_3	Electrospinning and thermal diffusion	175 W mercury lamp	MO	300 mg/L	10 ppm	75 min	90%	[59]
La-Fe co-doped SrTiO_3	Solid state reaction	Visible light	MO	600 mg/L	5 ppm	150 min	90%	[60]
SrTiO_3	Sol-gel auto combustion	108 W UV	MB	500 mg/L	10 ppm	8 h	39%	This study
Nb-doped SrTiO_3 (Nb = 0.05)							55%	

4. Conclusion

SrTi_{1-x}Nb_xO₃ (STNO) nanopowder with $x = 0, 0.01, 0.03$, and 0.05 was successfully synthesized by the sol-gel auto combustion technique with two fuel mixtures. The STNO nanopowder exhibited a pure phase with cubic perovskite structures. The increased Nb doping content increased the lattice parameter. Also, the unit cell density increased while the particle size decreased with a non-porous structure. The electron-hole pair recombination and charge transfer resistance on the surface of the STNO photoelectrode materials decreased with increased Nb doping content. These factors promoted the transportation of charge carriers, leading to improved photocolorization efficiency. Therefore, STNO nanopowder with $x = 0.05$ is the optimal level for photocatalytic decolorization of MB under UV irradiation. These findings demonstrate that the structural, optical, and electrochemical properties of STNO nanopowder synthesized by the sol-gel auto-combustion technique enhance photocatalytic activity.

Acknowledgments

This work was supported by Thailand Science Research and Innovation (TSRI) through the Royal Golden Jubilee Ph.D. Program (RGJ) (Grant No. PHD/0049/2560) and The National Science, Research and Innovation Fund (NSRF) through Naresuan University (R2565B028). Additional support was provided by the School of Renewable Energy and Smart Grid Technology, Naresuan University, Thailand. We also thank Miss Jiraphorn Wongsan and Miss Sunisa Chaiyarat, Faculty of Liberal Arts and Science, Roi Et Rajabhat University, Miss Sasinan Thongchuay, and Miss Phakawadee Khiawyai, Faculty of Science and Technology, Surattani Rajabhat University and Miss Sunanta Yimsabai, Department of Physics, Faculty of Science, Naresuan University for their support for synthesis activity. Thanks also to Mr. Roy I. Morien of the Naresuan University Graduate School for his efforts in editing the grammar, syntax, and English expression in this paper.

Disclosure statement

No potential conflict of interest was reported by the author(s).

ORCID

Tawat Suriwong  <http://orcid.org/0000-0002-8674-622X>

References

- [1] Hassanpour M, Safardoust-Hojaghan H, and Salavati-Niasari M. Degradation of methylene blue and Rhodamine B as water pollutants via green synthesized Co₃O₄/ZnO nanocomposite. *J Mol Liq.* 2017;229:293–299.
- [2] Koe WS, Lee JW, and Chong WC, et al. An overview of photocatalytic degradation: photocatalysts, mechanisms, and development of photocatalytic membrane. *Environ Sci Pollut Res Int.* 2020 ;27 (3):2522–2565.
- [3] Jabbar ZH, and Graimed BH. Recent developments in industrial organic degradation via semiconductor heterojunctions and the parameters affecting the photocatalytic process: a review study. *Journal of Water Process Engineering.* 2022;47:102671.
- [4] Al-hamoud K, Shaik MR, and Khan M, et al. Pulicaria undulata extract-mediated eco-friendly preparation of TiO₂ nanoparticles for photocatalytic degradation of methylene blue and methyl Orange. *ACS Omega.* 2022;7(6):4812–4820.
- [5] Passi M, and Pal B. A review on CaTiO₃ photocatalyst: activity enhancement methods and photocatalytic applications. *Powder Technol.* 2021;388:274–304.
- [6] Xian T, Yang H, Dai JF, et al. Photocatalytic properties of SrTiO₃ nanoparticles prepared by a polyacrylamide gel route. *Mater Lett.* 2011;65(21–22):3254–3257.
- [7] Saito G, Nakasugi Y, Sakaguchi N, et al. Glycine–nitrate-based solution-combustion synthesis of SrTiO₃. *J Alloys Compd.* 2015;652:496–502.
- [8] Narath S, Korothe SK, Shankar SS, et al. Cinnamomum tamala leaf extract stabilized zinc oxide nanoparticles: a promising photocatalyst for methylene blue degradation. *Nanomaterials.* 2021;11(6):1558.
- [9] Akilarasan M, Tamilalagan E, and Chen S-M, et al. An eco-friendly low-temperature synthetic approach towards micro-pebble-structured GO@SrTiO₃ nanocomposites for the detection of 2,4,6-trichlorophenol in environmental samples. *Mikrochim Acta.* 2021;188 (3):72.
- [10] Irshad M, Ain QT, and Zaman M, et al. Photocatalysis and perovskite oxide-based materials: a remedy for a clean and sustainable future. *RSC Adv.* 2022 ;12 (12):7009–7039.
- [11] Kumar A, Kumar A, and Krishnan V. Perovskite Oxide Based Materials for Energy and Environment-Oriented Photocatalysis. *ACS Catal.* 2020 2020;10 (17):10253–10315.
- [12] Phoon BL, Lai CW, Juan JC, et al. Recent developments of strontium titanate for photocatalytic water splitting application. *Int J Hydrogen Energy.* 2019;44 (28):14316–14340.
- [13] Monsef R, Soofivand F, and Abbas Alshamsi H, et al. Sonochemical synthesis and characterization of PrVO₄/CdO nanocomposite and their application as photocatalysts for removal of organic dyes in water. *J Mol Liq.* 2021;336:116339.
- [14] Kuang Q, and Yang S. Template synthesis of single-crystal-like porous SrTiO₃ nanocube assemblies and their enhanced photocatalytic hydrogen evolution. *ACS Appl Mater Interfaces.* 2013;5 (9):3683–3690.
- [15] Kato H, Kobayashi M, and Hara M, et al. Fabrication of SrTiO₃ exposing characteristic facets using molten salt flux and improvement of photocatalytic activity for water splitting. *Catal Sci Technol.* 2013;3 (7):1733–1738.
- [16] Yu H, Ouyang S, Yan S, et al. Sol-gel hydrothermal synthesis of visible-light-driven Cr-doped SrTiO₃ for efficient hydrogen production. *J Mater Chem.* 2011;21 (30):11347.

- [17] Saadetnejad D, Yildirim R. Photocatalytic hydrogen production by water splitting over Au/Al-SrTiO₃. *Int J Hydrogen Energy*. 2018;43(2):1116–1122.
- [18] Puangpetch T, Chavadej S, Sreethawong T. Hydrogen production over Au-loaded mesoporous-assembled SrTiO₃ nanocrystal photocatalyst: effects of molecular structure and chemical properties of hole scavengers. *Energy Convers Manag*. 2011;52(5):2256–2261.
- [19] Aravinthkumar K, John Peter I, and Anandha Babu G, et al. Enhancing the short circuit current of a Dye-Sensitized Solar cell and photocatalytic dye degradation using Cr doped SrTiO₃ interconnected spheres. *Mater Lett*. 2022 ;319:132284.
- [20] Karczewski J, Bochentyn B, and Gazda M, et al. Electrical and structural properties of Nb-doped SrTiO₃ ceramics. *J Electroceram*. 2010;24:326–330.
- [21] Ming T, Suntivich J, May KJ, et al. Visible light photo-oxidation in Au nanoparticle sensitized SrTiO₃ Nb photoanode. *J Phys Chem C*. 2013;117(30):15532–15539.
- [22] Drozd E, and Kolezynski A. The structure, electrical properties and chemical stability of porous Nb-doped SrTiO₃ – experimental and theoretical studies. *RSC Adv*. 2017;7(46):28898–28908.
- [23] Mei B, Byford H, and Bledowski M, et al. Beneficial effect of Nb doping on the photoelectrochemical properties of TiO₂ and TiO₂-polyheptazine hybrids. *Sol Energy Mater Sol Cells*. 2013;117:48–53.
- [24] Su H, Huang Y-T, Chang Y-H, et al. The synthesis of Nb-doped TiO₂ nanoparticles for improved-performance dye sensitized solar cells. *Electrochim Acta*. 2015;182:230–237.
- [25] Bantawal H, Shenoy US, and Bhat DK. Tuning the photocatalytic activity of SrTiO₃ by varying the Sr/Ti ratio: unusual effect of viscosity of the synthesis medium. *J Phys Chem C*. 2018;122(34):20027–20033.
- [26] Aruna, ST , and Mukasyan, AS. Combustion synthesis and nanomaterials. *Curr Opin Solid State Mater Sci*. 2008;12(3):44–50.
- [27] Bhagwat VR, Humbe AV, and More SD, et al. Sol-gel auto combustion synthesis and characterizations of cobalt ferrite nanoparticles: different fuels approach. *Mater Sci Eng B*. 2019;248:114388.
- [28] Vahdat Vasei H, Masoudpanah SM, and Adeli M, et al. Photocatalytic properties of solution combustion synthesized ZnO powders using mixture of CTAB and glycine and citric acid fuels. *Adv Powder Technol*. 2019;30(2):284–291.
- [29] Meng YY, He MH, and Zeng Q, et al. Synthesis of barium ferrite ultrafine powders by a sol-gel combustion method using glycine gels. *J Alloys Compd*. 2014;583:220–225.
- [30] Panthong P, Klaytae T, and Boonma K, et al. Preparation of SrTiO₃ nanopowder via Sol-gel combustion method. *Ferroelectrics*. 2013;455(1):29–34.
- [31] Nunocha P, Kaewpanha M, and Bongkarn T, et al. A new route to synthesizing La-doped SrTiO₃ nanoparticles using the sol-gel auto combustion method and their characterization and photocatalytic application. *Mater Sci Semicond Process*. 2021;134:106001.
- [32] Konstas P-S, Konstantinou I, Petrakis D, et al. Development of SrTiO₃ photocatalysts with visible light response using amino acids as dopant sources for the degradation of organic pollutants in aqueous systems. *Catalysts*. 2018;8(11):528.
- [33] Pan W, Cao M, Hao H, et al. Defect engineering toward the structures and dielectric behaviors of (Nb, Zn) co-doped SrTiO₃ ceramics. *J Eur Ceram Soc*. 2020;40(1):49–55.
- [34] Jiao S, Yan J, Sun G, et al. Electronic structures and optical properties of Nb-doped SrTiO₃ from first principles. *J Semicond*. 2016;37(7):072001.
- [35] Souza AE, Santos GTA, and Barra BC, et al. Photoluminescence of SrTiO₃: influence of particle size and morphology. *Cryst Growth Des*. 2012;12(11):5671–5679.
- [36] Demydov D, Klabunde KJ. Characterization of mixed metal oxides (SrTiO₃ and BaTiO₃) synthesized by a modified aerogel procedure. *J Non-Crystalline Solids*. 2004;350:165–172.
- [37] Blennow P, Hansen KK, and Wallenberg LR, et al. Synthesis of Nb-doped SrTiO₃ by a modified glycine-nitrate process. *J Eur Ceram Soc*. 2007;27(13):3609–3612.
- [38] Wunderlich W, Ohta H, and Koumoto K. Enhanced effective mass in doped SrTiO₃ and related perovskites. *Phys B Condens Matter*. 2009;404(16):2202–2212.
- [39] Pinheiro AN, Firmiano EGS, Rabelo AC, et al. Revisiting SrTiO₃ as a photoanode for water splitting: development of thin films with enhanced charge separation under standard solar irradiation. *RSC Adv*. 2014;4(4):2029–2036.
- [40] Gosens I, Post JA, de la Fonteyne LJJ, et al. Impact of agglomeration state of nano- and submicron sized gold particles on pulmonary inflammation. *Part Fibre Toxicol*. 2010;7(1):37.
- [41] Liu D-Q, Zhang Y-W, and Kang H-J, et al. Effect of Nb doping on microstructures and thermoelectric properties of SrTiO₃ ceramics. *Chin Phys B*. 2018;27(4):047205.
- [42] Newbury DE, Ritchie NWM. Is scanning electron microscopy/energy dispersive X-ray spectrometry (SEM/EDS) quantitative? *Scanning*. 2013;35(3):141–168.
- [43] Suriwong T, Thongtem T, and Thongtem S. Thermoelectric and optical properties of CuAlO₂ synthesized by direct microwave heating. *Curr Appl Phys*. 2014;14(9):1257–1262.
- [44] Xia Y, He Z, Lu Y, et al. Fabrication and photocatalytic property of magnetic SrTiO₃/NiFe₂O₄ heterojunction nanocomposites. *RSC Adv*. 2018;8(10):5441–5450.
- [45] Agilandewari K, Ruban Kumar A. Optical, electrical properties, characterization and synthesis of Ca₂Co₂O₅ by sucrose assisted sol gel combustion method. *Adv Powder Technol*. 2014;25(3):904–909.
- [46] Posadas AB, Lin C, Demkov AA, et al. Bandgap engineering in perovskite oxides: al-doped SrTiO₃. *Appl Phys Lett*. 2013;103(14):142906.
- [47] Townsend TK, Browning ND, and Osterloh FE. Nanoscale strontium titanate photocatalysts for overall water splitting. *ACS Nano*. 2012;6(8):7420–7426.
- [48] Cao J, Huang X, Liu Y, et al. Enhanced photocatalytic activity of SrTiO₃ photocatalyst by topotactic preparation. *Mater Res Express*. 2016;3(11):115903.
- [49] Kumar V, Choudhary S, and Malik V, et al. Enhancement in photocatalytic activity of SrTiO₃ by tailoring particle size and defects. *Phys Status Solidi A*. 2019;216(18):1900294.
- [50] Muralidharan M, Anbarasu V, Elaya Perumal A, et al. Carrier mediated ferromagnetism in Cr doped SrTiO₃ compounds. *J Mater Sci*. 2015;26(9):6352–6365.

- [51] Padmini E, Ramachandran K. Investigation on versatile behaviour of Cd doped SrTiO₃ perovskite structured compounds. *Solid State Commun.* **2019**;302:113716.
- [52] Wang XL, Fang WQ, and Li YH, et al. Bottom-Up enhancement of g-C₃N₄ photocatalytic H₂ Evolution utilising disordering intermolecular interactions of precursor. *Int. J.Photoenergy.* **2014**;2014:1–8. .
- [53] Cai T, Liu Y, and Wang L, et al. Silver phosphate-based Z-Scheme photocatalytic system with superior sunlight photocatalytic activities and anti-photocorrosion performance. *Appl Catal B Environ.* **2017**;208:1–13. .
- [54] Chachvalvutikul A, Luangwanta T, and Pattison S, et al. Enhanced photocatalytic degradation of organic pollutants and hydrogen production by a visible light-responsive Bi₂WO₆/ZnIn₂S₄ heterojunction. *Appl Surf Sci.* **2021** ;544:148885.
- [55] Yang C, Dong W, and Cui G, et al. Highly efficient photocatalytic degradation of methylene blue by P2ABSA-modified TiO₂ nanocomposite due to the photosensitization synergetic effect of TiO₂ and P2ABSA. *RSC Adv.* **2017**;7(38):23699–23708.
- [56] Shenoy S, and Tarafder K. Enhanced photocatalytic efficiency of layered CdS/CdSe heterostructures: insights from first principles electronic structure calculations. *J Phys.* **2020**;32(27):275501.
- [57] Yang D, Zou X, Sun Y, et al. Fabrication of three-dimensional porous La-doped SrTiO₃ microspheres with enhanced visible light catalytic activity for Cr(VI) reduction. *Front Chem Sci Eng.* **2018**;12(3):440–449.
- [58] Jiang J, Jia Y, Wang Y, et al. Insight into efficient photocatalytic elimination of tetracycline over SrTiO₃ (La,Cr) under visible-light irradiation: the relationship of doping and performance. *Appl Surf Sci.* **2019**;486:93–101.
- [59] Jing P, Lan W, Su Q, et al. High photocatalytic activity of V-doped SrTiO₃ porous nanofibers produced from a combined electrospinning and thermal diffusion process. *Beilstein J Nanotechnol.* **2015**;6:1281–1286.
- [60] Abdi M, Mahdikhah V, and Sheibani S. Visible light photocatalytic performance of La-Fe co-doped SrTiO₃ perovskite powder. *Opt Mater.* **2020**;102:109803.

Appendix C Thermoelectric properties of La-doped A-site SrTiO₃ ceramics synthesised by the sol-gel auto-combustion technique.

MATERIALS RESEARCH INNOVATIONS
https://doi.org/10.1080/14328917.2023.2196479



Thermoelectric properties of La-doped A-site SrTiO₃ ceramics synthesised by the sol-gel auto-combustion technique

Pornnipa Nunocha^a, Theerachai Bongkarn^{b,c}, Adul Harnwungmoung^d, Sora-at Tanusilp^e and Tawat Suriwong^{a,c}

^aSchool of Renewable Energy and Smart Grid Technology, Naresuan University, Phitsanulok, Thailand; ^bFaculty of Science, Department of Physics, Naresuan University, Phitsanulok, Thailand; ^cResearch Center for Academic Excellence in Applied Physics, Faculty of Science, Naresuan University, Phitsanulok, Thailand; ^dFaculty of Science and Technology, Rajamangala University of Technology Suvarnabhumi, Nonthaburi, Thailand; ^eDepartment of Electrical Engineering, Faculty of Engineering, Khon Kaen University, Khon Kaen, Thailand

ABSTRACT

Sr_(1-x)La_xTiO₃ (SLTO) nanopowder ($x = 0, 0.01, 0.05, 0.07$, and 0.10) were effectively synthesised by the sol-gel auto-combustion process. Bulk ceramics samples were produced by spark plasma sintering (SPS) in an Ar atmosphere. The XRD pattern of the undoped SLTO nanopowder showed the pure phase and the impurity phase (TiO₂) was detected in the La-doped SLTO samples. However, the impurity phase disappeared after producing the bulk samples with the SPS process. All the samples exhibited a negative Seebeck coefficient (S). The electrical conductivity (σ) and negative S of all the SLTO samples increased with increasing temperature and reached a maximum value at 800 K. The thermal conductivity (κ) decreased with increasing temperature and increasing La content. The SLTO with $x = 0.01$ showed the largest σ , negative S , power factor ($S^2\sigma$) and dimensionless figure of merit (ZT) at 800 K.

ARTICLE HISTORY

Received 24 November 2022
Accepted 21 March 2023

KEYWORDS

Oxide thermoelectric materials; Electrical property; Seebeck coefficient; Thermal property; Thermoelectricity

1. Introduction

Heat waste accounts for more than 60% of the total energy produced globally. Thermoelectric (TE) materials have been widely used for both electricity generation and cooling. The efficiency of thermoelectric materials can be calculated by the dimensionless figure of merit (ZT) [1,2], which define as:

$$ZT = \frac{S^2\sigma T}{\kappa} \quad (1)$$

where S is the Seebeck coefficient (TE power) ($\mu\text{V/K}$), σ is the electrical conductivity (S/m), T is the absolute temperature (K), and κ is the total thermal conductivity (W/mK). With a large $S^2\sigma$ and a low κ , a high ZT can be attained; however, it is challenging to achieve an ideal ZT , due to the S , σ and κ being interrelated and strongly coupled with each other [3].

The advantages of oxide TE materials include a low cost, being environmentally friendly, and operating at high temperatures [4]. In the last 10 years, the most studied oxide TE materials are $\text{Ca}_3\text{Co}_2\text{O}_9$ for the p-type and ZnO , SrTiO_3 , and CaMnO_3 for n-type [5], and there has been recent interest in the use of the perovskite oxide SrTiO_3 in TE applications. It is well known that SrTiO_3 is made of metal oxide candidates with a cubic perovskite structure (lattice parameter $a = b = c = 3.905 \text{ \AA}$) [6] that exhibits a very high melting point of 2080°C , suggesting the potential for TE application at high temperatures [7], known as n-type TE materials. Although undoped SrTiO_3 has a large S of around $850 \mu\text{V/K}$, it also has low σ and high κ [8]. The strategy to improve the TE properties of TE materials is to modify the material with element doping and to modify the material's nanostructure. Presently, the ZT value of SrTiO_3 is still low, as shown in the previous report at approximately 0.05 [9].

Researchers are applying several concepts to achieve the highest ZT of TE materials. Doping is beneficial for

improving charge carrier mobility in the electric field in the crystal lattice, resulting in increased σ [4]. Controlling cationic vacancies at the A-site is also gaining traction to improve TE characteristics [8]. The can be reduced by optimising doping levels and elements and introducing point defects [10]. In the case of $\text{Sr}_{(1-x)}\text{La}_x\text{TiO}_3$ (SLTO), La doping at an A-site has been widely used as a promising way to improve the TE properties of SrTiO_3 . At the same time, the La doping on the Sr site of SrTiO_3 increases the σ [11] and decreases κ [12]. Also, the thermoelectric properties of SrTiO_3 have been improved by incorporating phonon scattering centres to minimise heat conductivity while simultaneously enhancing the power factor [8]. As shown in a previous report, La-doped STO can improve the electrical conductivity where a low La doping level (2 mol%) of STO can be improved up to 19 times higher than undoped [13]. The La-doped STO can reduce as the κ declines from approximately 6.7 W/mK for $\text{La} = 0$ to 5.4 W/mK for $\text{La} = 0.08$ at 300 K [13]. As well, $\text{La}_{0.12}\text{Sr}_{0.88}\text{TiO}_3$ samples showed the lowest κ of 2.45 W/mK at 873 K [14]. The maximum ZT values of STO have also been enhanced by La doping. That variation depends on the La doping level; a La doping level of 8 mol% of STO showed the maximum ZT value of 0.20 at 1000 K [13], and the $\text{La}_{0.12}\text{Sr}_{0.88}\text{TiO}_3$ sample had the largest ZT of 0.28 at 773 K [14], and the ZT value of La-doped SrTiO_3 was 0.37 at 1045 K for $\text{La} = 0.08$ [15].

There have been many investigations of the preparation method of SrTiO_3 , including conventional solid-state reaction [4,11], mechanical alloying [13], spray pyrolysis [1], combustion synthesis [15], high-energy ball milling [16], and sol-gel auto-combustion method [17]. The sol-gel auto-combustion has shown good chemical uniformity, high product purity and crystallinity, easy stoichiometry control, and short processing time [18]. The sol-gel auto-

combustion has been widely used for the preparation of SrTiO₃. At the same time, sol-gel auto-combustion using a fuel mixture of glycine and citric acid produced a nanosized sample that was useful in enhancing its TE properties. Spark plasma sintering (SPS) is one of the advanced methods to rapidly produce nanostructured bulk samples [19]. The SPS method uses a high direct current (DC), fast heating rates, high pressure, and short dwell durations during the process, and the microstructure may be manipulated to retain ultra-fine grains with relative theoretical density [20].

The TE properties of SLTO synthesised by sol-gel auto-combustion are currently unknown, although these were recently reported to be almost created when conventional techniques were used. Therefore, in the present study, we sought to fully identify the TE properties of SLTO by synthesising SLTO samples with different La concentrations by sol-gel auto-combustion, following the SPS process for producing SLTO bulk samples. The TE properties of SLTO samples were investigated from room temperature to 800 K.

2. Experimental

A number of samples containing compound Sr_(1-x)La_xTiO₃ (SLTO, $x = 0, 0.01, 0.05, 0.07$, and 0.10) were synthesised by the sol-gel auto-combustion reaction. The raw materials included the commercial reagents strontium nitrate (Sr(NO₃)₂, Sigma-Aldrich), titanium(IV) butoxide (C₁₆H₃₆O₄Ti, Sigma-Aldrich), lanthanum(III) nitrate hexahydrate, (La(NO₃)₃·6 H₂O, Loba Chemie), citric acid monohydrate (C₆H₈O₇·H₂O, Loba Chemie), ethylene glycol (C₂H₆O₂, Loba Chemie), ammonium nitrate (NH₄NO₃) and glycine (C₂H₅NO₂, Ajax FineChem). The sol-gel auto-combustion method and the fuel ratio of auto-combustion reaction followed previous work [17,21]. The mixture solution of Sr(NO₃)₂, C₁₆H₃₆O₄Ti, La(NO₃)₃·6 H₂O, C₆H₈O₇·H₂O, NH₄NO₃ and C₂H₅NO₂ in DI water was heated and continuously stirred at 353 K for 2 hr to achieved homogenous nitrate precursor in transparent solution form. To form the metal/organic gels, C₂H₆O₂ was added. The mixture solution was heated and stirred continuously until it became a viscous gel which was immediately placed in the oven, which had been warmed to 473 K, for self-ignite combustion. In 1 hr, the precursor powder was successfully auto-combusted. The powder sample was calcined at 1173 K for 4 hr, which differed from previous work due to the production scale of the sample. The final products were pressed into a disk, followed by spark plasma sintering (SPS-515A, DR.SINTER LAB) in a flowing Ar atmosphere under a uniaxial pressure of 50 MPa at 1473 K for 5 min.

The phase composition of the powder and bulk samples was characterised by X-ray diffraction (XRD, Rigaku, Ultima IV) by using Cu-K_α radiation ($\lambda = 1.5406$ Å) over Bragg's angles ($2\theta, 10^\circ - 120^\circ$) at a step size of 0.02 and the step time of 0.5 s. The density (d) of the bulk samples was evaluated by the weight and dimensions of the samples. The surface morphology, microstructure and chemical compositions were determined using a scanning electron microscope (SEM, JEOL, JSM-6500F) outfitted with an energy-dispersive spectrometer (EDS), which was used to investigate the ratio between Sr and La in the STO. The electrical resistivity (ρ) and Seebeck coefficients (S) of the 10 mm × 2 mm × 1 mm SLTO sample were measured simultaneously in the

temperature range from 375 K to 800 K by a commercial instrument (ZEM-3, ULVAC) under Ar atmosphere/vacuum. The thermal conductivity (κ) was calculated based on $\kappa = \alpha C_p d$, where α is the thermal diffusion coefficient measured by laser flash apparatus (Netzsch, LFA-467), C_p was estimated from the Dulong-Petit rule, $C_p = 3nR$, where n is the number of atom per formula unit, R is the gas constant and d is the measured density of the bulk samples. The TE properties of the SLTO sample were investigated in the temperature range from room temperature to 800 K.

3. Result and discussion

The XRD pattern of the powdered SLTO sample after calcination is shown in Figure 1(a). Almost all the samples with a peak at the $2\theta = 22.78^\circ, 32.44^\circ, 40.08^\circ, 46.54^\circ, 52.51^\circ, 57.87^\circ, 67.90^\circ, 77.26^\circ, 81.77^\circ, 86.24^\circ, 95.14^\circ, 104.17^\circ, 113.67^\circ$ belonging to (100), (110), (111), (200), (210), (211), (220), (310), (311), (222), (321), (400), (330) planes exhibited a cubic perovskite SrTiO₃ phase, which agrees with JCPDS no. 00-35-0734. Although the impurity phase (TiO₂ anatase) at the $2\theta = 25.26^\circ$ was detected when La doping content increased, undoped STLO ($x = 0$) has no such impurities. Compared to our previous study [17], the formation of a small amount of anatase TiO₂ occurred probably due to insufficient calcination time for completely removing certain inorganic contaminants due to the scale-up preparation process. These impurity phases agree with the La-doped SrTiO₃ with $x = 0.10$ prepared by conventional solid-state reaction followed by sintering in 5%H₂/Ar, which found TiO₂ as an impurity [11]. The XRD pattern of SLTO bulk samples is presented in Figure 1 (b), together with the JCPDS no. 035-0734 of a cubic perovskite SrTiO₃ phase. It was found that all samples presented a pure SrTiO₃ phase, regarding the increasing temperature of the SPS process leading to entirely eliminated inorganic impurities [22,23]. This result means that the SPS process could promote the phase change from TiO₂ to SrTiO₃ and stabilise SrTiO₃.

The Rietveld refinement technique has been used to investigate the crystal structure of the composite material and unit cell information such as space group, cell location, cell orientation, and atomic distances using the Full-Prof program [17,21]. Figure 2 illustrates the final output from the Rietveld refinement analysis undertaken in our study of the SLTO sample for $x = 0.10$, including powder and bulk samples. The quality of fit of the refinement in terms of reliability indices, including goodness-of-fit (χ^2), R -factor (R_p , R_{wp} , R_{exp}), lattice parameter and cell volume of all samples in both powder and bulk, are summarised in Table 1. The quality of fit can vary depending on the quality of the experimental data, the complexity of the crystal structure, and other factors [24]. In both cases of SLTO powder and bulk samples, as shown in Figure 2, the quality of fit indicates a good agreement between the measured and calculated intensity profiles of all samples due to the $\chi^2 < 4$. In the case of SLTO powder (Figure 2(a)), the TiO₂ with anatase phase was a contaminant in the sample. This confirms that all bulk samples are in a cubic perovskite SrTiO₃ phase with no such impurities after the SPS process.

The lattice parameters obtained from the Rietveld refinement of both powder and bulk samples are presented in Table 1. The lattice parameters of undoped SLTO ($x = 0$) in our powder and bulk samples correspond to the literature

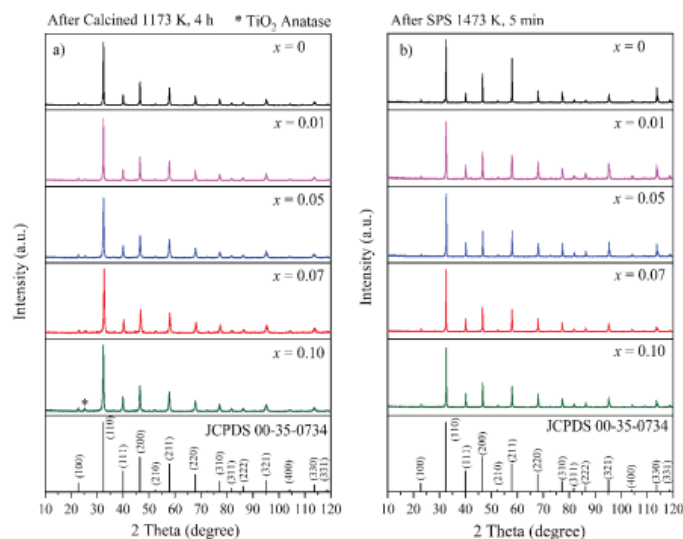


Figure 1. XRD pattern of SLTO sample with different La content ($x = 0, 0.01, 0.05, 0.07$, and 0.10): a) after calcination, and b) after SPS process.

data (JCPDS no. 035–0734). When the La doping contents increased, the lattice parameters of SLTO samples also increased due to lattice defects through the substitution of the larger ionic radius La^{3+} (1.15 Å) at that smaller ionic radius Sr^{2+} (1.13 Å), the difference valences of La^{3+} and Sr^{2+} ions, contain internal strain or local distortions, which was identified in previous work [6,17,25–27]. This occurred because the lattice parameters increased with the La content, which led to unit cell expansion of the SLTO samples. Besides, the Lattice parameter of SLTO bulk samples is relatively smaller than those of powder for the same composition as results of the sintering powders at high temperature and high pressure during SPS processing methods. As a result, the interatomic distances between the atoms in the bulk samples become smaller, and the lattice parameters decrease. The calculated unit cell density (d_{cal}) is expressed as mass of unit cell/volume of unit cell, which is obtained from the results of Rietveld refinement analysis. The d_{cal} of both the undoped SLTO powder and the bulk samples is relatively similar to the literature data. In contrast, the d_{cal} of the doped-SLTO samples increased with increasing the La content because the atomic mass of La is larger than Sr. During the SPS sintering process, the SLTO powders undergo plastic deformation and grain growth, which leads to the individual particles to fuse together and form a dense solid with a reduction in porosity and an increase in the density of the material.

Figure 3 shows the variation of the measured densities (d) and relative density ($d/d_{\text{cal}} \times 100\%$) of the SLTO bulk samples as a function of the La content (x). The d increased with increases in the La content, according to the d_{cal} , as described in Table 1. The d is very high and is above 96% of the theoretical density. The quality of d of the SLTO bulk samples synthesised by sol-gel auto-combustion was achieved using the SPS process, similar to the high d (5.12 g/cm³) of

La-doped SrTiO_3 prepared by combustion synthesis with post-SPS with a 5 min holding time [15].

The SEM of the SLTO powder samples with different La concentrations ($x = 0, 0.01, 0.05, 0.07$, and 0.10) are shown in Figure 4. The morphology of all the SLTO samples is a spherical shape. The particle size of the samples has a homogenous distribution of approximately 100 nm, indicating that the La doping content had an insignificant effect on the particle size. In addition, the brightness or contrast in SEM images is observed, indicating that the surface level of the sample is not flat with the working distance (WD) of the primary electron beam during SEM measurement. The brightness area represents the hilltop of the powder location of the sample, while the dark grey area represents the valley region of the powder. These results correspond to our previous work, where the particle size slightly decreased with an increase in the La concentration [17], together with the average grain size of $\text{Sr}_{1-x}\text{La}_x\text{TiO}_3$ nanopowders [28].

The SEM and EDS mapping analysis of images of all the SLTO bulk samples are presented in Figure 5. In the SEM images, the surface of all the bulk samples is homogenous without cracks. However, numerous pores were observed on the surface of the SLTO samples with $x = 0.0, 0.01$, and 0.05 , while the SLTO samples with $x = 0.07$ and 0.1 had a smooth surface. We can surmise that the pores probably occurred after the sample was cut and polished because the SLTO samples with $x = 0.0, 0.01$, and 0.05 present a higher relative density (Figure 3), leading to high stress and hardness with a brittle composition. The EDS analysis revealed that Sr, Ti, O or La were uniformly composed and distributed on all sample surfaces. The SEM and EDS mapping analysis confirmed that all the SLTO samples were homogenous without any impurity phases, which corresponded to the XRD results. The quantitative EDS analysis indicates that the

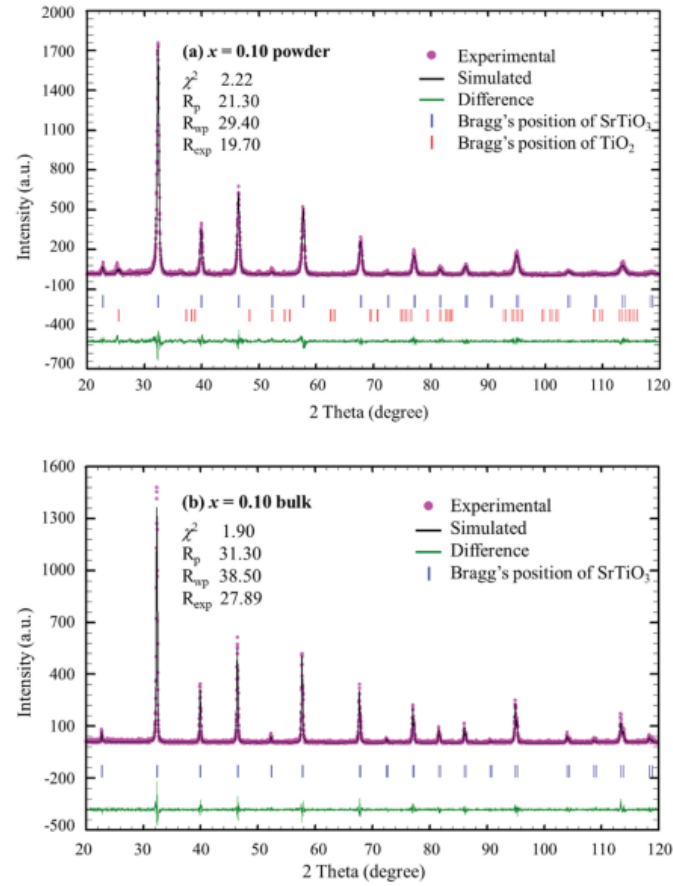


Figure 2. Typical Rietveld refinement analysis of SLTO sample for $x = 0.10$: (a) powder and (b) bulk samples.

Table 1. Chi-square (χ^2), R-factors (R_p , R_{wp} , R_{exp}), lattice parameter, cell volume, and calculated cell density (d_{cal}) of SLTO ($x = 0, 0.01, 0.05, 0.07$, and 0.10) powder and bulk.

Samples	χ^2	R_p	R_{wp}	R_{exp}	Lattice parameter $a = b = c$ (Å)	Cell volume (cm^3)	d_{cal} (g/cm^3)
JCPDS 00-035-0734					3.90500	59.550	5.120
Powder							
SLTO-0	2.35	16.30	23.90	15.61	3.90507	59.551	4.995
SLTO-0.01	2.22	16.10	23.90	16.03	3.90703	59.639	5.218
SLTO-0.05	2.25	24.00	30.60	20.39	3.90990	59.772	5.233
SLTO-0.07	2.19	20.50	37.80	25.55	3.91024	59.792	5.280
SLTO-0.10	2.22	21.30	29.40	19.70	3.91626	59.826	5.374
Bulk							
SLTO-0	2.84	42.90	46.60	27.63	3.90581	59.585	5.003
SLTO-0.01	2.30	27.30	35.70	23.56	3.90660	59.620	5.179
SLTO-0.05	2.45	22.80	31.40	20.05	3.90872	59.718	5.218
SLTO-0.07	2.09	19.20	28.40	19.61	3.90910	59.735	5.233
SLTO-0.10	1.90	31.30	38.50	27.89	3.91016	59.784	5.280

average chemical composition of all the samples was in relatively good agreement with the nominal compositions.

Figure 6 shows the temperature dependence of the electrical properties of the SLTO bulk samples. As shown in

Figure 6(a), the electrical conductivity (σ) of the La-doped SLTO samples slightly increased with the temperature rise, indicating a semiconductive behaviour. Unfortunately, the undoped SLTO sample could not be measured due to the

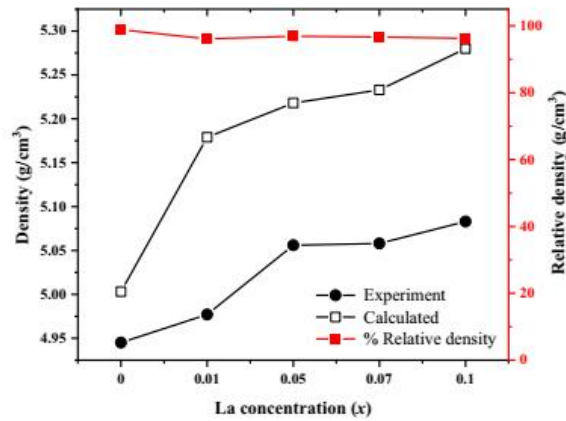


Figure 3. Variation of the measured density (d), calculated density (d_{cal}) and relative density of SLTO bulk samples as a function of La content (x).

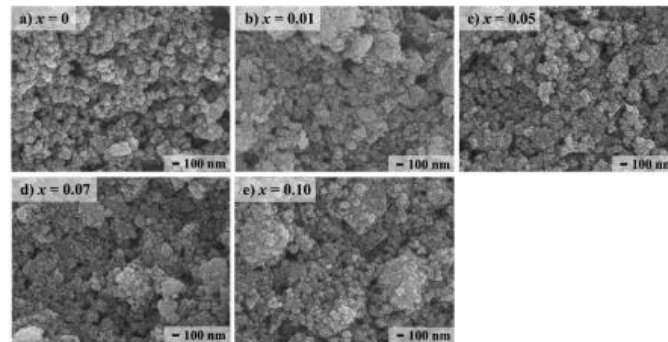
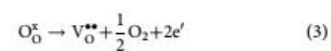
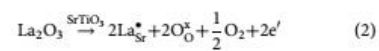


Figure 4. SEM of the SLTO powder sample with different La content ($x = 0, 0.01, 0.05, 0.07$, and 0.10).

large electrical resistivity (ρ). These results showed that the σ of the SLTO sample were improved by La doping due to increasing carrier concentration (n) by introducing oxygen vacancies (Eqs. 2-4). In addition, La dopant ionised reasonably well at all doping concentrations. Particularly, the σ of the SLTO sample with $x = 0.01$ was the largest of the samples, probably due to the optimisation of n and μ . Based on Eq. 4, uniform La doping can tune the n , thereby increasing the σ while reducing the μ . Therefore, it is necessary to perform the Hall measurements in order to further discuss the magnitude correlation in the electrical properties. When the La contents were larger than $x = 0.01$, lower values of σ were observed. These results may be caused by more structural distortion resulting from an increase in the La content leading to a change in the Fermi energy level, which is regularly investigated in polycrystalline and nanocrystalline materials due to decreasing the crystal size accelerating the structural distortion [13,29–31]. The defect reaction equations are expressed with La^{3+} as a typical donor-substituted SrTiO_3 , together with σ related to n through the carrier mobility (μ) and electrical charge (e), as follows [13,32–34]:



$$\sigma = ne\mu \quad (4)$$

The σ value of the La-doped SLTO sample was close to the order of magnitude σ of the $\text{La}_{0.08}\text{Sr}_{0.92}\text{TiO}_3$ ceramics samples prepared by a sol-gel process with different temperatures of SPS [35]. Compared to the related SLTO materials within the temperature range 300–600 K, these results corresponded to the 7.7 mol% La-doped SrTiO_3 nanostructured bulk produced by the SPS of chemically synthesised colloidal nanocrystals [31], nanoscale porosity of La-doped SrTiO_3 bulk [36], 10% mol% La-doped SrTiO_3 bulk with nano-scale modulation doping [37], and $\text{Sr}_{1-x}\text{Gd}_x\text{TiO}_{3-\delta}$ ceramics prepared by sol-gel process and SPS [32], together with co-doped SrTiO_3 such as La-Bi co-doped SrTiO_3 ceramics [4], and 10–30 mol% La-Nb co-doped SrTiO_3 [37].

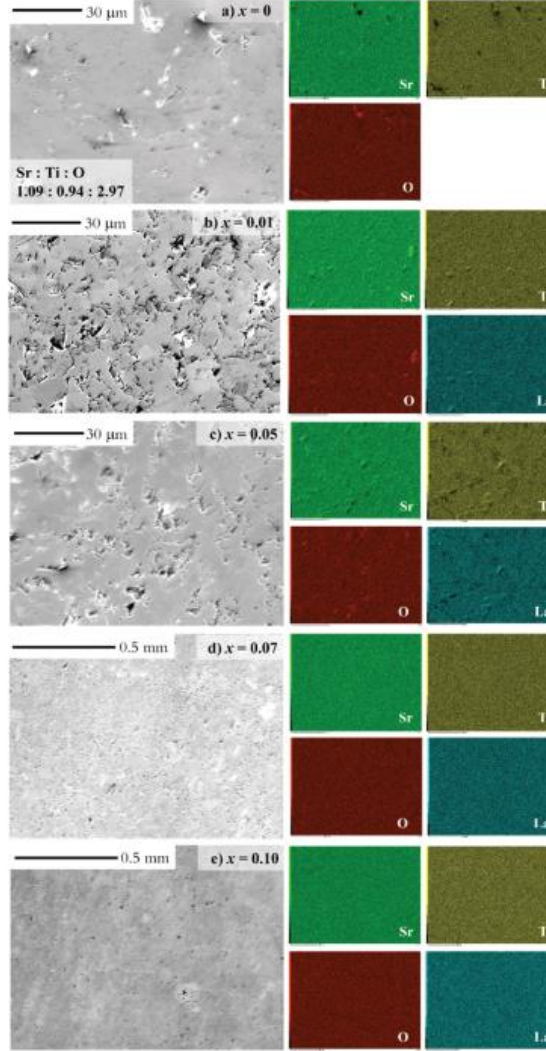


Figure 5. SEM and EDS mapping analysis of the SLTO bulk samples.

A negative Seebeck coefficient (S) value was observed for all samples, as shown in Figure 6(b), indicating that most charge carriers were electrons. These properties confirm that all the SLTO samples were typical n -type oxide TE ceramics. The absolute S ($|S|$) increased with increasing temperature. For the increase in the La content, the $|S|$ of $x = 0.01$ was the largest and reached a maximum ($417.4 \mu\text{V/K}$) at 800 K. At $x = 0.05$, those SLTO samples were lower. The $|S|$ of the related SLTO materials have been reported in the range of $165 \mu\text{V/K}$ to $250 \mu\text{V/K}$ at 1073 K [4,31,33,35,36,38]. In most cases of metal or degenerate semiconductors (parabolic band, energy-independent

scattering approximation), the S and σ will change opposite, according to the carrier concentration (n). The S is given by:

$$S = \frac{8\pi^2 k_B^2}{3eh^2} m^* T \left(\frac{\pi}{3n} \right)^{2/3} \quad (5)$$

where k_B is Boltzmann's constant, h is Planck's constant, e is the elementary charge, T is the absolute temperature, and the effective mass is m^* . However, A. Kikuchi et al. have presented that the S can also be expressed as [15]:

$$S = -\frac{k_B}{e} \left\{ r + 2 + \ln \frac{nh^3}{2(2\pi m^* k_B T)^{3/2}} \right\} \quad (6)$$

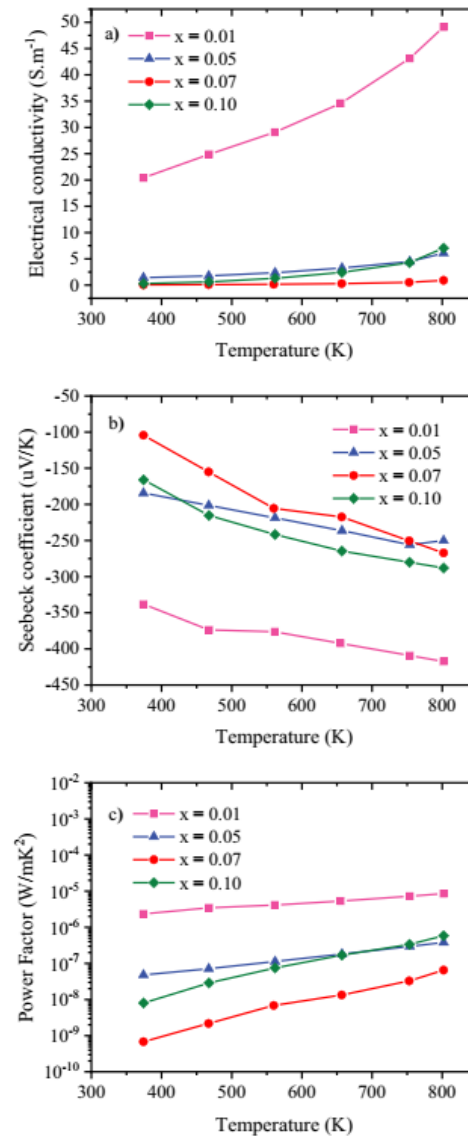


Figure 6. Temperature dependence of the electrical properties of SLTO bulk samples: (a) electrical conductivity (σ), (b) Seebeck coefficient (S), and (c) power factor (PF , $S^2\sigma$).

where r is the scattering factor. From Eqs. (4) and (6), it is found that the σ and S are proportional to the n . However, there are two situations where the $|S|$ may increase with increasing σ . One such situation is when the scattering of carriers is dominated by impurities or defects in the SLTO materials rather than by phonons or other scattering mechanisms. In this case, increasing the n can increase the σ while still maintaining a large $|S|$, resulting in an increase in

both properties. Another situation where the $|S|$ may increase with increasing σ is when the μ increases. If the μ increases, then the σ will also increase, but the $|S|$ may also increase if the n remains relatively low. This is because the μ can affect the thermoelectric power of the material, leading to an increase in the $|S|$. So, there are situations where the $|S|$ may increase with increasing σ . These situations may arise when the scattering of carriers is dominated by impurities or

defects or when the μ increases [39–41]. Both σ and the negative S values of all the samples increased with the increase in temperature, which accords with the behaviour of an n-type semiconductor. These trends correspond to the behaviour of related SLTO samples with specific temperature ranges of 300–600 K, such as the $\text{Sr}_{0.9}\text{La}_{0.1}\text{TiO}_3$ ceramics [4] and nanoscale porosity of La-doped SrTiO_3 bulk [36], or other related TE materials including the $\text{Ag}(\text{Sb}_{0.97}\text{Sn}_{0.03})\text{Te}_2$ compound [42] and poly[$\text{Cu}_x(\text{Cu-ett})$]-based organic TE material [43].

Based on the σ and S values, the power factor ($S^2\sigma$) was calculated and plotted as a function of temperature, as presented in Figure 6(c). The $S^2\sigma$ of all the samples gradually increased with increasing temperature and reached maximum values at 800 K. The SLTO sample with $x = 0.01$ exhibited a larger $S^2\sigma$ than other La content samples due to achieving a large S and σ simultaneously. The highest $S^2\sigma$ of the SLTO sample with $x = 0.01$ was $8.56 \times 10^{-6} \text{ W/mK}^2$ at 800 K, which was close to that of the $\text{Sr}_{0.9}\text{La}_{0.1}\text{TiO}_3$ ceramics [4], but lower than the $\text{Sr}_{0.92}\text{La}_{0.08}\text{TiO}_3$ ceramics prepared by SPS [35] and the $\text{Sr}_{0.9}\text{La}_{0.1}\text{TiO}_3$ ceramics [4,38] and 20 at % La-doped SLTO ceramics [36].

Figure 7(a) presents the temperature dependencies of thermal conductivity (κ) of the SLTO bulk samples. The κ of all the samples sharply decreased with increasing temperature, indicating that the κ comes mainly from lattice thermal conductivity (κ_{lat}). The lattice thermal conductivity (κ_{lat}) was evaluated by subtracting the electronic thermal conductivity (κ_{el}) from the thermal conductivity (κ), expressed as $\kappa_{lat} = \kappa - \kappa_{el}$. The κ_{el} was determined as $\kappa_{el} = L\sigma T$, where L is the Lorentz number ($L = 2.45 \times 10^{-8} \text{ W}\Omega\cdot\text{K}^{-2}$), σ is the electrical conductivity, and T is temperature. As shown in Figure 7(b), the κ_{el} also decreased with increasing temperature, roughly according to a T^{-1} relationship. Significantly, the reduction in κ was controlled by their reduction in κ_{lat} , which dominates κ in these SLTO ceramics. When temperature increases, the phonons are scattered by defects, grain boundaries, collision and/or impurities, which reduce the mean free path of the phonons. These trends are similar to those reported in previous reports [4,31,33,35,36,38]. In the case of increasing the La content, the κ decreased with the increase in the La content, which is related to the σ in terms of carrier concentration, according to the electrical properties (Figure 6). The minimum κ values for all SLTO samples were 4.44 W/mK ($x = 0.01$), 3.61 W/mK ($x = 0.05$), 3.59 W/mK ($x = 0.07$), and 3.55 W/mK ($x = 0.10$), at 800 K. It agrees

well with the previous study for SrTiO_3 with/without doped La [4,13,14,31,33,36,38,44]. The phenomenon could be explained by it being based on the different La content with the same SPS condition, which makes the large mass contrast in the lattice atoms (A-sites), indicating the mass difference between La^{3+} and Sr^{2+} was insignificantly affecting the reduction of κ . Especially, the sample with $x = 0.01$ exhibited the largest κ along the measured temperature range as the result of the largest σ (Figure 6(a)) and the high relative density (Figure 3).

The temperature dependence of the figures of merit (ZT) for the SLTO bulk samples with different La content is shown in Figure 8. In the whole measurement temperature range, the ZT increased with the increasing temperature, particularly where the SLTO with $x = 0.01$ steeply increased. The maximum ZT values of the SLTO sample with $x = 0.01$ was 1.5×10^{-3} at 800 K. Compared to the ZT values of La-doped SrTiO_3 , the maximum ZT values of the $\text{La}_{0.08}\text{Sr}_{0.92}\text{TiO}_3$ prepared by mechanical alloying was 0.20 at 1000 K [13], the $\text{La}_{0.12}\text{Sr}_{0.88}\text{TiO}_3$ prepared by conventional solid-state reaction sample exhibited maximum ZT of 0.28 at 773 K [14], a large ZT of $\text{Sr}_{0.92}\text{La}_{0.08}\text{TiO}_3$ prepared by combustion synthesis with the post-SPS process was 0.37 at 1045 K [15]. The $\text{Sr}_{1-3x}/2\text{La}_x\text{TiO}_3$ ($x = 0.15$) prepared by a solid-state reaction method with sintering in $\text{N}_2/5\% \text{H}_2$ presented the largest ZT = 0.41 at 973 K [33]. The $\text{Sr}_{0.09}\text{La}_{0.91}\text{TiO}_3$ synthesised by the colloidal method together with the SPS process exhibited a maximum ZT of ~0.37 at 973 K, which is one of the highest values for La-doped

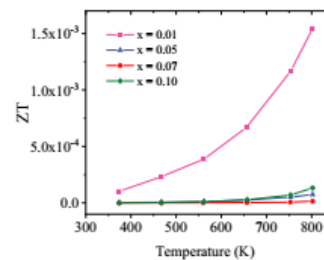


Figure 8. Temperature dependence of dimensionless figure-of-merit ZT of the bulk SLTO sample with different La concentrations.

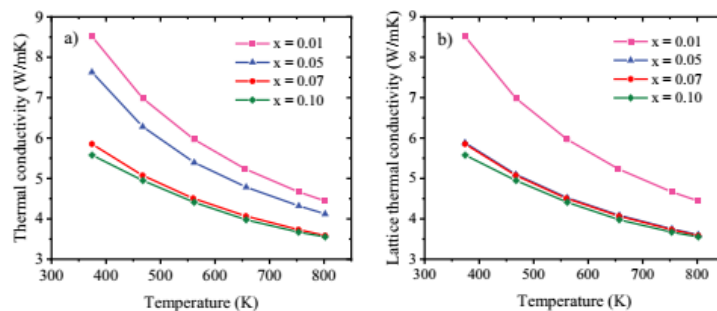


Figure 7. Temperature dependence of (a) thermal conductivity (κ) and (b) lattice thermal conductivity (κ_{lat}) of the SLTO bulk samples.

SrTiO₃ reported previously [31]. In addition, the TE properties of La-doped SrTiO₃ depend on the chemical composition, preparation, and processing condition, according to the particle sizes and grain mixtures from micro-to nanoscale [7,33,45]. So, the ZT of the SLTO synthesised by sol-gel auto-combustion exhibited a lower value than the SLTO that was prepared by several other methods such as mechanical alloying, conventional solid-state reaction, combustion synthesis and colloidal method due to lower σ . However, our study confirmed that the La dopant could enhance the TE property of SrTiO₃ with a lower concentration than previously reported.

4. Conclusion

The high-density SLTO bulk ceramics were effectively synthesised by the sol-gel auto-combustion method, following the SPS process. The impurity phase (TiO₂) was detected in the SLTO powder before it was transformed to SrTiO₃ and the SrTiO₃ phase was stabilised after the SPS process. Both the σ and negative S values of all the samples increased with temperature increases, in accordance with known n-type semiconductor behaviour. The κ of all the samples sharply decreased with temperature increases, indicating that the κ comes mainly from lattice thermal conductivity (κ_{lat}). The ZT increased with increasing temperature, particularly the SLTO with $x = 0.01$, which steeply increased and reached the maximum of 1.5×10^{-3} at 800 K. However, the ZT in this study was very low compared to previous studies due to a lower σ , probably affected by the preparation and processing conditions.

Highlights

- The present study is the first report on the TE property of La-doped SrTiO₃ (SLTO) synthesised by sol-gel auto-combustion.
- The La dopant can enhance the TE property of SLTO with a lower concentration than previously reported.
- The ZT of the SLTO exhibited a lower value due to lower electrical conductivity.

Acknowledgments

We would like to thank The National Science, Research and Innovation Fund (NSRF) through Naresuan University (R2565B028) and Thailand Science Research and Innovation (TSRI) through the Royal Golden Jubilee Ph.D. Program (PHD/0049/2560), which provided the budget. Many thanks also to the Institute for Faculty of Science and Technology, Rajamangala University of Technology Suvarnabhumi, Nonthaburi and Integrated Radiation and Nuclear Science, Kyoto University, Osaka, Japan for providing a facility for our thermoelectric measurements. We also wish to thank Mr Roy I. Morien of the Naresuan University Graduate School for his assistance in editing the grammar, syntax and English expression in this article.

Disclosure statement

No potential conflict of interest was reported by the author(s).

References

- [1] Singh SP, Kanas N, Desissa TD, et al. Thermoelectric properties of A-site deficient La-doped SrTiO₃ at 100–900 °C under reducing conditions. *J Eur Ceram Soc.* 2020;40(2):401–407.
- [2] Koumoto K, Wang Y, Zhang R, et al. Oxide thermoelectric materials: a nanostructuring approach. *Ann Rev Mater Res.* 2010;40(1):363–394.
- [3] Shi X-L, Wu H, Liu Q, et al. SrTiO₃-based thermoelectrics: progress and challenges. *Nano Energy.* 2020;78:105195.
- [4] Gong C, Dong G, Hu J, et al. Effect of reducing annealing on the microstructure and thermoelectric properties of La-Bi co-doped SrTiO₃ ceramics. *J Mater Sci - Mater Electron.* 2017;28(19):14893–14900.
- [5] Yin Y, Tudu B, Tiwari A. Recent advances in oxide thermoelectric materials and modules. *Vacuum.* 2017;146:356–374.
- [6] Janotti A, Jalan B, Stemmer S, et al. Effects of doping on the lattice parameter of SrTiO₃. *Appl Phys Lett.* 2012;100(26):262104.
- [7] Fergus JW. Oxide materials for high temperature thermoelectric energy conversion. *J Eur Ceram Soc.* 2012;32(3):525–540.
- [8] Srivastava D, Norman C, Azough F, et al. Improving the thermoelectric properties of SrTiO₃-based ceramics with metallic inclusions. *J Alloys Compd.* 2018;731:723–730.
- [9] Muta H, Kurosaki K, Yamanaka S. Thermoelectric properties of reduced and La-doped single-crystalline SrTiO₃. *J Alloys Compd.* 2005;392(1–2):306–309.
- [10] Sun J, Singh DJ. Thermoelectric properties of n-type SrTiO₃. *APL Mater.* 2016;4(10):104803.
- [11] Li X, Zhao H, Zhou X, et al. Electrical conductivity and structural stability of La-doped SrTiO₃ with A-site deficiency as anode materials for solid oxide fuel cells. *Int J Hydrogen Energy.* 2010;35(15):7913–7918.
- [12] Buscaglia MT, Maglia F, Anselmi-Tamburini U, et al. Effect of nanostructure on the thermal conductivity of La-doped SrTiO₃ ceramics. *J Eur Ceram Soc.* 2014;34(2):307–316.
- [13] Liu D, Zhang Y, Kang H, et al. Direct preparation of La-doped SrTiO₃ thermoelectric materials by mechanical alloying with carbon burial sintering. *J Eur Ceram Soc.* 2018;38(2):807–811.
- [14] Shang P-P, Zhang B-P, Liu Y, et al. Preparation and thermoelectric properties of La-Doped SrTiO₃ ceramics. *J Electron Mater.* 2011;40(5):926–931.
- [15] Kikuchi A, Okinaka N, Akiyama T. A large thermoelectric figure of merit of La-doped SrTiO₃ prepared by combustion synthesis with post-spark plasma sintering. *Scripta Mater.* 2010;63(4):407–410.
- [16] Liu D, Wang Y, Jiang X, et al. Ultrahigh electrical conductivities and low lattice thermal conductivities of La, Dy, and Nb Co-doped SrTiO₃ thermoelectric materials with complex structures. *J Mater Sci Technol.* 2020;52:172–179.
- [17] Nunocha P, Kaewpanha M, Bongkarn T, et al. A new route to synthesizing La-doped SrTiO₃ nanoparticles using the sol-gel auto combustion method and their characterization and photocatalytic application. *Mater Sci Semicond Process.* 2021;134:106001.
- [18] Sutka A, Mezinskis G. Sol-gel auto-combustion synthesis of spinel-type ferrite nanomaterials. *Front Mater Sci.* 2012;6(2):128–141.
- [19] Kabir A, Colding-Jørgensen S, Molin S, et al. Electrical conductivity of nanostructured acceptor-doped ceria fabricated by spark plasma sintering (SPS). *Mater Lett.* 2020;279:128513.
- [20] Anselmi-Tamburini U, Garay JE, Munir ZA. Fast low-temperature consolidation of bulk nanometric ceramic materials. *Scripta Mater.* 2006;54(5):823–828.
- [21] Nunocha P, Kaewpanha M, Bongkarn T, et al. Effect of Nb doping on the structural, optical, and photocatalytic properties of SrTiO₃ nanopowder synthesized by sol-gel auto combustion technique. *J Asian Ceram Soc.* 2022;10(3):583–596.
- [22] Rahman MYA, Samsuri SAM, Umar AA. TiO₂-SrTiO₃ composite photoanode: effect of strontium precursor concentration on the performance of dye-sensitized solar cells. *Appl Phys A.* 2019;125(1):59.
- [23] Zavjalov AP, Shichalin OO, Tikhonov SA, et al. Features of reactive SPS of SrTiO₃-TiO₂ biphasic ceramics. *IOP*

- Conference Series: Materials Science and Engineering; 2020 Sep 21st-25th; Tomsk, Russia. 2021. p. 012034.
- [24] Toby BH. R factors in rietveld analysis: how good is good enough? *Powder Diffr.* 2006;21(1):67–70.
- [25] Kobayashi S, Ikuhara Y, Mizoguchi T. Lattice expansion and local lattice distortion in Nb- and La-doped SrTiO₃ single crystals investigated by x-ray diffraction and first-principles calculations. *Phys Rev B.* 2018;98(13):134114.
- [26] Yang D, Zou X, Sun Y, et al. Fabrication of three-dimensional porous La-doped SrTiO₃ microspheres with enhanced visible light catalytic activity for Cr(VI) reduction. *Front Chem Sci Eng.* 2018;12(3):440–449.
- [27] Miyauchi M, Takashio M, Tobimatsu H. Photocatalytic activity of SrTiO₃ codoped with nitrogen and lanthanum under visible light illumination. *Langmuir.* 2004;20(1):232–236.
- [28] Songwattanasin P, Karaphun A, Phokha S, et al. Influence of La concentration on structural, morphological, optical and magnetic properties of Sr_{1-x}La_xTiO₃ nanopowders. *Phys B Condens Matter.* 2019;571:213–221.
- [29] Wang HC, Wang CL, Su WB, et al. Synthesis and thermoelectric performance of Ta doped Sr_{0.9}La_{0.1}TiO₃ ceramics. *Ceram Int.* 2011;37(7):2609–2613.
- [30] Santander-Syro AF, Copie O, Kondo T, et al. Two-dimensional electron gas with universal subbands at the surface of SrTiO₃. *Nature.* 2011;469(7329):189–193.
- [31] Park K, Son JS, Woo SI, et al. Colloidal synthesis and thermoelectric properties of La-doped SrTiO₃ nanoparticles. *J Mater Chem A.* 2014;2(12):4217–4224.
- [32] Li L, Liu Y, Qin X, et al. Enhanced thermoelectric performance of highly dense and fine-grained (Sr_{1-x}Gd_x)TiO_{3-δ} ceramics synthesized by sol-gel process and spark plasma sintering. *J Alloys Compd.* 2014;588:562–567.
- [33] Lu Z, Zhang H, Lei W, et al. High-Figure-of-Merit thermoelectric La-Doped A-Site-Deficient SrTiO₃ ceramics. *Chem Mater.* 2016;28(3):925–935.
- [34] Qin M, Gao F, Wang M, et al. Fabrication and high-temperature thermoelectric properties of Ti-doped Sr_{0.9}La_{0.1}TiO₃ ceramics. *Ceram Int.* 2016;42(15):16644–16649.
- [35] Shang P-P, Zhang B-P, Li J-F, et al. Effect of sintering temperature on thermoelectric properties of La-doped SrTiO₃ ceramics prepared by sol-gel process and spark plasma sintering. *Solid State Sci.* 2010;12(8):1341–1346.
- [36] Ahmed AJ, Nazrul Islam SMK, Hossain R, et al. Enhancement of thermoelectric properties of La-doped SrTiO₃ bulk by introducing nanoscale porosity. *R Soc Open Sci.* 2019;6(10):190870.
- [37] Wang J, Zhang B-Y, Kang H-J, et al. Record high thermoelectric performance in bulk SrTiO₃ via nano-scale modulation doping. *Nano Energy.* 2017;35:387–395.
- [38] Hanbo LI, Ganhong Z, Zhenxiang DAL, et al. Thermoelectric properties of Sr_{0.9}La_{0.1}TiO₃ and Sr_{2.7}La_{0.3}Ti₂O₇ with 15% Ag addition. *J Rare Earth.* 2014;32(4):314–319.
- [39] Snyder GJ, Toberer ES. Complex thermoelectric materials. *Nature Mater.* 2008;7(2):105–114.
- [40] Heremans JP, Jovovic V, Toberer ES, et al. Enhancement of thermoelectric efficiency in PbTe by distortion of the electronic density of states. *Science.* 2008;321(5888):554–557.
- [41] Zebbarjadi M, Esfarjani K, Dresselhaus MS, et al. Perspectives on thermoelectrics: from fundamentals to device applications. *Energy Environ Sci.* 2012;5(1):5147–5162.
- [42] Mohanraman R, Sankar R, Chou F-C, et al. Influence of nanoscale Ag₂Te precipitates on the thermoelectric properties of the Sn doped P-type AgSbTe₂ compound. 2014;2(9):096114.
- [43] Sun Y, Sheng P, Di C, et al. Organic thermoelectric materials and devices based on p- and n-Type poly(metal 1,1,2,2-ethene tetrathiolate)s. *Adv Mater.* 2012;24(7):932–937.
- [44] Rahman JU, Nam WH, Van Du N, et al. Oxygen vacancy revived phonon-glass electron-crystal in SrTiO₃. *J Eur Ceram Soc.* 2019;39(2–3):358–365.
- [45] Li J-F, Liu W-S, Zhao L-D, et al. High-performance nanostructured thermoelectric materials. *NPG Asia mater.* 2010;2(4):152–158.